High-Voltage Monolithic Active Pixel Sensors
for the PANDA Luminosity Detector
and
Search for the Decay $e^+e^- \rightarrow \eta_c\eta\pi^+\pi^-$ at Center of Mass Energies
between 4.23 - 4.36 GeV at BESIII

Dissertation
zur Erlangung des Grades
"Doktor
der Naturwissenschaften"
am Fachbereich Physik, Mathematik und Informatik
der Johannes Gutenberg-Universität
in Mainz

TOBIAS WEBER

geb. in Neuwied
Mainz, den 1. Juni 2016

Datum der mündlichen Prüfung: 26.10.2016

ABSTRACT

Although quantum chromodynamics is regarded as the quantum field theoretical description of the strong interaction, many open questions remain. Especially the existence of so called exotic states is an open issue. In recent years it has drawn attention to it by the discovery of many new, unexpected states in the charmonium mass region. The properties of these resonances are not consistent with previously known bound states of quantum chromodynamics, i.e. mesons and baryons. The most famous of these states are the X(3872) and the $Z_c(3900)^{\pm}$. To reveal the internal structure of these new states, precise measurements of their line shapes are needed. Furthermore, new states have to be searched for to understand the underlying pattern amongst the new states. The BESIII experiment in Beijing and the planned PANDA experiment in Darmstadt will play an important part in this task.

PANDA will use energy scan measurements to determine the line shape of resonances with high precision. The luminosity is needed for the relative normalization of the individual scan points, and enters as a systematic uncertainty into such a measurement. Therefore, PANDA will use a dedicated luminosity detector to measure the luminosity with high accuracy. It will employ four layers of novel silicon pixel sensors (HV-MAPS) to measure the tracks of elastically scattered antiprotons to determine the luminosity. In this work a data acquisition system and a tracking station have been developed. With this setup the sixth prototype version of the HV-MAPS sensor has been completely characterized, e.g. in terms of the signal-to-noise ratio and the hit detection efficiency.

The second part of this work deals with the search for new resonances at BESIII. The $Z_c(3900)$ was discovered by the BESIII collaboration in the decay $Y(4260) \to J/\psi\pi^+\pi^-$ and has been found in all three charged states by now. Its discovery suggest the existence of the up to now unobserved isospin triplet $\eta_c\pi^{\pm,0}$ and of the $\eta_c\eta$ isospin singlet. Using the high statistic datasets at center of mass energies between 4.23 GeV and 4.36 GeV available at BESIII, a resonant substructure in the $\eta_c\eta$ subsystem of the decay $e^+e^- \to \eta_c\eta\pi^+\pi^-$ is searched for. As no significant η_c signal is found, upper limits on the cross section of the reaction $e^+e^- \to \eta_c\eta\pi^+\pi^-$ at the center of mass energies of 4.23, 4.26 and 4.36 GeV are established to be 3.47, 5.98 and 19.02 pb respectively.

ZUSAMMENFASSUNG

Obwohl die Quantenchromodynamik als feldtheoretische Beschreibung der starken Wechselwirkung weithin akzeptiert ist, verbleiben viele ungelöste Fragen. Insbesondere die mögliche Existenz von so genannten exotischen Zuständen hat in den letzten Jahren durch die Entdeckung neuer, unvorhergesagter Resonanzen in der Charmoniummassenregion viel Aufmerksamkeit auf sich gezogen. Die Eigenschaften dieser Zustände können nicht mit denen bereits bekannter Zustände der starken Wechselwirkung in Einklang gebracht werden. Die bekanntesten dieser Zustände sind das X(3872) und das $Z_c(3900)^{\pm}$. Zur Aufklärung der inneren Struktur ist zum einen die exakte Vermessung der Linienform bereits bekannter Zustände nötig. Ferner muss nach neuen Zuständen gesucht und deren Zerfälle untersucht werden, um das zugrunde liegende Muster hinter diesen Zuständen aufzudecken. Sowohl das BESIII Experiment in Peking als auch das zukünftige PANDA-Experiment in Darmstadt werden hier wichtige Beiträge liefern.

PANDA wird anhand von Energiescan-Messungen die Linienform von Resonanzen vermessen. Hierbei wird die Luminosität zur relativen Normierung der Scanpunkte untereinander benötigt und geht als systematische Unsicherheit in eine solche Messung ein. Daher wird PANDA einen dedizierten Luminositätsdetektor verwenden, um die Luminosität mit hoher Genauigkeit zu messen. Dieser besteht aus vier Lagen von neuartigen Siliziumpixelsensoren (HV-MAPS), um die Spuren von elastisch gestreuten Antiprotonen zu rekonstruieren und mit diesen die Luminosität zu bestimmen. Für diese Arbeit wurden ein Datenerfassungssystem zum Test von Prototypen dieser Sensoren und eine Tracking Station aufgebaut. Mit diesem Aufbau wurde die sechste Iteration von Prototypen der HV-MAPS vollständig charakterisiert und Eigenschaften wie das Signal-zu-Rauschverhältnis oder die Rekonstruktionseffizienz von Treffern bestimmt.

Der zweite Teil der Arbeit beschäftigt sich mit der Suche nach neuen Zuständen bei BESIII. Das $Z_c(3900)$ wurde von der BESIII Kollaboration im Zerfall Y(4260) $\rightarrow J/\psi\pi^+\pi^-$ entdeckt und inzwischen in allen drei Ladungszuständen nachgewiesen. Seine Existenz legt nahe, dass auch das bislang unbeobachtete Isospin-Triplet $\eta_c\pi^{\pm,0}$ und das Isospin-Singlet $\eta_c\eta$ existieren. Mit den umfangreichen Datensätzen, die BESIII in e^+e^- Kollisionen bei Schwerpunktsenergien zwischen 4.23 GeV und 4.36 GeV aufgezeichnet hat, wurde im $\eta_c\eta$ Subsystem der Reaktion $e^+e^- \rightarrow \eta_c\eta\pi^+\pi^-$ nach resonanten Strukturen gesucht. Da kein signifikantes η_c Signal gefunden wurde, wird eine obere Grenze für den Wirkungsquerschnitt der Reaktion $e^+e^- \rightarrow \eta_c\eta\pi^+\pi^-$ bei den drei Schwerpunktsenergien 4.23, 4.26 und 4.36 GeV zu 3.47, 5.98 und 19.02 pb extrahiert.

CONTENTS

MOTIVATION

The standard model of particle physics summarizes our theoretical understanding of particle physics using three interactions. Quantum Electrodynamics (QED) describes the interaction of electrically charged particles and includes classical electrodynamics as a border case. The weak interaction governs the decay of particles like the decay of the neutron. Together with QED it can be unified to the electroweak interaction. The behavior of the quarks, the constituents of the nucleons, is ruled by the strong interaction or Quantum Chromodynamics (QCD) which is also responsible for the attractive forces between the nucleons in the atomic nucleus. All three interactions are formulated as gauge theories, quantum field theories with an underlying local symmetry, where the interaction is mediated by gauge bosons (particles with even spin). The symmetry group of the standard model is

$$SU(3)_C \otimes SU(2)_L \otimes U(1)$$

where $SU(3)_C$ is the symmetry group of QCD and $SU(2)_L \otimes U(1)$ is the symmetry group of the electroweak interaction. The properties of the arising gauge bosons are summarized in table 1. The photon is the gauge boson of QED. Since the photon is massless, the range

gauge boson	mass GeV/c^2	spin	interaction
photon	0	1	electro-magnetism
W$^\pm$/Z	$80.3 \pm 00.15/91.187 \pm 0.002$	1	weak
gluon(s)	0	1	strong
graviton	$< 6 \cdot 10^{-41}$	2	gravitation

Table 1: Gauge bosons of the standard model with masses taken from the particle data group [1]. Note that the existence of the graviton has only been postulated by theory.

of electromagnetism is infinite. The weak interaction is mediated by the massive W and Z bosons which leads to the short range of the weak interaction. The strong interaction is mediated by eight gauge bosons who are also called gluons. In contrast to the other interactions, gravity has not yet been expressed as a quantum field theory. Its postulated gauge boson, the graviton, should have a vanishing mass to explain the infinite range of gravitation.

In addition to the forces, the standard model contains twelve elementary particles: six quarks, six leptons, and their corresponding antiparticles. The quarks are the building blocks of the hadrons which are bound by the strong interaction. The leptons on the other hand only interact weakly or electromagnetically. All elementary particles are fermions with odd spin 1/2. They are organized in three families, or generations, that are shown in table 2. The first family consists of the two lightest quarks and the electron/electron neutrino and forms the natural matter. The second family generates unstable particles and is a good field for hadron spectroscopy, i.e the spectroscopy of bound states generated by QCD. The third family contains the heaviest constituents and the life time of the top-quark is too short to build bound states. The origin of mass of the elementary particles, especially the W and Z gauge bosons, is explained with the Higgs-mechanism. It introduces a scalar field whose interaction with the elementary particles generates their masses. An important

Generation	I		II		III	
Quarks						
	up	**d**own	**c**harm	**s**trange	**t**op	**b**ottom
mass [MeV/c^2]	$2.3^{+0.7}_{-0.5}$	$4.8^{+0.5}_{-0.3}$	1275 ± 25	95 ± 5	(173.21 ± 0.51)k	4180 ± 30
charge	$\frac{2}{3}$e	$-\frac{1}{3}$e	$\frac{2}{3}$e	$-\frac{1}{3}$e	$\frac{2}{3}$e	$-\frac{1}{3}$e
I(J^{P})	$\frac{1}{2}\left(\frac{1}{2}^{+}\right)$	$\frac{1}{2}\left(\frac{1}{2}^{+}\right)$	$0\left(\frac{1}{2}^{+}\right)$	$0\left(\frac{1}{2}^{+}\right)$	$0\left(\frac{1}{2}^{+}\right)$	$0\left(\frac{1}{2}^{+}\right)$
Leptons						
	e	ν_e	μ	ν_μ	τ	ν_τ
mass [MeV/c^2]	0.511	$< 2 \cdot 10^{-6}$	105.66	< 0.19	1776.82 ± 0.16	< 18.2
charge	1 e	0	1 e	0	1 e	0

Table 2: The three generations of elementary particles with masses in the $\overline{MS}$ scheme according to the particle data group [1]. $I(J^P)$ gives the strong isospin I, total angular momentum J, and parity P.

prediction of the Higgs-mechanism is the Higgs-boson. A neutral boson compatible with a standard model Higgs-boson and a mass of

$$m = 125.7 \pm 0.4 \ \mathrm{GeV}/c^2$$

was discovered in 2012 at CERN [1, 2, 3]. Although the standard model is able to describe many phenomena, it leaves many open questions. These questions include, for example, the nature of dark matter and issues in QCD.

In the field of QCD the existence of so called exotic states has long been predicted. In contrast to already established bound states of QCD which consist either of a quark anti-quark pair (mesons) or three quarks (baryons), these exotic states have another internal configuration. These possible configurations include bound states of gluons called glueballs, hybrid states made of quarks and gluons, tetra-, and pentaquark states. However, no experimental evidence for the existence of such states had been found for a long time. Excitement has been caused by the recent discovery of unpredicted states in the charmonium ($c\bar{c}$ states) mass region. The most prominent examples are the $X(3872)$ and the $Z_c(3900)^{\pm}$. The decays and properties of these new particles suggest that they have a different, so far unobserved, internal structure. Precision measurements with high statistics and searches for new resonances are needed to reveal the true internal structure of these states and to solve other open questions. Two key experiments looking to accomplish this, are the Beijing Electron Synchroton III (BESIII) experiment in Beijing and the planned Antiproton Annihilation at Darmstadt (PANDA) experiment at the FAIR facility in Darmstadt.

For many measurements at PANDA the luminosity needs to be determined with high precision. For this reason a dedicated luminosity detector is foreseen which will be placed inside vacuum close to the beam axis. It measures the luminosity by reconstructing the tracks of elastically scattered antiprotons in four layers of silicon pixel sensors. Because of the requirements imposed on the sensors, it was decided to use novel silicon pixel sensors (HV-MAPS) for the PANDA luminosity detector. One aim of this thesis was to characterize prototypes of these sensors in terms of their analogue performance and efficiency. For this reason a data acquisition system and a tracking station were developed.

The discovery of the $Z_c(3900)^{\pm}$ suggests the existence of an yet unobserved $Z_c^{\pm,0}$ decaying into $\eta_c \pi^{\pm,0}$. If such an isospin triplet exists, one also could expect the existence of an isospin singlet $Z_c^0 \to \eta_c \eta$. The observation of this resonance would add important information to the underlying pattern of new states and would enhance the understanding of their internal structure. Therefore, the second aim of this thesis was to search for resonant substructures in the $\eta_c \eta$ and $\eta_c \pi^{\pm}$ systems of the reaction $e^+ e^- \to \eta_c \eta \pi^+ \pi^-$ using the high statistics datasets collected by the BESIII collaboration at center of mass energies between 4.23-4.36 GeV.

In the first chapter a brief introduction to the theoretical background of QCD is given and the present knowledge in the field of hadron spectroscopy is summarized. Chapter two introduces the physics programs and the detectors of the two experimental collaborations, PANDA and BESIII. In the third chapter the concept of the luminosity measurement at PANDA is discussed and the current design of the PANDA luminosity detector is presented while chapter four gives an introduction to semiconductor detectors and different silicon sensor technologies suitable for position sensitive particle detection. The results of laboratory measurements with sensor prototypes are discussed in chapter five, along with the outcome of beam time measurements with a tracking station consisting of four layers of prototype chips. In the sixth chapter the event selection for the decay $e^+ e^- \to \eta_c \eta \pi^+ \pi^-$ is described while the performance of the event selection in terms of efficiency and background rejection is described in chapter 7. Chapter 8 shows the outcome of the data analysis and an upper limit is calculated on the signal cross section after the systematic uncertainties of the measurement have been studied. Chapter 9 summarizes the outcome of this work.

1
QUANTUM CHROMODYNAMICS

1.1 The QCD Lagrangian

In the 1950s a large number of new particles, called hadrons, were discovered by experimental particle physics. The properties of these particles could be explained by postulating the existence of three new particles with fractional charge. These particles, which make up the hadrons, are called quarks [4, 5]. However, some hadrons (e.g. the Δ^{++}) would possess a completely symmetric wave function in spite of being fermions. This is a contradiction to the Pauli principle. This issue was solved by introducing a new degree of freedom called the color-charge [6, 7]. The existence of quarks was proven by deep inelastic scattering experiments and one source of evidence for color-charge is given by the ratio of the annihilation cross sections [8]

$$R = \frac{\sigma(e^+e^- \to \text{hadrons})}{\sigma(e^+e^- \to \mu^+\mu^-)}.$$

Today's quantum field theory formulation of this model is called Quantum Chromodynamics (QCD). The Lagrangian density of QCD is given by

$$\mathcal{L}_{QCD} = \sum_f \bar{q}_f(i\slashed{D} - m_f)q_f - \frac{1}{4}\mathcal{G}_{\mu\nu,a}\mathcal{G}_a^{\mu\nu} \tag{1.1}$$

where f is the quark flavor index, m_f the quark mass, and q_f is defined as

$$q_f = \begin{pmatrix} q_{f,\textbf{red}} \\ q_{f,\textbf{green}} \\ q_{f,\textbf{blue}} \end{pmatrix}$$

with a Dirac spinor for each of the three colors. $\bar{q}_f$ and $\slashed{D}$ are given by

$$\bar{q}_f = q_f^\dagger \gamma^0$$
$$\slashed{D} = \gamma_\mu D^\mu$$

where γ_μ are the so called γ matrices. The covariant derivative D_μ and the field strength tensors $\mathcal{G}_{\mu\nu,a}$ are given by

$$D_\mu q = \partial_\mu q + ig_s \sum_{a=1}^8 \frac{\lambda_a^c}{2}\mathcal{A}_{\mu,a}q \tag{1.2}$$

$$\mathcal{G}_{\mu\nu,a} = \partial_\mu \mathcal{A}_{\nu,a} - \partial_\nu \mathcal{A}_{\mu,a} - g_s f_{abc}\mathcal{A}_{\mu,b}\mathcal{A}_{\nu,c} \tag{1.3}$$

with the massless gauge fields $\mathcal{A}_{\nu,a}$, the Gell-Mann matrices λ_a, and the structure constants f_{abc} of the SU(3) color symmetry group. The gauge fields are called gluons. As the SU(3) group is a non-abelian gauge group, the field strength tensors contain a term which is quadratic in the gauge fields. This leads to interaction terms between three and four gauge fields in addition to the "normal" interaction of the gauge field with matter. All
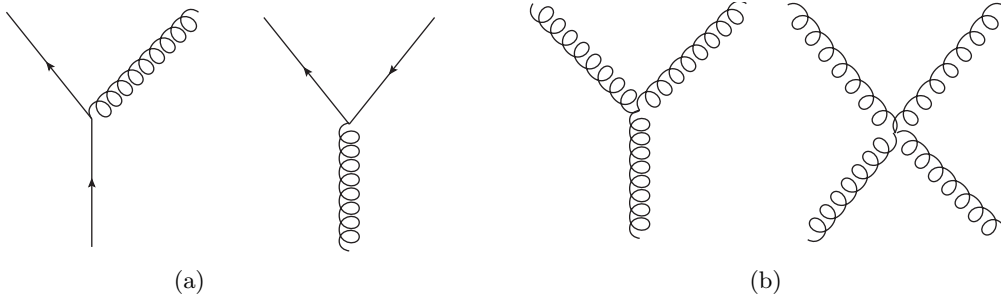
Figure 1: Interactions of quarks and gluons in QCD. (a) Radiation of a gluon by a quark and gluon decay to a quark antiquark pair. (b) Self-coupling of three or four gluons.

possible couplings occur with the same coupling strength g_s. The possible interactions of QCD are shown in figure 1. This self-interaction between the gluons leads to two important properties of QCD: *confinement* and *asymptotic freedom*. The coupling strength which can be redefined to be

$$\alpha_s = \frac{g_s^2}{4\pi},\tag{1.4}$$

depends on the momentum transfer Q^2 during an interaction. Two processes contribute to the momentum transfer dependence. The decay of gluons into a quark and anti-quark pair leads to a screening of the color charge. Analogous to Quantum Electrodynamics (QED) this would lead to an increase of the effective coupling strength with increasing Q^2 (or decreasing distance between the quarks as $r \propto Q^{-2}$). Due to the self interaction of gluons, however, a gluon can decay into a gluon loop which results in an anti-screening effect. Because of this the net charge reduces with increasing Q^2 and the coupling strength gets smaller. For QCD the behavior of the coupling strength can be derived using perturbation theory [9]

$$\alpha_s(Q^2) = \frac{12\pi}{(11n_c - 2n_f)\ln(Q^2/\Lambda^2)} \text{ with } Q^2 \gg \Lambda^2 \tag{1.5}$$

where n_c is the number of colors and n_f is the number of quark flavors. For $n_c > 2/11 \cdot n_f$ the coupling strength will decrease for increasing momentum transfer Q^2. Λ is a free parameter of QCD and is estimated to be in the range of $100\,\text{MeV} < \Lambda < 500\,\text{MeV}$ from experimental measurements [9]. The dependence of the coupling strength on the momentum transfer is depicted in figure 2. The coupling strength decreases with increasing momentum transfer and quarks are asymptotically free at short distances, while at larger distances or low momentum transfer the coupling strength increases and quark pairs cannot be separated and are confined within a color neutral state. Because of this the range of the strong interaction is limited in spite of the gluons being massless. This is in agreement with experimental observation.

Due to the high strength of the coupling, the low Q^2 region is not accessible for theoretical calculations using perturbation theory. Several alternative approaches have been developed. The most general approach is *Lattice QCD* where space-time is discretized to reduce the continuum theory to a numerical problem [10]. The resulting numerical computations are very resource intensive, but offer a calculation of QCD effects from first principles. Another approach are *effective* field theories. An effective field theory at low energies is chiral perturbation theory. It makes use of the left-right symmetry of the QCD Lagrangian
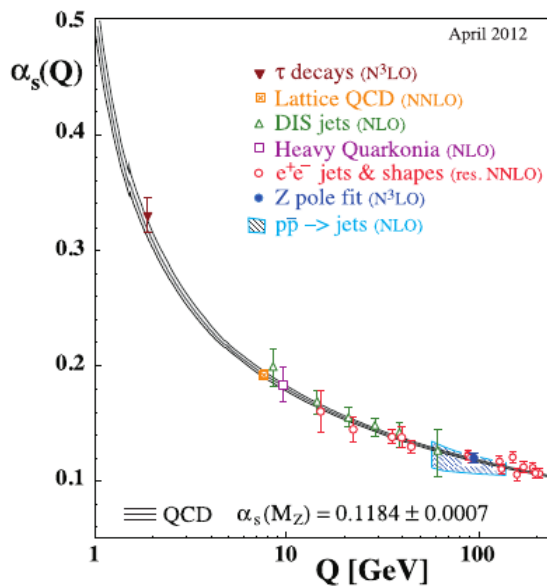
Figure 2: Dependence of the strong coupling constant α_s on the momentum transfer Q [1]. Shown are the results of measurements at different vales of Q. The degree of QCD perturbation theory used during the extraction of α_s is indicated in brackets. The curves represent QCD predictions for different values of Λ.

in the limit of vanishing quark masses by constructing an effective theory with the light mesons as degrees of freedom. A further method used for heavy quarkonia is *non-relativistic QCD*. Here one makes use of the fact that relativistic effects are small in bound states of heavy quark anti-quark pairs like charmonium. Furthermore, an effective potential can be derived for heavy quarkonia in analogy to the positronium potential. The so called Cornell potential is given by [11]

$$V = -\frac{4}{3}\frac{\alpha_s(r)}{r} + k \cdot r \tag{1.6}$$

with the distance r between the quark and anti-quark and the string tension k. For small distances the interaction is dominated by one-gluon exchange. Therefore, the potential resembles a Coulomb potential which arises from the one photon exchange in QED with the electromagnetic coupling constant replaced by α_s. The factor 4/3 accounts for the contribution of differently colored gluons to the process. The confinement at high distances is described by the second term which increases linearly with increasing distance. To accurately describe the observed masses of quarkonia, the Cornell potential is modified by spin-orbit and spin-spin interaction terms of the quarks.

Bound states of QCD are called hadrons. Two different kinds of hadrons, mesons and baryons, are known. In the *constituent quark model*, which absorbs the QCD dynamics into the quark masses, mesons consist of a quark anti-quark pair whereas baryons are composed of three quarks.

1.2 Light Meson and Baryon Systems

The lightest mesons are composed of the u-, d-, and s- quarks and their antiquarks. As quarks carry an internal spin of 1/2, the total angular momentum of the light mesons is either 1 or 0, assuming an angular momentum L equal to zero between the quark and the anti-quark. Mesons with $J^P = 1^-$ are called *vector mesons*, while mesons with $J^P = 0^-$ are called *pseudo-scalar mesons*. Here P denotes the eigenvalue of the wave

function of the meson under parity transformation. The underlying symmetry ruling the combination of u-, d-, and s-quarks to mesons is the $SU(3)$ group. Because of this, both vector and pseudo-scalar mesons can each be arranged into eight particles belonging to an octet and one singlet. Figure 3 shows both meson multiplet states classified by their third isospin component and *strangeness*. From the observation that the neutron and the proton have roughly the same mass, the isospin was introduced to describe both as a doublet state. Quantum mechanically the isospin behaves like an angular momentum quantum number and is conserved under the strong interaction. While u- and d-quark are assigned $|I, I_3\rangle = |1/2, +1/2\rangle$ and $|1/2, -1/2\rangle$ the strange quark does not carry an isospin. The strangeness is an additive quantum number and describes the flavor of the s-quark. The strangeness can only change in weak processes. In the pseudoscalar meson
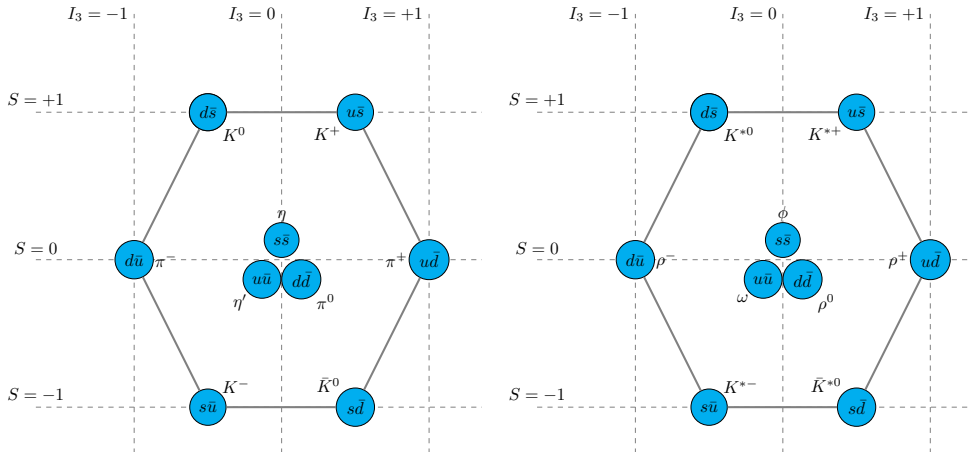

Figure 3: The light pseudo-scalar (left) and vector (right) meson multiplets.

multiplet the pions form an isospin triplet where $\pi^\pm$ is in the isospin state $|1, \pm1\rangle$. The π^0 corresponds to the $|1, 0\rangle$ state and has the quark content

$$|\pi^0\rangle = \frac{1}{\sqrt{2}} \left(|u\bar{u}\rangle - |d\bar{d}\rangle \right).$$

Since they belong to a triplet state, the pions have approximately the same mass. The equivalent triplet for the vector mesons is formed by the ρ-mesons. Adding the strange quark leads to the addition of kaons to the multiplets. They build isospin doublets with strangeness $S = \pm1$. Their masses differ from the pion mass since the higher mass of the s-quark breaks the SU(3) symmetry. The breaking of the SU(3) symmetry also leads to a mixing of the singlet and octet states with $I_3 = 0$ and $S = 0$. This mixing, however, differs for the pseudo-scalar and vector mesons. For the latter the mixing occurs in a way that the ϕ is almost a pure $s\bar{s}$ state, while the quark content for the ω is given by a linear combination of u- and d-quarks

$$|\phi\rangle = |s\bar{s}\rangle$$
$$|\omega\rangle = \frac{1}{\sqrt{2}} \left(|u\bar{u}\rangle + |d\bar{d}\rangle \right).$$

In the case of the pseudo-scalar mesons the mixing is very weak and the η and η' are almost pure singlet and octet states

$$|\eta\rangle \approx |\eta_8\rangle = \frac{1}{\sqrt{6}} \left(|u\bar{u}\rangle + |d\bar{d}\rangle - 2 |s\bar{s}\rangle \right)$$
$$|\eta'\rangle \approx |\eta_1\rangle = \frac{1}{\sqrt{3}} \left(|u\bar{u}\rangle + |d\bar{d}\rangle + |s\bar{s}\rangle \right).$$

Baryons are fermions consisting of three quarks. Their wave function can be written as

$$|qqq\rangle_A = |color\rangle_A \cdot |\text{space, spin, flavor}\rangle_S$$

where the color wave function is an antisymmetric SU(3) singlet. Therefore, their combined space, spin and flavor wave function has to be symmetric. In the case of no angular momentum ($L = 0$) between the quark pairs inside the baryon, the space wave function is symmetric. For the lightest baryons consisting only of u, d, and s quarks, spin and flavor can be combined into a spin-flavor SU(6) symmetry. This leads to the formation of several multiplets

$$6 \otimes 6 \otimes 6 = 56_S \oplus 70_M \oplus 70_M \oplus 20_A$$

where S, M, A denote symmetric, mixed, and antisymmetric wave functions under exchange of quark flavors or spins. The 56-plet denotes the ground state with $L = 0$ and decomposes into the two flavor SU(3) multiplets

$$56 = {}^4 10 \oplus {}^2 8$$

where the superscript is equal to (2S+1) and indicates the spin S. The baryons in the decuplet carry $J^P = 3/2^+$ and the octet states like the proton and neutron carry $J^P = 1/2^+$. Decuplet and octet are shown in figure 4 classified according to their I_3-component and strangeness.
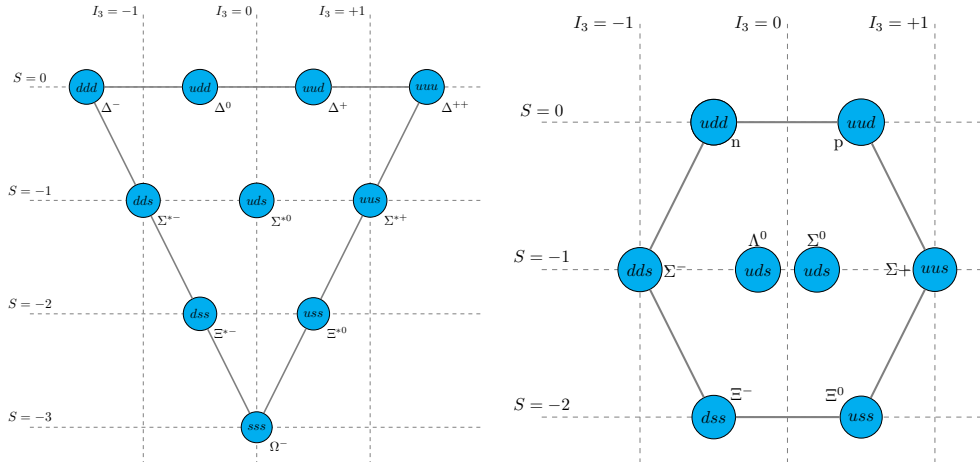

Figure 4: The baryon decuplet with $J^P = \frac{3}{2}^+$ and octet with $J^P = \frac{1}{2}^+$.

1.3 Charmonium Spectroscopy

In 1974 the J/ψ meson was independently discovered at SLAC in $e^+ e^-$ annihilation and at Brookhaven in the reaction $p + \text{Be} \rightarrow e^+ + e^- + x$ [12, 13]. The new particle had a very high mass ($m_{J/\psi} = 3.096 \text{ GeV}/c^2$), was electrically neutral, and had a very long life time of about 10^{-20} s which is much longer compared to other particles in this mass region. Finally the J/ψ was interpreted as a meson built by the quark anti-quark combination of a fourth quark flavor, the charm quark [9]. The existence of a fourth quark had already been proposed theoretically by the GIM[1]-mechanism [14]. Without the GIM mechanism the calculated decay rate of $K^0 \rightarrow \mu^+ \mu^-$ was greater than experimentally observed. The introduction of a fourth quark leads to an additional contribution to the decay amplitude

---

1 Glashow-Iliopoulos-Maiani

which cancels with the already existing terms. Shortly after the discovery of the J/ψ, evidence for the first charmed baryon Λ_c^+ was seen [15]. Due to its importance for the acceptance of the quark model, the discovery of the J/ψ and its aftermath are called the *November Revolution* (of particle physics).

The Charmonium Spectrum

Due to the high mass of the charm quark, $c\bar{c}$ bound states can be described by non-relativistic quantum mechanics using the Schödinger equation with an interaction potential given, for example, by the Cornell potential (see equation 1.6). The low lying energy levels of the emerging level scheme resemble the energy levels of positronium which is an electron-positron bound state formed by the electroweak interaction. Hence bound $c\bar{c}$ states are called *charmonium*. Studying the excitation spectrum of charmonium states allows one to make deductions about the interaction potential between a heavy quark antiquark pair. The charmonium spectrum including established states is shown in figure 5.

Figure 5: The spectrum of established charmonium states ordered according to J^{PC} quantum numbers [1]. Only hadronic transitions are shown while radiative decays are omitted for clarity. Note that the states X(4260)/X(4360) are commonly referred to as Y(4260)/Y(4360).

The states are labeled using the notation $X(nL)$ where n is the radial excitation, which is equal to 1, 2, 3,..., and L is the angular momentum between both quarks (usually the capital letters S, P, D, F are used for L). Additionally they are sorted according to their J^{PC} quantum numbers. J gives the total angular momentum

$$|L - S| \leq J \leq L + S.$$

where S is the combined spin of the quark and anti-quark pair. Singlet and triplet S-wave states are called η_c and ψ respectively, while triplet P-wave states (spin 0, 1 and 2) are referred to as χ_c. The h_c is a P-state with $S = 0$. Analogous to the positronium one finds

a strong splitting of the charmonium states due to spin-spin interactions. The splitting between the $\eta_c(1S)$ and the J/ψ is in the order of 120 MeV/c^2. A similar splitting can also be seen between the χ_{c0}, χ_{c1}, and χ_{c2} which is, however, caused by the different spin-orbit interaction.

Charmonium states below the $D\overline{D}$ threshold at 3.730 GeV/c^2 are relatively long lived as their strong decays are suppressed by the OZI[2]-rule. The rule states that processes mediated by the strong interaction are suppressed if the associated Feynman diagram can be split by cutting only internal gluon lines. Starting with the $\psi(3770)$, which lies just above the $D\overline{D}$ threshold, strong decay channels are no longer suppressed and the lifetime of the charmonium states is decreased. These states predominately decay to D-mesons. D-mesons are mesons consisting of a charm quark and one of the three light quarks.

Exotic States

The established bound states of the strong interaction are baryons and mesons. However QCD is not limited to these bound states, but any states involving quark and gluon combinations that fulfill the restrictions of QCD are possible. Various models for new configurations exist and the most common are listed below:

tetra-quarks: states consisting of two tightly bound quark-antiquark pair $qq\bar{q}\bar{q}$.

penta-quarks: a baryon with an additional quark-antiquark pairs $qqqq\bar{q}$. Recently the LHCb collaboration has observed a resonance in the $J/\psi p$-system in the decay $\Lambda_b^0 \to J/\psi p K^-$ [16] which might be compatible with a pentaquark.

molecular states: two mesons forming a bound state comparable to a tetra-quark, but well separated and bound by pion-exchange at long distances and gluon exchange at shorter distances.

hadrocharmonium: states built by a preformed charmonium state which is surrounded by a light quark cloud.

hybrid states: mixed states of quarks and excited gluons (e.g $q\bar{q}g$).

glueballs: pure gluon states gg or ggg.

The possible existence of tetra- and penta-quarks had already been proposed by Gell-Mann. In the quark model mesons can only form a limited set of quantum numbers. The quantum number combinations $J^{PC} = 0^{--}$, 0^{+-}, 1^{-+}, 2^{+-} etc. are forbidden for mesons and are, therefore, called exotic quantum numbers. If one observers a state with exotic quantum numbers, it is most probable one of the configurations mentioned above. On the other hand these configurations could also carry non-exotic quantum numbers. These states could mix with normal mesons and baryons and their internal structure could not be easily identified. In the mass region below 2.5 GeV/c^2 the search for new states is difficult due to the high density of normal meson states.

In the charmonium mass region such a search is much simpler since there is a smaller number of states which are much narrower than the light quark states. Because of this new states can be easily resolved. A lattice QCD calculation of the resonance spectrum with the quantum numbers and expected masses for hybrids and glueballs is shown in figure 6.
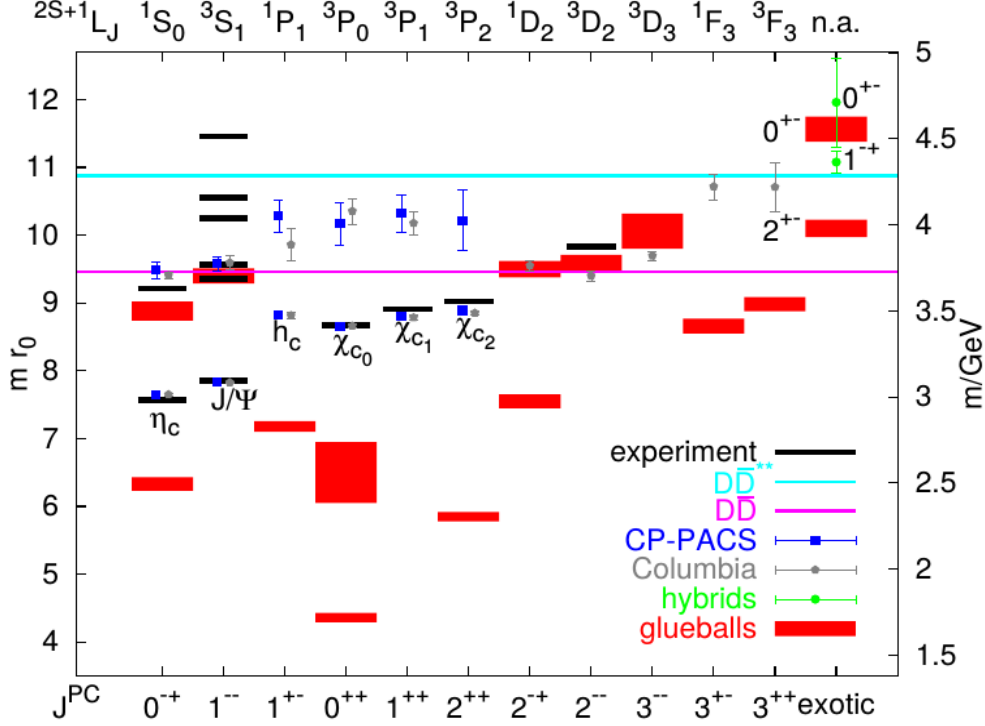
---

2 Okubo-Zweig-Iizuka

Figure 6: Charmonium spectrum from quenched lattice QCD calculations with the scale parameter $r_0^{-1} \approx 394$ set from potential models [17].

Several new charmonium-like states have been observed in the last few years. The X(3872) was discovered by the Belle collaboration in the decay $B^{\pm} \to K^{\pm}X$, $X \to J/\psi\pi^+\pi^-$ [18] and was confirmed by other experiments[19, 20]. Its mass is known rather precisely, while for the width only an upper limit of 2.3 MeV/c^2 exists [1]. The quantum numbers of the X(3872) are determined to be $J^{PC} = 1^{++}$ by its decay modes and a measurement of the angular correlations in the decay $B^+ \to K^+X$ by the LHCb collaboration [21]. Due to the closeness of the X(3872) to the $D^0\bar{D}^{0*}$ threshold it has been speculated that it is a molecular state where a D^0 and $\bar{D}^{0*}$ are bound together. Other interpretations include that it is a conventional charmonium or a tetra-quark state. In addition, the BESIII collaboration has observed the decay $Y(4260) \to \gamma X(3872)$ [22] which suggests that both states could share the same internal structure. In order to discriminate between different hypotheses a detailed measurement of the line shape of the X(3872) has been suggested [23, 24].

Belle observed two charged resonances, Z_1 and Z_2, in the $\chi_{c1}\pi^+$ subsystem of the reaction $\bar{B}^0 \to K^-\pi^+\chi_{c1}$ at 4051 MeV/c^2 and 4248 MeV/c^2 [25]. However, no evidence for both resonances was found in an independent analysis by the BaBar collaboration [26].

The Y(4260) and Y(4360) resonances were first observed by the BaBar experiment in the initial state radiation reactions $e^+e^- \to \gamma_{ISR}J/\psi\pi^+\pi^-$ and $e^+e^- \to \gamma_{ISR}\psi'\pi^+\pi^-$ [27, 28] and were subsequently confirmed by Belle and other collaborations [29, 30, 31]. Due to the production mechanism, their J^{PC} has to be 1^{--}, but their exact properties and interpretation are unknown. They decay strongly to hadronic final states, but not preferentially to open charm states like other states above the $D\bar{D}$ threshold [32, 33, 34]. These states were investigated by the BESIII collaboration, as well. The BESIII collaboration reported a charmonium-like state $Z_c(3900)^{\pm}$ decaying into $J/\psi\pi^{\pm}$ in the reaction $e^+e^- \to J/\psi\pi^+\pi^-$ at $\sqrt{s}$=4.26 GeV. This resonance was confirmed by the Belle experiment [35]. The neutral partner $Z_c(3900)^0$ was found in CLEO-c data [36] and confirmed

by BESIII [37]. Due to its decay to charmonium and being a charged state, the $Z_c(3900)^{\pm}$ can not be explained as a normal meson. A resonance in the $D\overline{D}^*$ system at a mass of 3888.9 GeV/c^2 has been observed in the decay $Y(4260) \to \pi D\overline{D}^*$ [38] and may be identified as $Z_c(3900)$. Interpretations of the $Z_c(3900)$, therefore, favor it to be either a tetra-quark state or a D-Meson molecule. A further charged resonance $Z_c(4020)^{\pm}$ was found in the $h_c\pi^{\pm}$ subsystem during the decay $Y(4260) \to h_c\pi^+\pi^-$ [39] and later its isospin partner $Z_c(4020)^0$ was discovered [40]. Furthermore, structures have been observed by the BESIII collaboration in the reactions $e^+e^- \to \pi^+(D^*\overline{D}^*)^-$ and $e^+e^- \to \pi^0(D^*\overline{D}^*)^0$ whose poles are compatible with the $Z_c(4020)$ [41, 42].

These discoveries have triggered intensive searches for new resonant structures in the charmonium region using final states that contain other charmonium resonances like the η_c.

2
CHARMONIUM SPECTROSCOPY EXPERIMENTS

To understand the underlying structure of all these new states described in the previous chapter, the whole charmonium spectrum has to be searched for new states. Furthermore, the transitions between those states have to be analyzed in order to understand their relationships. In addition, detailed scans of the line shapes have to be performed to discriminate between different models for their structure. This requires high statistics datasets which can be found at BES-III and high quality beams that will be available at the PANDA experiment. Both experiments have dedicated research programs in the field of hadron and charmonium spectroscopy. As this thesis contains studies done for both collaborations, an overview of the collaborations is given in the following sections.

2.1 The BESIII Experiment

The BESIII detector is located at the Beijing electron-positron collider (BEPC-II) of the Institute of High Energy Physics (IHEP) in Beijing. The BEPC-II, which replaced the original BEPC, is a multi-bunch collider with an energy range of $\sqrt{s}$ =2 - 4.6 GeV. The design luminosity is $\sim 10^{33}$ cm^{-2}s^{-1} at a center of mass energy of 2 x 1.89 GeV. The double rings have a circumference of 237.5 m. In addition to the BESIII detector a synchroton radiation source is placed at the opposite side of the accelerator (see figure 7). The operation parameters of BEPC-II are summarized in table 3.

Parameter	Design	Achieved	
		e^- ring	e^+ ring
E [GeV]	1.89	1.89	1.89
I_{beam} [mA]	910	650	700
I_{bunch} [mA]	9.8	>10	>10
bunches	93	93	93
crossing angle [mrad]	11x2	11	11
Inj. rate [mA/min]	200(e^-) 50(e^+)	>200	>50

Table 3: Design and operation parameters of the BEPCII accelerator [43].

2.1.1 The BESIII Physics Program

The BESIII physics program includes a vast collection of different topics. One cornerstone is the study of open charm physics including the properties of D and narrow D_s states. The $\psi(3770)$ decays mainly in $D^0 - \bar{D}^0$ and $D^+ - D^-$ pairs allowing for background suppression by tagging one D-meson. Measurements of semi-leptonic decays allow for the determination
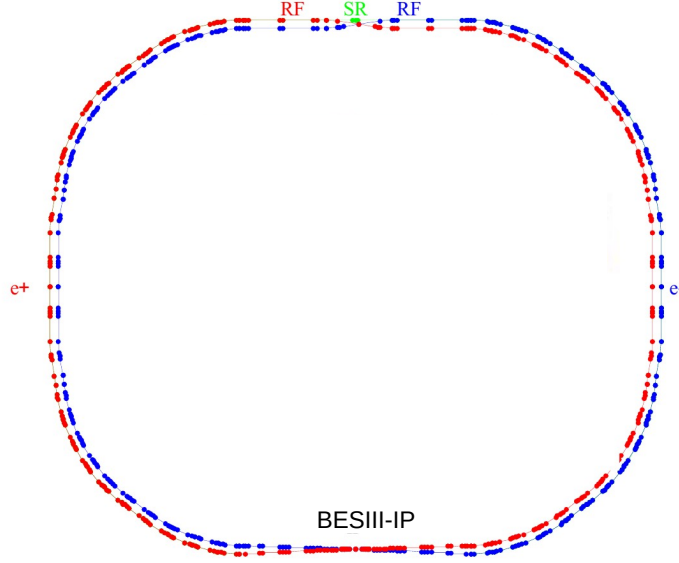
Figure 7: Layout of the BEPC-II double ring accelerator at IHEP, Beijing. The BESIII detector is positioned at the lower half of the rings, while the synchroton light source (SR) is located at the opposite side.

of the V_{cs} and V_{cd} elements of the CKM-matrix. With its high statistic dataset BESIII is able to improve the measurements of branching ratios of rare and forbidden D decays [44]. BESIII offers good experimental conditions in terms of background and resolution compared to B-factories for the study of properties of the τ-lepton. The measurements of branching ratios for τ decays including charged kaons are improved. In addition, the τ mass can be measured with high precision at BESIII. The study of hadronic τ decays allows a precise determination of the strange quark mass and the V_{us} element of the CKM-matrix. Furthermore, the measurement of the Michel parameters[1] will be improved by a factor 2-4 due to higher statistics combined with low background [44]. Lastly BESIII searches for CP-violation in τ decays and will measure the g-factor of the τ.

In addition, studies of light hadrons and their decay properties have been conducted. Examples here are the measurements of the matrix elements of $\eta \to \pi^+\pi^-\pi^0$ and $\eta' \to \pi^0\pi^0\pi^0$ [45], and the observation of a Dalitz decay $\eta' \to \gamma e^+ e^-$ [46].

The analysis performed in this work falls into another cornerstone of the BESIII physics program, charmonium physics. BESIII studies the decay properties of the J/ψ, $\psi(2S)$ and $\psi(3770)$. The total decay widths are supposed to be measured with a precision of 1%. In addition, rare decays of these charmonia are investigated. Furthermore, searches for glue balls, hybrid states and tetra-quark states are conducted. BES-II observed a near threshold enhancement in the $p\bar{p}$ system in the radiative decay $J/\psi \to \gamma p\bar{p}$ [47]. The so called X(1835) was seen in the channel $J/\psi \to \gamma\pi^+\pi^-\eta'$ as well [48]. Meanwhile the X(1835) has been confirmed by BESIII, while two additional resonances $X(2120)$ and $X(2370)$ have been observed in the $\pi^+\pi^-\eta'$ system [49].

In addition, the BESIII collaboration discovered the new states $Z_c(3900)$ and $Z_c(4020)$ which were already discussed in section 1.3.

---

1 bilinear combinations of leptonic decay constants

2.1.2 The BESIII Detector

The BESIII detector has been optimized for the expected event topology and multiplicity, the types of primary particles, their energy spectra and high data rate. The average multiplicity is in the order of four charged particles and photons in the final state. In typical final states the most probable momentum of charged particles is expected to be 0.3 GeV/c with an upper limit of 1.0 GeV/c for most particles. The average energy of photons is 100 MeV [50]. A drawing of the BESIII detector is shown in figure 8. It is built inside and around a 1 T superconducting solenoid and its flux return. The solid angle coverage $\Omega/4\pi$ is 0.93. The beam pipe is manufactured from beryllium to reduce multiple scattering of primary particles. The main detector components are described in the next paragraphs [50].

MULTILAYER DRIFT CHAMBER   The beam pipe is surrounded by a Multilayer Drift chamber (MDC). The MDC measures the momentum of charged particle tracks by their curvature inside the solenoidal magnetic field. It covers a θ-range down to $cos(\theta) = 0.93$ and has an inner radius of 59.2 mm and an outer radius of 810 mm measured from the beam pipe. It is split into an outer and inner chamber. The latter can be replaced in case of radiation damage. It uses a small cell design with 43 layers of drift cells. The inner chamber consists of eight layers, while the remaining 35 layers form the outer chamber. Each drift cell consists of one sense wire surrounded by eight field wires. In total there are 6796 sense wires. The 43 layers are arranged in 11 superlayers. Each superlayer is composed of four layers with the exception of the last layer that only has three sense wires. The sense wires are produced out of gold plated tungsten with a diameter of 25 µm, while the field wires are made of 110 µm thick gold plated aluminum in order to reduce multiple scattering. Neighboring cells in one superlayer share the field wires. The gas filling is a helium-propane mixture ($He - C_3H_8$ 60:40) and minimizes multiple scattering of the low momentum particles while keeping a good dE/dx resolution. The single cell position resolution in the r-ϕ plane is 130 µm while the resolution in beam direction is 2 mm. The momentum resolution is $\delta p/p = 0.5\%$ at 1.0 GeV/c. The energy loss resolution for particles is 6% leading to a 3 σ π/K separation up to 0.7 GeV/c. Two superconducting quadrupoles (SCQs) are positioned in the conical shaped MDC end caps and focus the beam onto the interaction point.

TIME-OF-FLIGHT SYSTEM   The Time-of-Flight (TOF) provides particle identification by measuring the flight duration of particles. It consists of a barrel layer and two end caps. The barrel layer has a mean radius of 870 mm and is built from two layers of staggered scintillating bars, while the end caps only have a single layer of scintillators with an inner radius of 410 mm and an outer radius of 890 mm. The TOF covers a solid angle of $|cos(\theta)| < 0.83$ in the barrel region and $0.85 < |cos(\theta)| < 0.95$ in the end caps. In total it consists of 88 plastic scintillators in the barrel and 44 in the end caps. The scintillating bars are read out by fine mesh photomultiplier tubes and achieve a timing resolution of 90 ps in the barrel and 70 ps in the end caps [44]. This allows a 3σ π/K separation up to momenta of 0.7 GeV/c. In addition, the TOF delivers a fast trigger signal for charged particles.

ELECTROMAGNETIC CALORIMETER   The task of the Electromagnetic Calorimeter (EMC) is to measure the energy and flight direction of photons and to provide trigger signals. The EMC consists of 6272 CsI(Tl) crystals and is located between the TOF system and the superconducting solenoid. It has an inner radius of 940 mm. It is split
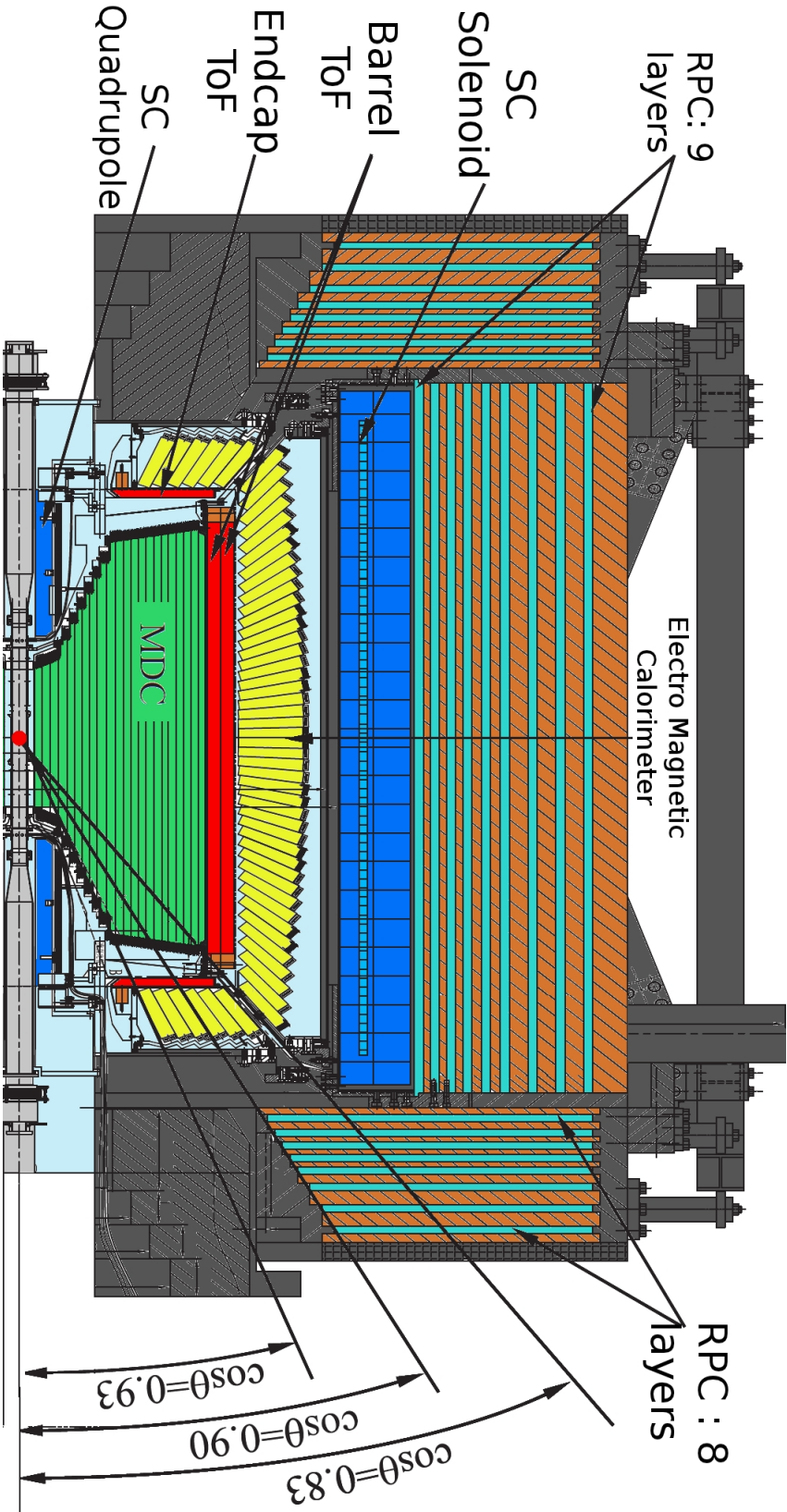
Figure 8: Cut through the BESIII spectrometer at IHEP. The detectors from inner to outer are a multilayer drift chamber, the time-of-flight system, an electromagnetic calorimeter and the muon detector in the solenoid magnet flux return. For a detailed description of the detector see text.

into a barrel region covering a solid angle of $|cos(\theta)|$ <0.82 and two end caps covering 0.83< $|cos(\theta)|$ <0.93. One crystal is 28 cm long which corresponds to 15 radiation lengths and is read out by a silicon photo-diode. The energy resolution of the EMC is given by σ_e/E =2.5% at 1 GeV and the position resolution for showers is 0.6 cm/$\sqrt{E[\text{GeV}]}$. It can separate electrons and pions for momenta higher than 200 MeV/c by means of their energy deposition.

MUON SYSTEM   The muon system identifies muons and discriminates other charged particles by their hit patterns in resistive plate counters. A resistive plate counter is made of two electrodes separated by an isolating gas. The ionization of a passing charged particle leads to a voltage signal. The resistive plate counters are inserted into the iron flux return of the superconducting magnet. The barrel muon system has nine layers of iron plates with a total thickness of 41 cm and nine layers of resistive plate counters. In the end caps the muon system only consists of eight layers of steel/resistive plate counter pairs. The muon system starts to become effective for momenta above 0.4 GeV/c. This is due to the bending of muon tracks in the solenoidal magnetic field and energy loss in the EMC crystals.

TRIGGER SYSTEM AND EVENT FILTER   The expected background rate at the J/ψ peak is 10 MHz, which is dominated by beam related backgrounds, while the physics rate is only 2 kHz. Due to this an effective trigger and event filter system is necessary to suppress background events. The BESIII trigger system employs two trigger levels. The first level (L1) is a hardware trigger largely implemented in FPGA based hardware. The L1-trigger uses sub-trigger information from the MDC, EMC, and TOF that are processed by the global trigger logic. The L1-trigger clock is synchronized to the accelerator and operates at 41.65 MHz. The maximum trigger rate from the L1-system is 4 kHz at the J/ψ peak. The next trigger level (L2) is a software trigger to further suppress background events. The trigger software runs on a commercial server farm. After the trigger system the maximum data rate saved on permanent storage is 40 MB/s at the J/ψ peak with a 2 kHz physics event rate and a 1 kHz background event rate.

LUMINOSITY DETERMINATION   The luminosity is determined by using the three QED processes $e^+e^- \rightarrow e^+e^-, \mu^+\mu^-, \gamma\gamma$. The cross sections of these reactions are well known and very large. The luminosity is calculated from the rate of these processes after correcting for detector efficiency and acceptance. The integrated luminosity can be measured with a precision of 1% and is limited by the trigger efficiency determination, radiative corrections, and background event suppression.
In addition, luminosity monitors made out of fused silica blocks are installed near the interaction point. They measure the relative bunch-by-bunch luminosity using the rate of incident photons from radiative Bhabha scattering.

2.2 The PANDA Experiment at FAIR

The PANDA experiment is a planned particle detector using antiproton-proton annihilation to investigate various topics of hadron physics at the Facility for Antiproton and Ion Research (FAIR).
FAIR is a planned accelerator and experiment facility that will be built at the Helmholtzzentrum für Schwerionenforschung (GSI) site close to Darmstadt, Germany. An overview of FAIR is shown in figure 9. The completion of the construction work and first beams are foreseen

to take place in 2022. The already existing linear accelerator UNILAC[2] and the heavy ion synchroton SIS18[3] will serve as injectors for the new heavy ion synchrotons SIS100 and SIS300. They will have a circumference of 1100 m. In addition the construction of a linear injection accelerator (p-Linac) is planned. The new accelerators will deliver high intensity primary beams of protons and highly charged ions up to uranium-92^{+}. Furthermore, secondary beams made of antiprotons and rare isotopes are going to be used by various experiments. Due to the accelerator design, four different experimental sites can be run in parallel [51].

The physics case connected to FAIR comprises different areas of fundamental research like atomic physics, biophysics, material science, and nuclear physics. In the last domain the PANDA collaboration will investigate topics in the field of hadron physics while the CBM[4] experiment will use heavy ion beams to study QCD at very high baryon densities [52]. The NUSTAR[5] collaboration will research nuclear structure and dynamics as well as topics related to nuclear astrophysics using beams of exotic nuclei [53]. The fourth experimental pillar of FAIR is the APPA[6] collaboration. It studies atomic and plasma physics and its application in biophysics, medical physics, and material science [54].
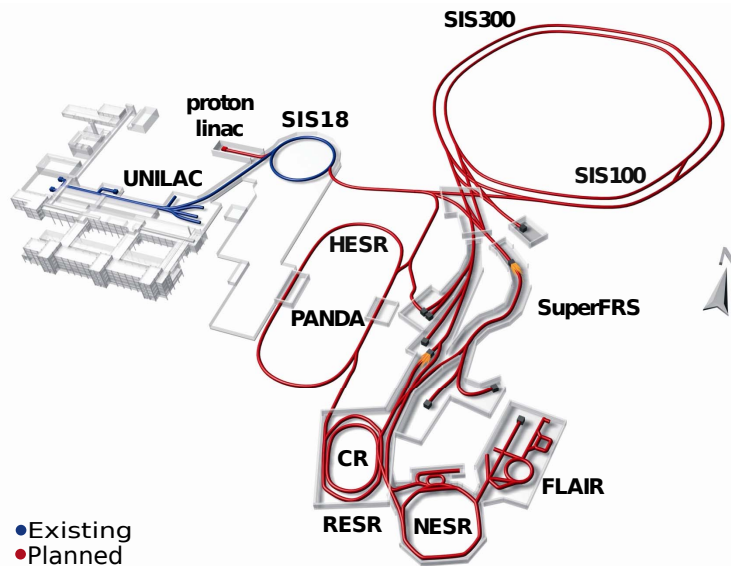
Figure 9: The FAIR facility at GSI in Darmstadt. The existing accelerators are shown in blue, while the planned facility is drawn in red. The PANDA experiment is located at the High Energy Storage Ring (HESR) [55].

2.2.1 Antiproton Production and the High Energy Storage Ring

The antiprotons needed for the PANDA experiment are produced in several steps. In a first step a beam of protons is accelerated to 70 MeV/c by a special proton-linac and is then injected into the heavy ion synchrotons SIS18 and SIS100 with a repetition rate of 4 Hz[56]. During this process the protons get accelerated in the SIS100 to 29 GeV/c and are compressed to bunches of $2 \cdot 10^{13}$ particles with a 50 ns bunch length. These pro-

---

2 UNIversal LINear Accelerator

3 SchwerIonen Sychnroton with a magnetic rigidity of 18 Tm

4 Compressed Baryonic Matter

5 NUclear STructure, Astrophysics and Reactions

6 Atomic, Plasma Physics and Applications

tons impact on a nickel target every ten seconds in order to produce antiprotons. The produced antiprotons will have a mean momentum of 3 GeV/c at an opening angle of 80 mrad with respect to the beam axis. Although a higher energy of the incident proton beam would produce more antiprotons, it would also require a higher bending power of the subsequent beam transport and storage system. A magnetic horn will collect the produced antiprotons emerging from the target within a cone of up to 80 mrad and a momentum of 3 GeV/c. In a next step a dipole magnet separates the antiprotons from primary protons and other produced particles. The antiprotons are then transferred to the Collector Ring (CR) where they are stochastically cooled. After extraction from the CR the antiprotons are accumulated in a subsequent storage ring until a number of 10^{10} particles is reached. In the first stage of FAIR the accumulation will take place directly in the High Energy Storage Ring (HESR) where PANDA is located. Since data taking is not possible during antiproton accumulation, the achievable average luminosity is decreased. Because of this a further ring, the Recycled Energy Storage Ring (RESR), will be added for antiproton accumulation in the second stage of FAIR [57]. With the RESR it will be possible to accumulate antiprotons in parallel to the experimental operation of the HESR.

The HESR is a storage ring which is able to acc- or decelerate antiprotons to momenta between 1.5-15 GeV/c. Its circumference amounts to 575 m with two straight parts of 130 m. The PANDA detector is located at one of these straight sections. The HESR will offer two different operation modes: the *high luminosity* and the *high resolution* mode. In the final stage of FAIR the high luminosity mode will deliver a luminosity of $2 \cdot 10^{32}$ cm^{-2}s^{-1} with a beam momentum resolution of $\delta p/p = 10^{-4}$. In the high resolution mode the momentum resolution is improved by the usage of electron cooling to $\delta p/p \leq 5 \cdot 10^{-5}$ while the luminosity decreases to 10^{31} cm^{-2}s^{-1}. In the high luminosity mode, or for beam momenta above 8.9 GeV/c, stochastical cooling is used instead of the electron cooling. In the initial version of FAIR the high resolution mode will not be available and the luminosity is reduced to 10^{31} cm^{-2}s^{-1}.

In addition to PANDA, two further experiments, KOALA [58] and SPARC [59], are placed at the HESR. KOALA will perform preparatory measurements to determine parameters of elastic antiproton proton scattering needed for the luminosity measurement (see chapter 3). The SPARC collaboration will determine the properties of highly charged nuclei by using techniques from atomic physics like doppler boosts of optical laser beams to the X-ray regime [59].

2.2.2 PANDA

The PANDA Physics Program

The main point of interest of the PANDA experiment are particle states containing charm or strange quarks and the search for states with exotic quantum numbers that can not be composed of a quark and antiquark pair alone, but have another internal structure. In contrast to e^+e^- collider experiments like BESIII, where only states with the quantum numbers of a virtual photon can be produced directly, the proton antiproton annihilation process will be used at PANDA. With this process hadronic states made of quark and antiquark pairs with arbitrary quantum numbers can be produced either in direct formation or in production with an additional recoil particle (see figure 10).

The high momentum resolution of the HESR allows the exact measurement of properties of new and already observed resonances using the energy-scan method: By systematical variation of the beam momentum the resonance is scanned at different center of mass
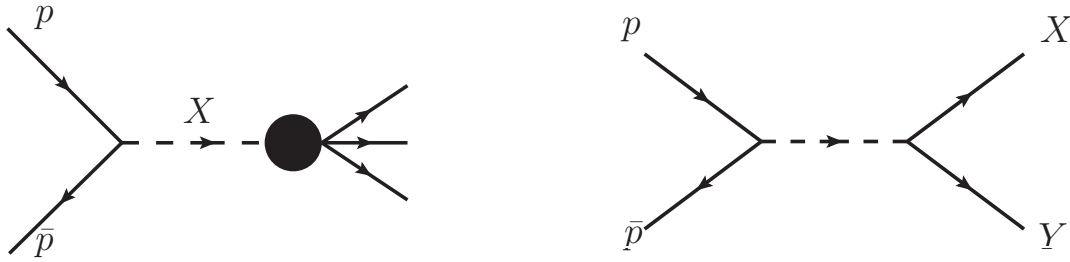
Figure 10: Creation of a particle X in direct formation (left) and in production with recoil particle Y (right).

energies and the production cross section at each scan point is determined. A deconvolution of the measured resonance shape with the momentum distribution of the antiproton beam yields the true line shape of the resonance. A scan is illustrated in figure 11. For the relative
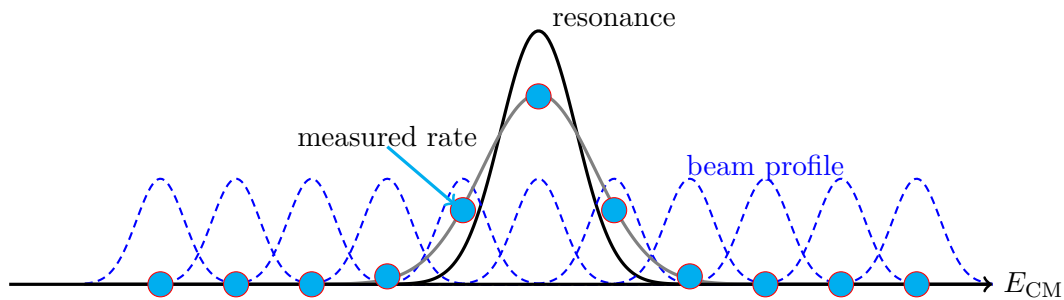

Figure 11: Illustration of a resonance scan where the measured line shape is the convolution of the true line shape and the beam energy profile.

normalization of each scan point the integrated luminosity needs to be known and the error of the luminosity measurement directly influences the precision of such a line shape measurement. In addition the integrated luminosity needs to be known if the absolute cross section of a particle reaction is to be determined. The luminosity measurement and the luminosity detector will be explained in detail in section 3. The next paragraphs will present the parts of the PANDA physics program that require a luminosity measurement.

CHARMONIUM SPECTROSCOPY   One of the key aspects of the PANDA physics program is charmonium spectroscopy without the limitation on directly producible quantum numbers. For example PANDA will make comparison studies of the hadronic decays of the J/ψ and $\psi(2S)$ and study the radiative decays of the spin-triplet χ_{cJ} states to gain insight into the interaction between the electromagnetic field and the quarkonium system. In addition, precision measurements will be performed on the h_c in order to study the spin dependent contributions of the $q\bar{q}$ potential. Above the $D\overline{D}$ threshold PANDA will perform systematic scans of the higher charmonium mass region in order to discover new charmonium states and study the nature of already discovered states. Of special interest is the nature of the X(3872). PANDA will perform a fine grained resonance scan of the X(3872) line shape in order to distinguish between various proposed models of this resonance. Furthermore, the transitions between the X, Y and Z states can be studied at PANDA with high statistics and high precision.

The search for new and exotic states is another cornerstone of the physics program. Exotic charmonium states are expected to exist in the mass region of 3-5 GeV/c^2 where they can be resolved unambiguously. Eight charmed hybrid states are predicted in the mass range accessible to PANDA, and the lowest lying exotic hybrid state should have

the quantum numbers 1^{-+} and a mass of approximatly 4.3 GeV/c^2. Furthermore, lattice QCD calculations predict the existence of about 15 glueballs in the PANDA momentum region.

NUCLEON STRUCTURE   To learn about the internal structure of the nucleon, PANDA will research *generalized parton distribution* functions and the time-like form factor of the proton in a wide range of momentum transfer. Reactions like $p\bar{p} \to e^+e^-$ and wide angle Compton scattering will be used for this. The luminosity is needed to normalize the single measurements at different momentum transfers before the dependency of the form factor on the momentum transfer can be determined.

HADRONS IN MEDIA   The in-medium properties of hadrons have been studied with hadrons formed by light quarks [60, 61, 62]. These studies help to understand the origin of hadron masses in chiral symmetry breaking of QCD and the change of hadron masses in atomic nuclei. PANDA is going to expand this research by using hadrons containing charm quarks. To study the absorption of hadrons in atomic nuclei in dependence of their momentum, scan experiments will be used.

The topics described above show that a precise determination of the luminosity is mandatory for a major part of the PANDA physics program. Other parts of the physics program, such as CP violation, the determination of branching ratios, and rare electro-weak decays, do not require a luminosity measurement.

The PANDA Detector

PANDA is a fixed target experiment at the HESR which is optimized to cope with the requirements of the physics program described above. PANDA is designed to have a high momentum and energy resolution, an angular acceptance close to 4π, and good particle identification at very high reaction rates of up to 20 MHz. The detector is depicted in figure 12. To account for the reaction topology of a fixed target experiment, the PANDA detector is split into a target- and a forward spectrometer. The complete PANDA detector has a length of 15 m, a width of 5 m, and a height of 10 m. The main components of the detector are described in the next paragraphs.

TARGET   In order to achieve the design luminosity of $2 \cdot 10^{32}$ cm^{-2}s^{-1} in the high luminosity mode with 10^{11} stored antiprotons and an interaction rate of 20 MHz, a hydrogen target with a density of 5×10^{15} atoms/ cm^2 is necessary. The *cluster jet target* uses a narrow jet of frozen hydrogen clusters which are created by the expansion of cold pressurized hydrogen gas into the beam pipe vacuum. One cluster usually contains between 10^3 to 10^6 hydrogen molecules. The jet is characterized by a homogeneous and adjustable density profile which allows to run the detector at a constant luminosity. It, however, has the disadvantage that the lateral spread of the clusters leads to an uncertainty in the position of the interaction point of several millimeters. The *pellet target* uses frozen hydrogen micro-spheres, called pellets. They are created by injecting liquified gas into a vibrating nozzle which breaks the liquid jet into droplets. These turn into solid pellets when injected into vacuum. The spheres have a size of 25-40 µm. As up to 100 antiprotons usually interact with a single pellet, its position can be reconstructed with the resolution of the MVD (see next paragraph). In addition, a optical pellet tracking system is foreseen which should be able to determine the position of individual pellets with a resolution of 50 µm. The caveats of the pellet target are the non-uniform time and thickness distribution of
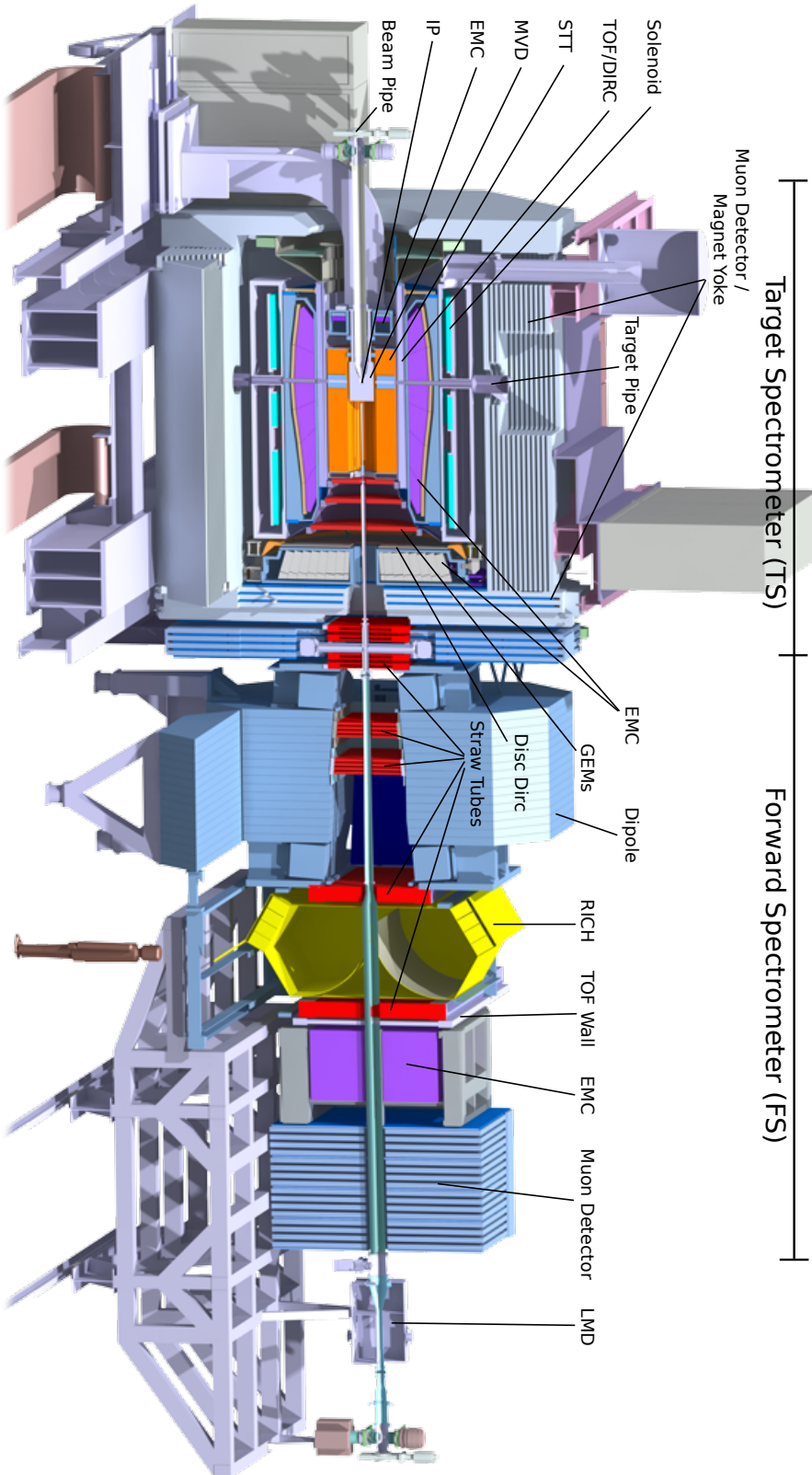
Figure 12: The PANDA detector. The luminosity detector (LMD) is located 11 m behind the interaction point [63].

the pellets which lead to changes in the instantaneous luminosity. Besides hydrogen, other gaseous substance like nitrogen and argon can be used by both targets.

MICRO VERTEX DETECTOR   The target spectrometer encloses the interaction point and measures charged tracks with a polar angle between 3 and 150° in a two tesla magnetic field of a super conducting solenoid. The innermost detector component is the Micro Vertex Detector (MVD). It offers the earliest possible measurement of particle tracks. Since it is installed close to the beam pipe, the influence of multiple scattering from the beam pipe material on the measured track parameters is kept minimal and thereby the MVD improves the precision of the decay vertex reconstruction. It consists of radiation hard silicon pixel and double sided strip detectors. The current design foresees four barrel layers and six layers perpendicular to the beam axis. The single hit resolution of the MVD is 6.9 µm/12.4 µm for the pixel/strip part. The spatial resolution of primary vertices is in the order of 100 µm [64].

STRAW TUBE TRACKER   The PANDA detector uses a Straw Tube Tracker (STT) as a central tracking chamber. It is made of 4636 self-supporting, over pressurized straws. The majority of the straws are aligned parallel to the beam axis to measure the track helix in the xy-plane. In addition, skewed straw layers will be used to determine the z-information of the tracks, too. Furthermore, decay vertices of particles decaying outside of the MVD volume will be reconstructed using the STT. MVD and STT allow for a momentum resolution of $\Delta p/p \approx 1\%$ and a vertex reconstruction with a resolution of 100 µm. They cover a polar angle between 5° and 170° and reach a track reconstruction efficiency of above 90% [65].

GASEOUS MICRO-PATTERN DETECTORS   In the beam direction the central tracker is supplemented by three gaseous micro-pattern detectors which are based on gaseous electron multiplication (GEM) foils as amplification stages. The detectors are positioned 1.1 m, 1.4 m, and 1.9 m from the interaction point and can reconstruct tracks with a minimal polar angle of down to 3°.

ELECTROMAGNETIC CALORIMETER   The EMC is used for the detection and energy measurement of photons, electrons, and positrons. It consists of lead tungsten crystals (PbWO$_4$) which are cooled to a temperature of -25°C to increase the light yield. The EMC reaches an energy resolution of $1.5\%/\sqrt{E/GeV}$ and a position resolution of 0.3 cm for photons with an energy above 1 GeV. Furthermore, the energy deposition of tracks and the shape of the electromagnetic showers inside the EMC can be used to separate electrons from hadrons and muons.

PARTICLE IDENTIFICATION DETECTORS   For Particle Identification (PID) of charged particles PANDA uses a system of Cherenkov and time-of-flight detectors. A Detector of Internally Reflected Cherenkov light (DIRC) is integrated into the barrel part and a Disc DIRC into the end caps of the target spectrometer. They allow identification of particles with momenta between 1 and 5 GeV/c by measuring the opening angle of the Cherenkov light cone given the momentum measured by the MVD and STT. Particles with lower momenta are identified via a time-of-flight measurement using scintillating tile detectors, with a timing resolution better than 100 ps, and their energy loss inside the MVD and STT detectors. The muon detectors which separate muons from pions and kaons are integrated into the magnet yokes.

FORWARD SPECTROMETER   The forward spectrometer is constructed with components similar to the target spectrometer. To determine particle momenta a dipole magnet with a bending force of 2 Tm bends the trajectories of charged particles. The tracks are reconstructed with a set of straw tube detectors. A momentum resolution of $\Delta p/p \approx 0.2\%$ at 3 GeV/c is expected. Charged particles are identified by a ring imaging Cherenkov detector and a time-of-flight detector. The energy of neutral particles is measured with a sampling calorimeter that is made of alternating layers of lead and scintillating material. The calorimeter is followed by a forward muon detector which uses nested layers of absorber material and aluminum drift tubes [66]. The luminosity detector completes the set of PANDA detectors and is placed 11 m downstream of the interaction point (for a detailed discussion see chapter 3).

DATA ACQUISITION SYSTEM   The Data Acquisition (DAQ) system of PANDA has to deal with high data rates of up to 200 GB/s at an average interaction rate of 20 MHz [67]. To reduce the amount of data being written to disk, the data has to be filtered for interesting events which are defined by the physics goals. At the same time, the DAQ has to allow for a very flexible trigger generation since signal and background events will be very similar in terms of track multiplicity, kinematic distribution, and event shape. Because of this, PANDA does not use a global hardware trigger. Instead every detector front end employs feature extraction algorithms to select relevant data from its free running front end electronics. The preprocessed data of several front ends is collected in data concentrators and sent to an event building network which consists of two stages. Compute nodes reconstruct the event on the fly in order to form a trigger decision. Interesting events are then written to tape. A sketch of the PANDA data acquisition is shown in figure 13. The compute nodes are mainly Field Programmable Gate Array (FPGA) boards, but
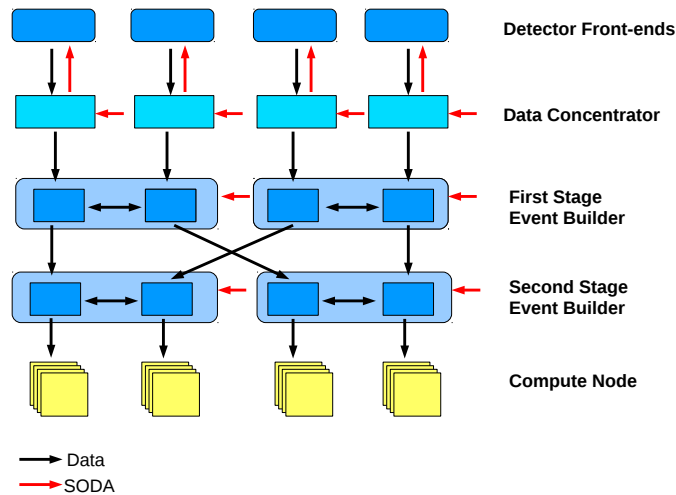

Figure 13: Sketch of the PANDA data acquisition system.

graphic processors or normal CPUs can be used as well depending on the data rate and the algorithms used. To synchronize the DAQ system between the different sub-detectors the Synchronization of Data Acquisition (SODA) protocol will be used. It offers a global clock with a jitter of less than 20 ps and timestamps coupled to the HESR beam structure. These global time stamps are used to sort and combine sub-events from the individual detectors. In addition, it controls the DAQ with a predefined set of common commands [68].

3
THE PANDA LUMINOSITY DETECTOR

As shown in section 2.2, a variety of items of the PANDA physics program require a luminosity measurement. For the determination of the time-dependent luminosity the tracks of elastically scattered antiprotons have to be measured precisely in terms of the scattering angle. Therefore, a tracking detector was developed which allows to reconstruct the antiproton tracks with high precision. The choice was to use novel silicon pixel sensors and to operate them in vacuum very close to the primary beam. This chapter gives an introduction to the concept and design of the luminosity detector at PANDA. This is followed by a discussion of silicon detectors and in particular *monolithic active pixel sensors* in chapter 4. Finally, the results of characterization studies of High Voltage Monolithic Active Pixel Sensor (HV-MAPS), a sensor technology which is the foreseen choice, are discussed.

3.1 Luminosity

For the determination of an absolute cross section or for the extraction of a line shape the time integrated luminosity needs to be known as the measured event rate $\dot{N}$, the cross section σ, and the instantaneous luminosity $\mathcal{L}$ are connected by

$$\dot{N} = \sigma \cdot \mathcal{L}. \tag{3.1}$$

The cross section is then given by the total number of measured events divided by the time integrated luminosity L

$$\sigma = \int \frac{\dot{N}}{\mathcal{L}} dt = \frac{N}{L}. \tag{3.2}$$

At a fixed target experiment like PANDA the luminosity can be defined as

$$L = n_{target} \cdot \Phi_{beam} \tag{3.3}$$

where n_{target} is the target density per unit area and Φ_{beam} is the beam particle flux. One way to measure the luminosity, therefore, is to monitor these two quantities. An alternative method uses a reference channel with a well known cross section and measures the event rate of this process.

3.2 Luminosity Measurement at PANDA

At the HESR the first method for luminosity determination described above will be used. The target thickness will be measured by the energy loss and emittance growth of the beam, while the beam flux will be measured with calibrated beam current transformers. However, there are two disadvantages to this method. First, only a relative precision of 10% can be achieved. Second, the beam cooling system has to be switched off during the luminosity measurement which means that the luminosity cannot be determined during data taking and the time integrated luminosity has to be interpolated between two luminosity measurements. Because of this, an independent luminosity detector is needed in

order to measure the instantaneous luminosity with high precision while PANDA acquires physics data.

The PANDA luminosity detector will use elastic antiproton-proton scattering to measure the luminosity. This process has the advantages of simple kinematic dependencies between the interacting particles and a very high cross section of 5-40 mb in the PANDA beam momentum range. The differential cross section can be split into three parts:

$$\frac{d\sigma}{dt} = \frac{d\sigma_{\text{Coul}}}{dt} + \frac{d\sigma_{\text{had}}}{dt} + \frac{d\sigma_{\text{int}}}{dt} \tag{3.4}$$

where σ_{Coul} denotes the long ranged Coulomb part of the interaction, σ_{had} the short ranged hadronic contribution, and σ_{int} the interference part. The momentum transfer, which is denoted by t, is related to the scattering angle Θ by the following relation

$$|t| = |p - p'|^2 = 4\mathbf{p}^2 \cdot \sin^2\left(\frac{\Theta}{2}\right) \tag{3.5}$$

as can be seen from figure 14.
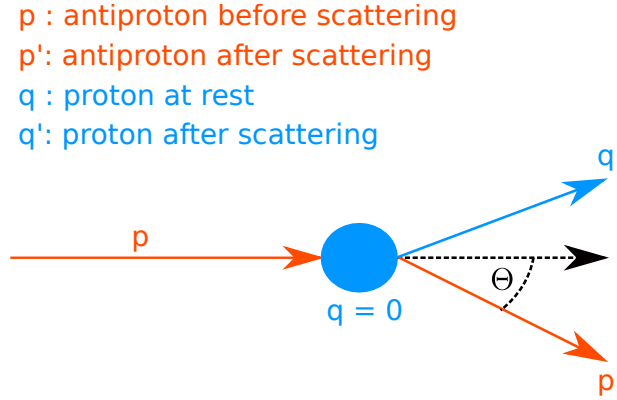
Figure 14: Kinematics of the elastic antiproton-proton scattering process.

A parametrization of the three parts is given by [69]:

$$\frac{d\sigma_{\text{Coul}}}{dt} = \frac{4\pi\alpha_{em}^2 G^4(t)(\hbar c)^2}{\beta^2 t^2}$$
$$\frac{d\sigma_{\text{had}}}{dt} = \frac{\sigma_{tot}^2}{16\pi(\hbar c)^2}e^{-bt}(1+\rho^2) \tag{3.6}$$
$$\frac{d\sigma_{\text{int}}}{dt} = \frac{\alpha_{em}\sigma_{tot}G^2(t)}{\beta|t|}e^{-\frac{1}{2}bt}(\rho cos(\delta) + sin(\delta)).$$

Here $G(t)$ is the proton dipole form factor given by

$$G(t) = \frac{1}{1 + (|t|/\Lambda^2)^2} \tag{3.7}$$

with $\Lambda^2 = 0.71$ GeV$^2/c^2$, α_{em} the fine structure constant, and ρ the ratio between the real and imaginary parts of the hadronic scattering amplitude. In addition, the parametrization depends on the relativistic speed β of the antiproton in the laboratory frame and the coulomb phase δ, i.e. the phase difference between the hadronic and Coulomb amplitudes which can be parameterized as

$$\delta = \alpha_{em}\left(\gamma + \ln\left(\frac{b|t|}{2}\right) + \ln\left(1 + \frac{8}{\Lambda^2 b}\right) + \frac{4|t|}{\Lambda^2}\ln\left(\frac{4|t|}{\Lambda^2}\right) + \frac{2|t|}{\Lambda^2}\right) \tag{3.8}$$
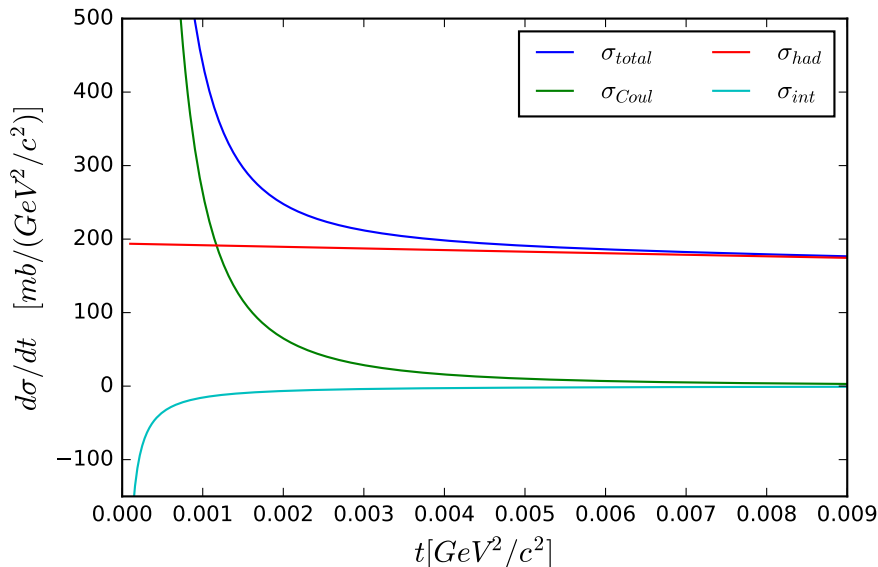
Figure 15: Hadronic and Coulomb part of elastic antiproton proton cross section at $p_{lab} = 6.2$ GeV/c. Values for ρ, b, and σ_{tot} from [69].

with $\gamma \approx 0.577$. The total hadronic cross section σ_{tot} has to be extracted from measurements, together with ρ and the slope parameter b. Figure 15 shows the behavior of the elastic cross section in terms of the momentum transfer for the three different contributions. It can be seen that at high momentum transfers the hadronic cross section dominates while the contribution of the Coulomb part increases for smaller momentum transfers. Since the Coulomb interaction is model independent and can be calculated with high precision, it can be used for a precise luminosity determination.

3.3 The Luminosity Detector

To determine the luminosity, the angular distribution of the elastically scattered antiprotons is measured with the luminosity detector. After transforming the model (equation 3.6) from the momentum transfer frame into the scattering angle frame, the parametrization of the elastic antiproton proton scattering cross section is fitted to the measured distribution with the luminosity used as a normalization constant.

In order to measure the model independent Coulomb part of the elastic scattering at typical PANDA beam momenta, the antiprotons have to be measured at very small momentum transfers or scattering angles. For this reason, the luminosity detector will cover an angular range of 3-8 mrad. Antiprotons scattered at larger angles would interact with the material of the beam pipe or parts of the forward spectrometer and can not be used for the luminosity determination as their original scattering angle at the interaction point can not be reconstructed. For lower scattering angles the antiprotons will be reintegrated into the antiproton beam. To cover the angular range from 3 to 8 mrad, the luminosity detector will be placed 11 m downstream of the interaction point and behind the dipole magnet and the forward spectrometer (compare figure 12). The dipole magnet will help to suppress background from other particles, but has the disadvantage that reconstructed antiprotons have to be propagated back to the interaction point in order to determine their scattering angle. This motivates the construction of a tracking detector which measures the momentum direction of the antiprotons. The performance requirements for the luminosity measurement are to determine the absolute time integrated luminosity with a

systematic uncertainty of 5% or less and to measure the relative time-integrated luminosity between physics runs with a relative uncertainty of 1% or less [63]. Furthermore, the instantaneous luminosity has to be measured in order to determine the bunch structure of the HESR beam and the trend of the luminosity during a run. The precision of the luminosity measurement is limited by the following points:

- The achievable statistics in the reconstructed angular distribution.

- The precision of the reconstructed scattering angle of the antiprotons. This is limited at low antiproton momenta by multiple scattering in the luminosity detector planes.

- Due to the small angular range covered by the luminosity detector, it is difficult to extract the luminosity and the model parameters ρ, b and σ_{tot} with high precision from a fit at the same time. Therefore, the KOALA experiment [58] will determine these parameters with high precision by simultaneously measuring the forward scattered antiproton and the recoil proton before PANDA starts data taking.

The luminosity detector has been designed considering the constraints given above. A CAD drawing is shown in figure 16. The detector consists of four tracking layers where
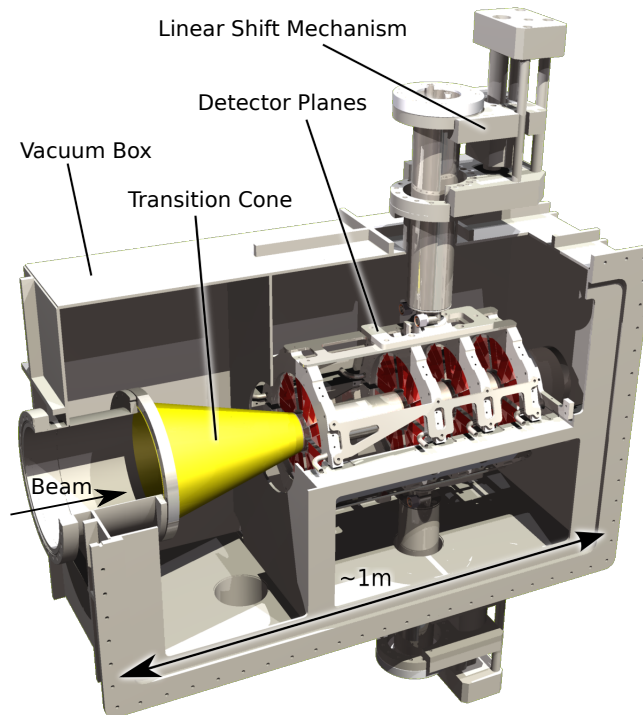
Figure 16: CAD drawing of the PANDA luminosity detector. The scattered antiprotons enter the detector through a thin transition foil (yellow) and are detected by four layers of silicon pixel sensors (drawn in red) [63]

the first layer is positioned 11.24 m behind the interaction point and following layers in distances of 20 cm, 30 cm, and 40 cm with respect to the first layer. This setup increases the tracking resolution due to the higher lever arm between the first two layers where the multiple scattering of the antiproton is still small. To achieve a good spatial resolution of hits while keeping the multiple scattering of the antiprotons low HV-MAPS are used as tracking detectors. The sensors have a thickness of only 50 µm. To avoid multiple scattering inside the beam pipe material, the detector planes are placed in vacuum. To

separate the luminosity detector vacuum from the vacuum in the beam pipe, a thin cone made out of boPET with a conducting layer of aluminum is used as a transition window for the antiprotons. The aluminum layer and the smoothly changing diameter of the cone ensure that distortions of the beam by a rapid change of the beam pipe conductivity are reduced. Each layer consists of 100 HV-MAPS arranged in a partially overlapping geometry to ensure a full ϕ coverage around the beam pipe as shown in figure 17 where one half plane is depicted. The heat produced by the HV-MAPS is conducted away from
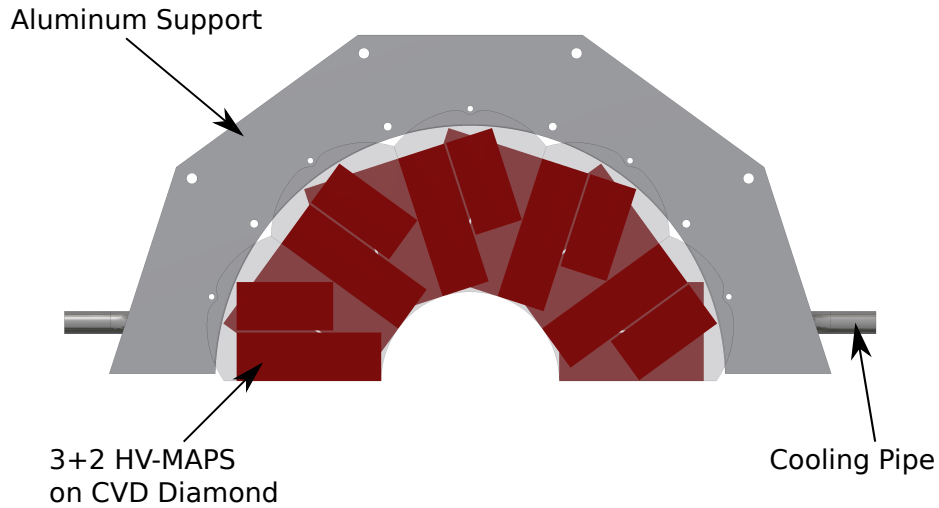
Figure 17: Aluminum support structure with HV-MAPS glued on CVD diamonds.

the sensors by polished diamond plates which are produced in a chemical vapor deposition (CVD) process. They have the advantage of combining high heat conductivity and a low material budget. The sensors are glued onto diamonds using a heat conducting glue with the diamonds themselves being attached to an aluminum support structure. Stainless steel pipes are fused into the aluminum support and are flowed with ethanol at a temperature of -25℃ as a cooling liquid. To avoid sensor damage due to bad beam conditions in the HESR during injection, each layer is divided into two half planes connected to linear shift mechanisms. During the injection phase the shift mechanisms retract the half planes out of the dangerous area. A detailed description of all parts of the luminosity detector can be found in [63].

4

CHOICE OF SENSORS - HIGH VOLTAGE MONOLITHIC ACTIVE PIXEL SENSORS

4.1 Sensor Requirements

The luminosity detector requires sensors with a good spatial resolution and a high rate capability. In addition, the sensors need to have a low radiation length to minimize multiple scattering and should be able to operate under vacuum conditions. These requirements lead to the choice of silicon sensors as the preferred detector technology. In detail the sensors should satisfy the following requirements:

- Antiprotons with a momentum between 1.5 -15 GeV/c are minimum ionizing particles with a most probable energy loss of ≈400 eV/µm according to the Bethe-Bloch equation [70]. This leads to 120 produced electron-hole pairs[1] per µm silicon. For this reason a sensor with effective charge collection and low noise front end electronics is needed. It is aimed to achieve a hit detection efficiency of nearly 100%.

- The placement of the sensors and front end electronics inside vacuum demands a low power consumption. Simulations and prototype tests have shown that a power consumption of 7 mW/mm^2 is acceptable [72].

- The optimal pixel size was estimated with Monte-Carlo simulations and was found to be 80 by 80 µm^2 [63]. For lower sizes multiple scattering starts to dominate the tracking resolution and would also increase power consumption and data rate due to a higher number of readout channels.

- The sensors need to resolve the 1.9 µs long beam bunches of the HESR to assign antiproton tracks to the corresponding bunch and fit into the general structure of the PANDA data acquisition system. In addition, it is planned to perform studies of the bunch structure which requires at least ten measurement points per bunch. This leads to a required timing resolution of better than 200 ns which will also help to reduce the number of fake or missing tracks during track reconstruction [63].

- The forward peaking of the antiproton-proton elastic cross section (compare figure 15) leads to a particle rate of 35 kHz/cm^2 on the inner sensors for an average luminosity of $1 \cdot 10^{32}$ cm^{-2}s^{-1}. This rate increases by a factor of two at peak luminosity. In addition, shifts or tilts of the antiproton beam would result in a further increase of the particle rate by 60%. This justifies the demand that the sensors should be able to handle a rate of up to 200 kHz/cm^2 [63].

- The PANDA data acquisition system requires trigger-less front end electronics.

The following section gives an introduction to semiconductor detectors and front end electronics. Furthermore, available semiconductor detectors for particle tracking applications are presented.

---

1 the average energy to create a electron-hole pair in silicon is 3.62 eV [71]

4.2 Semiconductor Detectors

The pn-Junction

The functional principle of all semiconductor detectors is based on the formation of a semi-conductor contact. The simplest configuration of such a contact is a pn-junction which is created by combining a p-doped semiconductor with a n-type material (a short introduction to semiconductors is given in appendix A). In practice there are two techniques to produce a pn-junction. The first technique is based on the diffusion of p or n-dopants into a block of n or p-type material, while the second employs particle accelerators to shot impurity atoms into the semiconductor. By varying the beam energy the depth profile and dopant concentration inside the semiconductor material can be controlled. In the contact region between the n- and p-type material a special boundary layer is formed. Due to the different concentrations of electrons and holes in the two materials, the holes start to diffuse into the n-type material and the electrons into the p-type material where they recombine. As the net charge of the semiconductor is neutral, the diffusion process creates stationary, positively charged ions in the n-type region and negatively charged ions in the p-type region. This creates an electric field pointing into a direction opposite to the diffusion current which finally stops the diffusion of electrons and holes. This way a so called *depletion layer* without free charge carriers is formed at the boundary layer. The thickness of the depletion layer can be calculated with the Poisson equation

$$\frac{d^2V(x)}{dx^2} = -\frac{\rho(x)}{\epsilon\epsilon_0} \tag{4.1}$$

with the charge concentration $\rho(x)$, the electric potential $V(x)$, and the dielectric constants ϵ and ϵ_0. By assuming that the charge concentration vanishes outside of the depletion layer and is box shaped inside of it (Schottky approximation), the Poisson equation can be solved yielding the thickness d

$$d = \sqrt{\frac{2\epsilon_0\epsilon V_0}{e}\frac{N_n + N_p}{N_nN_p}} \tag{4.2}$$

where N_n is the concentration of donor atoms, N_p the concentration of acceptor atoms, and V_0 the contact potential of the pn-junction [71]. The contact potential is typically in the order of the energy gap width (≈ 1 V) while the width of a depletion layer is usually between 10^2 and 10^4 Å [73].

Detection Principle

A charged particle passing through the depletion layer of a pn-junction loses ionization energy in the semiconductor material. The deposited energy leads to lattice vibrations (phonons) and the creation of electron-hole pairs. Due to the electric field inside the depletion layer, the electron-hole pairs are separated. The electrons are attracted towards the n-doped region while the holes migrate to the p-type region. As no additional charge carriers are present in the depletion layer, no recombination takes place and the electrons and holes create a signal at the junction electrodes. The principle is shown in figure 18. However, a plain pn-junction constitutes a very poor particle detector. The charge collection efficiency and sensitive part of the detector are very small since the depletion layer and the electric field are quite small. Due to reasons which will become apparent in section 4.3, the signal-to-noise ratio of a semiconductor detector is proportional to the junction capac-
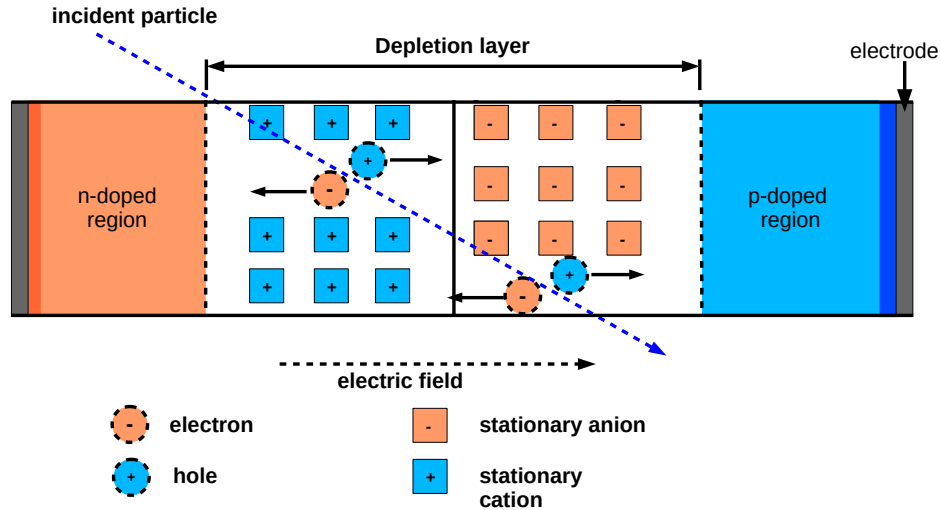
Figure 18: Usage of a pn-junction for the detection of ionizing radiation.

itance. As a result of the geometry of the depletion layer, the capacitance of a pn-junction can be calculated using the equation of a plate capacitor

$$C = \frac{\epsilon \cdot A}{d} \tag{4.3}$$

which is inversely proportional to the thickness of the junction. The detection characteristics can be improved by applying an external voltage to the pn-junction. Therefore, a negative voltage is connected to the p-side and a positive voltage to the n-side. The holes in the p-side are attracted towards the electrode of the p-side while the electrons in the n-doped region move towards the n-side electrode. This process leads to an increase of the depletion layer thickness and thus to a larger sensitive area and an improved signal-to-noise ratio. The thickness in the presence of an external voltage can be calculated by substituting V_0 in equation 4.2 with $V_0 + V_B$ where V_B is the applied voltage. Therefore, an external voltage of 60 V increases the thickness by roughly a factor of eight.

Properties of Semiconductor Detectors

Semiconductor detectors display excellent energy resolutions and stopping powers for charged particles. Detectors usually measure the energy deposit E of traversing particles by "counting" the number N of created charge carriers (ionization chamber, semiconductors) or photons (scintillators) by means of ionization. The error on the energy measurement ΔE is therefore proportional to the error on the counted charged carriers

$$E \propto N \Rightarrow \Delta E \propto \Delta N = \sqrt{N}.$$

Because of this, the energy resolution of a detector mainly depends on the amount of energy that is needed to create charge carriers. The average energy needed to create an electron-hole pair or electron-ion pair for different materials is listed in table 4. As can be seen semiconductor detectors produce between 10-100 times more electron-hole pairs than other detector materials. The energy resolution for a thin detector which is not able to stop the traversing particle completely is, therefore, given by

$$R = \frac{\Delta E_{FWHM}}{E} = 2.35 \frac{\sqrt{N}}{E} = 2.35 \sqrt{\frac{w}{E}} \tag{4.4}$$

Material	Detector Type	Mean Energy
Silicon	Semiconductor	3.62 eV
Germanium		3.81 eV
Helium	Gaseous	41 eV
C_4H_{10}		23 eV
NaI	Scintillator	25 eV
BGO		300 eV

Table 4: Average energy of different materials needed to create signal carriers [71].

where w is the average energy needed to create a electron hole pair.

However, in the case that the particles are completely stopped inside the sensitive detector material the equation above needs to be modified since the individual ionization processes are no longer independent of each other. This is expressed by introducing the so called Fano Factor F yielding

$$R = 2.35\sqrt{\frac{F \cdot w}{E}}. \tag{4.5}$$

The experimental measurement of the Fano Factor is challenging as various sources contribute to the overall resolution of a detector, but theoretical predictions give a value of $F = 1.115$ for silicon and $F = 1.13$ for germanium [74]. This further increases the achievable resolution.

Noise Sources and Radiation Hardness

The detection sensitivity of semiconductors is close to 100% and is only limited by the combined noise from the detector itself and the front end electronics (see section 4.3). The detector noise is caused by leakage current. Even in a reversely biased pn-junction a small fluctuating current can be measured and appears as noise at the detector output. The leakage current has several sources. The most important contribution stems from surface channels which depend on surface chemistry and contamination [71]. A second source is thermal generation of electron-hole pairs in the depletion layer. This effect can be increased by unwanted impurities and lattice defects. As described in the appendix, these create additional states in the energy band structure which serve as intermediate states between the conduction and valence bands. A last source is the movement of minority charge carriers, e.g. electrons, from the p-region across the junction towards the n-side. Furthermore, the leakage current depends on the irradiation of the detector and increases with increasing radiation dosage. There are two kinds of radiation damage:

Incident particles can displace lattice atoms from their original lattice side. This is called *displacement damage* and is specific to the type of the incident radiation. The displacement damage can be so large that type inversion occurs and a n-type material is transformed into a p-type material. This effect can be reversed by heating the semiconductor which leads to the diffusion of the displaced atoms back to their original lattice sides. During the annealing the former doping is restored and the leakage current is reduced, but remains at a higher level than before irradiation.

Ionization damage is caused by energy absorption in insulating layers of a semiconductor detector. Charge carriers are liberated and diffuse to other locations in the sensor. There they create unwanted charge concentrations and parasitic electric fields. This kind of damage mainly depends on the particle energy.

4.3 Front End Electronics

The main task of front end electronics is to amplify the small signal from the detector and shape the signal to a convenient form (depending on the application). A typical layout of a front end electronics circuit, therefore, consists of an amplifying and a signal shaping stage. To avoid pertubation of the small detector signals, the front end electronics are placed as close as possible to the detector.
There are three different types of amplifiers:

- current sensitive

- voltage sensitive

- charge sensitive

Radiation detectors generally are high impedance devices. In contrast current sensitive preamplifiers are usually used with low impedance devices [71] and are not discussed here further.
The voltage sensitive amplifier boosts any voltage signal that appears at its inputs. For radiation detectors the voltage arises from the collected charge Q and the detector capacitance C_D

$$U = \frac{Q}{C_D}. \tag{4.6}$$

Since the capacitance of semiconductor detectors may change with variations of the bias voltage or the temperature, voltage sensitive amplifiers are not used in connection with semiconductor detectors [71].
The detector capacitance can be circumvented by integrating the charge produced by the semiconductor on an additional capacitance C_F. This is done with charge sensitive amplifiers whose general layout is shown in figure 19a. The input voltage signal U_{in} from
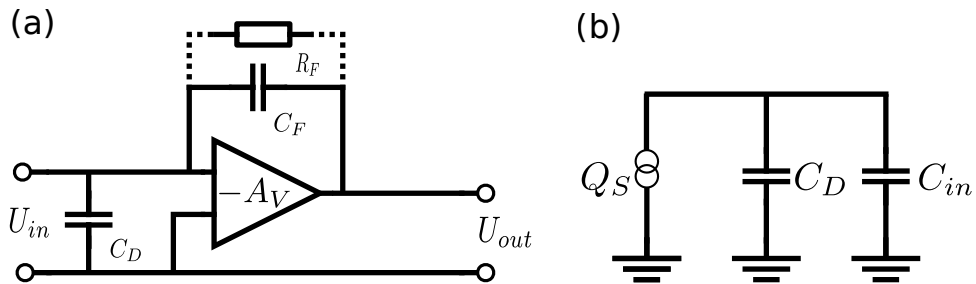
Figure 19: (a) Schematic of a charge sensitive preamplifier with voltage gain A_V connected to a detector with capacitance C_D. The output signal is fed back through a capacitance C_F and a resistor R_F. (b) Charge sharing of the collected sensor charge Q_S between the detector capacitance C_D and the input capacitance C_{in} of the preamplifier.

the detector is fed into an inverting voltage amplifier with the gain

$$A_V = -\frac{U_{out}}{U_{in}}. \tag{4.7}$$

The output voltage U_{out} of the amplifier is fed back to the input via a feedback capacitor with the capacitance C_F. In order to derive the output voltage, one first makes the as-

sumption that the amplifier has an infinite bandwidth and input impedance. In this case the complete input current flows across the feedback capacitor

$$
\begin{aligned}
I_{in} &= \frac{U_f}{Z_F} = \frac{U_{in} - U_{out}}{Z_F} \\
&\stackrel{4.7}{=} \frac{(A_V + 1)U_{in}}{Z_F} \\
&= (A_V + 1)U_{in} \cdot \omega C_F
\end{aligned}
\tag{4.8}
$$

with the feedback capacitor impedance

$$
Z_F = \frac{1}{\omega C_F}.
$$

The input impedance Z_{in} of the charge sensitive amplifier is then given by

$$
\begin{aligned}
Z_{in} &= \frac{U_{in}}{I_{in}} \stackrel{4.8}{=} \frac{1}{(A_V + 1) \cdot \omega C_F} \\
&= \frac{1}{\omega C_{in}} \text{ with } C_{in} = (A_V + 1)C_F.
\end{aligned}
\tag{4.9}
$$

Using the expression derived for the input capacitance C_{in} this leads to the equation for the voltage gain per input charge Q_{in}

$$
\begin{aligned}
A_Q &= \frac{U_{out}}{Q_{in}} \stackrel{4.7}{=} -\frac{A_V \cdot U_{in}}{C_{in}U_{in}} \stackrel{4.9}{=} -\frac{A_V}{A_V + 1}\frac{1}{C_F} \\
&\approx -\frac{1}{C_F} \text{ for } A_V \gg 1.
\end{aligned}
\tag{4.10}
$$

Therefore, the output voltage of a charge sensitive preamplifier is given by the equation

$$
U_{out} \approx -\frac{Q_{in}}{C_F}
\tag{4.11}
$$

which does not depend on the detector capacitance.

The charge collection efficiency of the charge sensitive preamplifier, i.e. the ratio between the total generated charge Q_S and the charge collected by the preamplifier Q_{in}, can be estimated from figure 19b as the charge sharing between the detector and the input capacitance

$$
\begin{aligned}
\frac{Q_{in}}{Q_S} &= \frac{Q_{in}}{Q_D + Q_{in}} \\
&= \frac{Q_{in}}{Q_{in} + \frac{Q_{in}C_D}{C_{in}}} \text{ using } \frac{Q_{in}}{C_{in}} = \frac{Q_D}{C_D} \\
&= \frac{1}{1 + \frac{C_D}{C_{in}}}.
\end{aligned}
\tag{4.12}
$$

Because of this, the charge collection efficiency approaches 100% if the input capacitance is much larger than the detector capacitance.

In addition to the signal charge, the detector noise gets amplified in the amplifier. To derive the input noise charge, one starts from the noise output voltage U_{no} which is fed back through the capacitive voltage divider C_F-C_D

$$
U_{no} = U_{ni}\frac{Z_F + Z_D}{Z_D} = U_{ni}(1 + \frac{C_D}{C_F})
\tag{4.13}
$$

where U_{ni} is the noise input voltage at the input of the amplifier. The equivalent input noise charge is then given by

$$Q_{ni} = \frac{U_{no}}{A_Q} \overset{4.10}{=} U_{no}C_F \overset{4.13}{=} U_{ni}(C_D + C_F).$$

Building the ratio of the input charge and noise input charge leads to

$$\frac{Q_S}{Q_{ni}} = \frac{1}{C_D + C_F} \frac{Q_S}{U_{ni}}. \tag{4.14}$$

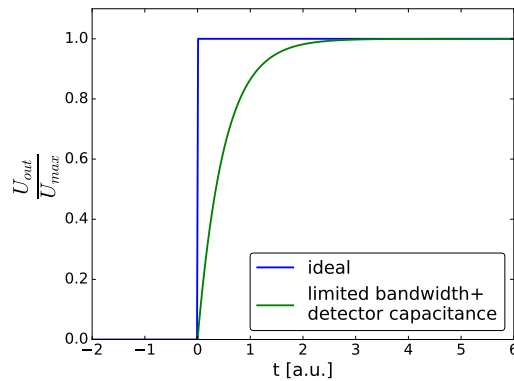The signal-to-noise ratio, therefore, depends on the detector capacitance and decreases for increasing detector capacitance.

Figure 20: Time domain response of a charge sensitive amplifier.

The response of a charge sensitive amplifier for a short detector signal pulse is shown in figure 20. For an ideal amplifier the time domain response is a step function. However, real amplifier circuits have a finite input impedance. Together with the detector capacitance this input impedance R_{in} forms a low pass filter which results in a time dependence of the amplifier output given by

$$U_{out} = U_{max}(1 - e^{-t/\tau}) \text{ with } \tau = R_{in} \cdot C_D.$$

In order to discharge the feedback capacitor faster, an additional resistor R_F can be added in parallel to the feedback capacitor. This adds an exponential tail to the amplifier output.
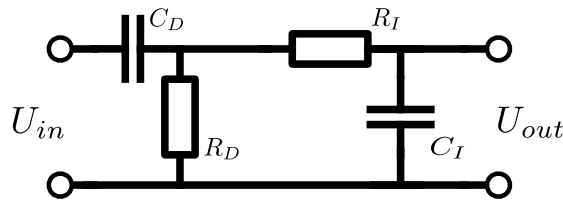
Figure 21: Schematic diagram of a CR-RC shaper.

The preampifier is in general followed by a shaping stage. This stage has the task to shape the preamplifier output to an application dependent form. There are two considerations that are generally in competition with each other and have to be optimized for the task at hand. The first is reducing the pulse width to avoid signal pile up. The second is limiting the frequency bandwidth of the front end electronics to decrease the amount of noise. The noise can have several sources. In general three noise mechanisms are distinguished. Noise caused by velocity fluctuations of moving charge carriers, for example in resistors, is called

thermal noise. Noise due to number fluctuations of charge carriers is called shot noise. Both are referred to as "white" noise since in the frequency domain their power per unit density is constant [75]

$$\frac{dP_{noise}}{d\omega} = const.$$

The third noise component is called $1/f$ noise due to its frequency distribution. It occurs when charge carrier fluctuations are not randomly distributed in time, for example recombination or trapping in semiconductor devices. These noise contributions can be limited by applying a frequency band pass where thermal and shot noise are limited by the width of the band pass and the contribution of the $1/f$ noise depends on ratio of the upper and lower frequency cut-off. In the case of detectors for timing applications, an additional requirement for the shaping stage is to keep a fast rise time of the detector signal.

A commonly used pulse shaper is the CR-RC shaper which is cascade of a CR differentiator and a RC integrator. The circuit is shown in figure 21. The time and frequency response
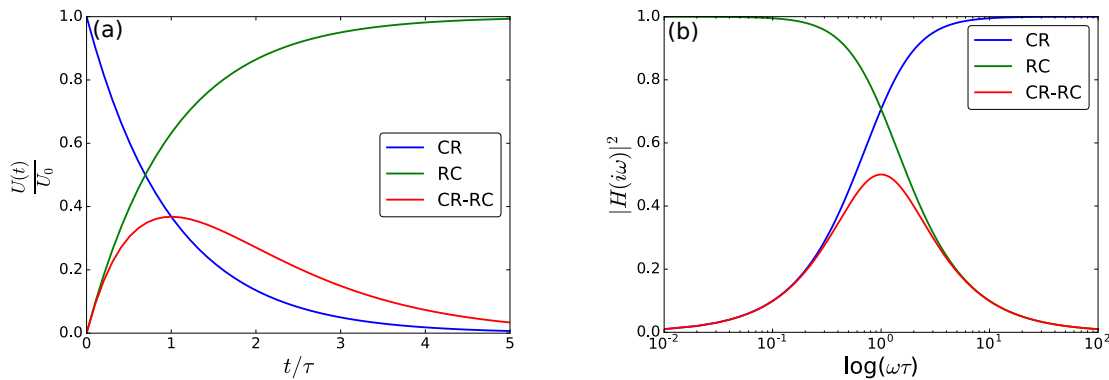
Figure 22: Time (a) and frequency (b) domain response functions of an CR-RC shaper with equal time constants τ. ω denotes the frequency of the input signal.

of a CR-RC shaper can be analyzed using the Laplace and Fourier transformation which is done in appendix B. Both responses are shown in figure 22 for equal time constants τ of the differentiator and the integrator circuit parts. Usually the best signal-to-noise ratio can be achieved for equal time constants [71]. The usage of an RC-circuit however has the disadvantage that it leads to a baseline undershoot of the shaped signal. This is caused by the finite tail of the preamplifier pulse. In order to correct this behavior, so called pole-zero cancellation can be used. Pole-zero cancellation is achieved by inserting an additional resistor into the CR circuit parallel to the capacitor. To further increase the signal-to-noise ratio, compared to CR-RC shaping, semi-Gaussian shapers can be used. Shaping the output to a Gaussian form can be achieved by adding several RC stages to the CR-RC shaper (typically 4-5 RC-stages are sufficient). This offers an 18% increase of signal-to-noise ratio on the price of much wider pulses which can lead to problems at high count rates [71].

For applications where fast timing is important, delay line shaping can be used. The step function output signal of the preamplifier is split in two and one signal is inverted, delayed, and again superimposed on the preamplifier signal. The result is a rectangular output pulse with fast rise and fall time. However, it suffers from a very bad signal-to-noise ratio compared to other shaping methods. Therefore this kind of shaping is ideal for detectors with a high internal gain like scintillators connected to photomultiplier tubes.

4.4 Silicon Sensor Technologies

DOUBLE SIDED SILICON STRIP SENSORS AND SILICON HYBRID PIXEL SENSORS
In order to reconstruct the track parameters of particles, the semiconductor detector has
to provide information on the spatial position where the particle hit the detector. This is
accomplished by segmenting the readout electrodes which leads to two different designs,
namely silicon strip and silicon pixel detectors. The simplified layout of a strip sensor is
shown in figure 23. It consists of a weakly n-doped main part called *bulk*. On one side
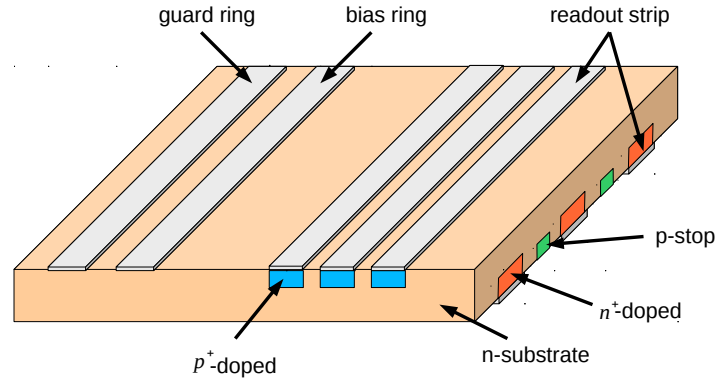
Figure 23: Schematic drawing of a double sided silicon strip detector.

of the sensor heavily p+-doped strips are created by ion implantation while on the other
side heavily n-doped strips are generated. The sides are referred to as the n- and p-side of
the sensor. The signal can be readout using thin metal contacts which are placed over the
heavily doped strips to form ohmic contacts. Due to the segmentation of the two sides, an
electric field is created which transports the generated charge carriers to the closest strip.
The x and y coordinates of the hit position can be reconstructed by rotating the strips of
the n-side with respect to the p-side by the so called *stereo angle*. In combination with the
fixed z-position of the sensor the three dimensional hit position can be determined. On the
n-side of the sensor small p-doped regions named *p-stops* are placed. They isolate the n-
strips and prevent the positive space charge created by low-mobility holes from attracting
electrons from the n-side. Furthermore, the active sensor area is surrounded by two metal
rings: the bias and guard ring. The bias ring is used to supply the sensor with the bias
voltage, while the guard ring is designed to prevent the breakthrough of the pn-junction
due to leakage of the electric field at the sensor edges. Since the electric field lines are
parallel to each other in the bulk and end on the readout strips, the achievable spatial
resolution would be limited by the pitch of the strips p. For evenly distributed tracks the
distribution of the hit position is equal to a uniform distribution with the variance [75]

$$\sigma^2 = \frac{p^2}{12}. \tag{4.15}$$

However, the achievable resolution can be improved by using the thermal diffusion of the
charge carriers and the transversal spread of the charge carrier creation by tracks which
are not perpendicular to the sensor front face. Furthermore, an external magnetic field will
lead to a deflection of the charge carriers by the so called Lorentz angle. These processes
can lead to the effect that the charge carriers are distributed over several readout strips.
By calculating the center of gravity of the charge carrier distribution, the spatial resolution
can be improved.

An alternative approach to strip sensors is hybrid pixel sensors shown in figure 24. Here the silicon sensor is segmented into readout pixels and the 2D hit information can be gained directly from the row and column address of the hit and the pitch between the pixels. Both technologies need a separate readout chip with the front end electronics that has
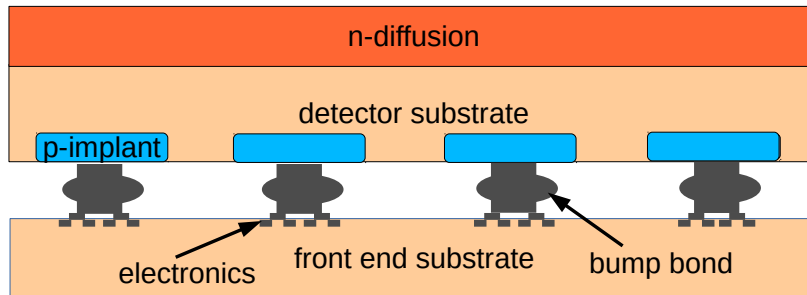

Figure 24: Schematic drawing of a hybrid pixel sensor bump bonded to a readout chip.

to be connected to the sensors. In the case of strip sensors the readout chips are usually attached to the sides of the sensor using wire bonds, while in the case of pixel sensors the readout chips are bump bonded to the backside.

Silicon strip sensors and hybrid pixel sensor are not well suited for usage in the luminosity detector. To obtain a full ϕ-coverage, the strip sensors have to be designed in a trapezoid shape. Therefore, the strips have a varying length which leads to different strip capacitances along the sensor and a position dependent noise distribution. In addition, the strip readout would give hit ambiguities during the track reconstruction at high rates. These issues can be solved by using hybrid pixel sensors. But the necessity of additional readout electronics bonded to the backside of the sensors, would increase the radiation length of one layer of the detector. Furthermore, an additional cooling structure would have to be added to remove the heat produced by the readout electronics which again increases the radiation length.

MONOLITHIC ACTIVE PIXEL SENSORS   Monolithic Active Pixel Sensor (MAPS) for charged particle tracking were developed starting from CMOS[2] devices for visible imaging. They combine the radiation sensitive diode structure with the readout electronics on one piece of silicon [76]. The structure of one pixel cell is shown in figure 25. To obtain a good charge collection and a high sensitive area, the sensor uses twin tubs implanted onto a lightly p-doped epitaxial layer which is grown onto a highly p-doped p^{++} substrate [76]. Due to the different dopant concentrations between the p-well/substrate and the epitaxial layer, potential barriers are formed which guide the electrons created by a passing charged particle to the sensing n-well. Transistors which are part of the readout electronics are placed inside the p-well. MAPS have an efficiency of nearly 100% and can be produced with high granularity with pixel sizes of about 20x20 µm^2 [77]. Furthermore, the chips can be thinned down to a thickness of 50 µm reducing multiple scattering. Compared to other silicon detectors, the production of MAPS is quite cheap as standard production processes can be used. However, the charge collection time is quite high, since free charge carriers are only collected by diffusion, and ranges between 20-150 ns depending on the thickness of the epitaxial layer [78].
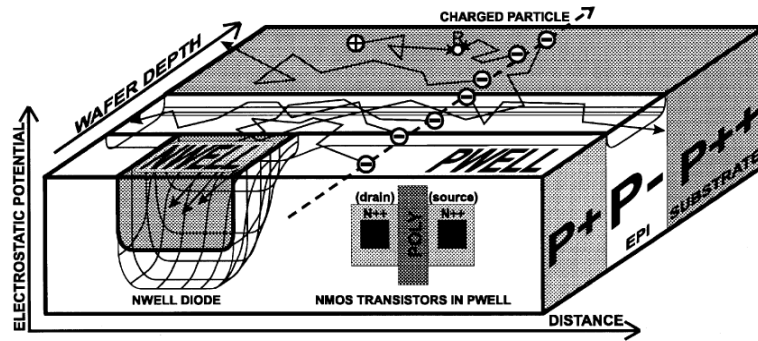
2 Complementary metal-oxide-semiconductor

Figure 25: Scheme of the pixel structure of a MAPS. The sensing n-well is grown into a p-epitaxial layer while the front end electronics transistors are integrated into the p-well [76].

The used pixel structure has the disadvantage that PMOS transistors can not be used in the sensitive areas of the chip as this would require additional n-well structures acting as substrate. But any n-well structures other than the charge collecting n-well, would also result in parasitic charge collection. Therefore, all structures requiring PMOS components (e.g. discriminators) need to be placed at the chip periphery outside of the active area. Because of this, MAPS are readout using a rolling shutter mode where the readout cycles through all rows and all pixels of one row are read in parallel. This leads to long readout times of 180 µs [77] in spite of zero-suppression of hits. Unfortunately this renders the sensors useless for an application in the luminosity detector.

4.5 High Voltage - Monolithic Active Pixel Sensors

To resolve the disadvantages of the MAPS design, so called HV-MAPS sensors have been developed [79]. They use high voltage CMOS technology. A pixel consists of a lowly doped n-well which is placed in a p-type substrate. N-well and p-substrate can be reversely biased with bias voltages in the order of 60 V which creates a depletion layer with a thickness of about 10 µm. PMOS and NMOS transistors are housed inside the n-well in low-voltage technology. This allows to use transistors with small gate lengths and to design complex CMOS circuits. The simplified layout of a HV-MAPS pixel is shown in figure 26. A charged particle crossing the sensor creates electron-hole pairs. Due to the high electric
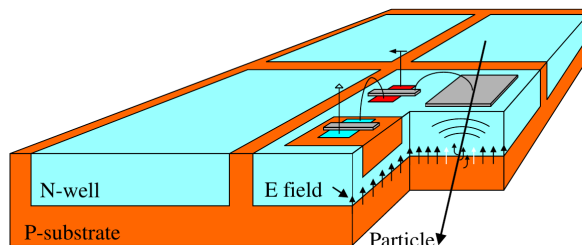

Figure 26: Four high-voltage pixels [79].

field in the depletion layer, the electrons are collected by drift in contrast to MAPS where charge collection is based on diffusion. The benefits are a faster charge collection in the order a few nano seconds and a higher radiation tolerance compared to MAPS since the trapping probability for the electrons is lowered. First prototypes were tested successfully. The sensors were irradiated with 10^{14} n_{eq}/cm^2 and X-rays up to 500 kGy and remained

functional. Only an increased noise level was observed which disappeared after the sensor was cooled to -35℃ [80].

Because of the successful tests the Mu3e collaboration from Heidelberg joined the development of the HV-MAPS technology [81]. Several prototypes called MuPix (Muon Pixel) were designed and tested. The fast charge collection and the integration of the front end electronics makes the MuPix the first choice sensor technology for the luminosity detector.

5

CHARACTERIZATION OF MUPIX PROTOTYPES

5.1 The MuPix 6 Prototype

Most of the measurement results presented in the following sections were obtained with the fifth version of the MuPix prototype. The MuPix 6[1] was developed to solve several issues found in its predecessor, the MuPix 4 prototype. Amongst others, a bug leading to a wrong readout of the row address was fixed. In addition, a second amplification stage was added to achieve a better signal-to-noise ratio compared to the MuPix 4. The compositions of the MuPix 6 analogue and digitals part are outlined in the next sections.

Chip Layout
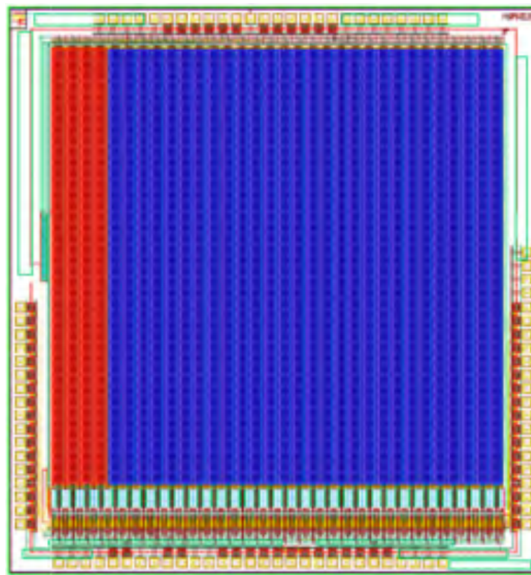
Figure 27: Layout of the MuPix 6 chip exported from the design software. The pixels with single/-double stage amplification are drawn in red/blue. The digital part is at the bottom of the drawing [82].

The MuPix 6, whose schematic layout is shown in figure 27, has a pixel matrix consisting of 40 rows and 32 columns. Each pixel has a size of 80 x 102 µm^2. This results in a total active area of 3.200 x 3.264 mm^2. The pixel matrix is split into two parts: pixels in the first four columns still feature the single-stage MuPix 4 amplification structure, while the other pixels have the two-stage amplification. This allows for the direct comparison of the performance of the two analogue schemes. The digital part is placed at one of the chip edges (compare bottom part of figure 27). Here the pixels are mapped in a 20 x 64 matrix. Since the hit address scheme uses the same mapping as the digital part, the readout address has

---

1 The MuPix 6 is the fifth prototype version of the MuPix series but was submitted with the wrong numbering to the producer. Hence, it is named MuPix 6.

to be decoded into the physical pixel address. The chip is surrounded by aluminum pads to connect external supply voltages and logical signals using wire bonding. The function of the pads is summarized in table C1 in the appendix.
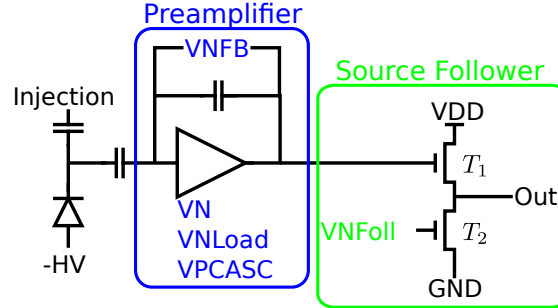
Analogue Part

Figure 28: Schematic of the in-pixel analogue part consisting of a charge sensitive amplifier (blue) and a source follower (green) [82].

Each pixel consists of a central diode surrounded by eight additional diodes. The diodes are constructed by a deep n-well in the p-substrate. To create a combined collecting electrode, all n-wells are electrically shortened. This layout was chosen to keep the total pixel capacitance small while retaining a homogeneous hit detection efficiency over the whole area of the pixel. The first stage amplification is implemented in the central diode. It comprises a capacitively coupled, charge-sensitive, preamplifier and a source follower. A simplified schematic is shown in figure 28. The source follower is built by two transistors (T_1 and T_2) and forms a voltage divider with the resistances R_{T_1} and R_{T_2}. The output voltage of the source follower is given by

$$U_{out}^{SF} = \frac{R_{T_1}}{R_{T_1} + R_{T_2}} V_{DD}.$$

(5.1)

The resistance R_{T_1} is modulated by the output voltage of the charge sensitive preamplifier and any change of the preamplifier output signal leads to a modulation of the output voltage (Out) of the source follower. This way the signal of the preamplifier is driven to the digital part where the second amplification stage is located. The preamplifier and source follower are controlled with one external voltage VPCasc[2] and four voltages generated by on-chip Digital-to-Analogue Converters (DACs) (VNFoll, VN, VNLoad and VNFB) which are also shown in figure 28.

The amplified signal is capacitively coupled to the second amplifier stage in the chip periphery. The simplified schematic of the analogue part in the chip periphery is shown in figure 29. It consists of a charge sensitive amplifier which is identical to its counterpart in the pixel. The voltages necessary for this amplifying stage are controlled by four additional DACs. The output signal of the second amplifier modulates the so-called baseline (BL). A comparator, which acts as a discriminator, compares the (modulated) baseline signal to a threshold voltage (THR). Both the baseline and the threshold voltage are defined by external voltage sources. As the two-times amplified signal has a negative polarity, the comparator produces a positive digital signal if the modulated baseline signal drops below the threshold. For that reason, an increase of the threshold voltage reduces the effective threshold "seen" by the signal. The comparator and the baseline restoration are

---

2 If not explicitly mentioned otherwise all described voltages are generated on the cip

controlled by two DACs. The BLRes DAC steers the baseline restoration, i.e. the speed the modulated signal returns to the baseline voltage, and VPComp adjusts the main current source of the comparator. The MuPix prototypes have a multiplexer circuit that combines
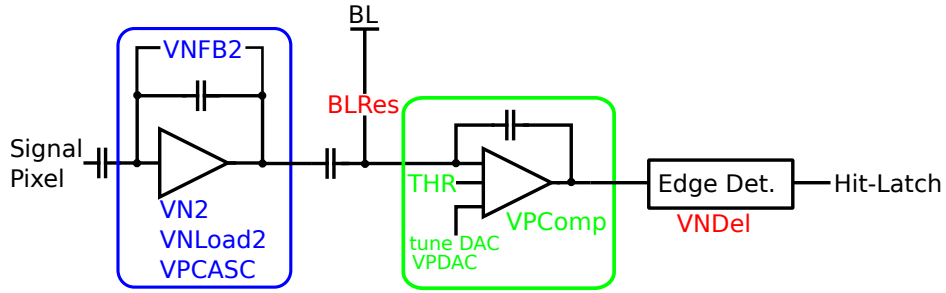

Figure 29: Schematic of the peripheral analogue part consisting of a second charge sensitive amplifier (blue) and comparator (green) [82].

the comparator outputs of all pixels and drives an external signal line which is called *hit-bus*. The pixel whose comparator output is driven to the hit-bus can be selected by the user. This way it is possible to measure the time-over-threshold (ToT) of the selected pixel, for example with an FPGA or an oscilloscope. To counterbalance differences in the pixel performance due to inhomogeneities in the chip production process, the working point of the comparator of each pixel can be changed using 4-bit tune DACs. The output voltage of the tune DAC is added to the baseline voltage and shifts it towards higher voltages. The overall tuning spread can be controlled with the VPDAC. A high value of the VPDAC leads to a larger baseline shift while a low value results in a smaller baseline shift per tune DAC value. An edge-detector (Edge Det.) identifies the transition of the comparator output signal from the logic low to logic high level. The delay of the signal issued by the edge detector can be adjusted with the VNDel voltage. In the case of a rising edge a hit flag is stored inside the hit-latch for each pixel individually. To obtain the time information of the hit, the time stamp of the rising edge of the comparator output is saved in eight capacitors for each pixel individually. These capacitors are charged or discharged by a global time stamp bus which has to be driven by an external source. If a rising edge at the comparator output occurs, the capacitors are locked in their current state. It has been shown that the time stamp frequency can reach up to 100 MHz [82].

Digital Part and Readout State Machine

In the case of the MuPix 6 prototype, the chip readout needs to be controlled from the outside. This task and the time stamp generation can be handled by an FPGA, for example. Apart from that, the readout logic is already fully implemented in the MuPix 6 chip.
The MuPix 6 readout uses two priority signals to indicate the presence of hits and achieve a zero suppressed readout. The first priority signal is generated internally in each chip column to indicate the presence of hits in that column. The second priority signal is generated in the chip column logic and used by the FPGA state machine during the chip readout.
The state machine responsible for the readout is implemented in the following way (see figure 30). At the start of the readout the *load pixel* signal is sent from the FPGA. This causes the state of the hit latches to be loaded into the so called pixel latches which are used to produce the column priority signal. After that the *pull down* signal is transmitted which pulls the address and time stamp buses to defined voltages. Now the *load column* signal is applied. The chip will check the internal priority signal of all columns. If the priority signal of a column is high, the hit flag, row address, and time stamp of the first
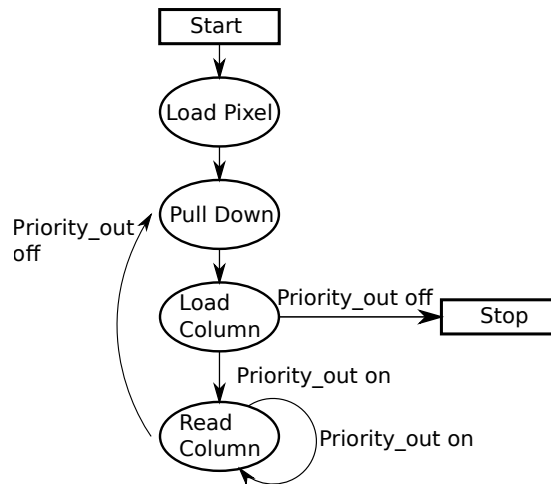
Figure 30: State machine for MuPix 4 and 6 readout.

hit in the column are driven to the column bus and latched in a column logic block assigned to that column. This is done for all columns in parallel. Following this the hit and pixel latch of the corresponding pixel are reset and the time stamp capacitors are unlocked. The pixel can now detect new hits. The column logic blocks are chained to produce the external priority signal. As long as this priority signal is high, the *read column* signal is issued repeatedly. At the rising edge of each read column signal the chip maps the column/row address and the time stamp of the hit in the next column logic block to the parallel address and time stamp fan-out. This fan-out is connected to the output pads of the MuPix chip where the hit informations are sampled by the FPGA. After the priority signal goes low, the state machine moves back to the pull down state. This sequence is repeated until the load column signal does not produce a high priority signal anymore and all hits have been read. In this case the readout stops until the next readout cycle is started. The timing between the different readout signals is controlled inside the FPGA using a set of counters. The exact settings of these counters depend on the internal clock speed of the FPGA and the length of the cables between the FPGA board and the board housing the MuPix prototype chip. The values used for this work are given in table C2. The total time required to complete a readout cycle depends, in addition, on the chip occupancy. In the case of five hits in different chip columns, using the values in table C2, the total readout time amounts to 1980 ns. If the five hits are located in the same column, the readout takes 3700 ns. This is due to the fact that in this case the readout state machine returns to the pull down state after each hit, while in the first case the state machine can stay in the read column state until all hits have been read.

Also implemented in the digital part are two different slow control registers. One register controls the chip DACs that steer the different components in the analogue part while the second controls the pixel tune DACs and selects the output of a pixel discriminator to be multiplexed onto the hit-bus line. Two different settings for the chip DACs were developed in Heidelberg using sensor simulations and measurements, and are given in table C3 in the appendix. The first uses quite aggressive settings to get a fast shaper signal while the second reduces the power consumption of the sensor at the cost of a slower shaping time. The power consumptions for comparable settings[3] have been measured to be 935 mW/cm^2

---

3 The main difference is the value for the BLRes DAC which is set to 0xA in [82], but does not have a heavy impact on the power consumption. The different settings used in this work were caused by a miscommunication.

and $223\,\mathrm{mW/cm^2}$ [82]. The aggressive settings are also called "normal" settings due to their earlier development.

MuPix Sensor Board

A printed circuit board was developed in Heidelberg to supply the MuPix 4 and 6 with the needed voltages and to provide the chip read-out. A picture of the board is shown in figure 31. From a 5 V input voltage the necessary supply and bias voltages are derived. The bias voltage (0-100 V) can be applied with an additional connector. Furthermore, the board houses two DACs to generate injection pulses to test the functionality of the chip. The first injection pulse is fed into the pixels of all odd numbered row-pairs, while the second injection circuit is connected to the pixels of all even numbered row-pairs. A third DAC generates a global threshold voltage common to all pixels. The board has two 40-pin connectors to attach an FPGA for slow control and read-out with single-ended signals.
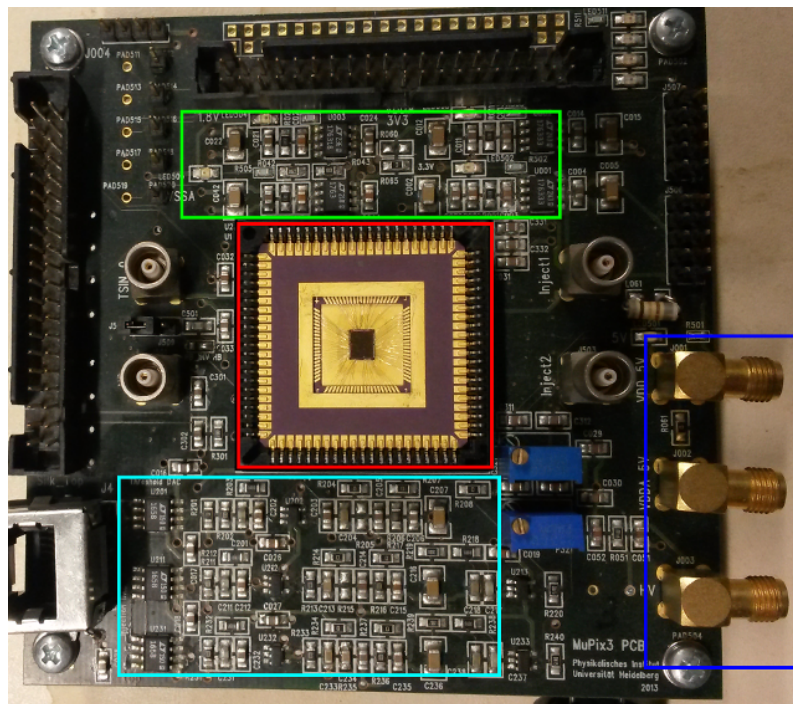
Figure 31: The MuPix sensor board developed in Heidelberg. The MuPix chip in a ceramic carrier(red), supply voltage generation (green), threshold and injection DACs (cyan), power connectors (blue).

5.2 Prototype Readout Chain

For testing of the MuPix prototypes a data acquisition system has been designed in the context of this work. The readout and slow control of the prototype sensors are handled by an FPGA board and a personal computer. The third revision of the Hades trigger and readout board (TRBv3) was chosen as the FPGA board. A picture of the TRBv3 is shown in figure 32. It features five ECP3 FPGAs manufactured by Lattice Semiconductors. Four FPGAs are mounted at the board periphery and are connected to a 208 pin expansion connector (QMS series by Samtec) to attach external sensors. The four peripheral FPGAs are connected to the fifth central FPGA using multi-gigabit transceivers. The central FPGA joins the data streams from the peripheral FPGAs and sends the data to the

downstream data acquisition components using eight SFP[4] transceivers which can be configured as gigabit-ethernet links [83]. Furthermore, the TRB is compatible with the PANDA data acquisition system and can be used as the front end FPGA-board of the final version of the luminosity detector. In order to readout the MuPix chips with the
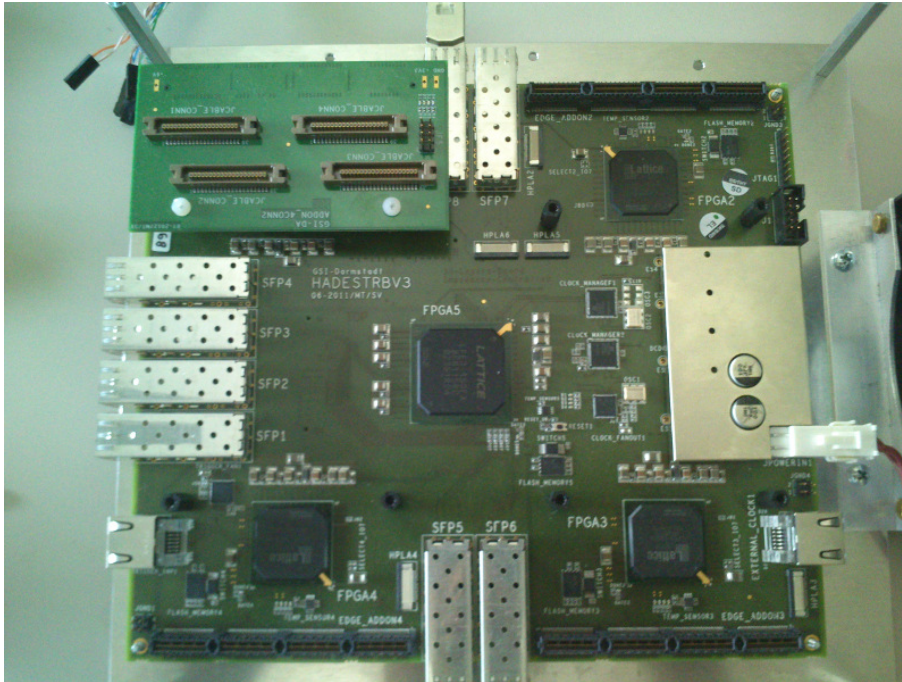

Figure 32: The Hades Trigger and Readout Board revision 3. The view of the fourth peripheral FPGA is blocked by an add-on board, which is used to attach flat ribbon cables, connected to one of the 208 pin expansion connector.

TRB, a firmware was developed using the VHDL[5] hardware description language. With this firmware it is possible to independently operate two MuPix 6 prototypes per peripheral FPGA. To allow for the readout of the chip, the state-machine described in figure 30 was implemented. After a trigger signal, generated either by an external trigger logic or by the user, the sensor hits are read and stored inside a FIFO[6]-buffer. From there the data is either flushed to the fast TRB readout interface or read by the slow control interface. The last option was implemented for debugging purposes and measurements in the laboratory, while the first readout option has been used during beam tests. Moreover, time-over-threshold and latency histograms of a single pixel are acquired inside the FPGA. It is important to note that the number of MuPix chips per FPGA is not limited by the logic circuits on the FPGA, but only by the available number of input/output connections of the expansion connectors. A readout scheme for a single MuPix 6 sensor is shown in figure 33. The add-on board, which is plugged into the expansion connectors, connects the slow control and readout signals of the TRB to the MuPix sensor board using two, 40-wire, flat ribbon cables.

In addition to the firmware, a data acquisition and slow control software has been developed in C++11. It processes the incoming UDP[7] network data stream which is sent by the TRB. The classes handling the decoding of sensor data, i.e. mapping of the column logic address to the physical address and sensor slow control, were implemented with a

---

4 Small Form-factor Pluggable
5 Very high speed Hardware Description Language
6 First-In First-out
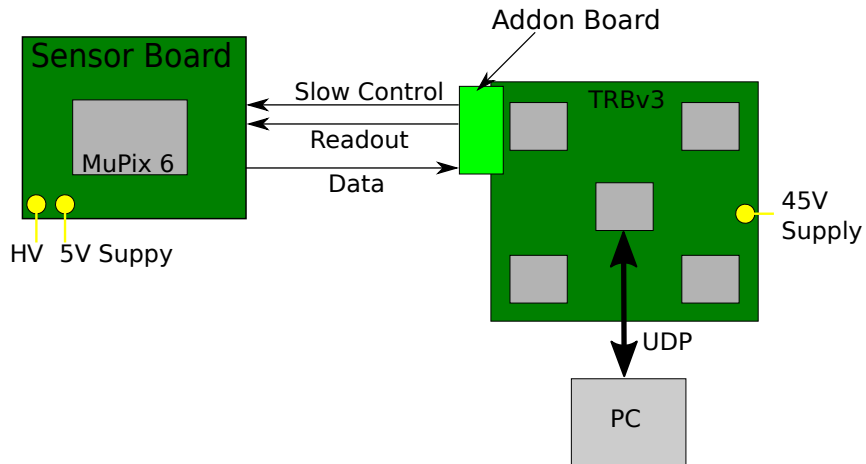7 User Datagram Protocol

Figure 33: Setup consisting of a single MuPix chip and the TRBv3. The add-on board houses four 40-pin pin headers.

common interface. This way it is possible to reuse the same code for different MuPix prototype versions. Moreover, the software handles the slow control of the setup using a library containing function calls to the TRB slow control deamon that is provided by the TRB developers.

To simplify the operation of the readout software, graphical user interfaces were created using the Qt framework [84] that visualize measurement results and display the current sensor settings. The graphical user interfaces for chip slow control and measurement steering are shown in figures 34 and 35.
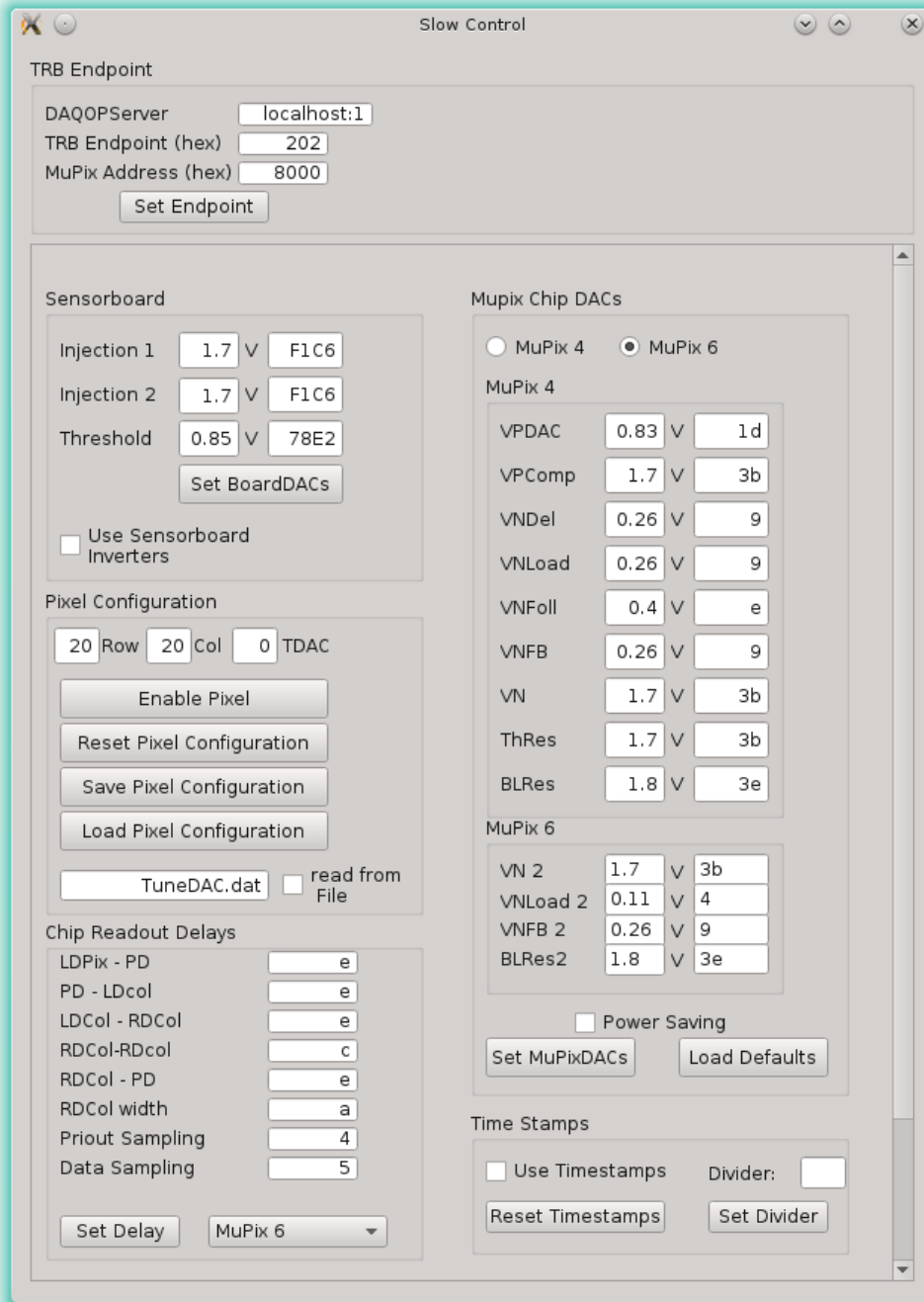
Figure 34: The chip slow control graphical user interface. It allows to adjust the sensor board injection and threshold DACs, Mupix Chip DACs, time stamp, and readout settings.
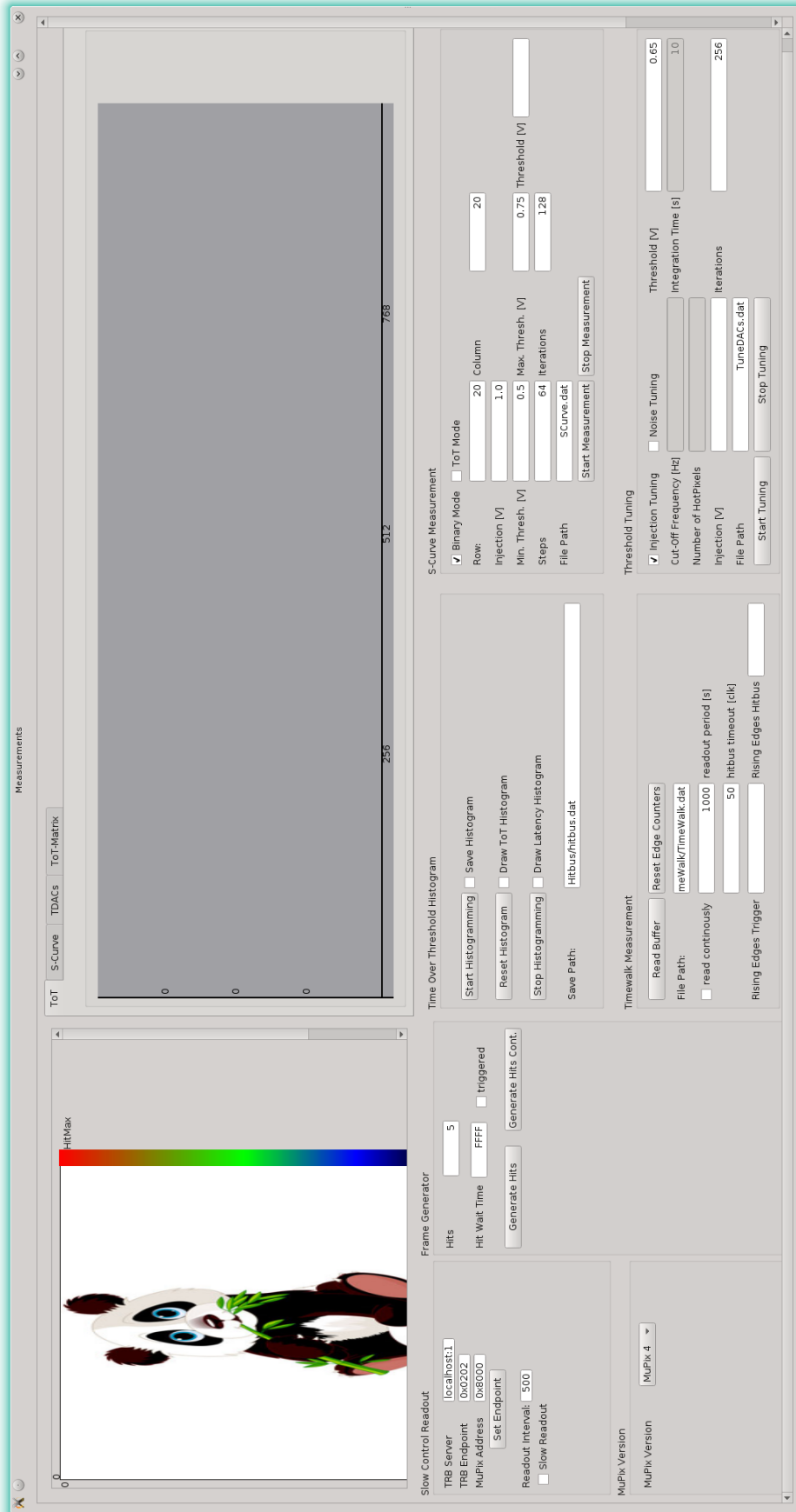
Figure 35: The measurement graphical user interface. It displays sensor hit patterns and summarizes measurement results as histograms. The available measurement routines range from simple charge injections into the sensor analogue circuits to the tuning of the sensor tune DACs.

5.3 Performance Measurements with a Single Sensor Setup

The aim of the measurements presented below was to check the functionality of the developed firmware and software with components suitable for PANDA as well as the characteristics of the MuPix 6 sensor. Most of these measurements were already performed in similar fashion in Heidelberg and were the topic of several bachelor and master theses [82, 85, 86, 87].

S-Curve Measurements

S-curve measurements allow the extraction of the pixel threshold and noise for different measurements presented below. A typical S-curve measurement proceeds as follow: For a given threshold a fixed number of injection pulses is inserted into the pixels of the chip and the number of detected pulses is counted. Then the threshold voltage is increased. For an ideal sensor the ratio between counted and injected pulses should be zero below the pixel threshold, and jump to one above the critical threshold. In the presence of noise this step-function gets smeared by a Gaussian function whose width is given by the width of the noise distribution. To extract the threshold voltage and the width of the S-curve the data is fitted with an error function

$$f_{fit}(U, \mu, \sigma) = 1 - 0.5 \cdot (1 + \mathrm{erf}((U - \mu)/(\sqrt{2}\sigma))) \tag{5.2}$$

with μ and σ being the pixel threshold and width of the noise distribution. There are two different methods to obtain an S-curve measurement with the MuPix 6. The first method counts the number of rising edges at the comparator output using the hit-bus output of the chip, whereas the second uses the binary readout of the MuPix 6 prototype to obtain the number of detected pulses. An example S-curve scan with a fit to the measured data is shown in figure 36 for both the normal and power saving DAC settings. Here the binary readout method was used. As can be seen, the detected pulse ratio stays at zero below a
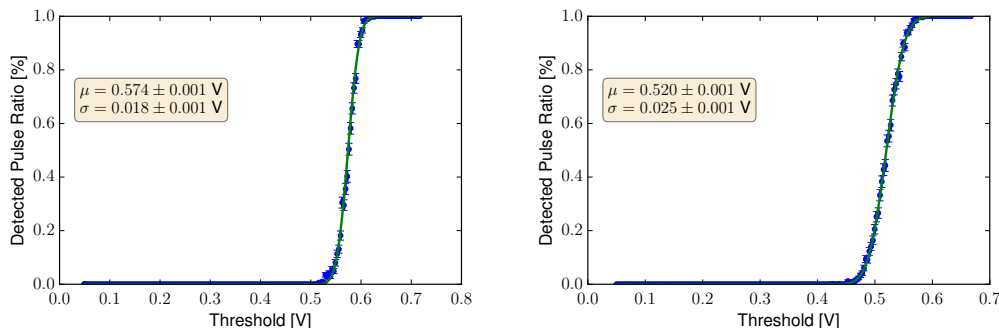

Figure 36: S-curve scan of a MuPix 6 pixel using the binary chip readout for normal DAC settings (left) and power saving DAC settings (right).

threshold of about 0.5 V and then starts to rise until all injection pulses are detected. One sees that the width of the S-curve in the case of the normal DAC settings is 18 mV which is 7 mV smaller than for the S-curve taken with power saving DAC settings. Furthermore, the mean of the S-curve measured with power saving settings is shifted by 54 mV.

Light and Radiation Sources for Laboratory Measurements

To characterize the MuPix 6, different light and radioactive sources have been used. The light was produced by a laser diode with a wavelength of 860 nm. The absorption length of the light can be calculated using the law of Beer-Lambert

$$I(x) = I_0 e^{-\mu x} \tag{5.3}$$

where μ is the absorption coefficient. μ depends on the wavelength of the incident light and can be parameterized for silicon in the following way

$$\mu(\lambda) = 10^{13.2131 - 36.7985\lambda + 48.1893\lambda^2 - 22.5562\lambda^3}[1/\text{cm}] \tag{5.4}$$

with the wavelength λ given in µm [88]. This yields an absorption coefficient of 0.072 µm^{-1} for 860 nm. The remaining light intensity I/I_0 in a depth of 10 µm is then equal to 48.4%. The usage of a laser diode is necessary at this wavelength as the energy of the emitted photons is not sufficient to create electron hole pairs directly, and an additional phonon is needed. Due to this, the high intensity of a laser is required. The laser diode, however, has the disadvantage that it emits a focused beam of light which does not irradiate the complete pixel matrix. To irradiate the complete sensor, a light emitting diode has been used. Since the light intensity of the LED is lower compared to the laser diode, a LED with a wavelength of 450 nm has been used to directly create electron hole pairs. The disadvantage of the LED is that its blue light has an absorption coefficient of 2.27 µm^{-1}. Because of this, the emitted light is absorbed almost directly on the sensor surface.

Iron-55 was used as radioactive source since it emits several monochromatic X-ray photons. ^{55}Fe decays via electron capture to an excited state of ^{55}Mn which decays by emission of a photon into its ground state.

$$^{55}Fe \xrightarrow{EC} {}^{55}Mn^* \rightarrow {}^{55}Mn + \gamma \tag{5.5}$$

The most probable photon energies are 5.9 keV with 16.9% probability and 6.5 keV with 1.6% transition probability. In the sensor the photon is absorbed by an electron which then creates electron-hole pairs by ionization.

Shaper Response Function

The shaper response function gives information about the dynamic range of the sensor. Furthermore, deviations from the expected shaper response give hints to possible design issues in the sensor analogue part. It is measured by irradiating the MuPix prototype with light from a laser diode which is in turn connected to a function generator. The measurement principle is illustrated in figure 37. To obtain a shaper response curve, the latency between the laser pulse and the rising edge of the sensor hit-bus, as well as the time-over-threshold, are determined for different thresholds. In order to achieve this, the output of the pixel comparator and the output of the function generator are connected to an oscilloscope. With the oscilloscope several measurements at each threshold are acquired, and the mean and standard deviation of the measurements are calculated. While the latency at different threshold settings defines the rising part of the shaper response, the falling part is given by the sum of time-over-threshold and latency. It should be noted that it is not possible to measure down to the baseline with this method as noise dominates the measurement for low thresholds.

Figure 38a shows the response function of a central pixel of the MuPix 6 prototype at a high voltage of 60 V. The data points were fitted with the response function of an ideal CR-RC shaping stage

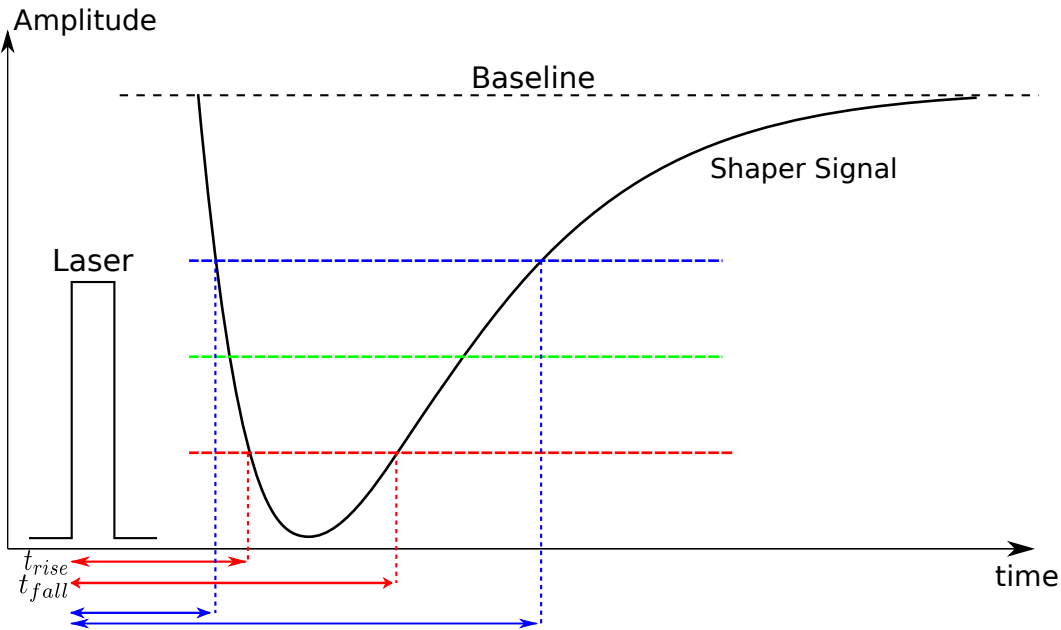$$U(t) = \frac{t_{rise}U_0}{t_{rise} - t_{fall}}(e^{-t/t_{rise}} - e^{-t/t_{fall}}) \tag{5.6}$$

Figure 37: Principle of the shaper response measurement. The shaper response can be determined by measuring the rise and fall time after the rising edge of the laser pulse at different thresholds.

where t_{rise} and t_{fall} denote the rise and fall time constants of the shaper signal. The fit yields a rise and fall time of

$$t_{rise} = 20.22 \pm 2.58 \text{ ns}$$
$$t_{fall} = 229.88 \pm 17.37 \text{ ns}$$

showing that the shaper signal is clearly dominated by the falling part of the signal. It has to be pointed out that the CR-RC response function only describes the expected behavior approximately. In the MuPix the signal shape is ruled by the preamplifiers, the comparator and the circuit bandwidth. The limited bandwidth leads to the exponential rise of the signal. The signal decay is influenced by the comparator and preamplifiers. While the capacitance of the first is discharged using a resistance which leads to an exponential decay, the feedback of the amplifiers results in a linear signal decrease [82]. This is not incorporated in the fitting function. As expected, the measured response does not completely match the fitting function. The fitted function approaches the baseline slower and also becomes negative at the top. Nevertheless, the deviations are small and can be ignored within the precision of this measurement. The comparison of the response functions for normal and power saving DAC settings is shown in figure 38b. It shows that the rise and fall times of the power saving settings are increased. Furthermore, one notes that the response function in the case of power saving settings deviates from the expected behavior by showing a very pronounced kink at 1500 ns. This effect is due to saturation in the shaper or preamplifier stage.

Lastly, the influence of the applied bias voltage on the shaper response was measured (see figure 38c). For a bias voltage of 5 V the rise and fall times of the shaper signal slightly change to

$$t_{rise} = 17.57 \pm 2.72 \text{ ns}$$
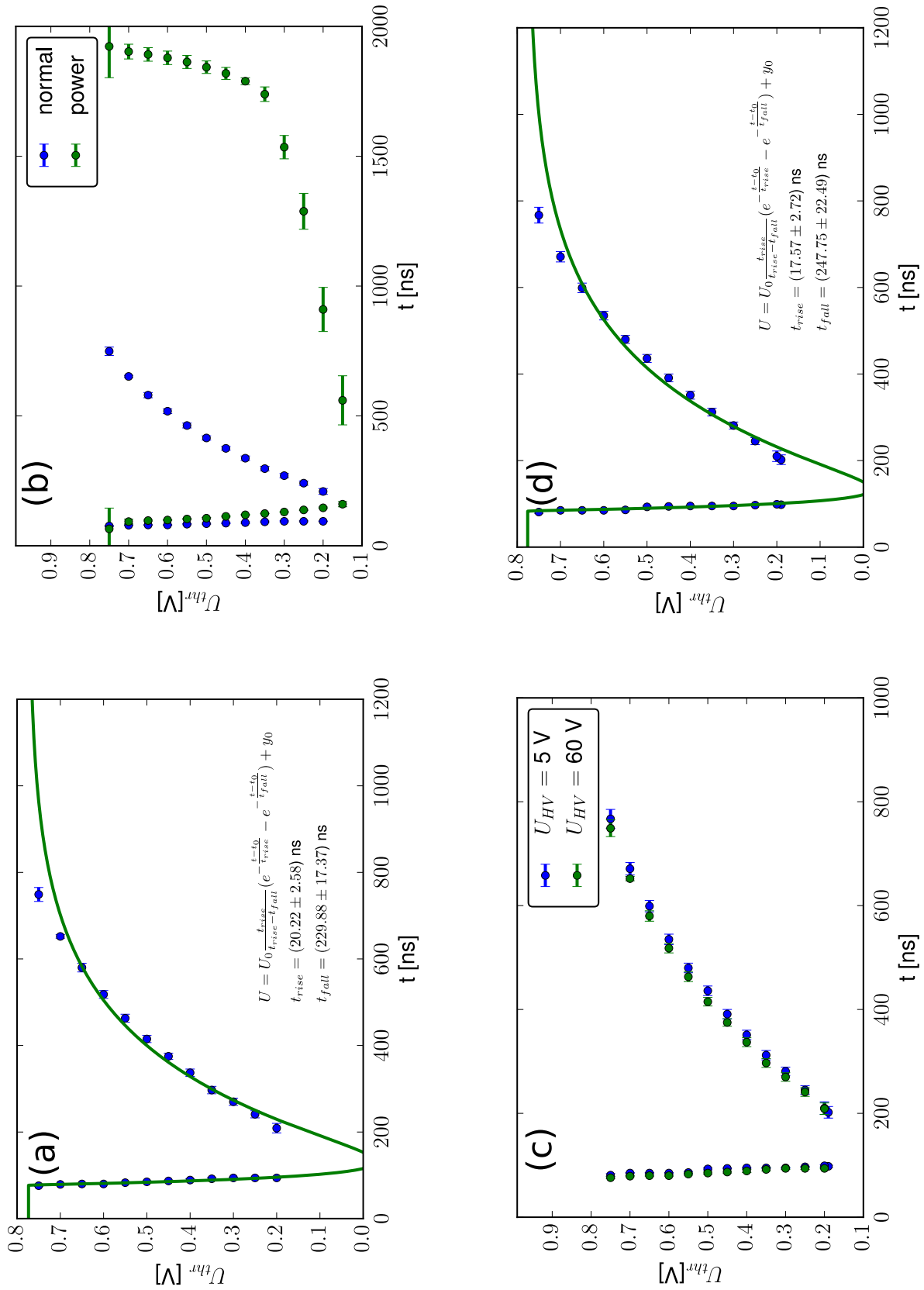$$t_{fall} = 247.75 \pm 22.49 \text{ ns}$$

Figure 38: Measured shaper response functions. (a) Fit with exsepcted function for CR-RC shaper for $U_{HV} = 60\,\text{V}$. (b) Comparison for different DAC settings. (c) Comparison for different applied bias voltages. (d) Fit with exsepcted function for CR-RC shaper for $U_{HV} = 5\,\text{V}$.

but agree within the errors with the values at 60 V. The fit for this scenario is shown in figure 38d. The bias voltage seems to have only a marginal influence on the shaper response function.

Not shown in the measurements is a baseline undershoot after the signal returns to the baseline. Due to the large noise close to the baseline, it is not possible to measure this effect with the described method. The undershoot, however, is seen in chip simulations [82] and in the digital readout at very low thresholds in the MuPix 4-like part of the sensor. As the fall time of the signal is much longer than the rise time for the tested DAC settings, the time-over-threshold is dominated by the exponential decay and will not increase linearly with the injected charge (measured in $U_{\text{Injection}}$) and hence with the collected charge. Instead, it increases logarithmically as can be seen from figure 39.
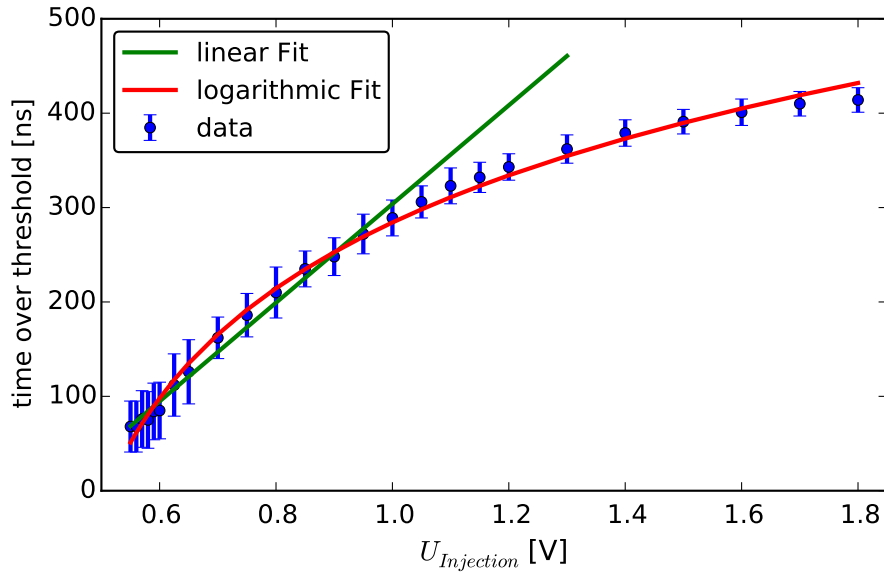
Figure 39: Dependence of time-over-threshold on the injected voltage which is proportional to the injected charge.

Measurement of the Energy Deposition

The comparator allows measurements of the energy deposition of particles crossing the sensitive area using the time-over-threshold method. A multiplexer is used to select the output of a single comparator from the pixel matrix, and the length of the time-over-threshold signal is sampled with the clock signal of the attached FPGA. Alternatively the hit-bus signal is directly measured with an oscilloscope. Measuring the time-over-threshold distributions allows one to study the energy resolution of the chip and gives first indications to estimate the sensor efficiency and noise performance.

For laboratory measurements the infrared light emitted by a laser diode and the gamma radiation from an iron-55 source were used to perform time-over-threshold measurements. The mean of the time-over-threshold distribution as a function of the bias voltage for the two different DAC settings is shown in figure 40. For this measurement the sensor was irradiated with the light of the laser diode, and the hit-bus signal was measured with an oscilloscope. It can be seen that the mean of the time-over-threshold steeply increases until it enters a plateau region at approximately 20 V. This plateau extends up to a bias voltage of about 80 V at which point that the time-over-threshold again increases more steeply. The reason for the observed increase at low bias voltages of the time-over-threshold is that
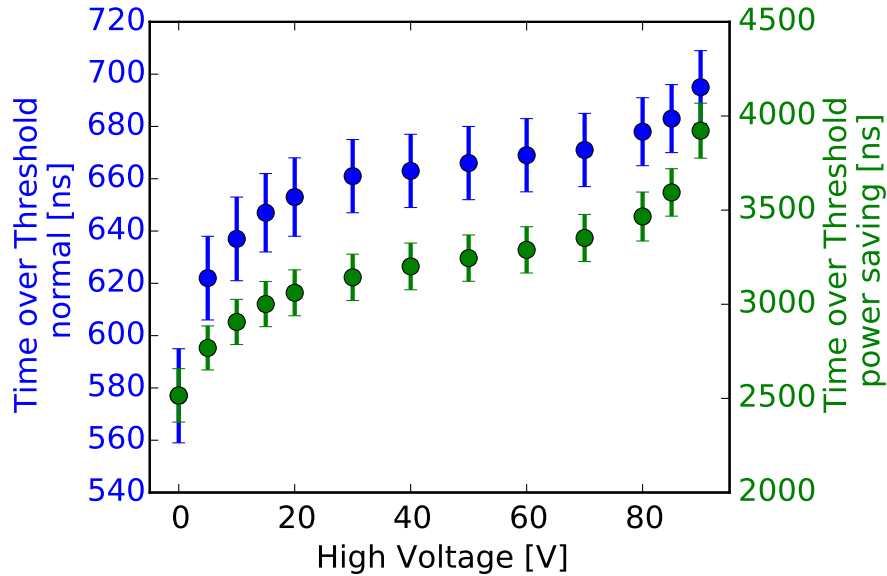
Figure 40: Mean time-over-threshold of a laser diode as a function of the bias voltage. The pulse length of the laser diode was 20 ns, while the sensor threshold was set to 0.68 V. Note the different scales for normal and power saving DAC settings.

the depletion zone of the sensor grows with increasing bias voltage. Because of this, more charge carriers are created within the sensitive area of the pn-junction. The fast increase above 80 V is caused by another effect. There the electric field across the pn-junction is big enough to create electron avalanches and the collected charge is no longer proportional to the initial energy deposition.

The measured energy deposition distributions of the iron-55 source are shown in figure 41 for the two settings of the chip DACs. Both measurements were taken at the same global threshold and the hit-bus output was sampled with the FPGA. The peak at the beginning of the distributions is caused by electronic noise. The 5.9 keV line of the iron-55 source can be seen in both histograms as broad peaks at about 350 ns and 1000 ns. The comparison of both distributions shows that the usage of the power saving settings leads to an additional broadening of the photo-peak due to a higher noise level. The 6.5 keV line can not be resolved by the MuPix 6 sensor and does not appear as a peak in the measured distributions. This is more or less expected since the analogue part was designed to deliver a fast shaper response rather than a good energy resolution. As a comparison, an iron-55 measurement performed with a MAP sensor is shown in figure 41c [89]. Here both X-ray transitions can be resolved. This is due to the thick epitaxial layer that is used for charge collection by the MAP sensor which results in a higher number of collected charges. Furthermore, the shaping time of MAP sensors is in general larger than the shaping time used for the measurements with MuPix chip.

In addition, time-over-threshold spectra were also acquired during a beam time at the MAMI accelerator facility at Mainz. The energy of the electrons was 1 GeV. Since the high energy electrons can not be stopped inside the sensor the energy loss distribution should have a Landau shape. Figure 42 shows the measured distributions. For the normal shaper settings the time-over-threshold distribution clearly follows the expected Landau shape. The maximal time-over-threshold value is slightly higher than 1 µs, one of the design restrictions of the MuPix 6. With the shaper settings optimized for power consumption, the energy loss information of the electrons is distributed between 500 ns and 3500 ns. A clear peak caused by noise can be seen below 500 ns. The position dependence of the most
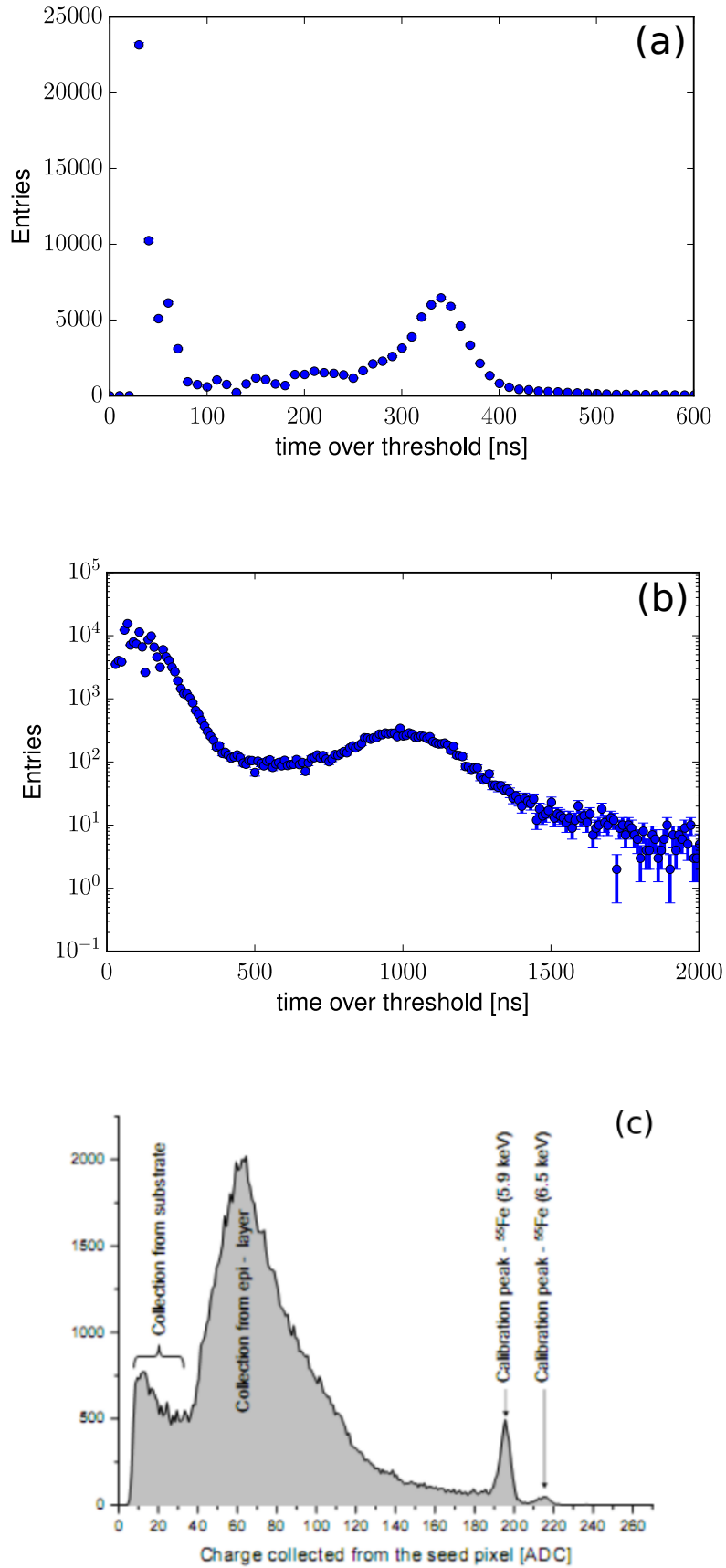
Figure 41: Energy deposition distributions of an iron-55 source. Time-over-threshold measured with MuPix 6 prototype at $U_{HV} = 60$ V with normal DAC settings (a) and power saving DAC settings (b). (c) Energy deposition measured with a Mimosa 26 MAP sensor [89].
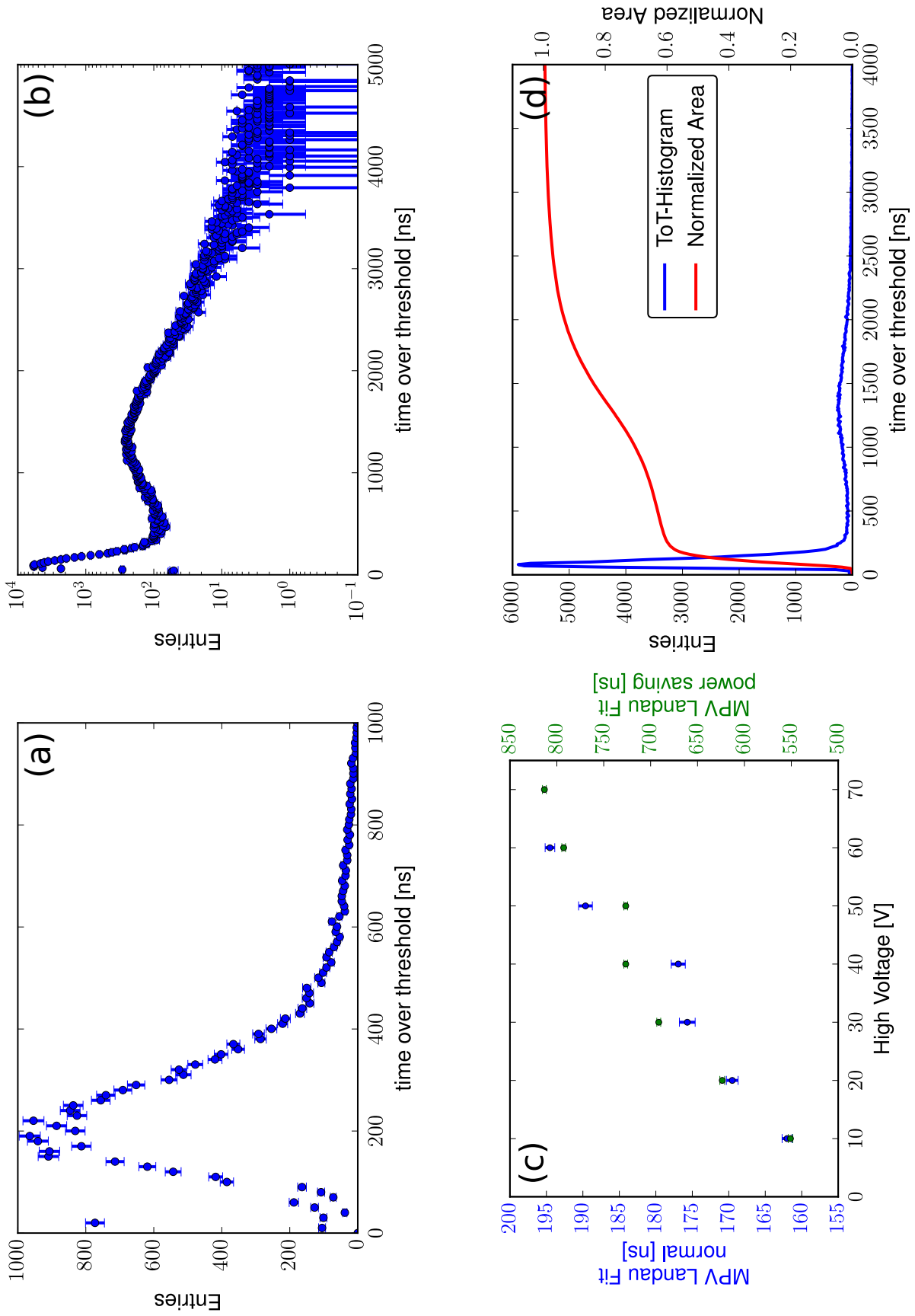
Figure 42: Time-over-threshold distributions measured with a 1 GeV electron beam with (a) normal and (b) power saving DAC settings. (c) Dependence of Landau most probable value position on the applied high voltage (note the different scales for both settings). (d) Signal-noise separation at power saving settings.

probable value of the Landau function on the applied bias voltage was studied by fitting the time-over-threshold distributions with the convolution of Landau and Gaussian functions in order to account for the sensor resolution. For both shaper settings, the position of the peak of the Landau gets shifted to higher time-over-threshold values with increasing bias voltage. This is due to the increased charge collection efficiency in the depletion layer between n-well and p-substrate and the increasing thickness of the depletion layer. The observed increase is most pronounced in the case of the power saving DAC settings for bias voltages below 20 V. Figure 42d shows a typical time-over-threshold histogram for power saving DAC settings. In addition the integral of the histogram, which has been normalized to unit area, is drawn. For a good separation of the signal from noise, the value of the integral should first increase due to contributions from the noise peak, then stay constant, and finally increase again as the signal contribution is integrated. Since the measured curve does not show a constant plateau, 100% efficiency will go along with a high noise level.

In addition, one should note that minimal ionizing electrons deposit more energy in the sensors than anti-protons in the momentum range of the PANDA experiment. Using the Bethe-Bloch equation [71] to calculate the energy-loss for electrons and protons one finds

$$\left(\frac{dE}{dx}\right)_{\text{electron}} = 4.9 \text{ keV}$$

$$\left(\frac{dE}{dx}\right)_{\text{proton}} = 3.9 \text{ keV}$$

in 10 µm silicon. Therefore, the signal-noise separation will be worse for the luminosity detector if the noise level stays the same. However, with implementing the complete digital part on chip a reduction of the noise level is expected.

Latency and Time Walk

Due to the shaper response function, the latency between a particle hit and a rising edge at the comparator output depends on the particle's energy deposition in the sensor. A large energy deposition leads to a large shaper output amplitude and a steeply rising signal at the comparator input. A smaller energy deposition results in a smaller shaper output value and a slower rise of the signal at the comparator input. This leads to a decreasing signal latency for increasing energy deposition. This effect is called time walk.

The signal latency was measured in the laboratory with a laser diode connected to a function generator, as already described in this section. The latency is again measured using an oscilloscope. The dependence of the signal delay on the applied high voltage is shown in figure 43. As the number of collected charges increases with increasing bias voltage, the measured sensor latency decreases. This tendency is most distinct for 0-20 V. Between 20 V and 80 V the latency only improves marginally. An avalanche behavior, like that for the time-over-threshold distribution in figure 40, can not be observed within the measurement errors, although at 90 V the latency decreases further in the case of the power saving chip DAC settings. Furthermore, it can be seen that the latency increases by approximately 15 ns between normal and power saving DAC settings. This information is important for the later correlation of hits in the luminosity detector with the other PANDA sub-detectors.

The time walk was explicitly measured with the MuPix prototype and a 1 GeV electron beam from MAMI. To measure the latency, a scintillator signal was used to trigger the start of a counter inside the TRB with the output signal of the comparator acting as the stop signal. The scintillator was placed in front of the MuPix sensor during the measurement. For every measured latency value, the corresponding time-over-threshold value was
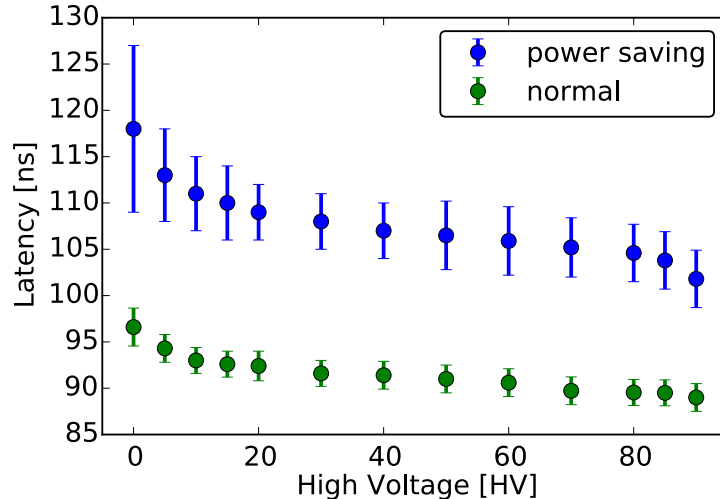
Figure 43: Dependence of the signal latency on the applied bias voltage. The pulse length of the laser diode was 20 ns, while the sensor threshold was set to 0.68 V. The larger errors in the case of the power saving settings are caused by a higher noise level.

measured as well. The resulting time walk distribution is shown in figure 44a. Here the
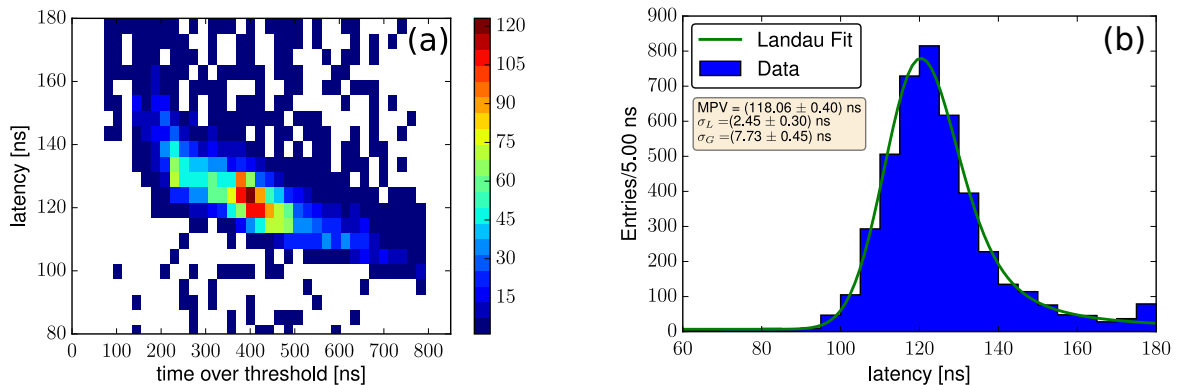

Figure 44: Time walk (a) and latency (b) distribution for a 1 GeV electron beam measured with the MuPix 6 prototype at $U_{HV} = 80$ V, $U_{thr} = 0.69$ V, and normal DAC settings.

normal DAC settings were used. The latency ranges from 100 ns to 180 ns and reduces with increasing energy deposition as was expected.

The projection of the time walk to the latency axis is shown in figure 44b. The distribution is fitted with a Landau function convoluted with a Gaussian resolution function. The most probable value of the latency is 118.06 ns at a bias voltage of 80 V. However, the time-over-threshold signal was delayed inside the FPGA by 80 ns to account for differences in cable length, so the fitted value does not represent the real sensor latency which is in the order of 30 ns. In the final version of the MuPix sensor the time-over-threshold information will not be accessible in the digital readout in order to reduce the data rate at the Mu3e experiment. Hence, a correction of the time walk is not possible. Assuming a time stamp granularity of 25 ns in the final sensor, we can see from figure 44b that the non-corrected time walk could spread the hits corresponding to one track over 3-4 time frames. This makes it necessary to combine several time frames for the track reconstruction.
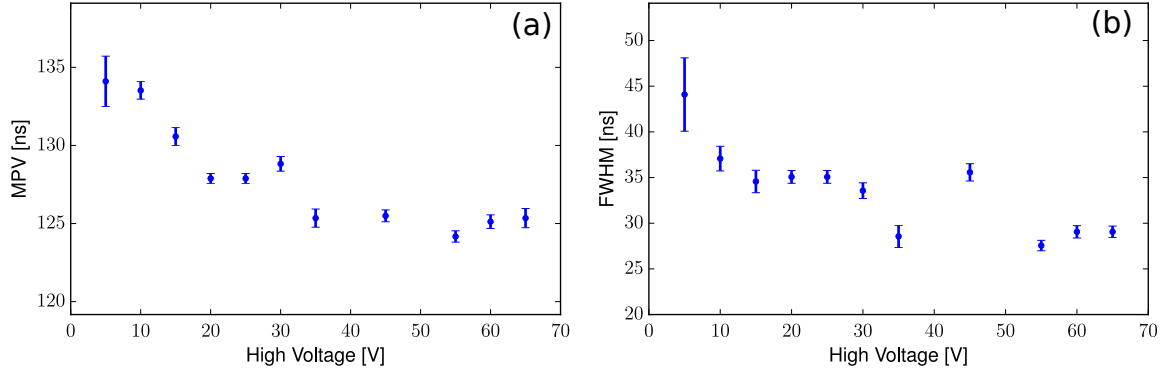
Figure 45: Dependence of most probable value (a) and FWHM (b) of the latency distribution of the MuPix 6 prototype on the applied bias voltage measured at $U_{thr} = 0.68$ V and normal DAC settings.

As already seen, the observed signal latency additionally depends on the applied high voltage. This is shown in figure 45a where the latency distributions obtained at different bias voltages are fitted with the convolution of a Landau and a Gaussian function. The observed behavior with the electron beam is in qualitative agreement with the measurements in the laboratory (see figure 43). The full width at half maximum of the latency distribution, depicted in figure 45b, also depends on the applied bias voltage. It becomes smaller with increasing bias voltage, and reduces by roughly 15 ns over the studied bias voltage range. This is also in good agreement with the explanation that for small bias voltages the number of charges collected is less than in the plateau region, and therefore the statistical uncertainty is larger which reflects itself in the larger width of the distribution.

Tune DACs

The threshold of each pixel can be adjusted individually by means of a tune DAC as described in section 5.1. By increasing the value of the tune DAC, the pixel baseline gets shifted to a higher voltage. This increases the offset between the baseline and the comparator threshold. The total achievable size of the shift is determined by the VPDAC setting. A higher VPDAC value leads to a larger total offset. The dependence of the means of S-curve measurements on different values of the tune DACs is shown in figure 46.
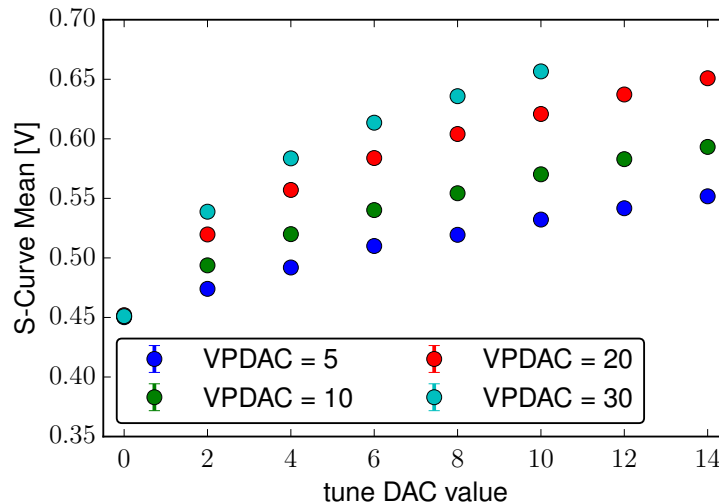
Figure 46: Dependence of the pixel threshold on the tune DAC value for different values of the VPDAC. The VPDAC setting is given as a decimal register value. In the case of VPDAC = 30, no points above a tune DAC value of 10 could be measured as the shaper output no longer crossed the threshold.

A constant injection voltage of 1.2 V was used for all measurements. As can be seen the estimated mean of the S-curves increases with increasing values of the tune DAC. This effect can be understood the following way. The constant injection voltage leads to an equal shape of the modulated baseline independent of the tune DAC setting. The different tune DAC settings only result in a global shift of the overall baseline to larger voltages. Because of this, the required threshold voltage to measure 50% of all injection pulses, which gives the mean of an S-curve, is shifted to larger values as well. However, the observed shift is only linear for small values of the VPDAC and becomes smaller for higher tune DAC values.

To adjust the values of the tune DACs two different algorithms have been developed. The first implemented algorithm is based on limiting the pixel noise rate. A low noise rate is desirable in order to save resources in the data acquisition system and to reduce the time spent on the track finding and reconstruction. The second algorithm uses injections to tune the pixel thresholds to a user defined value.

The **noise reduction algorithm** proceeds as follows:

1. Choose a maximum value for the pixel noise rate and set a high global comparator threshold. The threshold should be chosen to keep the initial noise rate well below the desired maximum noise rate.

2. Acquire the number of hits for each pixel in a specified time interval.

3a. If the hit rates of all pixels stay below the allowed rate decrease the global threshold proceed to step 4.

3b. Otherwise, increase the tune DAC by one unit for all pixels above the given limit and repeat step 2.

4. Proceed until a previously defined number of pixels have reached the maximal tune DAC value and exceed the maximum noise rate.

The distribution of the tune DAC values after running the tuning algorithm is shown in the left part of figure 47. As the sensor noise should follow a Gaussian distribution a
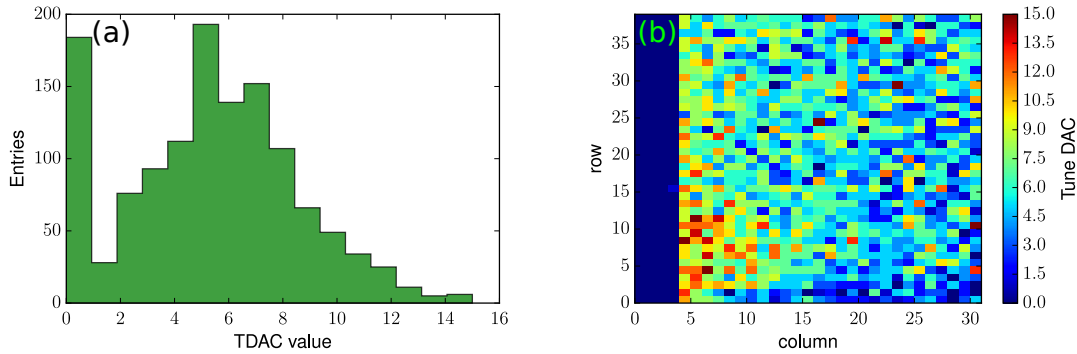

Figure 47: Tune DAC distribution after noise tuning. Frequency of tune DAC values (a) and 2D distribution of the tune DAC values across the pixel matrix (b).

similar distribution would be expected for the tune DACs. That is almost the case. The most frequent tune DAC values are 5 to 7. The peak at 0 is caused by the pixels with the MuPix 4 analogue part as can be seen in the right part of figure 47. One can also see there that the highest tune DAC values cluster at the bottom left corner of the chip. Figure 48 shows the obtained tune DAC distribution with the sensor illuminated by a laser diode during the tuning process. The spot of the laser light is clearly marked by the pixels with the highest tune DAC values.
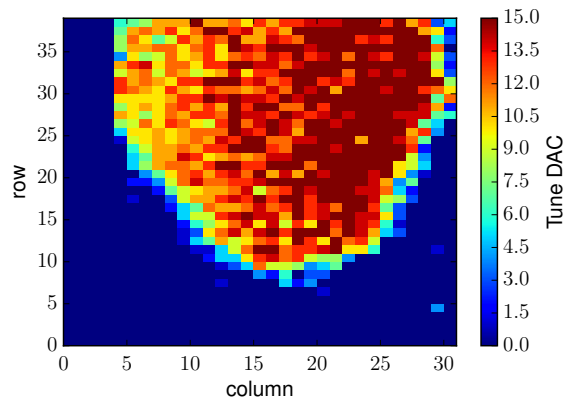

Figure 48: Tune DAC distribution after noise tuning while sensor was illuminated by a laser diode.

Although the tuning algorithm was developed to suppress noise at low global discriminator thresholds, the algorithm also leads to an equalization of the individual pixel thresholds for a fixed input charge. To determine the pixel thresholds, S-curve scans are performed. No external radiation sources are used during this measurement. Histograms showing the distribution of the S-curves mean and width are shown in figure 49 before and after application of the tuning algorithm. After tuning, the mean-distribution becomes much more narrow and symmetric around a central value of 0.55 V. The standard deviation of the pixel thresholds decreases from 0.11 V to 0.05 V. This means that after the noise

tuning a more uniform hit detection efficiency distribution can be expected. Furthermore, tails in the distribution of the noise width are reduced as well.
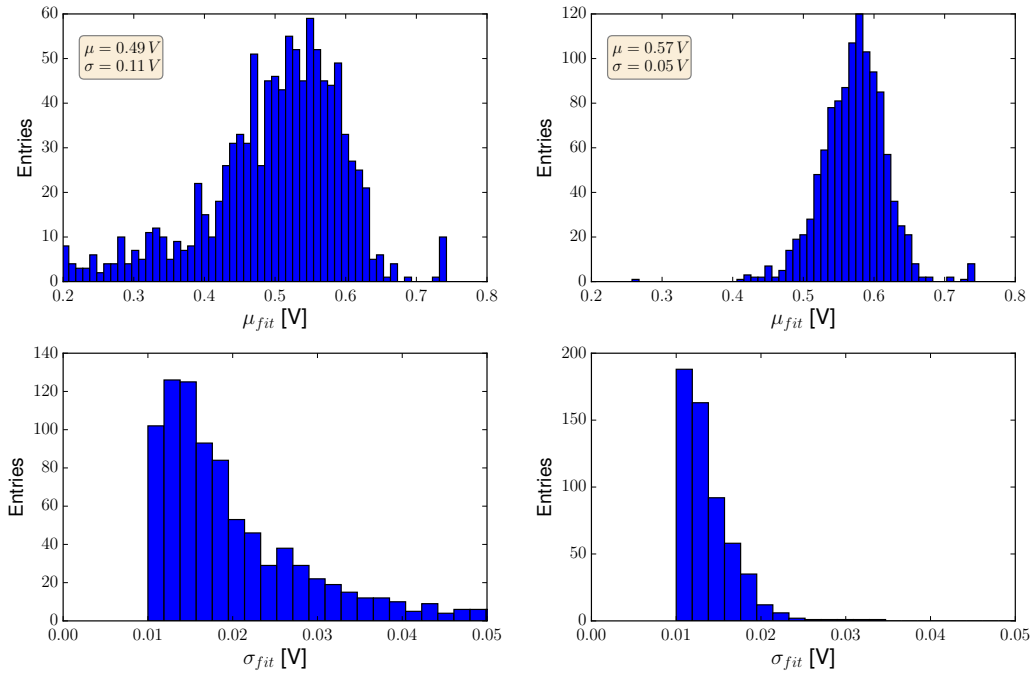

Figure 49: Distribution of S-curve mean and width before (left) and after (right) noise tuning of the pixel tune DACs.

The second **algorithm uses injection pulses** with fixed injection voltage to tune the pixel thresholds to a common value. For this a fixed number of injection pulses is generated for all possible values of the tune DACs and the ratio of detected pulses is computed for every pixel. The tune DAC value with a ratio closest to 50% is retained. The threshold distribution after application of the injection tuning with the desired pixel threshold set to 0.65 V is shown in figure 50. As can be seen the pixel threshold distribution is centered around a mean value of 0.65 V with a standard deviation of 0.02 V. Only a small asymmetry towards lower threshold voltages can be seen.

Both algorithms have in common that after the algorithm has finished the obtained values for the tune DACs are saved in a file. This way the obtained tuning data can be used for later measurements. Up to now the implemented algorithms ignore the possibility to adjust the chip VPDAC and the user has to choose a "good" value at the beginning of the tuning procedure. The result of an injection tuning with a VPDAC value that is too low can be seen in figure 51.
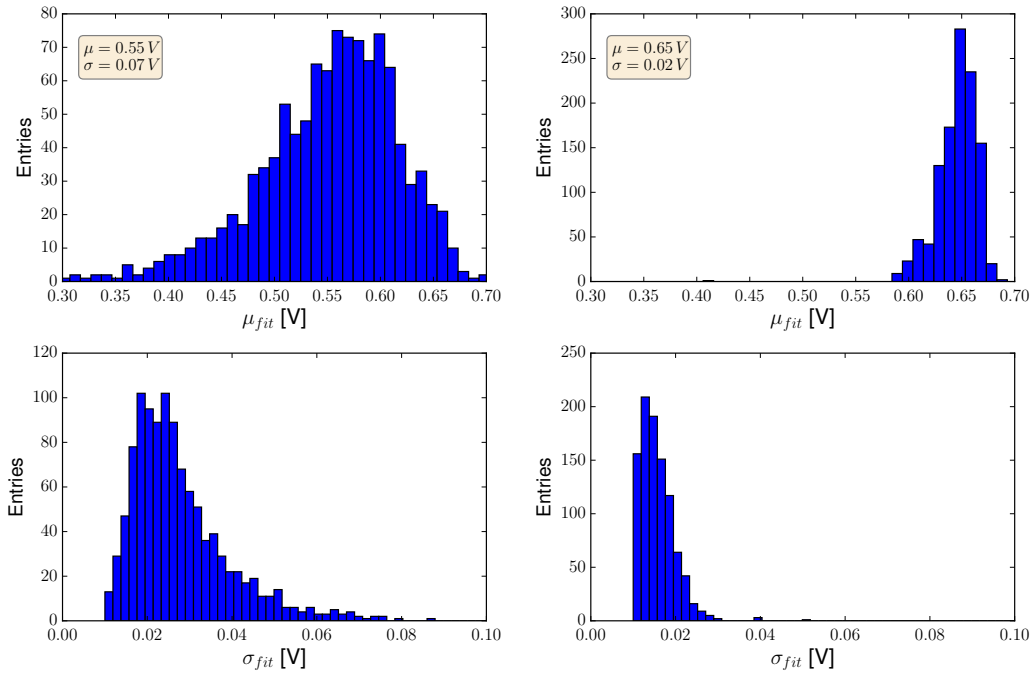
Figure 50: Distribution of S-curve mean and width before (left) and after (right) injection tuning of the pixel tune DACs. The VPDAC set to 0.8 V.
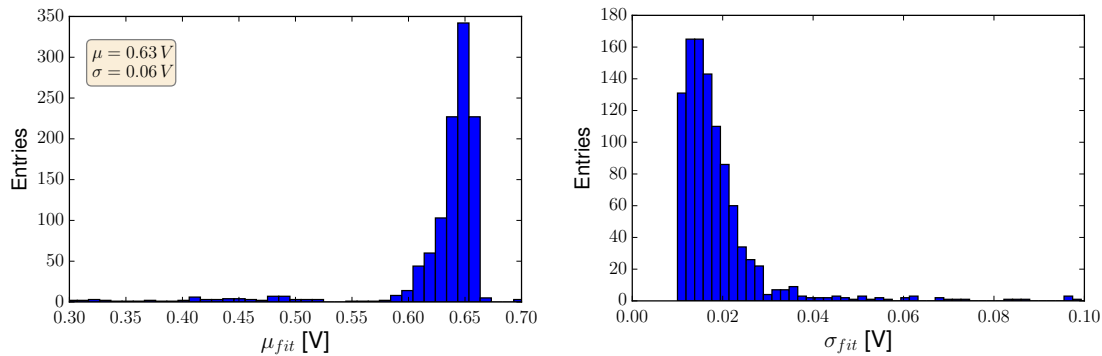

Figure 51: Distribution of S-curve mean (left) and width (right) with VPDAC set to 0.5 V.

The pixel threshold distribution shows a tails toward lower threshold voltages. Therefore, the VPDAC optimization needs to be included into the tuning algorithm to obtain satisfactory results.

Signal-to-Noise Ratio

The signal-to-noise ratio is an important property during sensor development. A high signal-to-noise ratio allows easy suppression of fake hits due to sensor noise in the later experiment. In the case of a low signal-to-noise ratio, track reconstruction and data acquisition have to cope with higher rates. To estimate the signal-to-noise ratio, S-curve scans can be used. During the S-curve measurement the injection voltage should be tuned to give a time-over-threshold distribution which is equal to a physical signal produced, for example, by a charged particle. The signal-to-noise ratio is then given by

$$\text{SNR} = \frac{\mu_{base} - \mu_{thr}}{\sigma} \tag{5.7}$$

where μ_{base} is the position of the sensor base line, μ_{thr} is the pixel threshold from the S-curve fit, and σ is an estimate for the pixel noise.

In principle μ_{base} and σ could be extracted directly from the comparator signal by performing an S-curve scan without doing injections and counting the number of rising edges. The result of such a measurement is shown in figure 52. The shape of the distributions
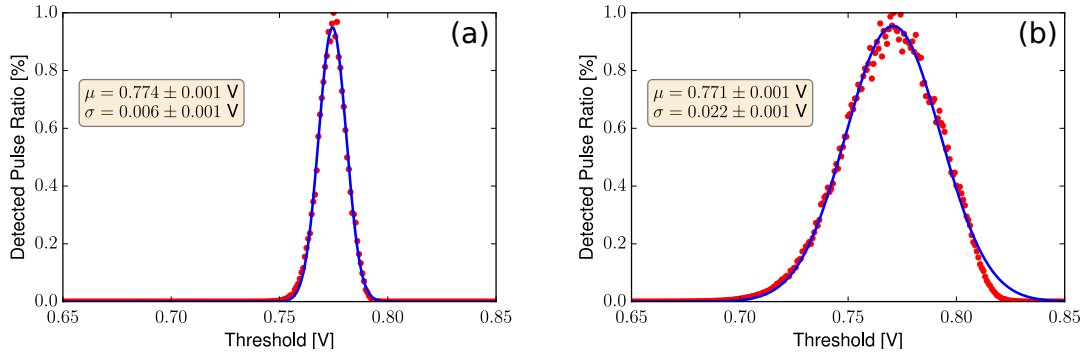

Figure 52: Baseline scan of MuPix 6 prototype at $U_{HV} = 80$ V for normal (a) and power saving (b) DAC settings.

originate from the fact that with an increasing threshold the rate of rising edges at the comparator output starts to rise as the threshold approaches the noise band. At a certain threshold voltage the number of rising edges starts to decrease since the noise signal stays above the comparator threshold most of the time. Furthermore, the limited double pulse resolution of the comparator and the clock speed of the sampling FPGA lead to the merging of single pulses into a longer pulse. This gives rise to an almost Gaussian shaped distribution. Comparing the distributions for the different DAC settings one sees that the power saving settings lead to a distribution which is roughly four times wider than the normal settings. However, this type of measurement is not well suited to give quantitative estimates about the chip baseline due to the described complications. Instead it should only be used for qualitative comparisons.

Because of this, a direct estimation of the baseline position μ_{base} of the pixel is not possible. However, the global baseline can be adjusted and measured on the sensor board. We make the assumption that the pixel baseline is equal to that global value, which is set to 0.8 V on the MuPix 6 sensor boards. The pixel noise σ is given by the width of the S-curve obtained when using injections. The dependence of the pixel noise on the applied bias voltage is shown in figure 53. Both the binary readout and the hit-bus method have been used to do the S-curve measurement. As can be seen in both measurements, the pixel noise becomes smaller with increasing bias voltage. This effect is most pronounced in the range of 0-30 V. Furthermore, the normal DAC settings result in a pixel noise which is approximately 6 mV smaller than for the power saving settings. A further observation is that the hit-bus and binary readout method seem to give equal results for the power saving DAC settings, while they disagree for the normal settings. Here the hit-bus method gives a 2 mV larger pixel noise. For the hit-bus method the comparator output signal is transmitted to the sampling FPGA. During the transmission the signal shape may be altered on the flat ribbon cable. In addition, the shortest pulse length that can be detected is 10 ns which is given by the FPGA clock speed. These effects may lead to an additional broadening of the measured S-curve. During the binary readout the comparator signal is already converted into a binary hit address inside the sensor and the sampled hit address is much less affected by changes of the signal shape during transmission. Therefore, the binary readout method should give more reliable estimates of the S-curve properties. Also shown in figure 53 is the mean of
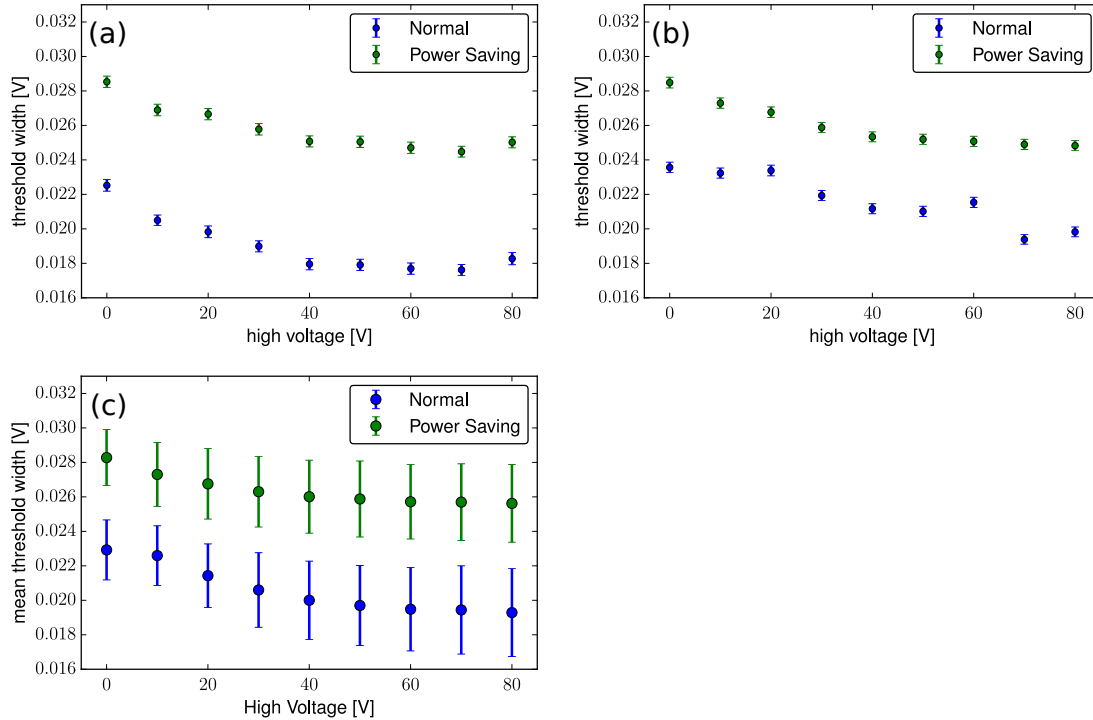
Figure 53: Dependence of the pixel noise from S-curve measurements on the applied bias voltage for normal and power saving DAC settings measured with the (a) binary readout and (b) hit-bus readout for a single pixel. (c) Mean of the S-curve width distribution measured with the binary readout for all pixels.

the S-curve width distribution of all pixels as a function of the bias voltage. The behavior is in good agreement with the single pixel measurements. This measurement can only be done with the binary readout within a reasonable time frame.

The dependence of the signal-to-noise ratio on the applied bias voltage is shown in figure 54. As a physical reference for the injection voltage, the measured most probable values of the time-over-threshold distributions of 1 GeV electrons from this section were used. The signal-to-noise values have been estimated from S-curves using the binary readout method. μ_{thr} and σ have been taken from these measurements. It can be seen that the signal-to-noise ratio improves with increasing bias voltage. The normal DAC settings systematically give a better signal-to-noise ratio. However, the difference to the power saving settings usually stays below one. The measured signal-to-noise ratios at 60 V are

$$\text{SNR}_{\text{normal}} = 12.8 \pm 0.2$$
$$\text{SNR}_{\text{power}} = 11.3 \pm 0.2.$$

With the binary method it is possible to measure the S-curves for all pixels of the MuPix 6 in parallel. These curves have been used to calculate the signal-to-noise ratio for the complete pixel matrix. The resulting distribution for a bias voltage of 60 V is shown in figure 55. The signal-to-noise distributions are rather wide ranging from a signal-to-noise ratio of 4 up to values of 25. The reason for this behavior is that the injection voltage for the S-curve measurement was chosen from the time-over-threshold distribution of a single pixel. Therefore, the derived injection voltage does not have the correct value for all pixels due to variations in the pixel performances and the injection capacitances. Figure 56 shows the dependence of the mean value of signal-to-noise ratio of the pixel matrix on the applied bias voltage. Like for the single pixel, the overall signal-to-noise ratio improves with increasing high voltage for both DAC settings. However, the signal-to-noise ratio
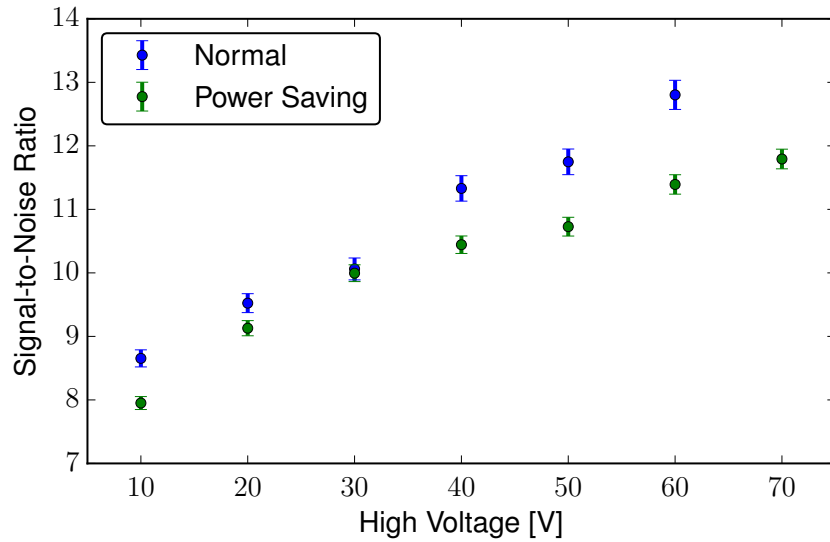
Figure 54: Dependence of the signal-to-noise ratio of a single pixel on the applied high voltage for normal and power saving DAC settings with the binary readout method.
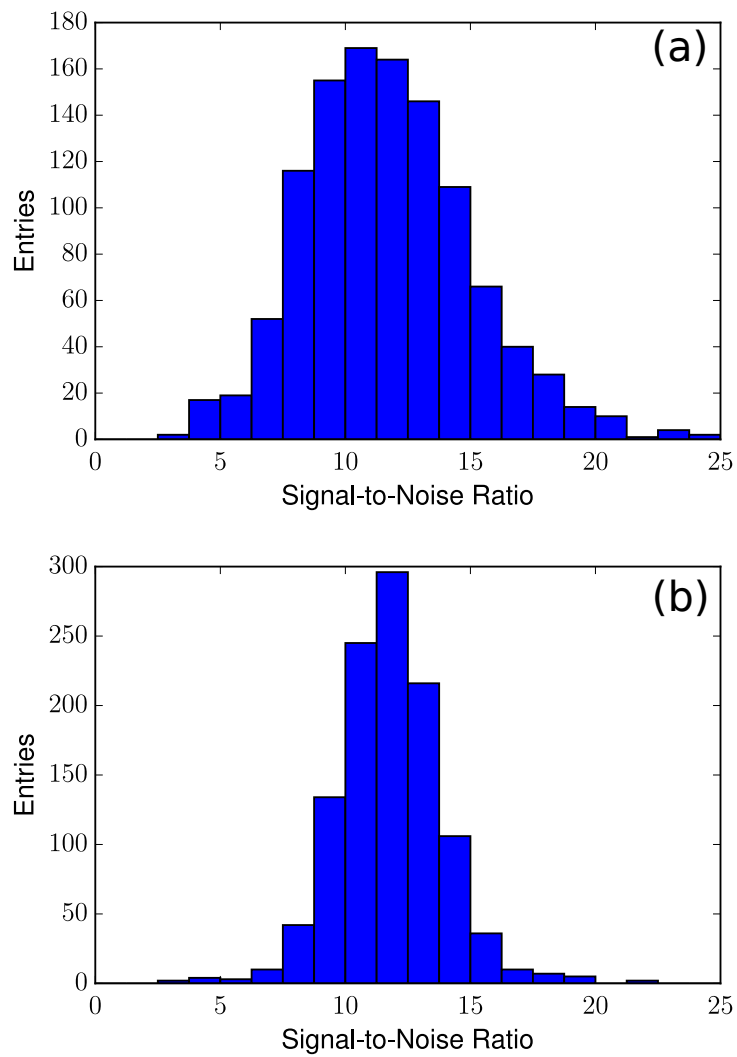

Figure 55: Signal-to-noise ratio distribution for MuPix pixel matrix in case of normal (a) and power saving DAC settings (b) at $U_{HV} = 60$ V.
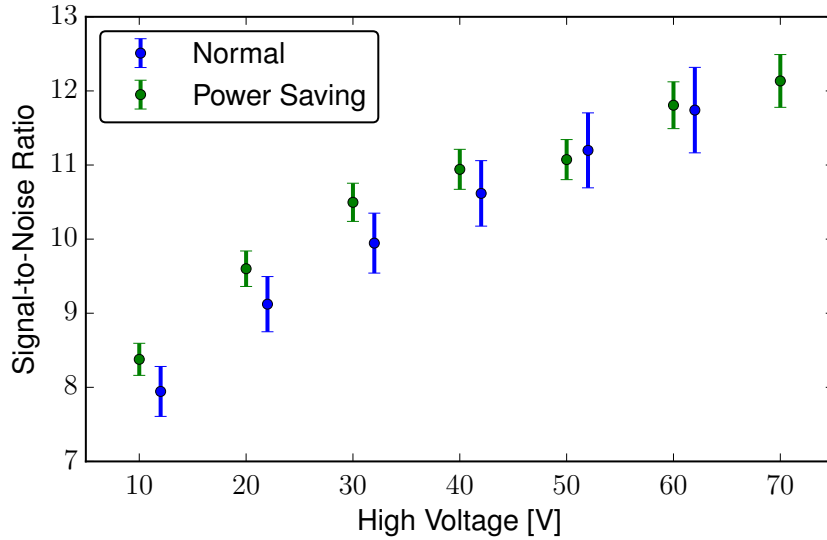
Figure 56: Dependence of the signal-to-noise ratio distribution on the applied high voltage for normal and power saving DAC settings.

is slightly better in the case of the power saving settings in contrast to the single pixel measurement and the spread of the signal-to-noise distribution is smaller compared to the normal DAC settings.

Both methods presented above, the hit-bus and binary readout method, have the disadvantage that the injection voltage applied during the threshold scans is given by fitting a measured time-over-threshold distribution to estimate the most probable energy loss and then finding the injection voltage that reproduces this fitted most probable value. This can be quite difficult especially for the power saving DAC settings where the time-over-threshold distribution gets smeared out considerably. Furthermore, it is not feasible to measure the signal-to-noise ratio of all pixels within a reasonable time frame as an individual energy loss measurement is needed to properly adjust the injection voltage for each pixel. With the available sources this would require a very long measurement time. Unfortunately, an alternative measurement method has not been found so far.

5.4 Mainz MuPix Tracking Station

In order to determine properties of the MuPix prototypes, like the hit detection efficiency, a tracking station to reconstruct particle tracks from accelerators is needed. To be independent of existing test facilities, like the EUDET telescope at DESY, it was decided to build a new tracking station using the MuPix 6 prototype. Furthermore, the tracking station will allow first tests of the online track reconstruction algorithms in real environments.

5.4.1 Tracking Station Setup and Readout

The tracking station consists of four layers of MuPix 6 prototype chips. The sensors on the first three layers were thinned down and glued on a thin capton foil to reduce multiple scattering of traversing particles. Since multiple scattering on the last layer is not an issue the sensor there was not thinned and is glued on a ceramic carrier. The four layers are read out using the TRB with pairs of sensors connected to one peripheral FPGA. The high voltage for the sensors was delivered by an EHS F205p power supply by ISEG, while the low voltage was supplied by a Wiener PL506 crate equipped with MEH-02/07 modules. Both power supplies are also foreseen to be used with the final luminosity detector and are controlled using the EPICS[8] slow control software.

The existing readout software for single chip measurement was extended for the tracking station. On the PC, the UDP data stream from the TRB is split into two identical data streams. One data stream is written to disk in a binary format containing the bare sensor information as well as an additional header and trailer marking the run number, the start, and end time of the data taking. The second stream is sent to an online monitoring application which decodes the data package, and displays sensor hit patterns and hit correlations between the tracking station layers. An online track reconstruction has not been implemented up to now. The slow control graphical user interface was expanded to control the sensor board and MuPix chip of each layer. All of these tasks are implemented as separate processes and communicate using the TCP[9] protocol with a master application that controls the data taking status and the trigger generation. For easy configuration, the geometry and readout setup of the tracking station are saved in xml-files which are read on start up by the above mentioned applications. The software framework also includes algorithms for hot pixel suppression, i.e suppression of pixels whose noise hit frequency heavily exceeds the average noise frequency, hit clustering, and track reconstruction which are described in the next section.

5.4.2 MAMI Beam Time

The setup used during the March and May 2015 beam time at MAMI is shown in figure 57. A schematic drawing of the readout setup is shown in figure 58. During the first data taking period, time stamps could not be used as the readout of the last layer broke down if time stamps were activated. The reason for this was that the last layer utilized an old revision of the MuPix sensor board. This revision employed level shifters to shift the 1.8 V signal voltage of the MuPix to the 2.5 V logical voltage of the FPGA in order to ensure a stable communication. The shifters, however, caused an increased noise level and cross talk between the logical signals which finally crashed the readout. These level shifters were only a precaution during the first design of the boards and it was found that the signal transfer is possible without them. For this reason the shifters were removed for the second

---

8 Experimental Physics and Industrial Control System
9 Transmission Control Protocol

beam time in order to be able to obtain time stamps. The thinned boards already used a revision without level shifters. In addition, the noise tuning algorithm for the tune DACs was implemented between March and May.
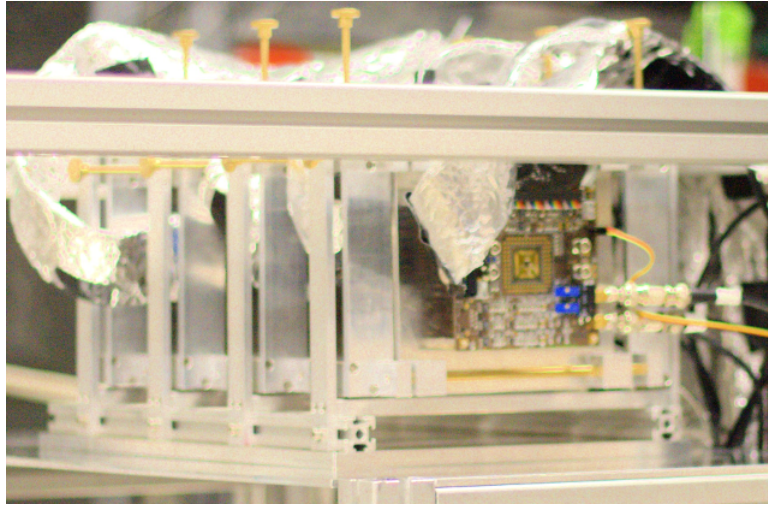

Figure 57: Picture of the tracking station. The first of the four sensors, which build the tracking station, is visible in the middle of the golden frame. The TRB is placed below the tracking station and is not depicted in the picture.
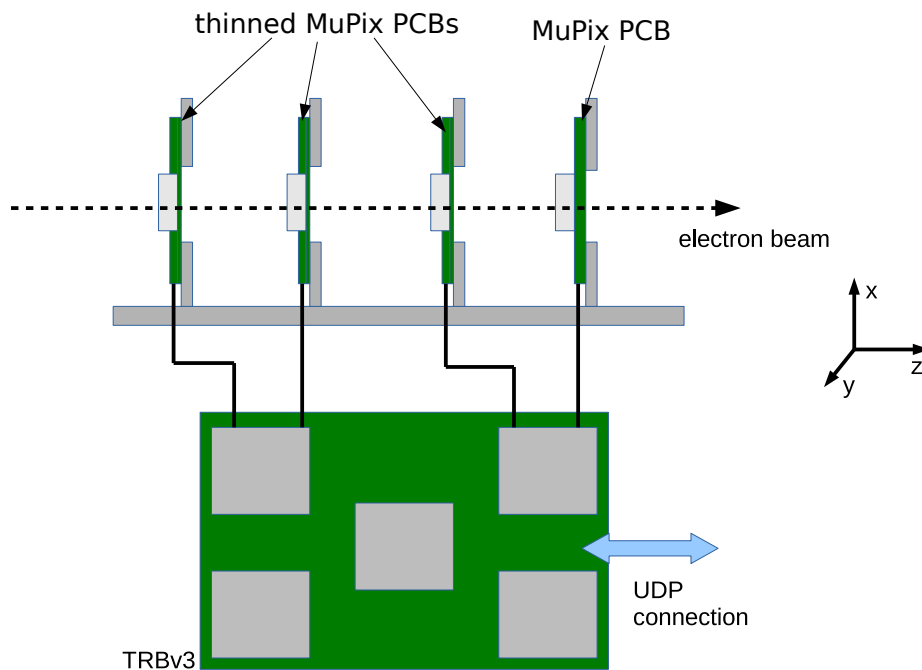

Figure 58: Schematic overview of the tracking station readout.

The beam time took place at the A2 experimental hall in Mainz where electron tracks could be measured parasitically during the normal A2 beam time. A scheme of the relevant parts of the A2 experiment is shown in figure 59. Electrons are accelerated to an energy of 1.5 GeV by the MAMI accelerator, and are directed onto a diamond radiator inside the A2 experimental hall. Within the radiator the electrons emit Bremsstrahlung photons
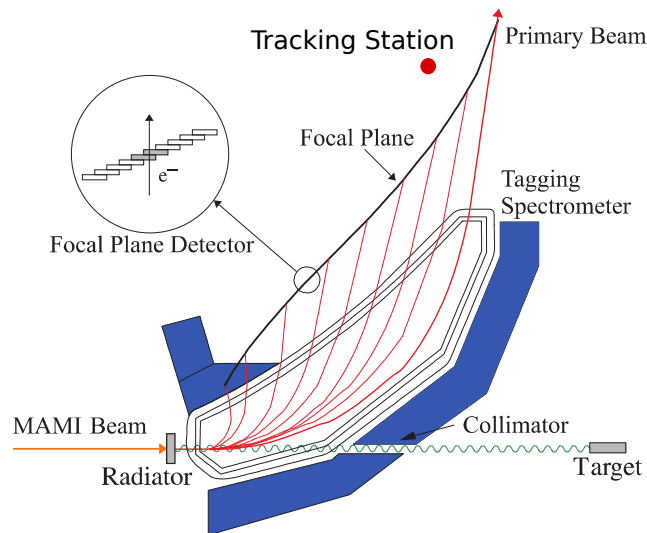
Figure 59: Position of the tracking station behind the A2 tagging spectrometer.

which are used for experiments by the A2 collaboration. To determine the photon energy the electrons are bent inside a magnetic field with a bending radius that depends on their remaining energy. The electrons are then detected by a ladder of scintillation detectors placed in the focal plane of the tagging spectrometer. The position of a firing scintillator is directly connected to the electron energy and the energy of the emitted photon. During the beam time the tracking station was positioned behind the tagging spectrometer and measured electron tracks with a momentum of approximately 1 GeV/c (red dot in figure 59).

Track Reconstruction

The complete work flow of the tracking station data analysis is shown in figure 60. As a first
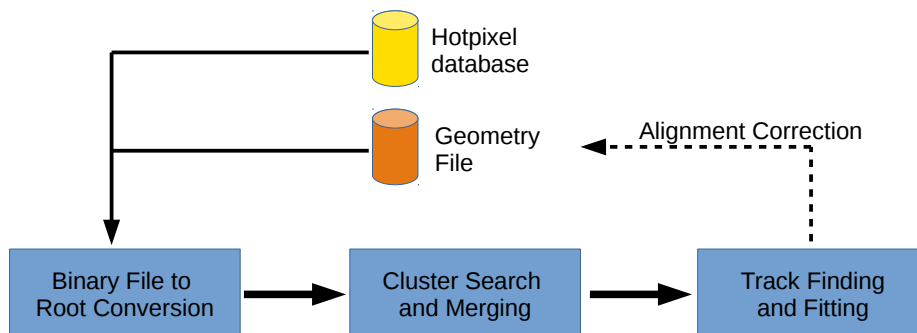

Figure 60: Data analysis flow of the MuPix tracking station.

step the binary files are converted into a root data format with individual root-trees for every sensor layer. The trees contain all information necessary for the later reconstruction steps like the 3 dimensional hit position and time stamps. In addition, the hits can be sorted by their time stamps and grouped into sub-events using a moving time window which slides across the complete event and forms chunks of hits whose time stamps are in

a certain range. In this process hot pixels are removed from the data set. A pixel is defined to be hot if its hit frequency exceeds either a user-defined frequency or

$$f \geq \mu_{freq} + n \cdot \sigma_{freq} \tag{5.8}$$

where μ_{freq} and σ_{freq} are the mean sensor hit frequency and the standard deviation. n can be defined by the user and was set to four for the analysis of the beam time data.

In the next step, a hierarchical cluster search and hit merging are performed. At the beginning of this process each hit is regarded as a cluster seed. Cluster seeds which are separated by a distance smaller than 1.5 times the pixel diagonal (0.0194 cm) are then merged to a new cluster. The merging is iteratively repeated until no clusters with neighbors are left. Large clusters caused by slow secondary particles are removed from the dataset if the cluster size, which is the number of pixels in one cluster, is larger than a predefined limit. For the MAMI beam time this limit was set to ten.

On this clustered data the track search and fit is performed. The corresponding algorithms were taken from the Panda-Root framework and modified to process the tracking station data. A cellular automaton algorithm is used for the track search [90]. The principle of the cellular automaton is shown in figure 61.
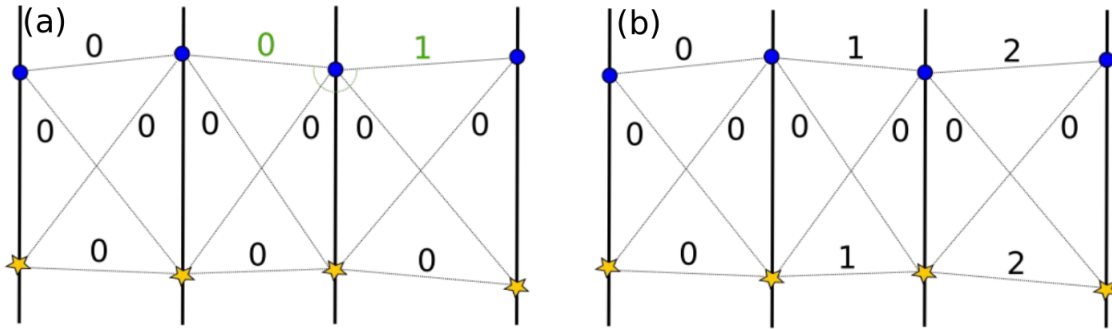

Figure 61: Working principle of the cellular automaton for two straight line tracks. (a) Search for neighbors by checking breaking angle between cells. The breaking angle should be close to 180°. (b) Final state of the cellular automaton after backward pass [91].

Cells are built between all possible combinations of hits in neighboring layers. Each cell has a state counter which is initially set to zero. Now a *forward evolution* takes place where each cell checks if it has a leftward neighbor. Two cells are considered to be neighbors if they share a point in a common plane and if the breaking angle between these cells is smaller than a maximal value which is optimized in terms of the expected multiple scattering. If a neighbor with the same state is found the cell increases its state by one. This process is repeated until no cells with neighbors in the same state are left. The *backward pass* starts from the cells with the highest state counter, setting them as track candidate seeds. For each of those cells a leftward neighbor with state lower by unity is searched for and is added to the track candidate. The newly added cell again again looks in the set of its left neighbors for a cell with a state lower by unity. This is repeated until a cell with state zero is assigned to the candidate. The implementation of the cellular automaton includes a *missing plane* algorithm which allows to find tracks from hits in only three planes of the tracking station. Afterwards, a track filter loops through all track candidates and removes tracks sharing at least three hits in the following way:

- In the case of an equal number of hits, the track candidate with the largest breaking angle sum is removed.

- In the case of an unequal number of hits, the track candidate with the smaller number of hits is removed.

In a next step, the track parameters are estimated using the method of broken lines which takes the kink angles of the particle scattered in the detector material into account [92] and correctly estimates the errors on the track parameters in the presence of multiple scattering. The three-dimensional track trajectory is described by

$$x_l = a + b \cdot t + \sum_{l=1}^{4} \alpha_l^x ((z_0 + t) - z_l) \Theta((z_0 + t) - z_l) \tag{5.9}$$

$$y_l = c + d \cdot t + \sum_{l=1}^{4} \alpha_l^y ((z_0 + t) - z_l) \Theta((z_0 + t) - z_l) \tag{5.10}$$

$$z_l = z_0 + g \cdot t \tag{5.11}$$

where a, b, c, d are the line parameters, z_l the z-coordinates of the tracking station layers, α_l^i the kink angles, Θ is the Heaviside-function and restricts the kink to forward directions, and g is given by

$$g = \sqrt{1 - b^2 - d^2}. \tag{5.12}$$

The χ^2 minimized during the fit takes the form

$$\chi^2 = \sum_{l=1}^{4} \left(\frac{\xi_l^x - x_l}{\sigma_x^2} + \frac{\xi_l^y - y_l}{\sigma_y^2} \right) + \sum_{J=1}^{4} \frac{\alpha_J^x + \alpha_J^y}{\sigma_s^2} \tag{5.13}$$

where ξ is the measured hit position, $\sigma_{x,y}$ the hit position resolution, and σ_s the error on the multiple scattering angle. For details on the cellular automaton and the broken line fit see [91].

Alignment

The mechanical pre-alignment of the tracking station was done with a laser spirit level. The alignment was then optimized using hit correlations (see next section). If these showed large shifts, the layer positions were adjusted to minimize these shifts. This was done either with a micrometer gauge if the tracking station was accessible or by updating the geometry parameters in the xml-file. For further improvement, a software alignment of the tracking station was performed using the reconstructed tracks and the Knossos tool. Knossos is a wrapper around the millipede algorithm [93]. Millipede minimizes the hit-track residuals of a large number of tracks by updating the tracking station geometry. For the alignment, tracks with one hit in each of the four layers were used, and translations in x, y direction and rotation around the z-axis were corrected. The obtained alignment parameters were used to correct the parameters in the geometry xml-file. The software alignment procedure was repeated several times until no further changes in the χ^2 distribution of the tracks and the residuals between the hit coordinates and the track intersections on the tracking layers were observed. These distributions are shown in figures 62 and 63. For the march beam time, after the first software alignment iteration no major changes in the χ^2 distributions were observed. The changes in the hit-track residuals stayed below 1 µm. Therefore, the alignment was stopped here. In the case of the May beam time, one iteration of the alignment procedure was not sufficient to reach a stable result and a second iteration had to be performed. After the software alignment the residuals were in the order of a few microns for both beam times. The position and rotation angle around the z-axis of each layer before and after the alignment are summarized in table 5.

Beam Time	Layer	x	y	z	γ	x_{align}	y_{align}	γ_{align}
March	1	0	0	0	0	0.0034	-0.0058	0.0036
	2	0	0	9.5	0	-0.0023	0.0048	-0.0241
	3	0	0	21.0	0	-0.0056	0.0078	-0.0085
	4	0	0	31.0	0	0.0046	-0.0068	0.0293
May	1	0	0	0	0	-0.0045	-0.0004	-0.0026
	2	0.0244	-0.0144	10.5	0	0.0301	-0.0130	-0.0323
	3	-0.0433	-0.0391	21.0	0	-0.0412	-0.0407	-0.0184
	4	-0.0868	-0.0102	31.8	0	-0.1030	-0.0052	0.0216

Table 5: Layer position before and after software alignment for the March and May beam times. The positions are given in centimeters and the rotation angle γ around z in radians.
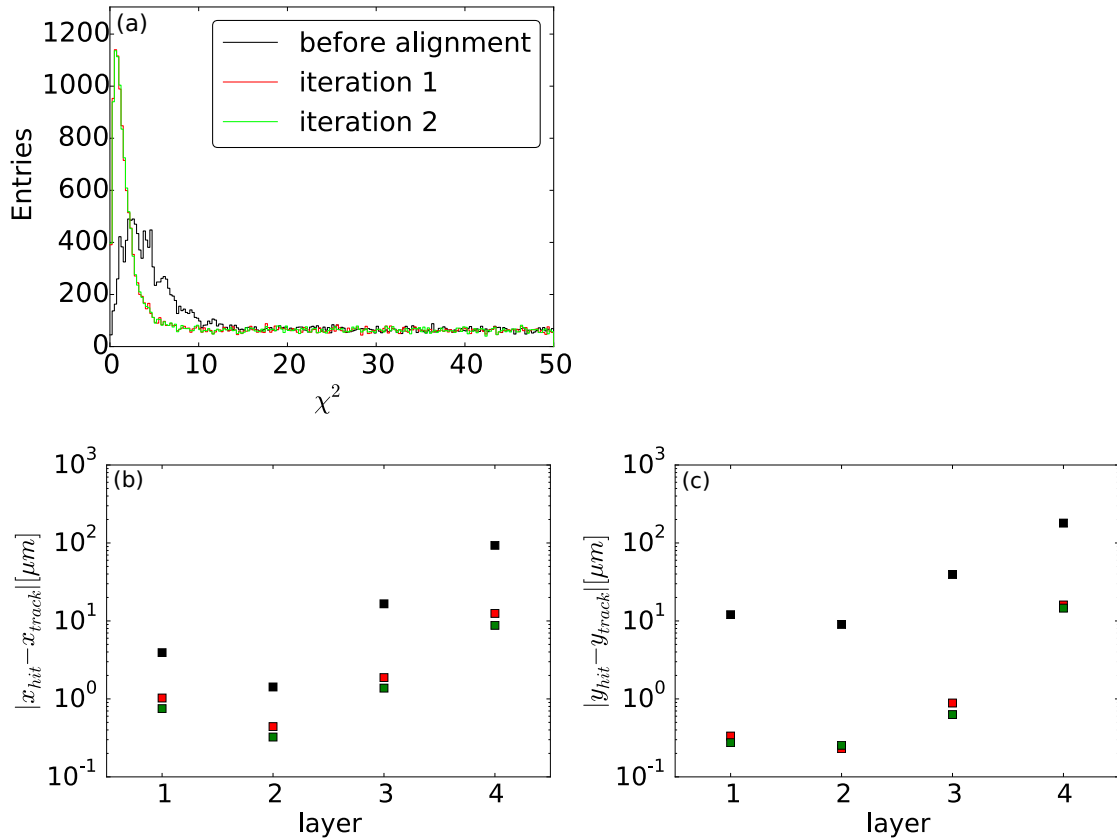

Figure 62: χ^2 and residual distributions of reconstructed tracks before and after several iterations of the software alignment for the March beam time. (a) χ^2 distribution, (b) x-Residuals, and (c) y-Residuals.
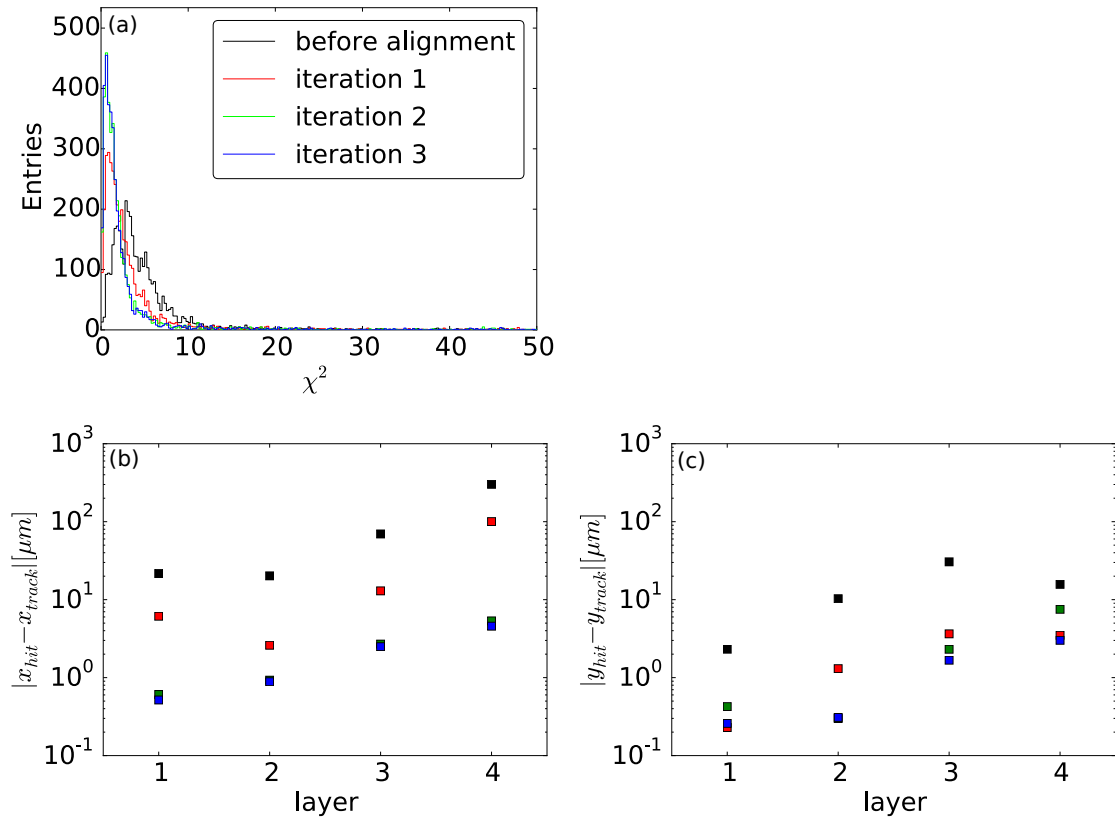
Figure 63: χ^2 and residual distributions of reconstructed tracks before and after several iterations of the software alignment for the May beam time. (a) χ^2 distribution, (b) x-Residuals, and (c) y-Residuals.

Hit Correlations

The hit and time stamp correlations between consecutive sensors are shown in figure 64 and 65 for the March and May beam time, respectively. For straight line tracks, diagonal bands are expected in the plots. These bands were used for the mechanical alignment of the layers, as they should be centered around zero in x and y dimension in the case of a well aligned tracking station. As can be seen from figure 64, a good alignment was achieved for the March beam time. The mechanical alignment for the May beam time (see fig. 65) was not as successful. A systematic shift can be seen in the correlations for the x-dimension. With activated time stamps, clear timing correlations can be seen as well. Figure 66 shows the x-coordinate correlation between layer 2 and 3 with and without the application of a cut on the time stamps. Including the additional information of the hit timing, the number of uncorrelated hits have been considerably reduced. Furthermore, the distribution of the hits violating the time stamp cut are flatly distributed and do not show a diagonal band.
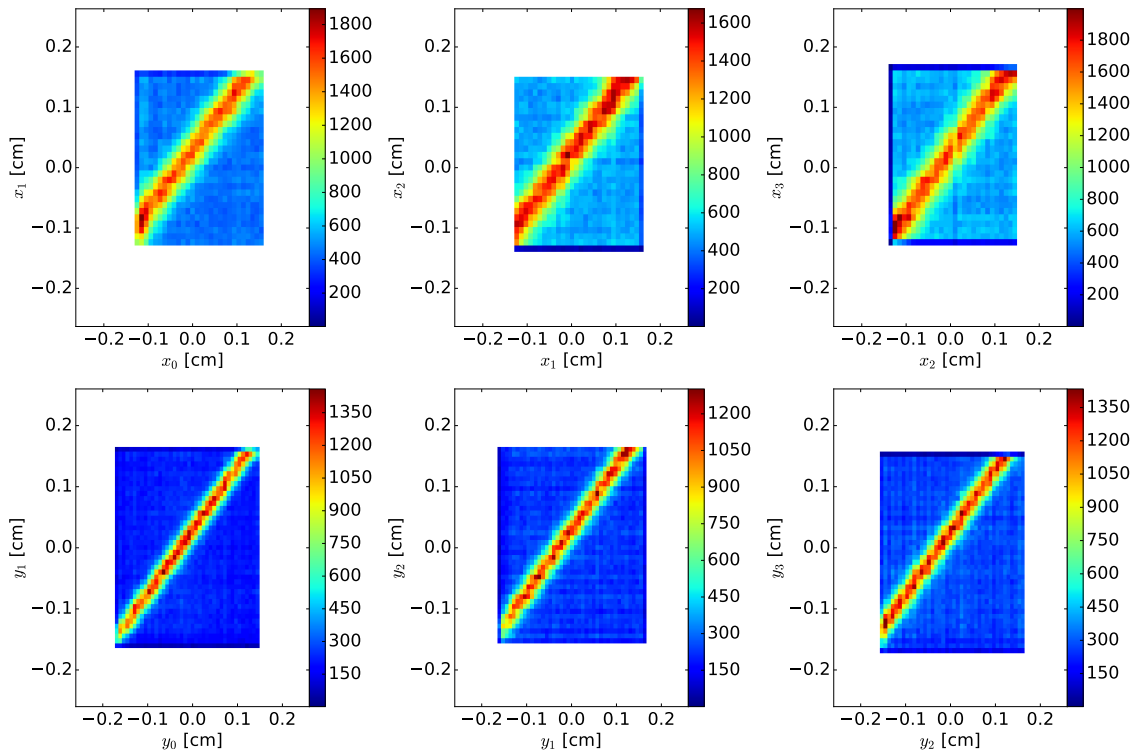

Figure 64: Hit coordinates x, y, and time stamp t correlations for the March beam time. Indices 0, 1, 2, 3 indicate the layers of the tracking station. As no time stamps were used, the corresponding correlation plots are empty and are not shown.
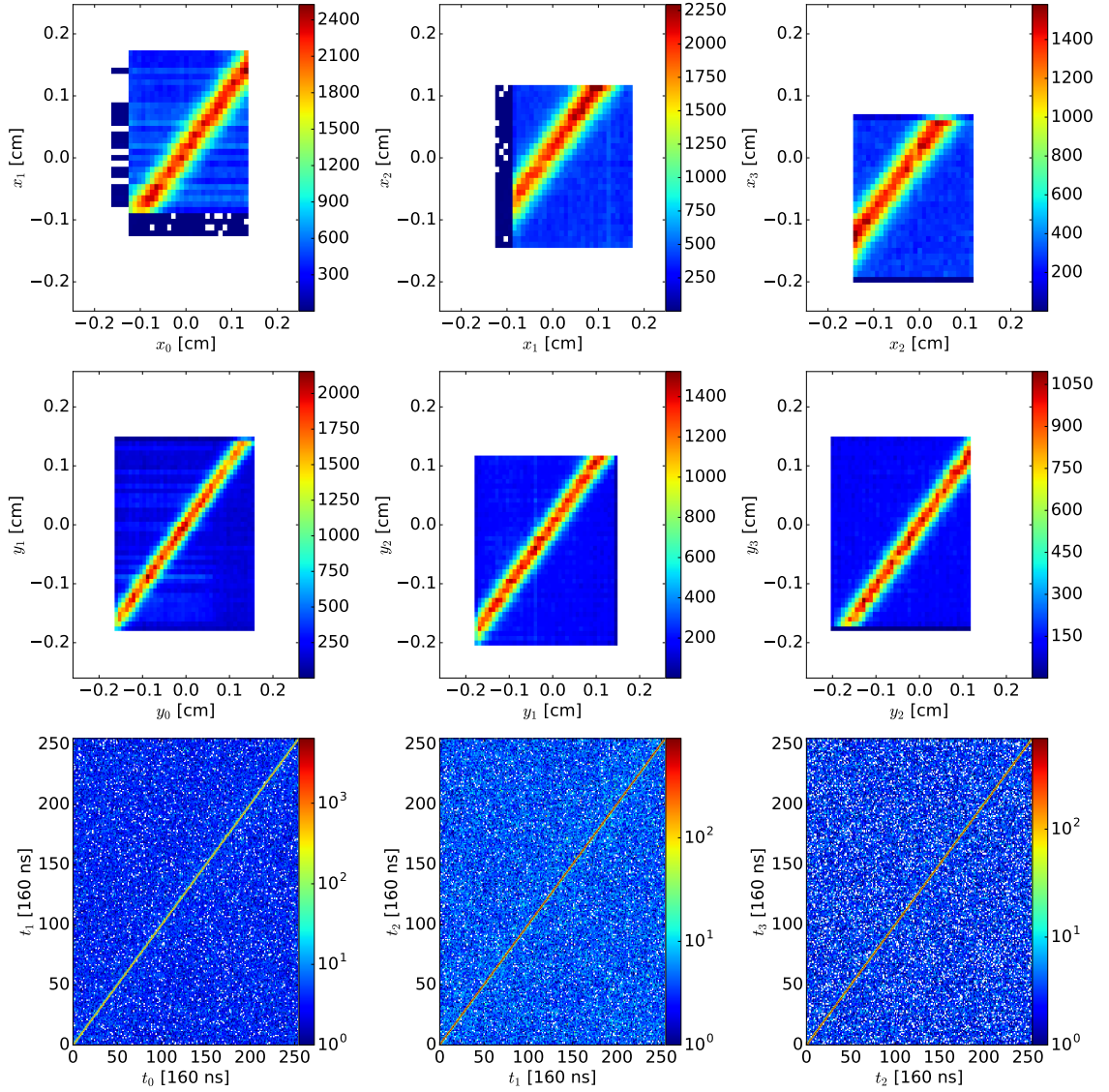
Figure 65: Hit coordinates x,y, and time stamp t correlations for the May beam. Indices 0, 1, 2, 3indicate the layers of the tracking station. Note the logarithmic scale in the time stamp plots.
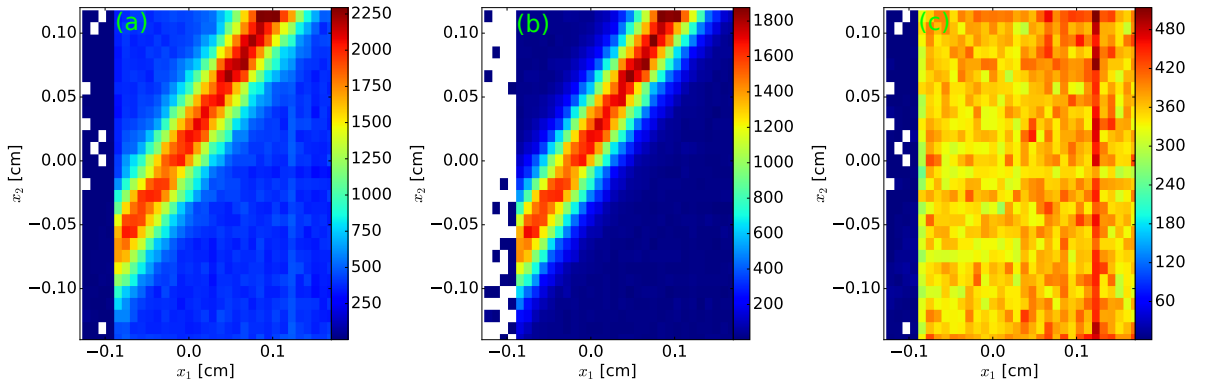

Figure 66: Influence of the time stamp cut on the x-coordinate correlations between layer 2 and 3. (a) Without time stamp cut. (b) With time stamp cut. (c) Hits violation time stamp cut.
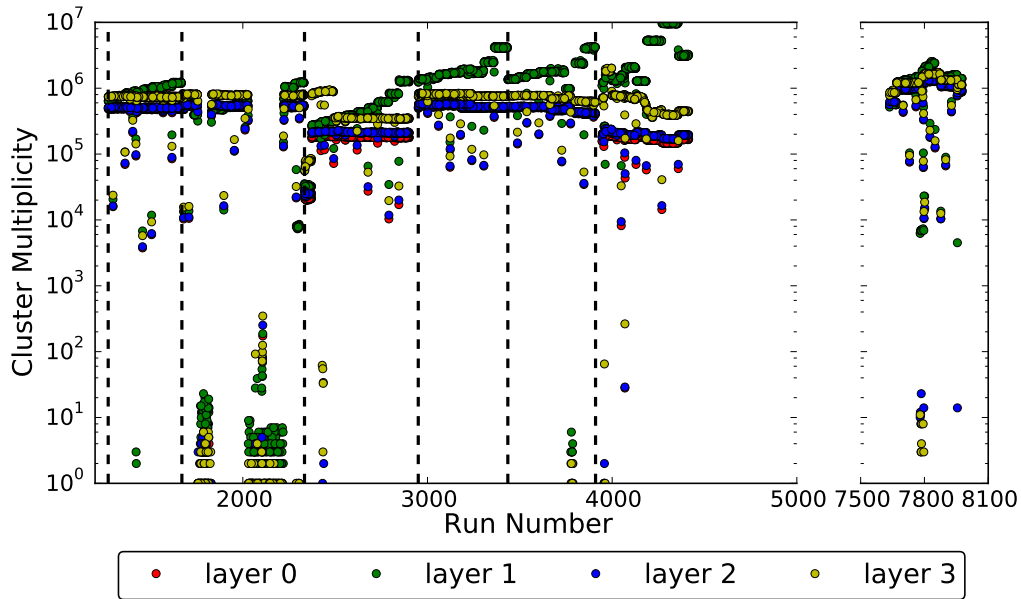
Cluster Multiplicity and Size

Figure 67: Number of clusters per run.

The number of clusters for the runs which were analyzed for the efficiency determination are shown in figure 67. During these runs the sensor threshold and the applied bias voltage for the second layer were changed. The settings of the other layers were kept fixed. The change of bias voltage is indicated by dashed black lines. The threshold of the test layer was always varied from a high to a lower threshold. This can be seen as an increase in the number of clusters during a threshold scan. These changes are most pronounced for the power saving settings (between run 3000-4500). Periods without beam can be clearly seen as well.

The dependence of the cluster size on the applied bias voltage was studied with a separate set of runs which were not used for the efficiency determination. In general one would expect a decreasing cluster size for increasing bias voltage. The reason for this is that the electric field collecting the charges in the pn-junction increases with higher bias voltages and fewer charges are collected by thermal diffusion. To verify this behavior, the cluster size was checked for different bias voltages in the range of 20-70 V by setting each of the first three layers of the tracking station to different bias voltages. It was found that the mean cluster size increases for layers further downstream of the beam, in spite of equal operating settings in terms of threshold and chip DACs on all layers. Because of this, the measured cluster size μ was corrected by normalizing the cluster size, with respect to the first layer, using data from a separate run. The corrected size is then given by

$$\mu_i^{corr} = \mu_i \frac{\mu_0'}{\mu_i'} \text{ with } i = 0, 1, 2. \tag{5.14}$$

The high voltage dependence of the cluster size is shown in figure 68. For thresholds between 0.60-0.66 V the expected behavior can be observed. For lower thresholds (0.67 and 0.68 V) the sensor noise contribution increases and no conclusions can be made. In addition, one may notice that the mean cluster size decreases with decreasing threshold. This counterintuitive behavior is caused by an increased single-hit efficiency while the threshold is still too high to register two hit clusters due to charge sharing. This shifts the mean cluster size to smaller values. Finally it should be noted that for all bias voltages and thresholds the number of single hit events is larger than 95%.
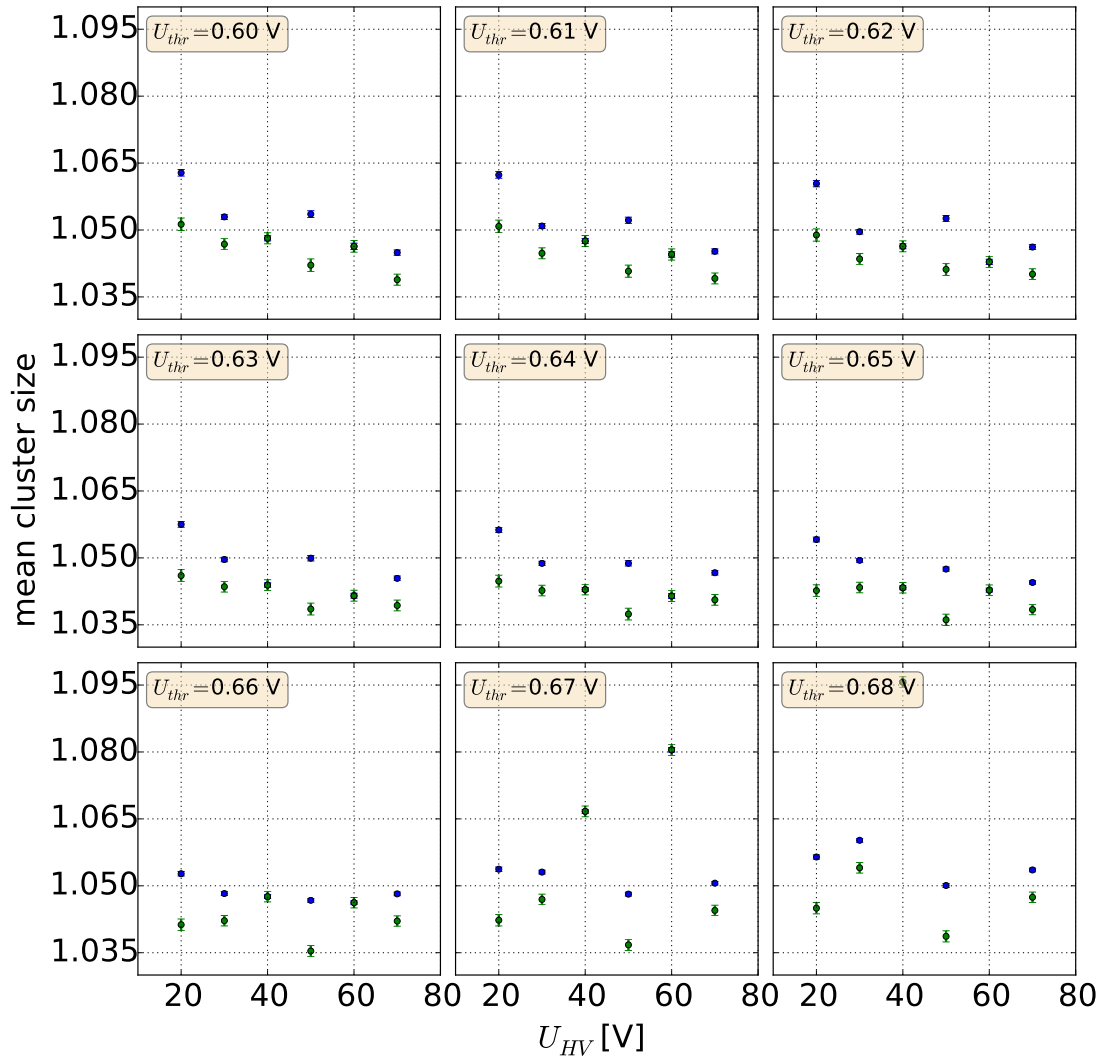
Figure 68: Cluster size for different sensor thresholds as a function of the applied bias voltage. Blue points show the mean cluster size before correction, while green data points represent the corrected data.

Sensor Efficiency

A tracking device should have a high hit reconstruction efficiency since several measurements are needed to reconstruct a track. The overall tracking efficiency is given by the product of the hit detection efficiency of each layer as well as the efficiency of the track search algorithm. For silicon detectors a hit reconstruction efficiency close to 100% is usually expected.

For the estimation of the sensor efficiency the second plane of the tracking station is employed. Therefore, tracks are reconstructed only from the hits in the other layers and are kept for further analysis if their χ^2 value is smaller than 10. In the next step, the intercept of the reconstructed track with the second layer is calculated. If the residual between the calculated intercept and the pixel hit coordinates is smaller than 0.0181 cm (1.4 times the pixel diagonal), the hit-track pair is matched. The efficiency is then given by the ratio

$$\epsilon = \frac{\text{number of matched tracks}}{\text{total number of tracks}}. \tag{5.15}$$

In order to avoid effects on the sensor edges, like charge sharing with insensitive parts, these areas are ignored during the analysis.

The efficiency as a function of the hit-track distance cut and the χ^2 cut are shown in figure 69 along with the corresponding distributions. The efficiency shows a steep rise for residual cuts smaller than 0.0129 cm (about the size of one times the pixel diagonal) and enters a plateau above this value. The dependency seems to be stronger in the May beam time data. The chosen cut value of 0.0181 cm (1.4 times the pixel diagonal) lies well inside the constant part for both beam times. A decrease of the χ^2 cut leads to an increase of the estimated sensor efficiency, especially in the March data. It seems that the efficiency obtained with the data taken in May is only weakly affected by the χ^2 cut. The reason for this is the long tail in the χ^2 distribution of the March data. It is caused by the higher level of fake tracks, produced by wrong combinations of hits during the track search, as no time stamps were used. In the end a cut value of 10 for both beam times was chosen as it is close to the peak in the χ^2 distribution in the case of the March beam time. In the case of the May beam time the χ^2 distribution almost vanishes above this value. The values for all cuts, and the analysis steps they are used in, are summarized in table 6.

Cut	Reconstruction Step	Value
frequency cut	Hot pixel	> 4 standard deviations
time window width	Binary File Converter	3 time stamps
cluster distance	Cluster Finder	< 1.5 pixel diagonal
cluster size		≤ 10
min. number of hits	Track Search and Fit	≥ 3
max. breaking angle		π - 0.001 mrad
track χ^2		≤ 10
residual cut	Efficiency	≤ 1.4 pixel diagonal

Table 6: Cuts used for the beam time analysis. The time window cut was only used for the May beam time analysis.

The obtained efficiencies for different bias voltages are shown in figure 70. As can be seen from the plots, the efficiency benefits from higher bias voltages. Due to a malfunction of the readout system, the efficiencies between the threshold voltages of 0.61 V and 0.67 V at
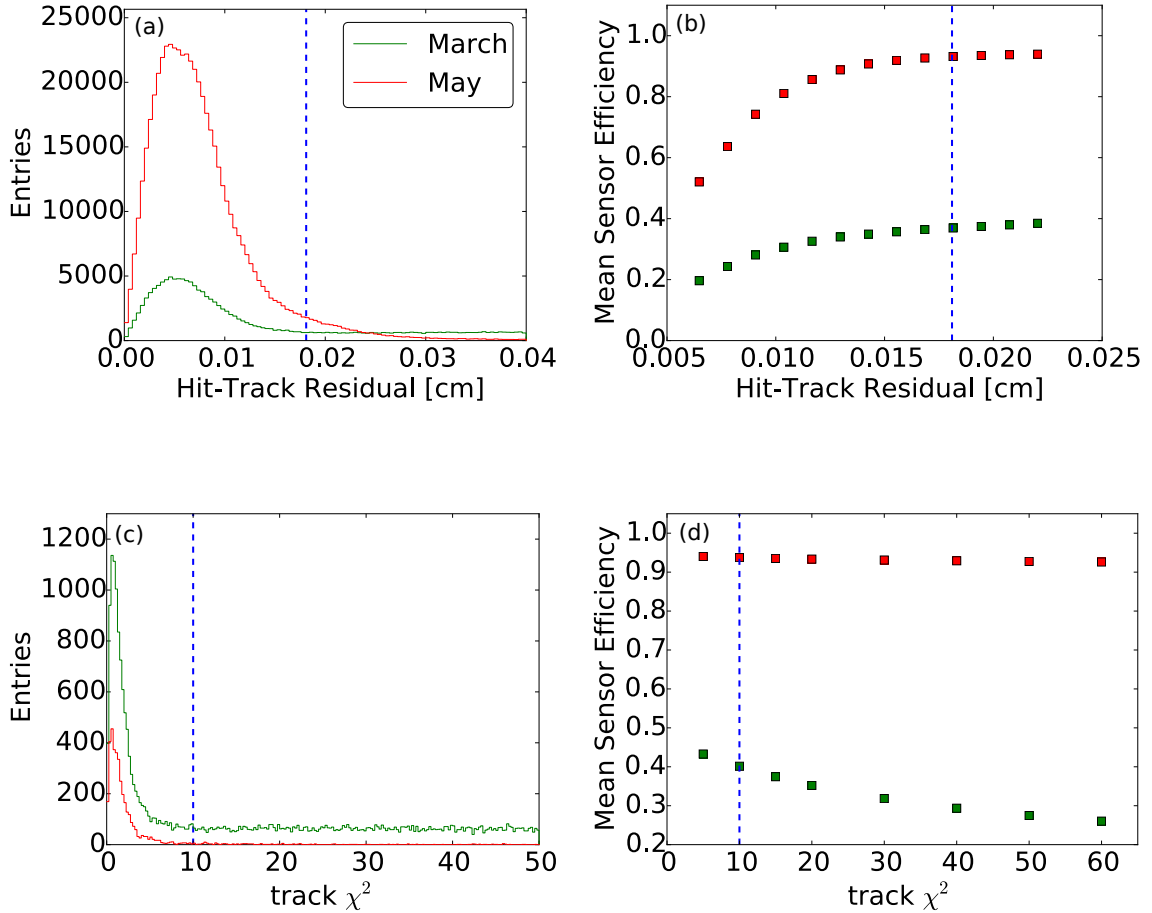
Figure 69: (a) hit-track residual distribution and (b) influence of the residual cut on the estimated efficiency. (c) χ^2 distribution and (d) influence of the χ^2 cut on the estimated efficiency. The chosen cut values are indicated as dashed lines.

$U_{HV} = 70$ V could not be measured. Otherwise for both chip DAC settings the expected behavior of the efficiency is observed. With increasing threshold voltage, which results in a decreasing threshold, the efficiency increases. With the power saving settings a higher efficiency of about 80% is reached in direct comparison with corresponding data points taken for normal settings which show an efficiency of about 60%. However, it should be noted that both settings are not directly comparable since the analogue properties of the MuPix change for the different settings and noise levels are expected to be much higher for power saving DAC settings. The difference in the slope can be explained with the different time-over-threshold distributions for both DAC settings. For the power saving settings the distribution is more stretched in comparison to the normal settings (compare figure 42b) and a change in the threshold cuts away less signal. The highest efficiency of about (93.76 ± 0.01)% was reached for a tuned sensor at $U_{HV} = 60$ V and $U_{thres} = 0.73$ V. The given error is purely statistical. A data point at the same threshold voltage and $U_{HV} = 70$ V is missing since the beam time of the A2 collaboration was finished before further data could be recorded with the tracking station. Two efficiency distributions of the complete pixel matrix are shown in figure 71. The left distribution was taken without adjustment of the tune DACs, while the right distribution was measured after application of the noise tuning algorithm. Both distributions are quite homogeneous except for the lower left corner of the
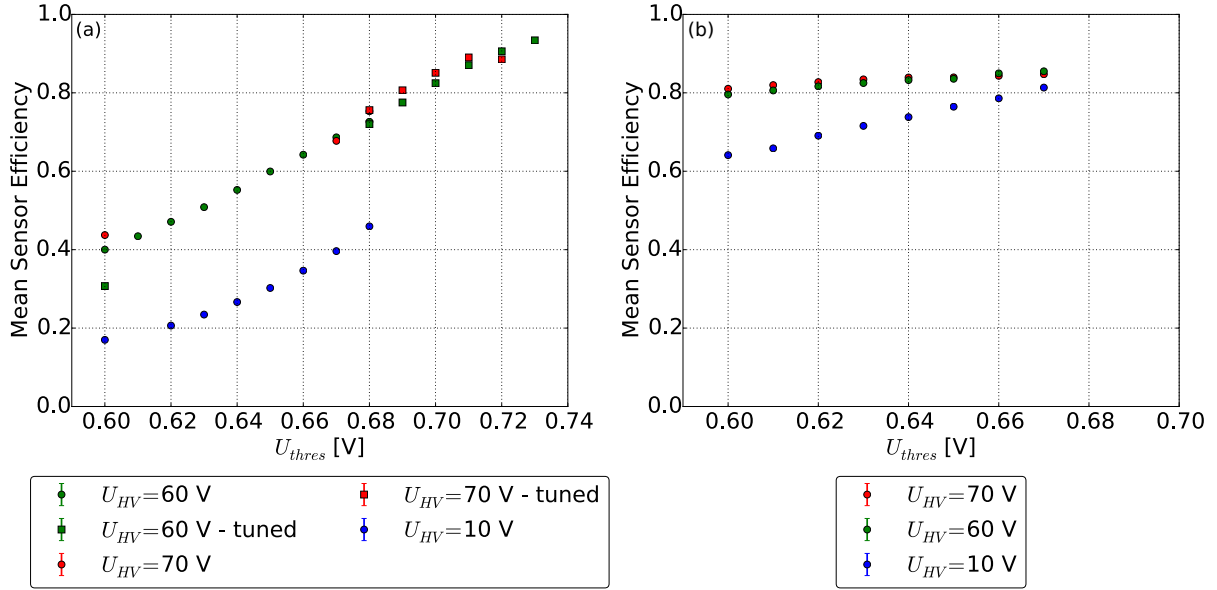
Figure 70: Sensor efficiency for the (a) normal and (b) power saving DAC settings in terms of the global threshold and bias voltages. The efficiency of the untuned matrix was only measured up to a threshold of $U_{thres} = 0.68$ V in the case of the normal DAC settings. All measurements with a tuned pixel matrix were taken during the March beam tests.
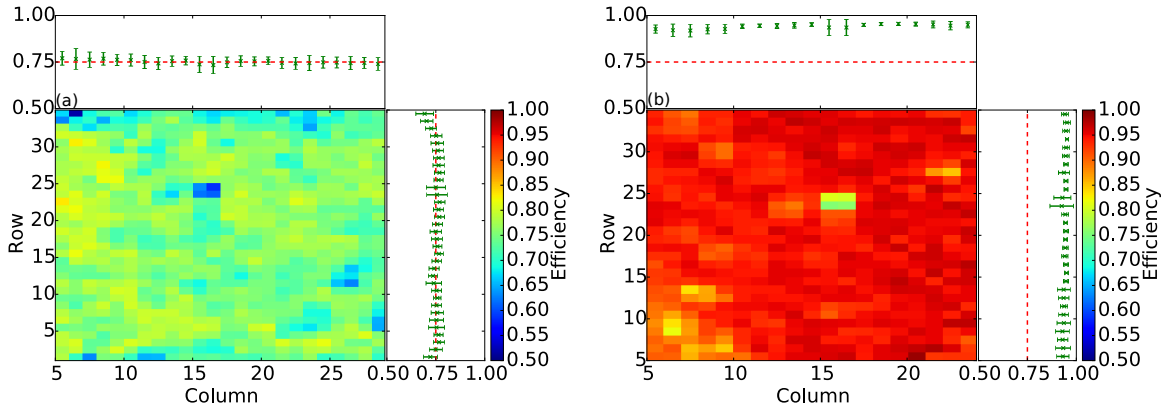

Figure 71: Efficiency distribution of the complete pixel matrix using normal DAC settings. (a) Untuned matrix, $U_{HV} = 70$ V and $U_{thres} = 0.68$ V (March beam time). (b) Tuned matrix, $U_{HV} = 60$ V and $U_{thres} = 0.73$ V (May beam time).

tuned pixel matrix. There the efficiency drops to values of only 80% while it reaches above 90% in the remaining parts of the matrix. This is most likely connected to the noise tuning algorithm which used an improper VPDAC setting, and therefore set the tune DACs in this region to incorrectly high values. The injection tuning algorithm was not used, as it is not suited well for this application. The injection voltage has to be chosen from the time-over-threshold distribution of a single pixel which might not be representative for the complete matrix.

Noise Estimation

Together with the efficiency, the noise rate for the MuPix 6 prototype was measured. For this the hits that could not be matched to tracks were counted to give an estimate of the noise rate. The estimation with this method is, however, biased to larger noise rates as the tracking efficiency and acceptance of the setup is not 100%. This leads to the effect that a particle is detected by a pixel, but no track is reconstructed in the event. This hit would then be registered as a noise hit. In order to correct for this effect, the noise rate at a threshold voltage of 0.68 V was taken as a reference value n_{ref}. Due to the high distance of this threshold to the noise band, the noise contribution to the number of unmatched hits can be neglected, and unmatched hits should only originate from the limited tracking efficiency. In addition, the different hit detection efficiencies at the individual thresholds have to be accounted for. Therefore, the unmatched hit distributions as well as n_{ref} were corrected with the measured hit detection efficiency at each threshold. The noise rate at each threshold is then given by

$$n_{\mathrm{thr}}^{\mathrm{cor}} = n_{\mathrm{thr}} \cdot \eta - n_{\mathrm{ref}} \tag{5.16}$$

where η is a further factor to correct for changes in the beam current between the reference rate and the rate at the measurement threshold n_{thr}. This factor was estimated by calculating the ratio of the clusters per second μ on layer one and three for the reference and measurement threshold

$$\eta = \frac{\mu_{ref}}{\mu_{thr}} \text{ with } \mu = \frac{1}{2}(\mu_1 + \mu_3). \tag{5.17}$$

The correction factors for each threshold are given in table 7. Between the measurements

U_{thr} [Volt]	Correction Factor η
0.69	1.008
0.70	1.007
0.71	1.002
0.72	0.741
0.73	0.749
0.74	0.662

Table 7: Correction factors to account for changes in the beam current used for the noise rate measurement.

done at 0.71 V and 0.72 V, η changes from roughly 1 to 0.75 which means that the cluster rate increased by 25%. This behavior could already be expected from figure 67 where the number of clusters increases around run 7800. The presented data were taken at these run numbers. The resulting mean noise rates per pixel for a tuned pixel matrix at 60 V bias voltage are shown in figure 72.

It can be seen that the uncorrected rates show an offset of about 10 Hz per pixel which stays constant until a threshold voltage of 0.71 V. Below a threshold voltage of 0.71 V, the corrected noise rate stays below 0.1 Hz and then starts to rise until, at 0.74 V, a drastic increase occurs with a noise rate of 800 Hz per pixel. At 0.73 V, a noise rate of 2.04 Hz is measured while the efficiency was estimated to be $(93.76 \pm 0.01)\%$. It should however be noted that this is only the per pixel noise rate. Extrapolating to the final sensor with 240 x 244 pixels the complete noise rate would be 0.12 MHz for one sensor and 47.78 MHz for the complete luminosity detector. At a time stamp interval of 25 ns
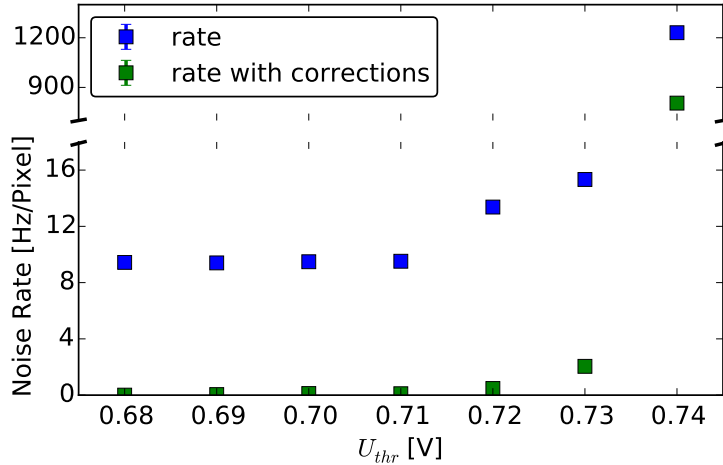
Figure 72: Noise rate per pixel at different thresholds and $U_{HV} = 60$ V. The rate before any correction is shown in blue. The green points show the rate after application of η and the subtraction of the reference rate.

this would correspond to one noise hit per time frame which can easily be coped with by the track search algorithms.

5.5 Spatial Resolution

The spatial resolution of a tracking device is an important contribution to the final momentum and angular resolution of the reconstructed tracks.

As the resolution of the MuPix tracking station is rather limited in the case of 1 GeV electrons from MAMI , the spatial resolution is measured using data taken during a beam time with the EUDET telescope [94] at DESY in October 2014. The beam time was conducted by the Mu3e group and analyzed in Heidelberg and Mainz. The EUDET telescope consists of six layers of Mimosa MAPS that reconstruct electron tracks with an energy of 5 GeV. The test chip is placed between the third and fourth layer of the telescope. The test chip used was the fourth revision of the MuPix chip. In contrast to MuPix 6 it has only a single amplification stage and a bug in the address readout of the hits. An example for a hit map is shown in figure 73.
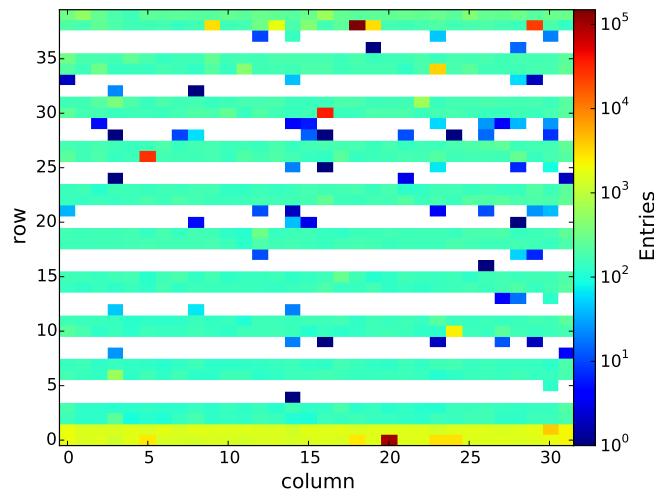

Figure 73: MuPix 4 hit map taken at DESY in October 2014.

In the hit map, white areas without any particle hits can be seen. This is caused by the readout malfunction. All hits in certain rows of the sensor get assigned a row address of zero due to, a timing issue with the internal chip reset signals. Because of the decoding of the chips internal pixel matrix to its physical representation, all such hits are assigned to the first two rows. The readout of the column address, on the other hand, works properly. This bug was fixed with the MuPix 6.

To extract the spatial resolution, the electron tracks are reconstructed with the EUDET software. The reconstruction steps are quite similar to the Mainz MuPix tracking station and do not need to be discussed in detail. The spatial resolution is given by the difference of the hit position measured by the MuPix 4 and the calculated intersection of the reconstructed track with the test chip plane. During this process, hits in the first two rows were ignored. The distribution is shown in figure 74. The pixel outline can be seen clearly.
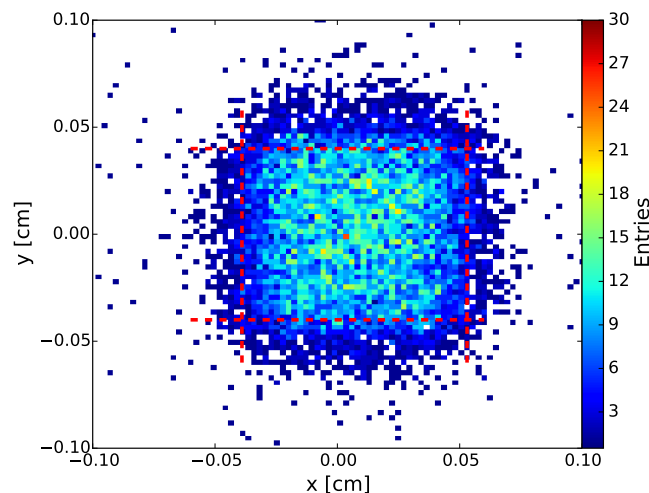

Figure 74: Hit-Track residuals of MuPix 4 test chips. The pixel size is indicated by red, dashed lines.

It is only slightly distorted by charge sharing between neighboring pixels, which happens in about 10% of the recorded events, and the resolution of the telescope, which is in the order of 3 µm after the software alignment. The standard deviations of the histogram are taken to be the sensor resolutions. This results in measured spatial resolutions of 26.4 µm in the x-dimension and 28.9 µm in the y-dimension, which are in good agreement with the expected values of 23.1 µm and 26.5 µm (see equation 4.15).

5.6 Future Measurements

To complete the studies on the MuPix 6 prototype, characterized sensor samples have to be irradiated with proton and neutron beams. After the irradiation, the signal-to-noise ratio has to be measured in the laboratory, and sensor efficiency and noise have to quantified in test beams with the MuPix tracking station. The obtained numbers have to be compared with results before irradiation. Although the behavior of the shaper response function for different temperature has already been checked in Heidelberg, and only a minor dependence has been found [85], the influence of temperature gradients on the chip performance still has to be measured. These gradients will arise in the luminosity detector due to the foreseen cooling concept. The temperature distribution across the sensors could lead to a position dependent noise distribution where warmer parts of the sensor are expected to

have a higher noise level. It needs to be checked if a homogeneous efficiency can be reached in spite of the different noise contributions.

The next prototype version of the MuPix chip (MuPix 7), which is already being tested in Heidelberg, has undergone some serious changes in the digital part. The time stamp generation has been moved from the FPGA onto the chip. In addition, the parallel readout has been replaced by a serial LVDS link and no external readout signals are required anymore. Instead the chip posses a free running readout. Therefore, the data rates produced by the sensor are now much higher and the existing data acquisition software and the FPGA firmware have to be adapted to cope with the increased data rate and different data structure. Because of the reduced number of external signals and the LVDS link, an improvement in the signal-to-noise ratio can be expected and has been proven by first test beams. The new sensor and data acquisition system then have to be characterized in test beam campaigns.

6

EVENT SELECTION FOR THE DECAY $e^+e^- \to \eta_c \eta \pi^+ \pi^-$ AT BESIII

6.1 Datasets and Monte Carlo Simulations

As already explained in the motivation, the discovery of the $Z_c(3900)$ suggests the existence of an yet unobserved $Z_c^{\pm,0}$ decaying into $\eta_c \pi^{\pm,0}$. If such an isospin triplet exists, one would also expect the existence of an isospin singlet $Z_c^0 \to \eta_c \eta$. The observation of this resonance would add important information to the underlying pattern of new states and would enhance the understanding of their internal structure. In the following chapters the event selection and results of the search for the reaction $e^+e^- \to \eta_c \eta \pi^+ \pi^-$ using the high luminosity datasets at center of mass energies between 4.23 - 4.36 GeV, which have been collected by the BESIII collaboration, are described. The luminosity of the data samples used for this analysis are listed in table 8.

ID	$\sqrt{s}$ [MeV]	Luminosity [pb^{-1}]
4.23	4225.54 ± 0.65	1091.74
4.26	4257.43 ± 0.66	825.67
4.36	4358.26 ± 0.62	539.84

Table 8: Integrated luminosity of the used data samples at the different center of mass energies. The center of mass energies are taken from [95]. Throughout the text the datasets will be referred to by their respective ID.

Monte Carlo simulations were used for the development of selection criteria and to study detector acceptance, efficiency and possible background channels. The simulation and analysis of Monte Carlo data was performed within the BOSS[1] framework which is also used for the reconstruction and analysis of real detector data. The simulation of the BESIII detector is based on GEANT4 [96] which simulates the propagation and interaction of particles in the detector. Initial charmonium resonances are produced with the KKMC generator [97] that takes into account initial state radiation up to second order QED calculations and the beam spread of the e^+e^- beams. The decays of daughter particles are generated by BESEvtGen [98]. It was developed from EvtGen which in turn was designed for B-physics experiments [99]. It has been adapted to tau-charm physics and provides access to additional generators like PHOTOS for the simulation of final state radiation. The decay chain

$$e^+e^- \to \eta_c \eta \pi^+ \pi^- \tag{6.1}$$

was generated as signal Monte Carlo dataset with the 13 different η_c final states being listed in table 9. The chain was generated for each the datasets, which are shown in table 8, using the appropriate center of mass energy and energy spread. During the signal Monte Carlo generation the η and π^0 particles were restricted to decay into a pair of photons while

---

1 BESIII Offline Software System

η_c final state	branching fraction [%]
$\pi^+\pi^-K^+K^-$	$0.95 \pm 0.17 \pm 0.13 \pm 0.09$
$2(K^+K^-)$	$0.22 \pm 0.08 \pm 0.03 \pm 0.02$
$2(\pi^+\pi^-)$	$1.72 \pm 0.19 \pm 0.25 \pm 0.17$
$3(\pi^+\pi^-)$	$2.02 \pm 0.36 \pm 0.36 \pm 0.19$
$K_\mathrm{s}K^\pm\pi^\mp$	$2.60 \pm 0.29 \pm 0.34 \pm 0.25$
$K_\mathrm{s}K^\pm\pi^\mp\pi^+\pi^-$	$2.75 \pm 0.51 \pm 0.47 \pm 0.27$
$K^+K^-\pi^0$	$1.04 \pm 0.17 \pm 0.11 \pm 0.10$
$K^+K^-\eta$	$0.48 \pm 0.23 \pm 0.07 \pm 0.05$
$\pi^+\pi^-\eta$	$1.66 \pm 0.34 \pm 0.26 \pm 0.16$
$\pi^+\pi^-\pi^0\pi^0$	$4.66 \pm 0.50 \pm 0.76 \pm 0.45$
$2(\pi^+\pi^-)\eta$	$4.40 \pm 0.86 \pm 0.85 \pm 0.42$
$2(\pi^+\pi^-\pi^0)$	$17.23 \pm 1.70 \pm 2.29 \pm 1.66$
$K^+K^-2(\pi^+\pi^-)$	$0.83 \pm 0.39 \pm 0.15 \pm 0.08$

Table 9: The 13 η_c decay channels used for the analysis. The branching fractions taken from [100]. The first and second error represent the statistical and systematic uncertainties. The third error gives the systematic uncertainty due to the uncertainty in the branching ratio $\psi(3686) \to \pi^0 h_c$ from [100]. For each η_c channel $2.5 \cdot 10^5$ signal Monte Carlo events were generated separately and for each center of mass energy.

the K_s^0 decays into two charged pions. The signal events are generated with BESEvtGen. After the generation the created particles are handed over to the detector simulation. During the simulation the particles are propagated through the BESIII detector using a full geometry model of the detector. The interaction and energy loss of particles inside the detector material is stored. In a next step the detector response to the simulated interactions is digitized using the calibration of the BESIII detector front ends which is loaded from a database. After the digitization EMC clusters and tracks of charged particles are reconstructed with the same algorithms which are also used for the reconstruction of real data taken with the detector. With these data samples the event selection described below was developed.

For background studies an inclusive Monte Carlo dataset is used. It contains a hadron and open charm sample that simulate Y(4260)/Y(4360) decays into charmomium and open charm channels, like $D\bar{D}$, respectively. Vector charmonium states (J/ψ, $\psi(2S)$, $\psi(3770)$) produced in initial state radiation processes are part of an ISR sample. The so called γXYZ sample contains initial state radiation production of other charmonium resonances. The known branching fractions are taken from the particle data group [1]. Non resonant $q\bar{q}$ events are produced with PYTHIA [101]. Furthermore, QED processes (e^+e^- to e^+e^-, $\mu^+\mu^-$ and $\tau^+\tau^-$) are simulated using a dedicated dataset.
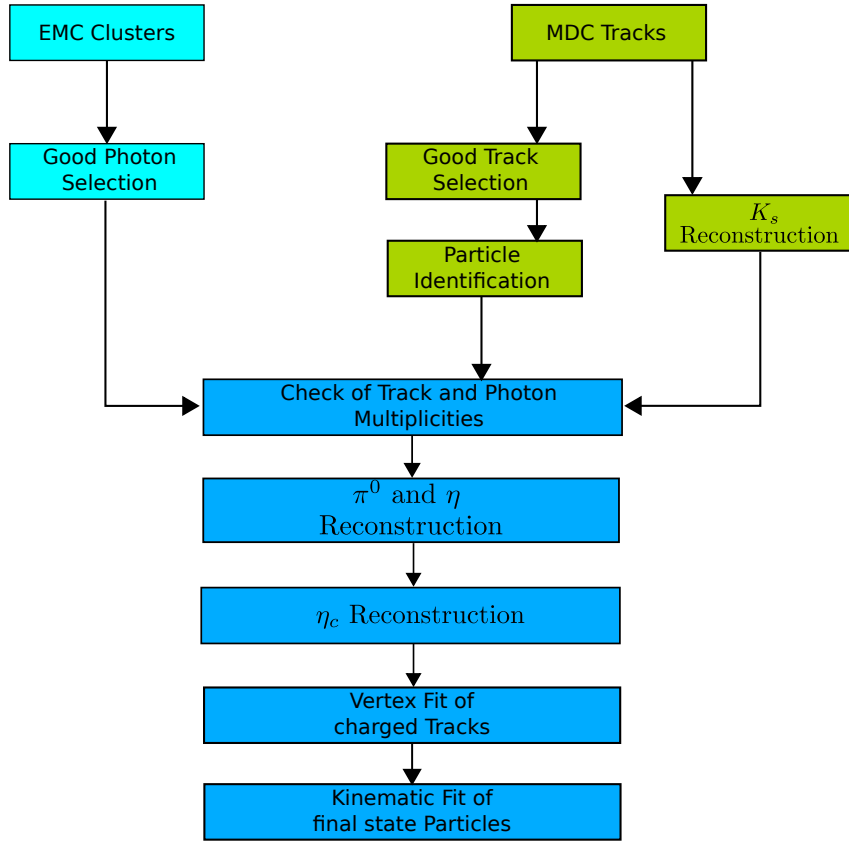
Figure 75: Process of the event selection for the decay $e^+e^- \to \eta_c\eta\pi^+\pi^-$. For a more detailed discussion see text.

6.2 Criteria for Particle Selection

The general work flow of the event selection is depicted in figure 75. In a first step candidates for good charged tracks are selected from the tracks reconstructed in the MDC, while photons are reconstructed from clusters in the EMC . The selection of good tracks and photons follows the standard selection used by the BESIII collaboration and is summarized in the next paragraphs.

Good Track Selection

The following criteria are required for charged tracks:

- The polar angle with respect to the beam axis of the charged tracks is in the acceptance of the drift chamber. Hence, it is required that $|\cos(\theta)|$ is smaller than 0.93.

- The point of closest approach of the charged track to the interaction point has to be within a cylinder around the interaction point. The cylinder has a radius of $V_{xy} = 1$ cm in the x-y plane and a length of $V_z = \pm 10$ cm along the beam axis. For tracks originating from the decay of long lived particles like the $K_{\rm s}$ the V_{xy} requirement is omitted while V_z is increased to ± 20 cm.

After the selection of good tracks a particle identification is performed to identify kaons and pions. For this the joint probability from the energy loss information of the MDC and the time-of-flight information of the TOF-detector is calculated for each particle species. In order for a particle to be identified as a kaon, the kaon probability calculated by

the PID-algorithms has to be larger than 0.1%. The same holds true for pions with the additional requirement that the pion probability has to be larger than the kaon probability $P(\pi) > P(K)$.
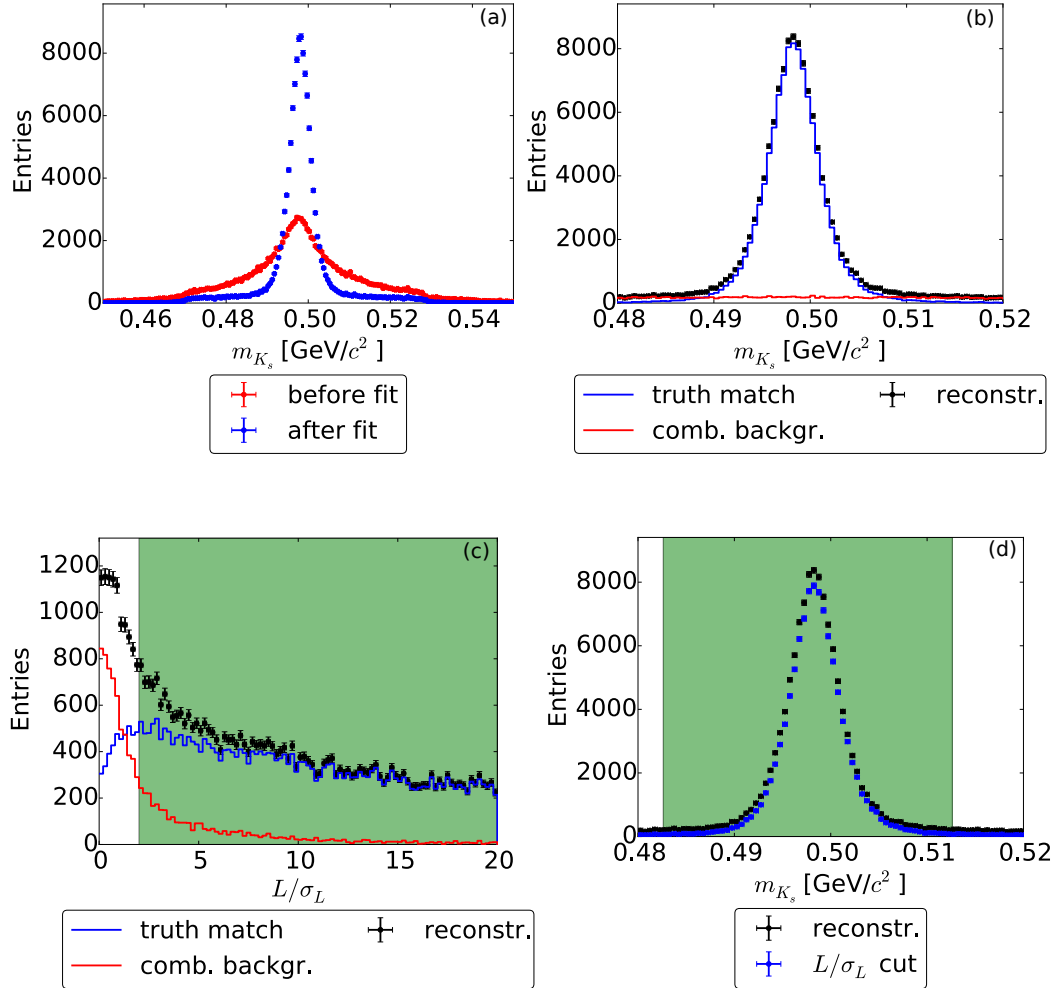
K_s Selection

Figure 76: K_s candidate reconstruction and selection from signal Monte Carlo sample at $\sqrt{s} = 4.26$ GeV. (a) K_s candidate mass distribution before and after the vertex fit. (b) K_s candidate mass distribution for truth matched K_s candidates and combinatorial background. (c) L/σ_L distribution of the K_s candidates. (d) K_s mass distribution before and after application of L/σ_L. All selection cuts are highlighted as green areas.

The K_s candidates are reconstructed from the decay $K_s \to \pi^+\pi^-$. Assuming all charged tracks to be pions a vertex fit of all pairs of charged tracks is performed. All combinations where the χ^2 of the vertex fit is smaller than 100 are kept as initial K_s candidates. The invariant mass distribution of these candidates before and after the vertex fit is shown in figure 76a. Before the vertex fit the invariant mass distribution is quite broad and shows an obvious non Gaussian shape with long tails. After the vertex fit the mass resolution has been considerably improved and the K_s invariant mass distribution shows a Gaussian peak over a flat background. By verifying the correct reconstruction with informations from the Monte Carlo generator, the invariant mass distribution has been separated into true K_s particles and candidates where at least one daughter pion does not originate from

a K_s decay. This is shown in figure 76b. A flat background from wrong pion combinations can be seen. To further reduce the background contribution, the K_s candidates satisfying the following requirements are kept as K_s candidates:

- To avoid pollution of the K_s sample by short lived particles, the ratio of the measured decay length L and the event-wise estimated decay length resolution σ_L has to be larger than two ($L/\sigma_L > 2$). The distribution of L/σ_L for true and misidentified K_s candidates is shown in figure 76c. The distribution for misidentified K_s particles peaks at $L/\sigma_L = 0$ and falls off quickly compared to the L/σ_L distribution of correctly reconstructed K_s particles. The invariant mass distribution after the cut on the decay length ratio is shown in figure 76d. The combinatorial background has been reduced while the mass resolution of the K_s stays constant.

- The invariant mass of K_s candidate has to be inside of a mass window around the nominal K_s mass ($m_{K_s} = 0.498 \text{ GeV}/c^2$) $|m_{\pi^+\pi^-} - m_{K_s}| < 15 \text{ MeV}/c^2$.

Good Photon Selection

Photons are reconstructed from clusters caused by electromagnetic showers in the EMC. To be accepted as a good photon, a cluster in the EMC has to fulfill the requirements which are listed below:

- To suppress noise from the EMC front end electronics, the reconstructed energy has to be at least $E_\gamma > 25 \text{ MeV}$ in the barrel of the EMC and $E_\gamma > 50 \text{ MeV}$ in the EMC end caps. The barrel region is defined by the polar angle with $|\cos(\theta)| < 0.8$, while the end caps are located at $0.84 < |\cos(\theta)| < 0.92$.

- To further bear down the noise contribution, the time difference between the event trigger and the EMC timing information has to be 0 ns $\leq t_{EMC} \leq 700$ ns.

- In order to separate clusters caused by photons from the interaction point and clusters formed by Bremsstrahlung emitted by charged particles, the angle between neutral clusters and the closest charged track has to be at least 10° in the EMC.

π^0 and η Selection

π^0 ($m_{\pi^0} = 0.135 \text{ GeV}/c^2$) and η ($m_\eta = 0.548 \text{ GeV}/c^2$) candidates are reconstructed from combinations of all good photon pairs that fulfill $0.11 \text{ GeV}/c^2 < m_{\gamma\gamma}^{\pi^0} < 0.15 \text{ GeV}/c^2$ and $0.50 \text{ GeV}/c^2 < m_{\gamma\gamma}^{\eta} < 0.57 \text{ GeV}/c^2$ respectively. The invariant mass spectra of $\gamma\gamma$ pairs from the signal Monte Carlo datasets of $\eta_c \to K^+K^-\pi^0$ and $\eta_c \to K^+K^-\eta$ are shown in figure 77. Both distributions have an asymmetric shape with longer tails to lower masses. The asymmetric shape is caused by the fact that the full photon energy can not be measured by the EMC due to insensitive material like the holding structure of the crystals. This propagates to the invariant mass distribution of the two photons.
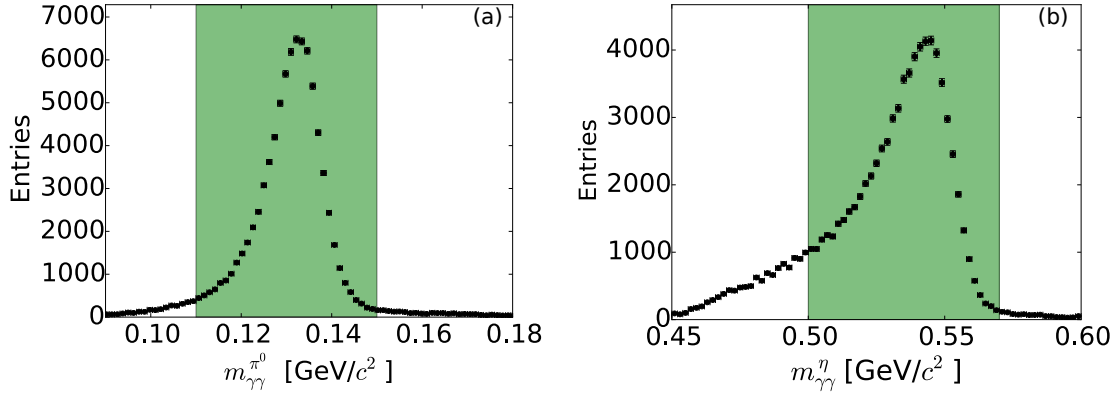
Figure 77: Reconstructed (a) π^0 and (b) η mass distributions from signal MC. The selected mass region is highlighted in green.

6.3 Event Selection

After the selection of good tracks and photons the track and photon multiplicities are checked. The number of tracks has to be equal to the expected number of tracks for the η_c final state in question and the total charge of all selected tracks has to be zero. The number of good photons has to be at least equal to the number of expected photons. For all events passing this requirement, η_c candidates are reconstructed selecting all η_c candidates within a wide mass window of

$$|m_{\eta_c} - m_{\eta_c}^{PDG}| < 0.45 \text{ GeV}/c^2$$

around the nominal η_c mass of $2.983 \text{ GeV}/c^2$ [1]. This is done in order to reduce the computing time which is spend by the following steps of the selection. After that a primary vertex fit of all charged tracks is performed. Tracks originating from a K_s are excluded from the fit. For all events with a converging vertex fit a kinematic fit is performed to increase the momentum resolution. The kinematic fit uses constraints on the initial four momentum of the e^+e^- pair and a mass constraint on the η mass. Additional mass constraints on the η, π^0 and K_s masses are employed for the appropriate η_c final states. The constraints of the kinematic fit for each final state are summarized in table 10. To reject background and badly reconstructed events, a χ^2 cut is employed. The χ^2 distribution for signal Monte Carlo events and for data events from η_c sideband regions is shown in figure 78. An event falls into the η_c sideband region if the reconstructed mass of the η_c candidate is inside the intervals

$$2.600 \text{ GeV}/c^2 < m_{\eta_c} < 2.854 \text{ GeV}/c^2 \text{ or } 3.112 \text{ GeV}/c^2 < m_{\eta_c} < 3.177 \text{ GeV}/c^2.$$

At the same time the η_c signal region has been defined as

$$2.887 \text{ GeV}/c^2 < m_{\eta_c} < 3.080 \text{ GeV}/c^2,$$

which corresponds to six times the width of the η_c meson. The χ^2 cut, which is shown as green area in figure 78, was chosen to retain 90% of the reconstructed signal events. All candidates sharing the minimal χ^2 from the kinematic fit in one event are retained for further analysis. Multiple candidates sharing the same χ^2 occur for η_c final states including pions. This is due to the combinatorial possibility to exchange prompt pions from the Y(4260) with pions from the subsequent η_c decay without changing the total four
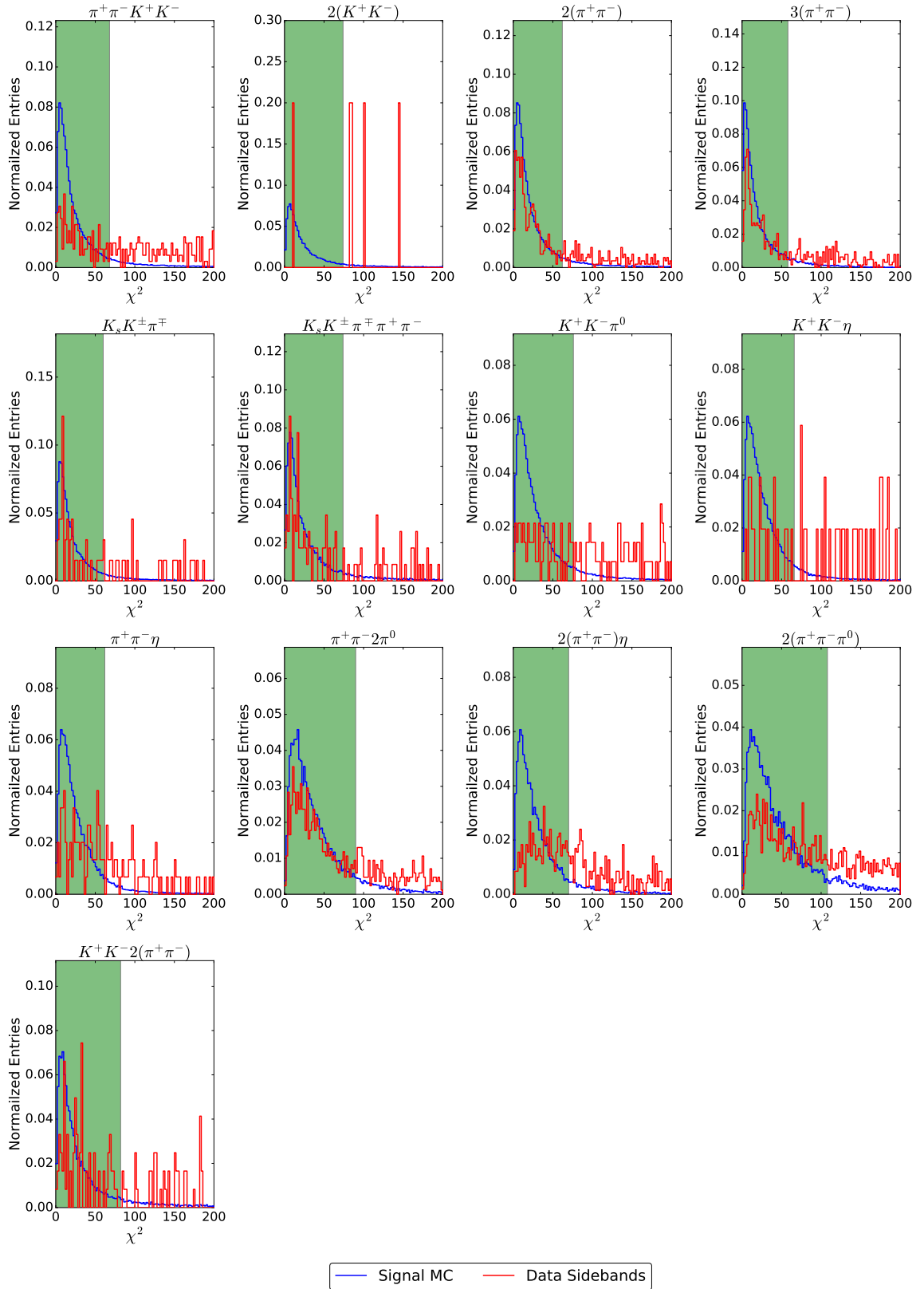
Figure 78: Distribution of the χ^2 value from the kinematic fit for the investigated η_c final states. Candidates with a χ^2 inside the green area are accepted. The distributions have not been normalized to each other.

Figure 79: Candidate multiplicities for the analyzed final states. Before cuts includes all basic selection criteria for good photons and tracks, while after cuts includes all described cuts including the χ^2 cut. In addition the number of candidates sharing the same, minimal χ^2 value in the event are shown.

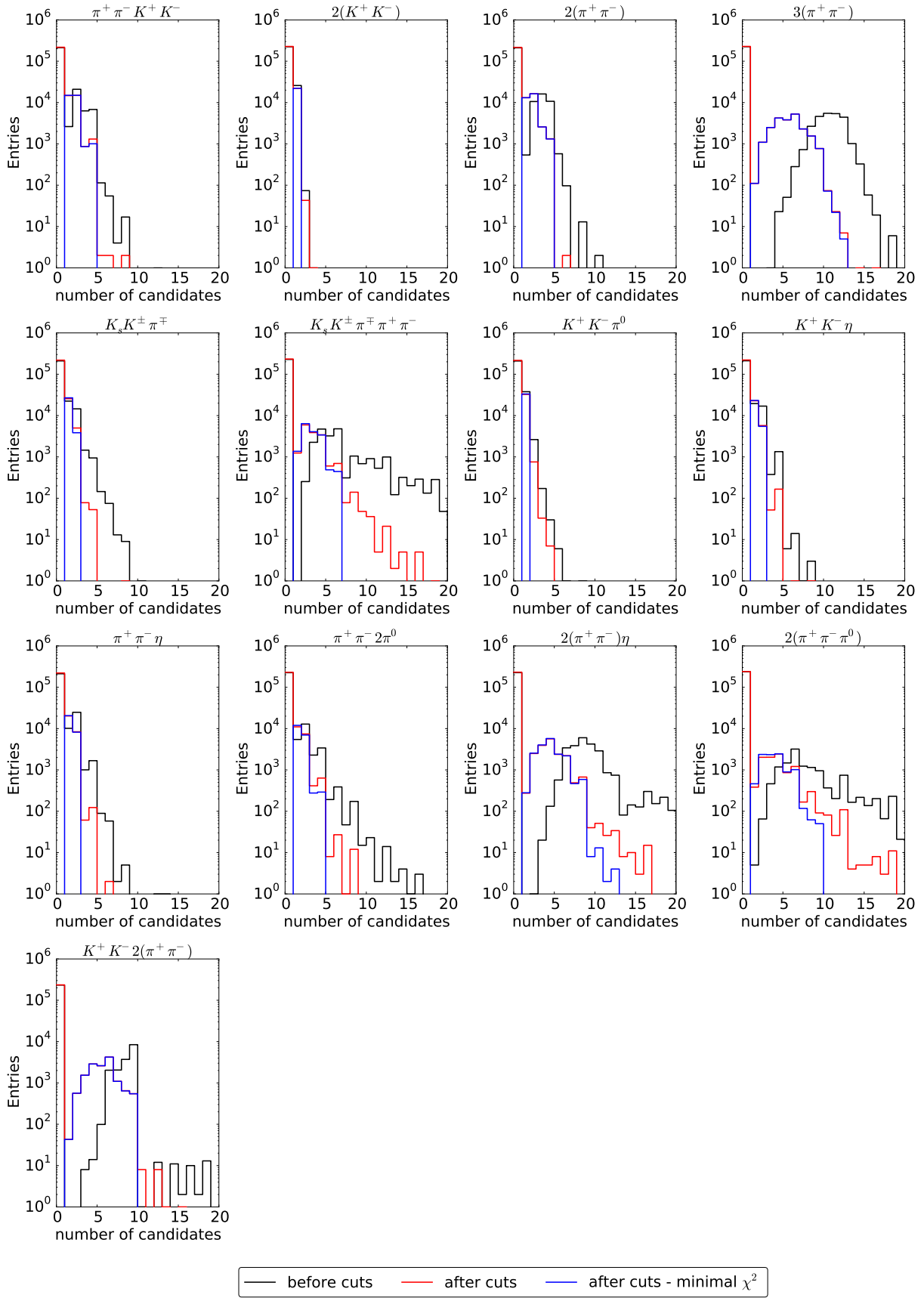| η_c final state	additional constraints	number of constraints	χ^2 cut
$\pi^+\pi^- K^+K^-$	-	5	68
$2(K^+K^-)$	-	5	74
$2(\pi^+\pi^-)$	-	5	62
$3(\pi^+\pi^-)$	-	5	58
$K_s K^{\pm}\pi^{\mp}$	m_{K_s}	6	64
$K_s K^{\pm}\pi^{\mp}\pi^+\pi^-$	m_{K_s}	6	78
$K^+K^-\pi^0$	m_{π^0}	6	76
$K^+K^-\eta$	m_η	6	66
$\pi^+\pi^-\eta$	m_η	6	62
$\pi^+\pi^-\pi^0\pi^0$	$m_{\pi^0,1},\, m_{\pi^0,2}$	7	90
$2(\pi^+\pi^-)\eta$	m_η	6	70
$2(\pi^+\pi^-\pi^0)$	$m_{\pi^0,1},\, m_{\pi^0,2}$	7	108
$K^+K^-2(\pi^+\pi^-)$	-	5	82

Table 10: Constraints and χ^2 cut used during the kinematic fit. For all channels a constraint on the initial four momentum and the η mass has been used. The χ^2 cut is chosen to retain 90% of the signal events.

momentum of the event. Therefore, the kinematic fitter is insensitive to these exchanges. The candidate multiplicities are shown in figure 79. It shows the number of candidates before the application of the cuts described above (excluding good photon and track selection) and after the application of cuts. Additionally, the number of candidates which share the minimal χ^2 value is depicted. For the $2(K^+K^-)$ final state only one candidate per event is expected as there are no additional pions from the η_c decay. The few events with multiple candidates are caused by wrongly reconstructed η particles and disappear after the minimal χ^2 requirement is applied. In the case that further constraints can be imposed on the pions, the number of additional candidates can be reduced by selecting only candidates with the minimal χ^2 value. This is the case for the η_c decays to $K_s K^{\pm}\pi^{\mp}$ and $K_s K^{\pm}\pi^{\mp}\pi^+\pi^-$. For other η_c decays the number of candidates can increase to more than 10 candidates per event. This leads to high levels of combinatorial background contributions as can be seen in the next section. A further discriminating variable to distinguish between pions from the η_c and the $Y(4260)$ like transverse momentum or angles between decay particles could not be found.

7
EVENT RECONSTRUCTION PERFORMANCE

7.1 η_c Reconstruction at 4.26 GeV Center of Mass Energy

In this section the η_c reconstruction performance in terms of correctness, efficiency, and resolution at a center of mass energy of 4.26 GeV is discussed. In the corresponding plots the four η_c decay channels $2(K^+K^-)$, $2(\pi^+\pi^-)$, $K_s K^{\pm}\pi^{\mp}$ and $2(\pi^+\pi^-\pi^0)$ are presented here, while the plots for the remaining channels can be found in appendix D.

Correctness
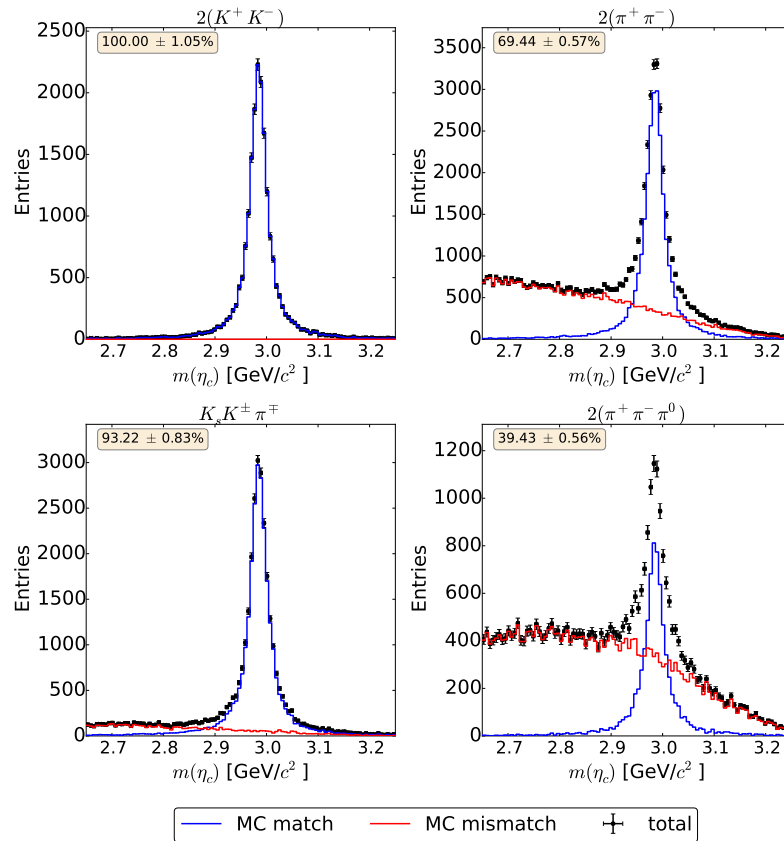
Figure 80: Distribution of the η_c invariant mass of the four exemplary selected η_c final states at a center of mass energy of 4.26 GeV separated into incorrectly and correctly reconstructed events.

The correctness of the event reconstruction was studied by using informations from Monte Carlo generator. Each event where the reconstructed decay tree of at least one candidate completely matched the Monte Carlo simulated decay tree was considered as being

correctly reconstructed. All other candidates within the same event have been wrongly reconstructed and are assigned to be mismatched candidates. The resulting η_c mass distributions of the matched and mismatched candidates for the four example final states are shown in figure 80. The best correctness is achieved for η_c final states containing no further pions ($2(K^+K^-)$, $K^+K^-\pi^0$) as could already be seen from figure 79. The $K^+K^-\eta$ final state has a lower correctness as the η particle can be permuted with the prompt η meson from the $Y(4260)$ decay. With increasing number of pions from the η_c decay the number of combinatorial background events increases as well. The combinatorial background contribution, however, is smooth and no peak is observed at the nominal η_c mass of $2.983\,\mathrm{GeV}/c^2$. The correctness, defined as the ratio of the number of correctly reconstructed events to the total number of reconstructed events in the η_c signal region, is summarized in table 11.

η_c final state	Correctness [%]
$\pi^+\pi^-K^+K^-$	73.50 ± 0.61
$2(K^+K^-)$	100.00 ± 1.05
$2(\pi^+\pi^-)$	69.44 ± 0.57
$3(\pi^+\pi^-)$	28.87 ± 0.26
$K_s K^\pm \pi^\mp$	93.22 ± 0.83
$K_s K^\pm \pi^\mp \pi^+\pi^-$	48.59 ± 0.54
$K^+K^-\pi^0$	100.00 ± 0.87
$K^+K^-\eta$	90.04 ± 0.82
$\pi^+\pi^-\eta$	86.17 ± 0.78
$\pi^+\pi^-\pi^0\pi^0$	79.57 ± 0.88
$2(\pi^+\pi^-)\eta$	36.37 ± 0.36
$2(\pi^+\pi^-\pi^0)$	39.43 ± 0.56
$K^+K^-2(\pi^+\pi^-)$	27.84 ± 0.30

Table 11: Correctness of the event reconstruction of $e^+e^- \to \eta_c\eta\pi^+\pi^-$ for different η_c final states at a center of mass energy of 4.26 GeV extracted from signal Monte Carlo.

Efficiency and Resolution

The reconstruction efficiency after the application of the event selection criteria is estimated by a fit to the reconstructed invariant mass distributions of the η_c candidates. This is feasible since the combinatorial background is smooth beneath the η_c peak position (see figure 80). For the estimation an extended maximum likelihood fit is performed which was implemented with the RooFit package [102]. The signal is fitted with a Breit-Wigner function B with the mean μ_{η_c} and width Γ_{η_c} fixed to the input values of the η_c meson which were used during the simulation. To account for detector effects, the Breit-Wigner function is convoluted with a Gaussian resolution function G with mean μ and width σ which are extracted by the fit as well. The combinatorial background distribution is modeled as a sum of Chebyshev polynomials T. The complete fitting function depending on the mass m is given by

$$f_{\text{fit}}(m) = n_{\text{signal}} B(m, \mu_{\eta_c}^{\text{PDG}}, \Gamma_{\eta c}^{\text{PDG}}) \otimes G(m, \mu, \sigma) + n_{\text{bkg}} \sum_{n=0}^{k} a_n T_n(m) \qquad (7.1)$$

where n_{signal} and n_{bkg} are the number of signal and background events. The order k and shape parameters a_n of the background polynomial T_n were fixed using the distribution of the mismatched candidates depicted in figure 107. The lowest order Chebyshev polynomial which allowed for a good fit was chosen. After the fit the estimated value of n_{signal} is divided by the number of simulated events which yields the reconstruction efficiency. The reconstructed mass distributions and the result of the fit for the four example final states are shown in figure 81. The obtained efficiencies are summarized in table 12. As can be
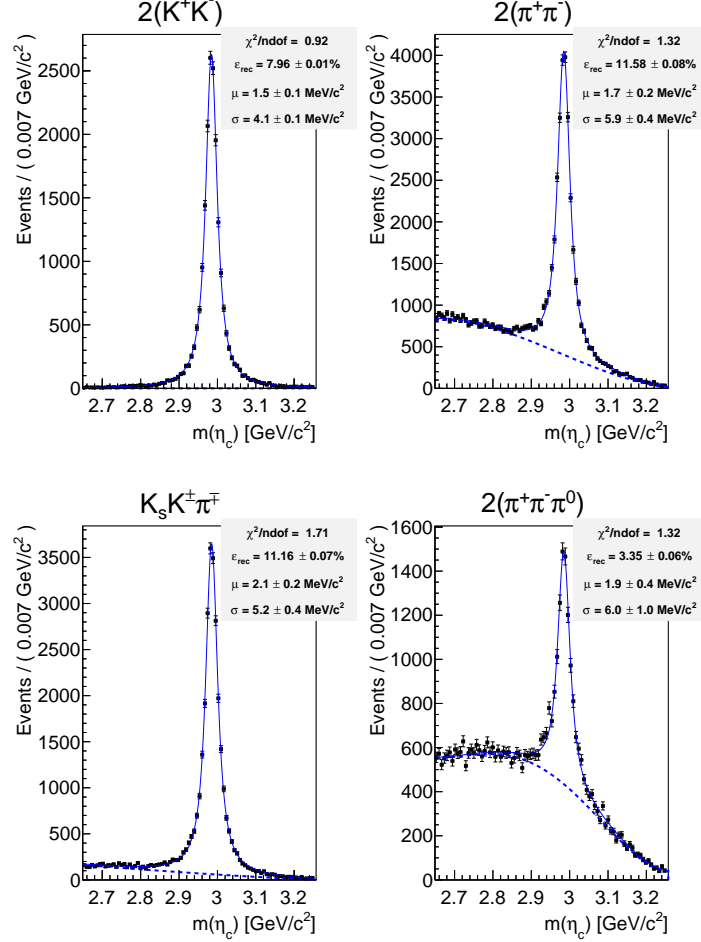

Figure 81: Fit to the reconstructed η_c mass distributions from signal Monte Carlo in oder to extract the reconstruction efficiency of $e^+e^- \to \eta_c\eta\pi^+\pi^-$ and resolution of the η_c mass for the the four exemplary selected η_c final states at a center of mass energy of 4.26 GeV.

expected the efficiency decreases with increasing multiplicity of charged tracks and photons in the event. The highest efficiency is reached for the $K^+K^-\pi^0$ final state of the η_c, while the $2(\pi^+\pi^-\pi^0)$ final state has the lowest reconstruction efficiency of all final states. Also given in table 12 are the parameters of the Gaussian used as resolution function. The η_c peak is systematically shifted towards larger masses with respect to the simulated value. The shift lies generally between 1-2 MeV/c^2 and is small compared to the width of 32.2 MeV/c^2 [1] of the η_c resonance. The resolution is in the order of 4-10 MeV/c^2. Charged final states of the η_c are usually reconstructed with a slightly better resolution than final states containing neutral particles like the η and π^0 which are reconstructed by their decay to photon pairs. The shift and the resolution are incorporated during the fit to the data distributions.

η_c final state	Polynomial Order	Efficiency [%]	μ [MeV/c^2]	σ [MeV/c^2]
$\pi^+\pi^- K^+K^-$	3	11.51 ± 0.08	1.5 ± 0.2	5.7 ± 0.4
$2(K^+K^-)$	1	7.96 ± 0.01	1.5 ± 0.1	4.1 ± 0.1
$2(\pi^+\pi^-)$	3	11.58 ± 0.08	1.7 ± 0.2	5.9 ± 0.4
$3(\pi^+\pi^-)$	4	7.22 ± 0.10	1.2 ± 0.3	5.4 ± 0.7
$K_s K^{\pm}\pi^{\mp}$	2	11.16 ± 0.07	2.1 ± 0.2	5.2 ± 0.4
$K_s K^{\pm}\pi^{\mp}\pi^+\pi^-$	4	5.58 ± 0.07	1.1 ± 0.3	5.4 ± 0.7
$K^+K^-\pi^0$	1	11.92 ± 0.01	2.1 ± 0.1	7.0 ± 0.3
$K^+K^-\eta$	3	10.41 ± 0.07	1.8 ± 0.2	7.3 ± 0.3
$\pi^+\pi^-\eta$	3	10.21 ± 0.07	2.1 ± 0.2	7.3 ± 0.4
$\pi^+\pi^-\pi^0\pi^0$	4	6.82 ± 0.06	1.6 ± 0.2	9.7 ± 0.4
$2(\pi^+\pi^-)\eta$	4	6.59 ± 0.08	2.1 ± 0.3	7.4 ± 0.6
$2(\pi^+\pi^-\pi^0)$	4	3.35 ± 0.06	1.9 ± 0.4	6.0 ± 1.0
$K^+K^-2(\pi^+\pi^-)$	4	5.18 ± 0.09	1.8 ± 0.4	6.4 ± 0.8

Table 12: Efficiency of the event reconstruction of $e^+e^- \to \eta_c\eta\pi^+\pi^-$ and η_c mass shift μ and mass resolution σ for different η_c final states at a center of mass energy of 4.26 GeV.

Channel Cross Feed

Due to wrong particle identification or event reconstruction, events of a specific η_c final state could be reconstructed by the reconstruction algorithms of different η_c final states. This is called cross feed and could result in a too high number of reconstructed η_c events. The cross feed between the different analyzed η_c final states is estimated by feeding the signal Monte Carlo sample of each η_c channel to the event selection algorithm of a specific η_c channel. The number of events in the η_c signal region are counted and the total number of events, which were originally generated in another channel, is calculated. The results are summarized in table 13 without an additional weighting with the branching ratios of the respective channels. In the ideal case of no cross feed only entries on the diagonal of the table would be non zero as there reconstruction algorithm and simulated η_c final state match. As can be seen from the table, some off-diagonal entries are larger than zero which means that cross feed between those channels exists. The cross feed is dominated by the misidentification of pions as kaons. This is due to the fact that pions are not suppressed in the kaon sample during the particle identification. In addition, it can be seen that some cross feed is caused by the wrongly reconstruction of neutral pions and η particles, for example between the $K^+K^-\pi^0$ and $K^+K^-\eta$ channels. However, the cross feed is found to be smaller than 0.12% for all final states and can be neglected in the further analysis.

Monte Carlo sample	Analyzed η_c decay												
	$\pi^+\pi^-K^+K^-$	$2(K^+K^-)$	$2(\pi^+\pi^-)$	$3(\pi^+\pi^-)$	$K_sK^\pm\pi^\mp$	$K_sK^\pm\pi^\mp\pi^+\pi^-$	$K^+K^-\pi^0$	$K^+K^-\eta$	$\pi^+\pi^-\eta$	$\pi^+\pi^-\pi^0\pi^0$	$2(\pi^+\pi^-)\eta$	$2(\pi^+\pi^-\pi^0)$	$K^+K^-2(\pi^+\pi^-)$
$\pi^+\pi^-K^+K^-$	35404	0	0	0	1	0	0	0	0	0	0	0	0
$2(K^+K^-)$	0	17962	0	0	1	0	0	0	0	0	0	0	0
$2(\pi^+\pi^-)$	9	0	38195	0	4	0	0	0	0	0	0	0	0
$3(\pi^+\pi^-)$	4	0	0	57301	0	4	0	0	0	0	0	0	0
$K_sK^\pm\pi^\mp$	269	0	67	8	27200	0	0	0	0	0	0	0	0
$K_sK^\pm\pi^\mp\pi^+\pi^-$	0	0	0	0	0	26614	0	0	0	0	0	0	20
$K^+K^-\pi^0$	7	0	0	0	0	0	26915	191	0	2	0	0	0
$K^+K^-\eta$	0	0	0	0	0	0	55	26309	0	0	0	0	0
$\pi^+\pi^-\eta$	0	0	0	0	0	0	3	8	27113	34	0	0	0
$\pi^+\pi^-\pi^0\pi^0$	0	0	0	0	0	0	63	9	17	19457	0	7	0
$2(\pi^+\pi^-)\eta$	0	0	0	0	0	0	0	2	0	0	42205	127	0
$2(\pi^+\pi^-\pi^0)$	0	0	0	0	0	0	0	0	0	0	36	19793	0
$K^+K^-2(\pi^+\pi^-)$	0	2	0	0	0	0	0	0	0	0	0	0	41915
total [%]	0.12	0.01	0.03	0.01	0.01	0.01	0.05	0.08	0.01	0.01	0.01	0.05	0.01

Table 13: Cross feed between the analyzed η_c final states at a center of mass energy of 4.26 GeV. For each input $2.5 \cdot 10^5$ events were generated. The diagonal elements do not enter into the total cross feed and the different channels have not been weighted according to their branching ratios.

Background Estimation

The composition of the different inclusive Monte Carlo datasets has already been described in section 6. The total number of events in each dataset at a center of mass energy of 4.26 GeV together with the scaling factor which scales the generated number of background events to the recorded luminosity of the data set is shown in table 14.

Background Source	Events	Scaling Factor
Hadrons	$7.6 \cdot 10^5$	2.9
$q\bar{q}$	$3.25 \cdot 10^7$	2.2
ISR	$2.1 \cdot 10^6$	1.9
$D\bar{D}$	$5.7 \cdot 10^6$	1.4
γXYZ	$2.6 \cdot 10^5$	8.4
Others	$2.84 \cdot 10^8$	2.3

Table 14: Number of generated events in inclusive Monte Carlo datasets and their respective scaling to the size of the dataset at 4.26 GeV center of mass energy. The channels to $e^+e^- \rightarrow e^+e^-$, $\mu^+\mu^-$ and $\tau^+\tau^-$ have been summarized in the others category.

The number of remaining events of each background source after application of the event selection criteria are shown in table 15. The dominant contribution for all η_c final states

η_c final state	hadrons	$q\bar{q}$	ISR	DD	γXYZ	others
$\pi^+\pi^- K^+ K^-$	46	1530	3	80	0	0
$2(K^+K^-)$	3	31	0	2	0	0
$2(\pi^+\pi^-)$	49	1618	8	5	0	0
$3(\pi^+\pi^-)$	33	1078	7	25	4	0
$K_s K^\pm \pi^\mp$	6	264	1	16	0	0
$K_s K^\pm \pi^\mp \pi^+ \pi^-$	4	437	3	52	0	0
$K^+ K^- \pi^0$	18	459	4	26	1	0
$K^+ K^- \eta$	7	131	1	6	0	0
$\pi^+\pi^-\eta$	9	198	8	0	0	0
$\pi^+\pi^- 2\pi^0$	78	3041	8	20	6	0
$2(\pi^+\pi^-)\eta$	54	1536	4	10	0	0
$2(\pi^+\pi^-\pi^0)$	280	13174	51	193	21	0
$K^+ K^- 2(\pi^+\pi^-)$	39	336	8	50	0	0

Table 15: Background contributions to different η_c final states at a center of mass energy of 4.26 GeV. The channels $e^+e^- \rightarrow e^+e^-$, $\mu^+\mu^-$ and $\tau^+\tau^-$ have been summarized in the others category.

originates from the continuum $q\bar{q}$ process. In the case of the $2(\pi^+\pi^-)$, $3(\pi^+\pi^-)$, $\pi^+\pi^-\eta$, $\pi^+\pi^- 2\pi^0$, $2(\pi^+\pi^-)\eta$ and $2(\pi^+\pi^-\pi^0)$ final states it surpasses the other processes by two to three order of magnitude. e^+e^- to e^+e^-, $\mu^+\mu^-$ and $\tau^+\tau^-$ events are completely suppressed by the event selection. Attempts to suppress jet-like $q\bar{q}$ events by the usage of Fox-Wolfram moments [103] or the event sphericity [104] were not successful due to the small center of mass energy of 4.26 GeV. The distribution of the η_c invariant mass for all η_c candidates
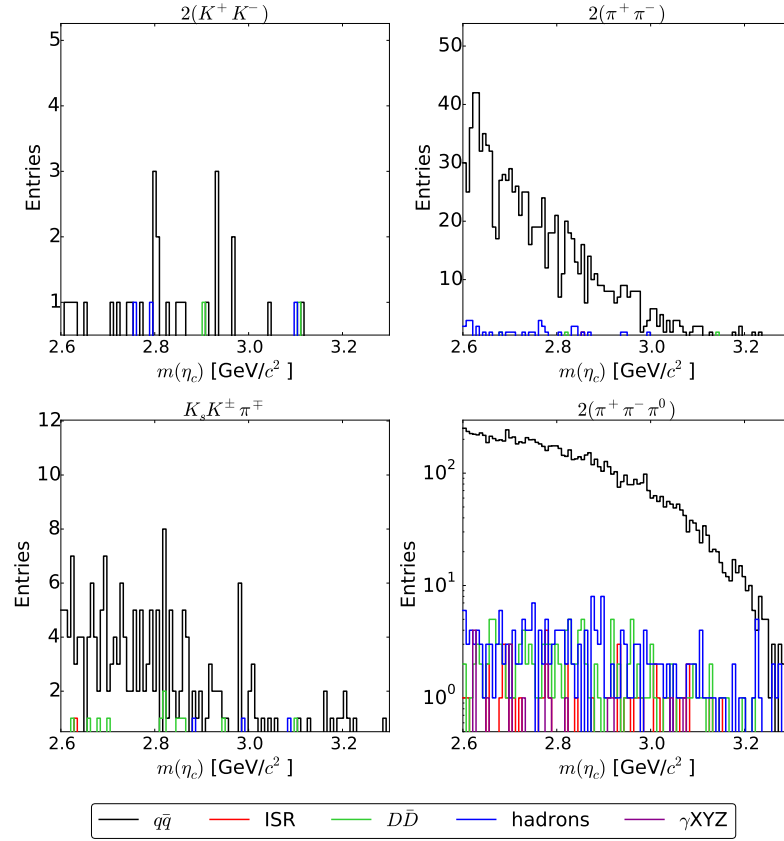
Figure 82: η_c candidate mass distribution at a center of mass energy of 4.26 GeV from inclusive Monte Carlo for the four exemplary selected η_c final states.

per event for the different background processes is shown in figure 82. The contributions from the different background sources appear to be smooth at the η_c invariant mass of 2.983 GeV/c^2 and no obvious peaking behavior can be seen.

7.2 η_c Reconstruction at Center of Mass Energies of 4.23 and 4.36 GeV

With the same methodology describe above signal Monte Carlo events generated at center of mass energies of 4.23 GeV and 4.36 GeV were analyzed. At both energies the cuts which had already been developed for 4.26 GeV have been used.

Correctness

The distribution of correctly reconstructed events at 4.23 GeV and 4.36 GeV for the two center of mass energies are shown in figure 83 and 84 respectively. The correctness stays approximately the same at the different center of mass energies, and the η_c invariant mass distributions of incorrectly reconstructed events stay smooth at the position of the η_c peak. The tables and figures summarizing the event correctness can be found in appendix D.
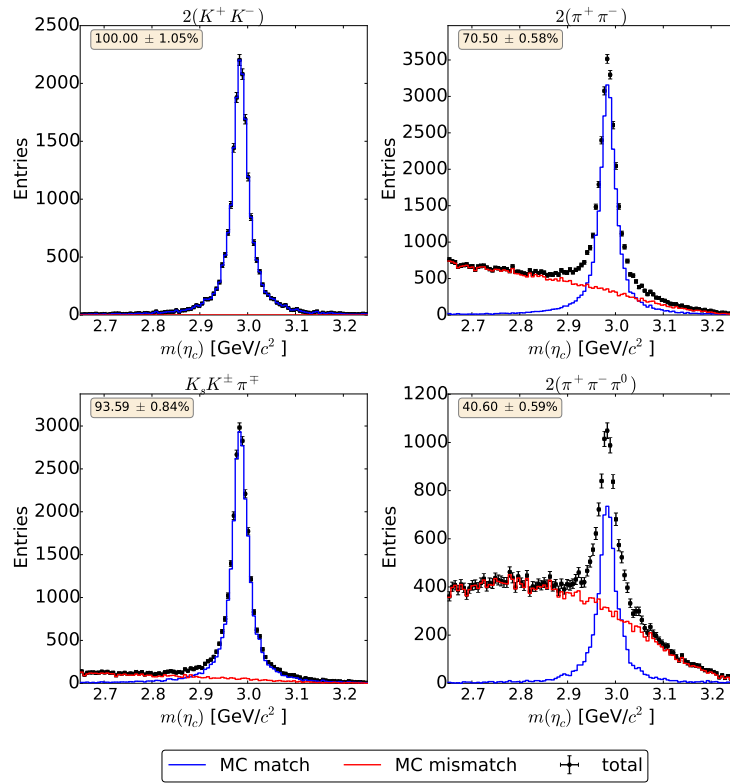
Figure 83: Distribution of the η_c invariant mass of the four exemplary selected η_c final states at a center of mass energy of 4.23 GeV separated into incorrectly and correctly reconstructed events.
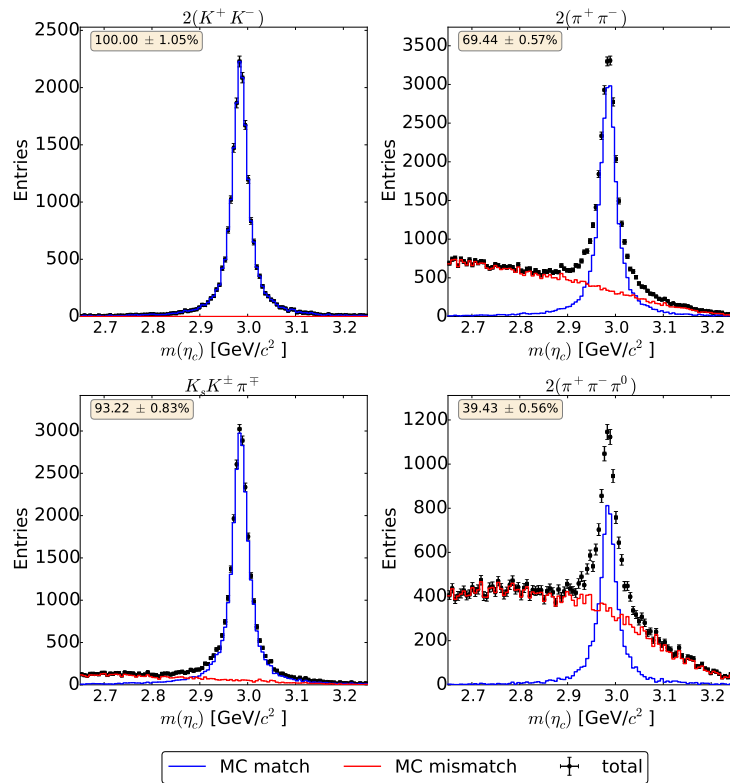

Figure 84: Distribution of the η_c invariant mass of the four exemplary selected η_c final states at a center of mass energy of 4.36 GeV separated into incorrectly and correctly reconstructed events.

Efficiency and Resolution

To extract the reconstruction efficiency and resolution, the reconstructed η_c mass is fitted with the function discussed in the previous section. The extracted efficiencies and resolution parameters at the center of mass energies of 4.23 GeV and 4.36 GeV are shown in the tables 16 and 17 respectively. The figures showing the fit results for all η_c final states can be found in appendix D. It can be seen that the reconstruction efficiency increases slightly for increasing center of mass energy. This is due to the increasing phase space which is available for the reaction. The shift and resolution estimated by the Gaussian resolution function stay in the same order of magnitude for all center of mass energies, and vary between 1-2 MeV/c^2 and 4-10 MeV/c^2 respectively.

η_c final state	Polynomial Order	Efficiency [%]	μ [MeV/c^2]	σ [MeV/c^2]
$\pi^+\pi^- K^+K^-$	3	11.30 ± 0.08	1.4 ± 0.2	5.6 ± 0.4
$2(K^+K^-)$	1	7.96 ± 0.06	1.7 ± 0.2	4.3 ± 0.5
$2(\pi^+\pi^-)$	3	11.63 ± 0.09	1.3 ± 0.2	4.0 ± 0.4
$3(\pi^+\pi^-)$	4	7.17 ± 0.09	1.4 ± 0.3	5.5 ± 0.7
$K_s K^\pm \pi^\mp$	2	10.98 ± 0.07	1.4 ± 0.2	4.5 ± 0.4
$K_s K^\pm \pi^\mp \pi^+\pi^-$	4	5.63 ± 0.07	1.4 ± 0.3	4.9 ± 0.7
$K^+K^-\pi^0$	1	11.78 ± 0.07	1.7 ± 0.2	6.9 ± 0.3
$K^+K^-\eta$	3	10.22 ± 0.087	1.6 ± 0.2	6.5 ± 0.4
$\pi^+\pi^-\eta$	3	10.16 ± 0.07	1.7 ± 0.2	6.6 ± 0.4
$\pi^+\pi^-\pi^0\pi^0$	4	6.70 ± 0.06	1.1 ± 0.2	8.5 ± 0.4
$2(\pi^+\pi^-)\eta$	4	6.49 ± 0.09	0.9 ± 0.3	6.1 ± 0.6
$2(\pi^+\pi^-\pi^0)$	4	3.21 ± 0.06	0.9 ± 0.4	8.0 ± 0.9
$K^+K^- 2(\pi^+\pi^-)$	4	5.11 ± 0.08	0.8 ± 0.4	6.3 ± 0.8

Table 16: Efficiency of the event reconstruction of $e^+e^- \to \eta_c\eta\pi^+\pi^-$ and η_c mass shift μ and mass resolution σ for different η_c final states at a center of mass energy of 4.23 GeV.

η_c final state	Polynomial Order	Efficiency [%]	μ [MeV/c^2]	σ [MeV/c^2]
$\pi^+\pi^-K^+K^-$	3	12.32 ± 0.09	1.6 ± 0.2	5.6 ± 0.4
$2(K^+K^-)$	1	8.58 ± 0.06	1.5 ± 0.2	4.0 ± 0.5
$2(\pi^+\pi^-)$	3	12.55 ± 0.09	1.6 ± 0.2	5.5 ± 0.4
$3(\pi^+\pi^-)$	4	7.88 ± 0.11	1.7 ± 0.3	5.4 ± 0.7
$K_s K^{\pm}\pi^{\mp}$	2	11.93 ± 0.08	2.0 ± 0.1	5.6 ± 0.4
$K_s K^{\pm}\pi^{\mp}\pi^+\pi^-$	4	6.16 ± 0.08	1.1 ± 0.3	5.0 ± 0.7
$K^+K^-\pi^0$	1	12.56 ± 0.05	1.9 ± 0.1	7.9 ± 0.1
$K^+K^-\eta$	3	11.17 ± 0.08	2.1 ± 0.2	6.9 ± 0.3
$\pi^+\pi^-\eta$	3	10.69 ± 0.08	1.9 ± 0.2	7.5 ± 0.4
$\pi^+\pi^-\pi^0\pi^0$	4	7.16 ± 0.07	1.6 ± 0.2	9.9 ± 0.4
$2(\pi^+\pi^-)\eta$	4	6.87 ± 0.09	1.7 ± 0.3	6.5 ± 0.7
$2(\pi^+\pi^-\pi^0)$	4	3.56 ± 0.06	1.0 ± 0.4	9.3 ± 0.7
$K^+K^-2(\pi^+\pi^-)$	4	5.60 ± 0.09	1.1 ± 0.3	3.9 ± 1.1

Table 17: Efficiency of the event reconstruction of $e^+e^- \to \eta_c\eta\pi^+\pi^-$ and η_c mass shift μ and mass resolution σ for different η_c final states at a center of mass energy of 4.36 GeV.

Background Analysis

The possible background event contributions at the center of mass energies of 4.23 GeV and 4.36 GeV have been studied with inclusive Monte Carlo datasets whose compositions are analogous to the inclusive Monte Carlo dataset at 4.26 GeV. The number of events in each subsample and their corresponding scaling factors to the recorded luminosity at each center of mass energy can be found in appendix D. The distributions of the η_c invariant mass of the remaining background events are depicted in figures 85 and 86. The dominating background contribution again arises from the continuum q$\bar{\text{q}}$ background. Like the background distributions at 4.26 GeV, the reconstructed distributions are smooth and no prominent structures can be seen.
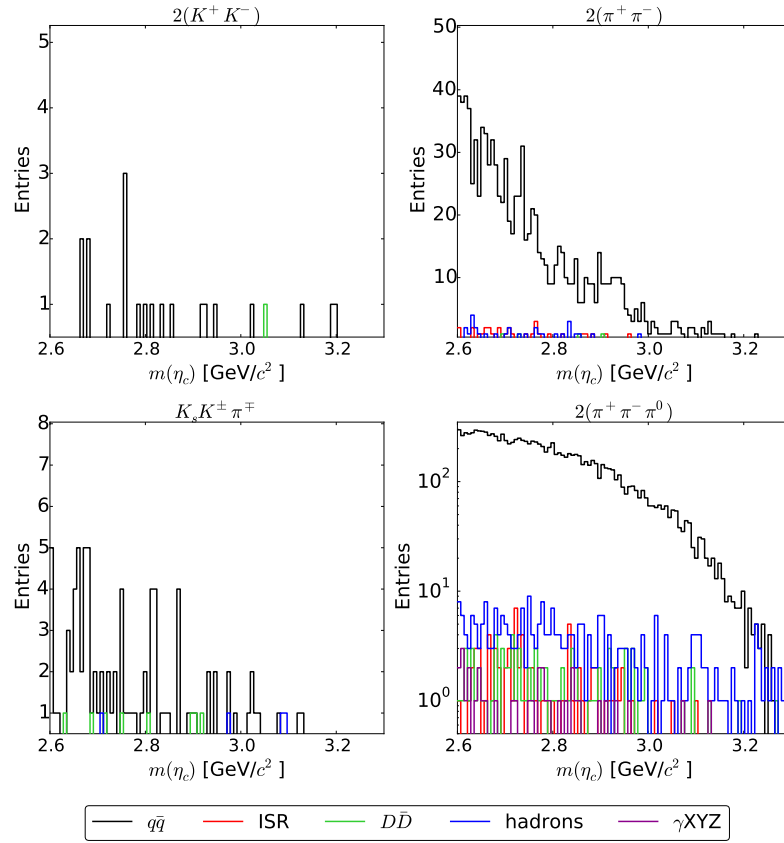
Figure 85: η_c candidate mass distribution at a center of mass energy of 4.23 GeV from inclusive Monte Carlo for the four exemplary selected η_c final states.
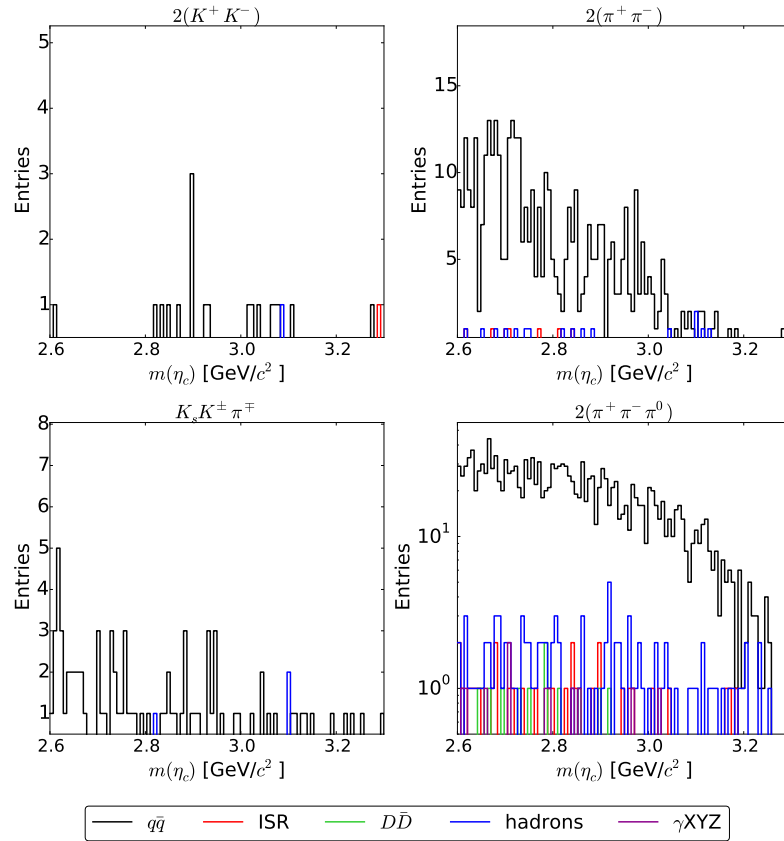

Figure 86: η_c candidate mass distribution at a center of mass energy of 4.36 GeV from inclusive Monte Carlo for the four exemplary selected η_c final states.

7.3 $\eta_c\eta$ and $\eta_c\pi^{\pm}$ Reconstruction at 4.26 GeV Center of Mass Energy

One aim of this study is to look for resonant structures in the $\eta_c\eta$ subsystem. Furthermore, the developed selection allows to study the $\eta_c\pi^{\pm}$ system while $\eta\pi^{\mp}$ acts as the recoil system. Because of this the correctness, efficiency, and resolution of the event reconstruction was also checked in these systems. The discussion of the subsystems is limited to the dataset at a center of mass energy of 4.26 GeV as it was found that the differences between the various center of mass energies are negligible.

To select correctly reconstructed η_c candidates, a mass window cut on the η_c candidate invariant mass is applied. The width of this window is identical with the previously defined η_c signal region

$$2.887 \text{ GeV}/c^2 < m_{\eta_c} < 3.080 \text{ GeV}/c^2.$$

Correctness

The event correctness was again checked by using informations from the Monte Carlo generator and checking the correct reconstruction of the complete event decay tree. The resulting mass distributions of the $\eta_c\eta$ and system $\eta_c\pi^{\pm}$ separated into matched and mismatched events are shown in the figures 87 and 88. In the case of the $\eta_c\eta$ system, the
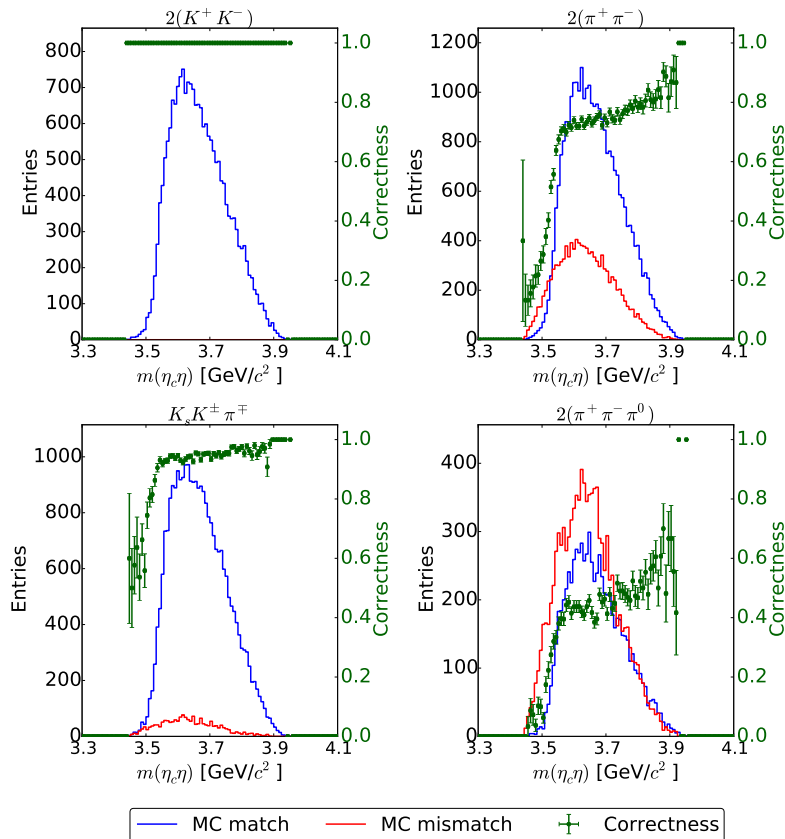

Figure 87: Bin wise reconstruction correctness of the $\eta_c\eta$ mass for the four exemplary selected η_c final states at a center of mass energy of 4.26 GeV. The correctness is shown on the right scale of the histograms.
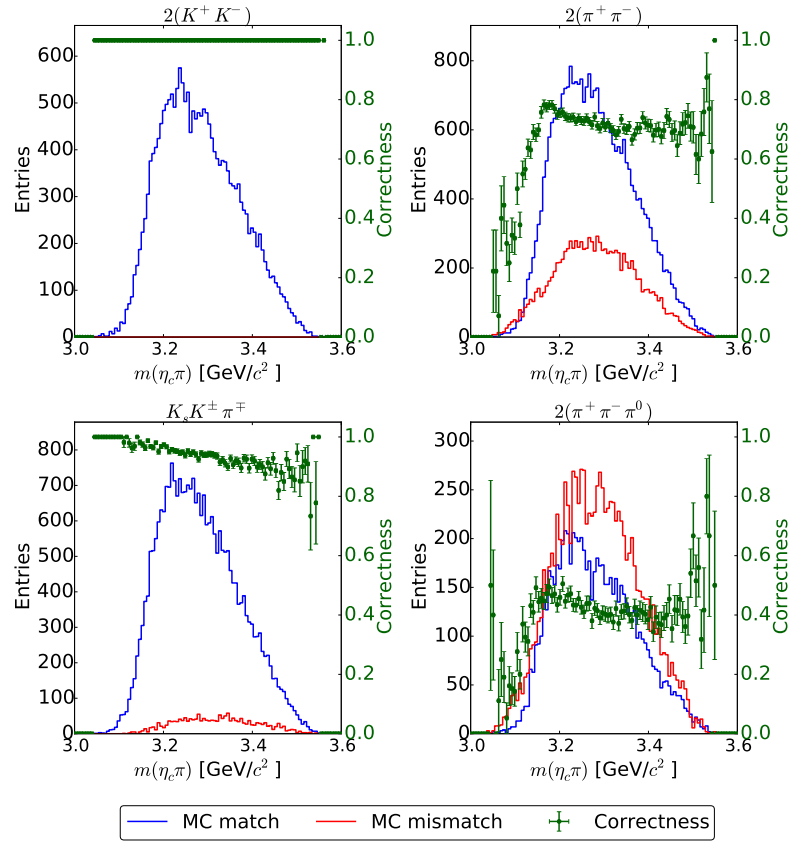
Figure 88: Bin wise reconstruction correctness of the $\eta_c\pi^{\pm}$ mass for the four exemplary selected η_c final states at a center of mass energy of 4.26 GeV. The correctness is shown on the right scale of the histograms.

matched distributions start at an $\eta_c\eta$ mass of roughly 3.5 GeV/c^2 which corresponds to the sum of the η_c and η rest masses

$$m_{\eta_c} + m_{\eta} = 2.983 \text{ GeV}/c^2 + 0.547 \text{ GeV}/c^2 = 3.530 \text{ GeV}/c^2.$$

The small tail towards lower masses is caused by the width of η_c resonance. The highest mass of the $\eta_c\eta$ system that can be reconstructed is at about 3.9 GeV/c^2. At this mass the momentum left for the $\pi^+\pi^-$ system is below 100 MeV/c and the pions can not be reconstructed properly anymore. Also shown in figures 87 and 88 is the bin wise reconstruction correctness which is defined as the ratio of entries in the matched and mismatched mass histograms at a given bin. In general the correctness starts to rise steeply at roughly 3.5 GeV/c^2 and then reaches a plateau where the correctness increases more slowly until 3.9 GeV/c^2. This behavior is only violated by the $2(K^+K^-)$, $K^+K^-\pi^0$ and $K^+K^-\eta$ final states of the η_c (see appendix D). The first two are always reconstructed correctly as there is no combinatorial background. In case of the $K^+K^-\eta$ combinatorial background is caused by exchanging the two η particles from the η_c and the prompt η produced at the interaction. Here the correctness is higher at low values of the $\eta_c\eta$ mass and then slowly decreases towards higher mass values.

The behavior of the correctness in the $\eta_c\pi$ is quite similar. It starts to rise around 3.1 GeV/c^2 and reaches a region where the correctness stays almost constant. Only a small declining tendency can be seen. In case of both systems the correctness is between 30% and 100%, and corresponds to the overall correctness reached for the reconstruction of the complete reaction channel.

Efficiency

Since the mass of an hypothetical resonance in the $\eta_c\eta$ and $\eta_c\pi$ subsystems is unknown and no theoretical predictions exist, no resonance was simulated in both subsystems. Therefore, an extraction of the efficiency with the fitting method used for the complete reaction channel by fitting the η_c mass distribution is not feasible. Instead a bin wise reconstruction efficiency is calculated. The efficiency in each bin is given by

$$\varepsilon = \frac{\text{number of reconstructed events}}{\text{number of simulated events}}. \tag{7.2}$$

In the case that multiple candidates are accepted by the event selection, a single candidate is randomly selected. The reconstruction efficiency for the $\eta_c\eta$ subsystem is shown in figure 91. It should be noted that the displayed efficiencies also include wrongly reconstructed
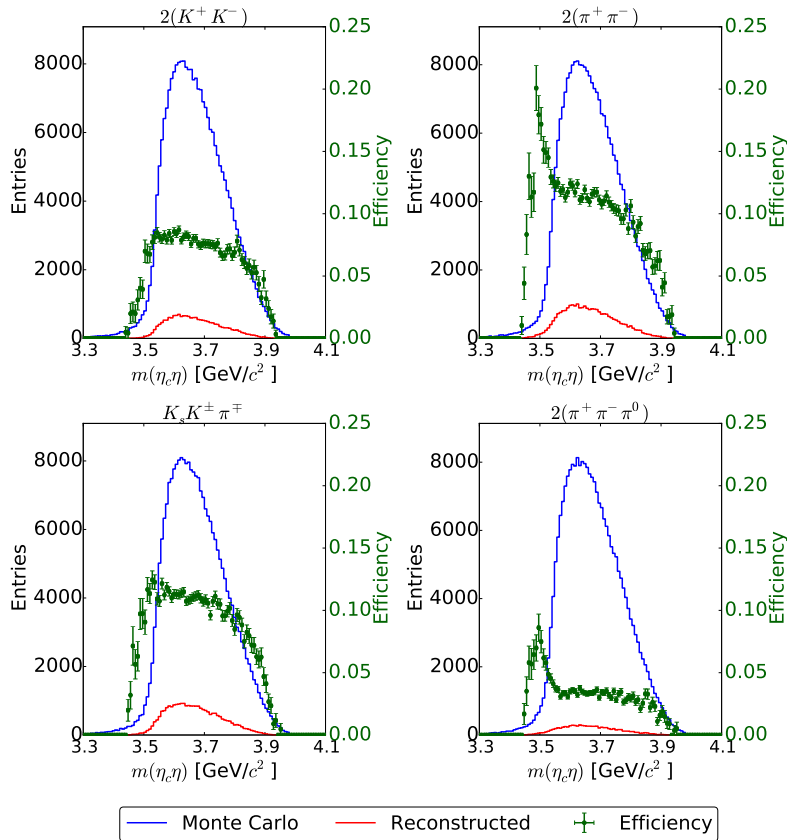

Figure 89: Bin wise reconstruction efficiency of the $\eta_c\eta$ mass for the four exemplary selected η_c final states at center of mass energy of 4.26 GeV. The efficiency is shown on the right scale of the histograms.

events. Depending on the number of multiple candidates also the wrong combination can be chosen as they cannot be separated by their event signature in the detector, and will appear for real data as well. In case of η_c final states without additional pions the efficiency stays flat until an $\eta_c\eta$ mass of 3.9 GeV/c^2 where the efficiency drops off. If the η_c decays into final states that include further pions, the efficiency curves show a step rise at masses lower than 3.5 GeV/c^2. This is due to the asymmetric invariant mass distribution of the mismatched η_c candidates. However, between 3.5 GeV/c^2 and 3.9 GeV/c^2 the efficiencies are smooth and no peaks are observed. Only a slight declining behavior can be seen. The reconstruction efficiency of the $\eta_c\pi$ subsystem (see figure 90) shows an analogue behavior. Although the peaking characteristic at small $\eta_c\pi$ masses is lower than for the $\eta_c\eta$ system. In addition the declining behavior of the efficiency is not as pronounced.
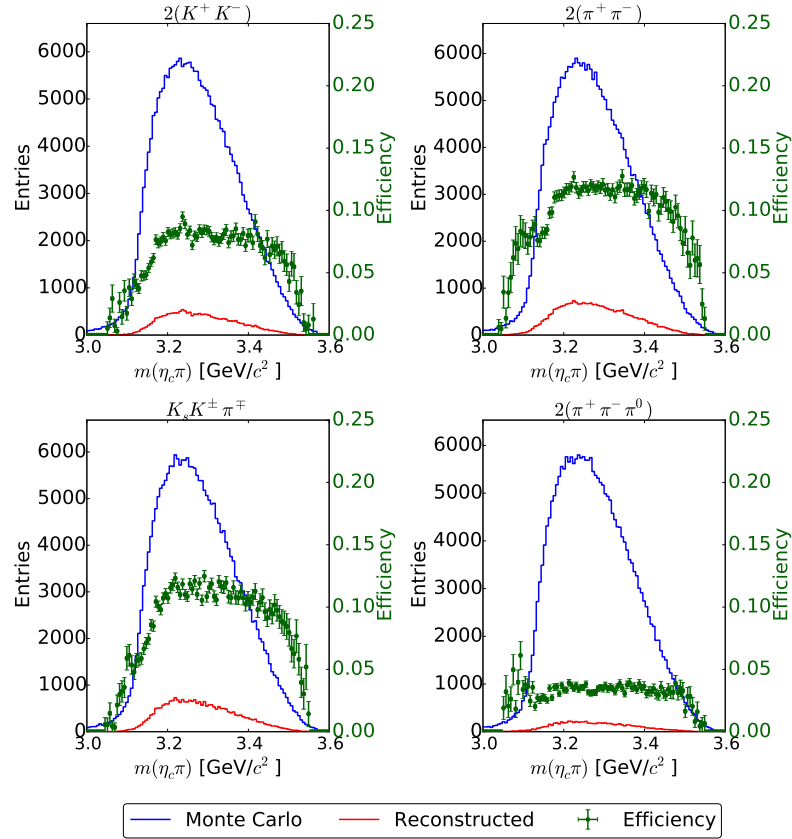
Figure 90: Bin wise reconstruction efficiency of the $\eta_c\eta$ mass for the four exemplary selected η_c final states at center of mass energy of 4.26 GeV. The efficiency is shown on the right scale of the histograms.

Resolution

The resolution of the $\eta_c\eta$ and $\eta_c\pi^\pm$ invariant masses are estimated by fitting the residuals of the generated and reconstructed masses of both subsystems. It is found that the sum of two Gaussian functions has to be used as resolution function in order to describe the distributions of the residuals. The combinatorial background is modeled by a second order Chebychev polynomial. The fitted distributions are shown in figures 91 and 92. The distributions are asymmetric and show a tail in the direction of higher reconstructed masses. This tail is modeled by the second Gaussian. Except for this tail, the reconstructed masses are centered around 0 MeV/c^2 in the case of the $\eta_c\eta$ system since the mass shift, which has been previously observed in η_c system, is canceled by the η particle. The mass shift of the central Gaussian in the case of the $\eta_c\pi^\pm$ system, on the other hand, is smaller than 1.5 MeV/c^2. The resolution, which is defined as the width of the central Gaussian, is better than 2.5 MeV/c^2 for the central Gaussian in the case of the $\eta_c\eta$ system and is slightly worse in the case of the $\eta_c\pi^\pm$ system where it is typically 1 MeV/c^2 higher. The reason for this is the larger phase space that is available to the $\eta_c\pi^\pm$ system. This leads to higher momenta of the involved particles which in turn increases the uncertainty on the reconstructed momentum and, therefore, the momentum and mass resolution.
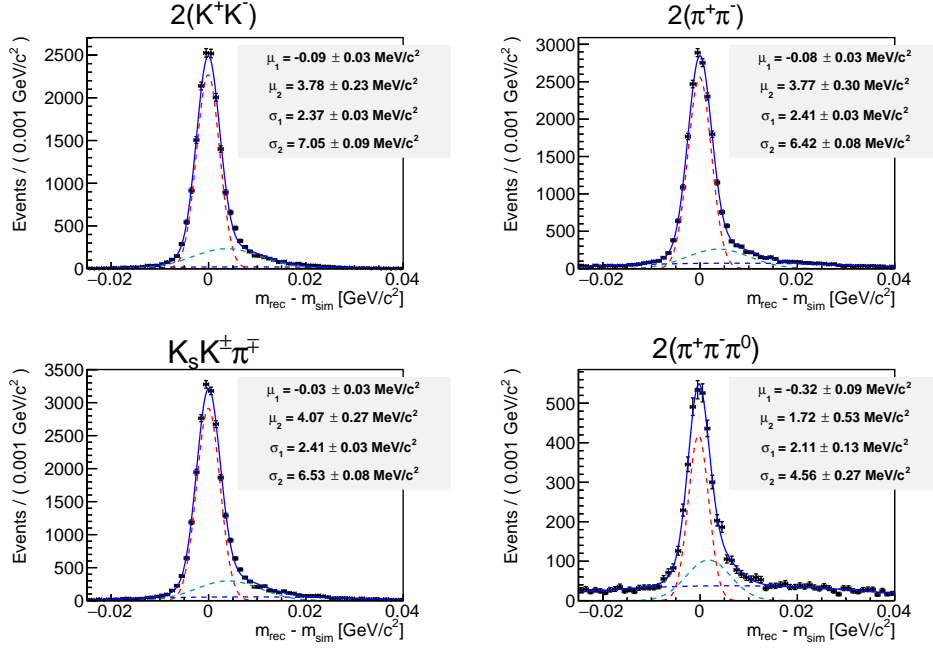
Figure 91: Residuals of the $\eta_c\eta$ mass for the four exemplary selected η_c final states at a center of mass energy of 4.26 GeV. The blue curve represents the total fit while the two Gaussian functions are drawn as dashed red and cyan lines. The blue dashed line shows the second order Chebychev polynomial. The parameters of the double Gaussian used to fit the resolution are shown in each plot.
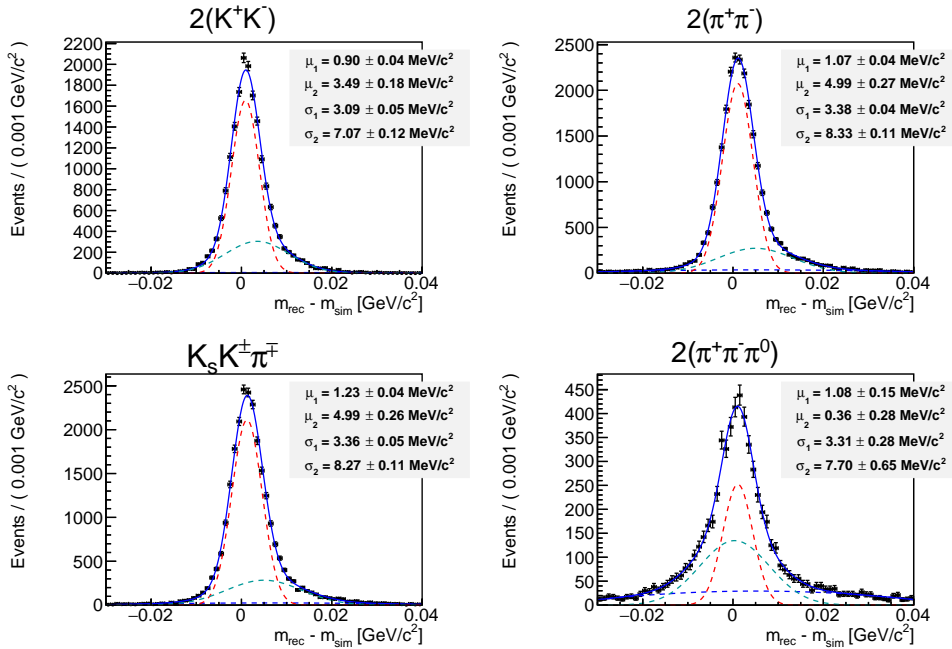

Figure 92: Residuals of the $\eta_c\pi^{\pm}$ mass for the four exemplary selected η_c final states at a center of mass energy of 4.26 GeV. The blue curve represents the total fit while the two Gaussian functions are drawn as dashed red and cyan lines. The blue dashed line shows the second order Chebychev polynomial. The parameters of the double Gaussian used to fit the resolution are shown in each plot.

Background Estimation

To complete the studies of the $\eta_c\eta$ and $\eta_c\pi^{\pm}$ subsystems the possible background contributions are estimated with the inclusive Monte Carlo dataset which was already introduced above. The invariant mass distributions of the different background channels of the $\eta_c\eta$ and $\eta_c\pi^{\pm}$ systems after application of the event selection and the η_c mass window are depicted in figures 93 and 94. As can be expected, the background distributions are again
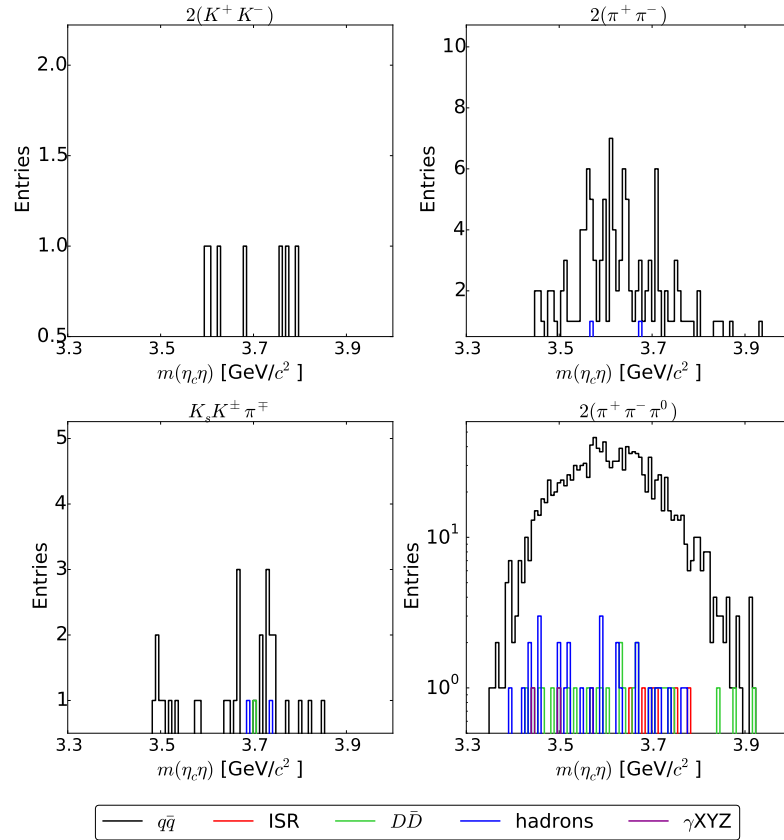

Figure 93: $\eta_c\eta$ candidate mass distribution from inclusive Monte Carlo for the four exemplary selected η_c final states at a center of mass energy of 4.26 GeV.

dominated by continuum $q\bar{q}$ events which spread across the allowed mass range. With the available statistics no clear peaking structures can be seen. Judging from this, the reconstruction efficiency and resolution discussed above, a search for substructures in the $\eta_c\eta$ and $\eta_c\pi^{\pm}$ subsystems seems feasible.
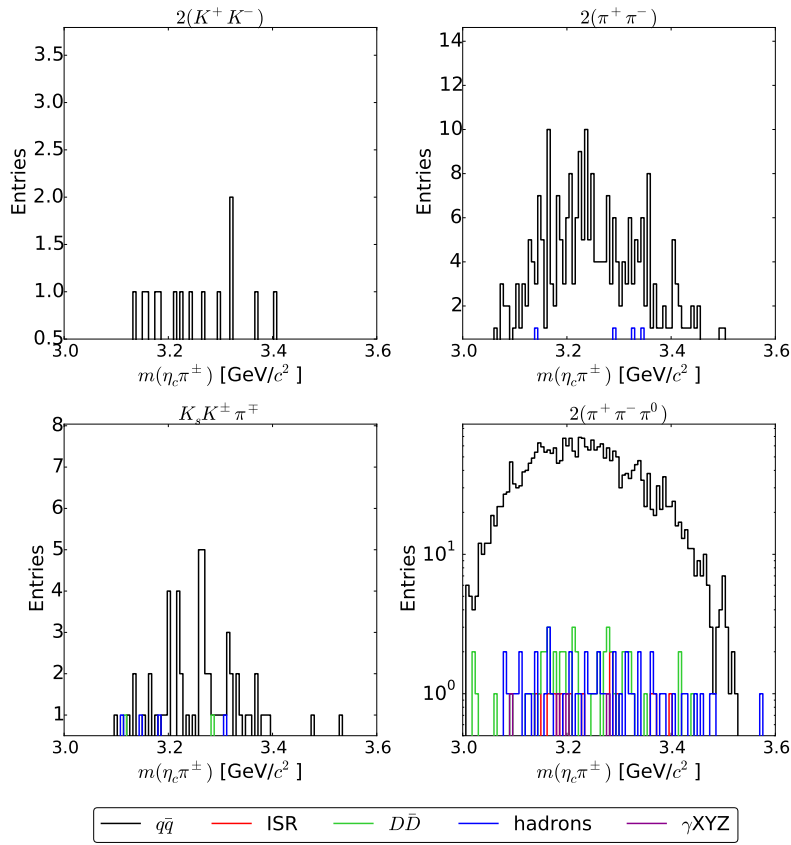
Figure 94: $\eta_c \pi^\pm$ candidate mass distribution from inclusive Monte Carlo for the four exemplary selected η_c final states at a center of mass energy of 4.26 GeV.

8

ESTIMATION OF AN UPPER LIMIT FOR $e^+e^- \to \eta_c \eta \pi^+ \pi^-$

8.1 Results of Data Analysis

With the event selection described in sections 6.2 and 6.3, the available data sets at center of mass energies of 4.23 GeV, 4.26 GeV and 4.36 GeV are analyzed. The invariant mass distributions are shown in figures 95, 96, and 97. As can be seen, the number of entries vary greatly between the analyzed channels. Unfortunately, the channels with the highest branching ratios of the η_c $(2(\pi^+\pi^-\pi^0), 2(\pi^+\pi^-)\eta$, and $\pi^+\pi^-2\pi^0)$ also show the largest background contributions. Other channels like $K_s K^\pm \pi^\mp$ have only moderate contributions from background events. Neither of the analyzed channels, however, shows a clear signal at the η_c mass.

To extract the cross section of the reaction $e^+e^- \to \eta_c \eta \pi^+ \pi^-$ for each center of mass energy a simultaneous maximum likelihood fit to all 13 invariant mass spectra of the different η_c final states is performed. During the fit the total number n_{total} of observed η_c candidates is related to the cross section σ via

$$n_{total} = \text{BR}(\eta \to \gamma\gamma)\, \mathcal{L}\, \sigma \tag{8.1}$$

where $\mathcal{L}$ is the integrated luminosity and $\text{BR}(\eta \to \gamma\gamma)$ is the branching ratio of η to two photons. The integrated luminosities are summarized in table 8. The number of η_c candidates in each sub-channel is given by

$$n_X = \varepsilon(\eta_c \to X)\, \text{BR}(\eta_c \to X)\, n_{total} \tag{8.2}$$

with $\varepsilon(\eta_c \to X)$ being the reconstruction efficiency of the η_c decay to the final state X, which is extracted from the study with Monte Carlo datasets, and $\text{BR}(\eta_c \to X)$ the corresponding branching ratio taken from table 9. If an η_c final state contains further unstable particles, e.g. a K_s decaying to $\pi^+\pi^-$, the branching ratios of these decays are taken from the PDG [1] and are included as well. The fit function is described in equation 7.1. It is constructed as the sum of a Breit-Wigner function convoluted with Gaussian resolution function and a Chebychev polynomial which accounts for background for every η_c final state. The mean and width of the Breit-Wigner are fixed to the nominal values from the PDG. The parameters of the Gaussian resolution function were extracted from signal Monte Carlo datasets, and are taken from table 12 for the center of mass energies of 4.26 GeV. The corresponding tables for 4.23 GeV and 4.36 GeV can be found in appendix D. For the majority of final states a second order Chebychev polynomial is chosen. Exceptions are the $2(K^+K^-)$, $K^+K^-\eta$, and $\pi^+\pi^-2\pi^0$ final states where a linear background function is used. This was done since the fits showed only a small dependence on the coefficient of the second order term for this datasets which leads to instabilities during the fitting procedure. For the $2(\pi^+\pi^-\pi^0)$ final state, on the other hand, a third order Chebychev polynomial is needed to describe the background distribution.

Figures 95, 96, and 97 also show the result of the simultaneous fit. The estimated values for the cross section are

$$\sigma_{4.23 \text{ GeV}} = -3.89^{+3.41}_{-3.01} \text{ pb}$$
$$\sigma_{4.26 \text{ GeV}} = -1.04^{+4.22}_{-3.66} \text{ pb}$$
$$\sigma_{4.36 \text{ GeV}} = 6.44^{+7.26}_{-6.77} \text{ pb.}$$

The errors are purely statistical and are calculated using the MINOS tool [105]. It calculates the one-dimensional confidence interval for a parameter of interest θ in the presence of nuisance parameters ν by calculating the two values of θ for which

$$\max_{\nu} \ln L(\theta, \nu) = \ln L(\hat{\theta}, \hat{\nu}) - \lambda.$$

Here $\hat{\theta}$ and $\hat{\nu}$ are the values that maximize the log-likelihood L, and λ is equal to 0.5 for a confidence interval with 68% coverage.

As no significant signal is observed, an upper limit on the cross sections will be calculated in the next sections. For the estimation of an upper limit, a scan of likelihood as a function of the signal cross section is used (see section 8.3). As the probability density function of the $2(K^+K^-)$ final state returns negative values during this scan, which results in malfunctions from RooFit, it was removed from the simultaneous fit. Without the $2(K^+K^-)$ final state, the following values for the cross section are obtained:

$$\sigma_{4.23 \text{ GeV}} = -3.97^{+3.42}_{-3.04} \text{ pb}$$
$$\sigma_{4.26 \text{ GeV}} = -1.65^{+4.19}_{-3.65} \text{ pb}$$
$$\sigma_{4.36 \text{ GeV}} = 7.86^{+7.38}_{-6.97} \text{ pb.}$$

They agree with the cross sections where the $2(K^+K^-)$ is included in the fit within their respective errors.

In the figures 98 and 99 the summed $\eta_c\eta$ and $\eta_c\pi^{\pm}$ invariant mass distributions of all analyzed η_c final states are depicted. Only events with an η_c invariant mass within the signal region are accepted. No clear peaking structures are observed at the different center of mass energies.
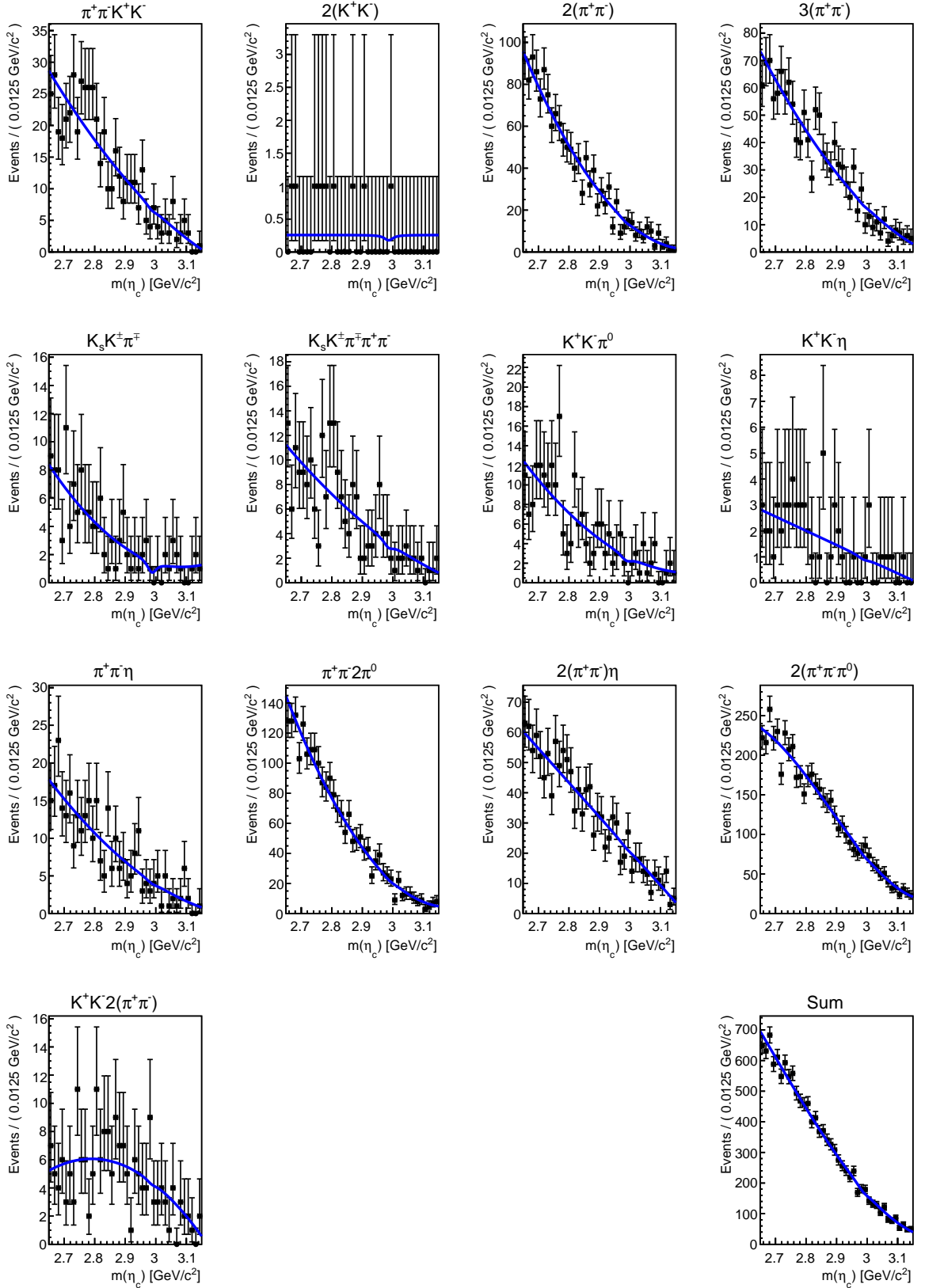
Figure 95: Reconstructed η_c invariant mass distributions from data at $\sqrt{s} = 4.23$ GeV. The black points show the Selected data, and the blue line the result of the simultaneous maximum likelihood fit to all 13 η_c final states.

Figure 96: Reconstructed η_c invariant mass distributions from data at $\sqrt{s} = 4.26$ GeV. The black points show the Selected data, and the blue line the result of the simultaneous maximum likelihood fit to all 13 η_c final states.

Figure 97: Reconstructed η_c invariant mass distributions from data at $\sqrt{s} = 4.36$ GeV. The black points show the Selected data, and the blue line the result of the simultaneous maximum likelihood fit to all 13 η_c final states.
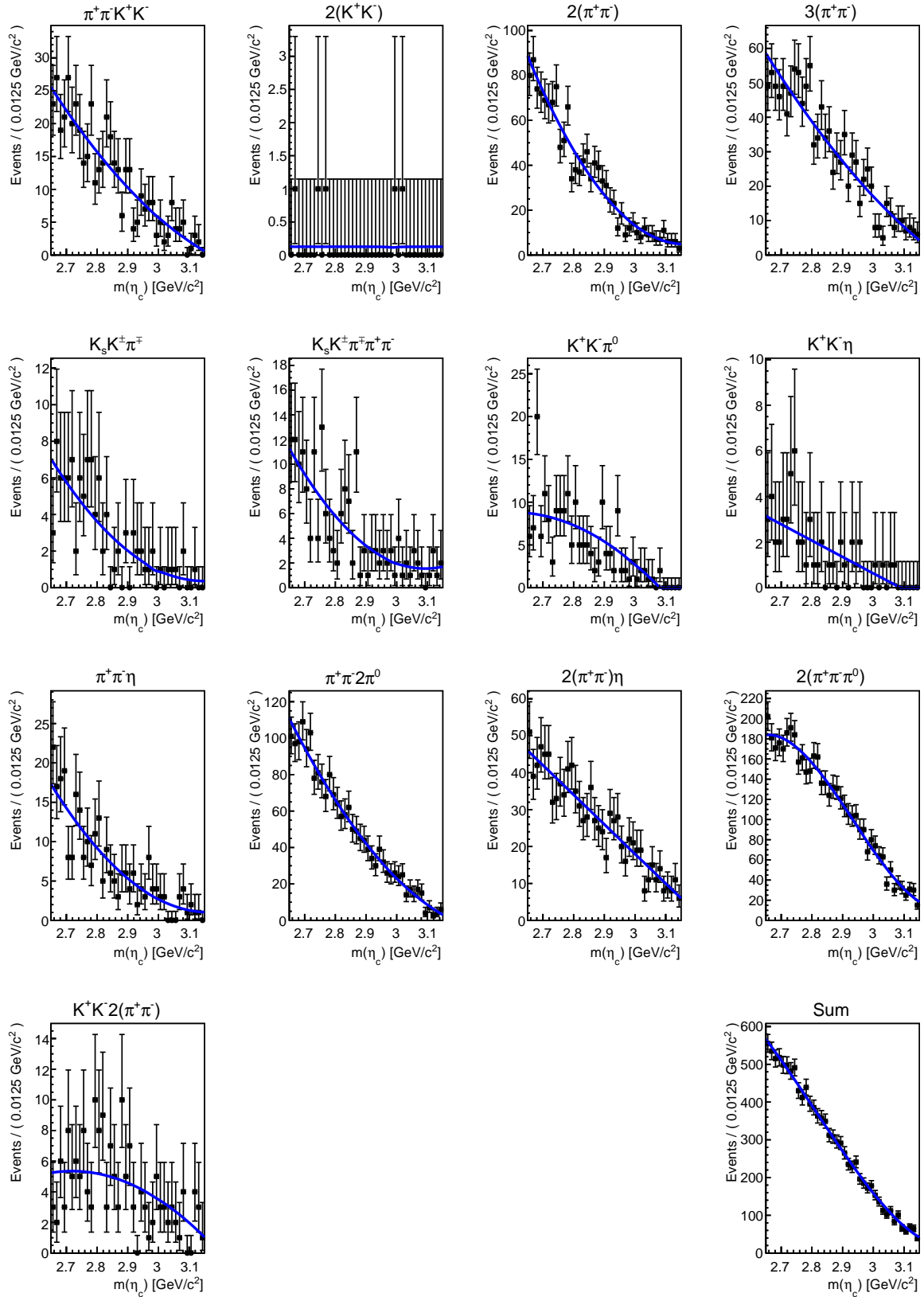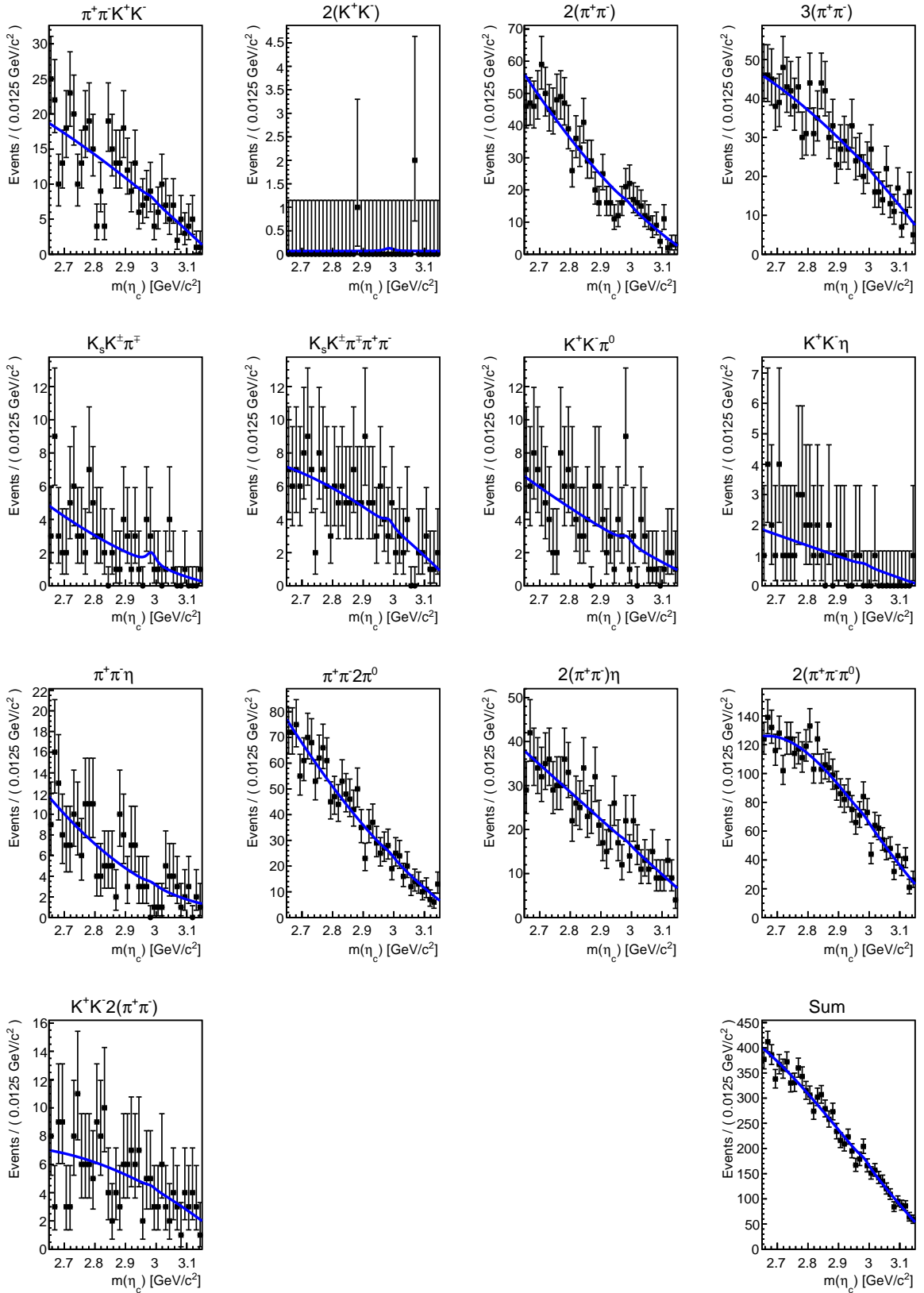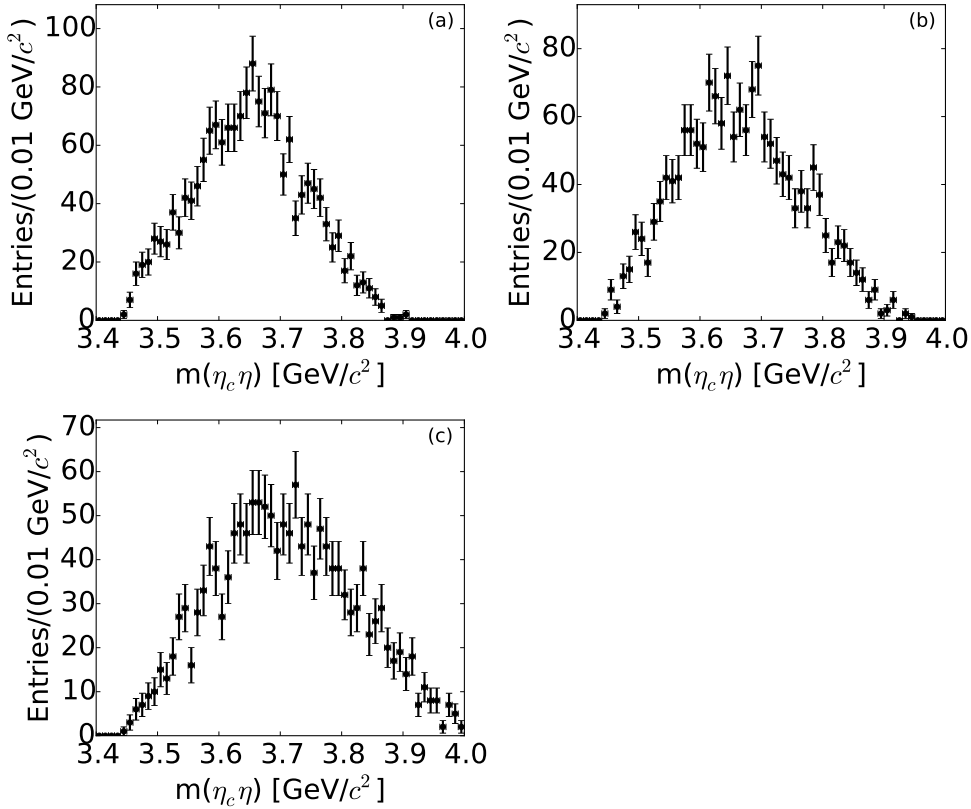
Figure 98: Reconstructed invariant mass distribution of the $\eta_c\eta$ system from data at $\sqrt{s} = 4.23$ GeV (a), $\sqrt{s} = 4.26$ GeV (b), and $\sqrt{s} = 4.36$ GeV (c).
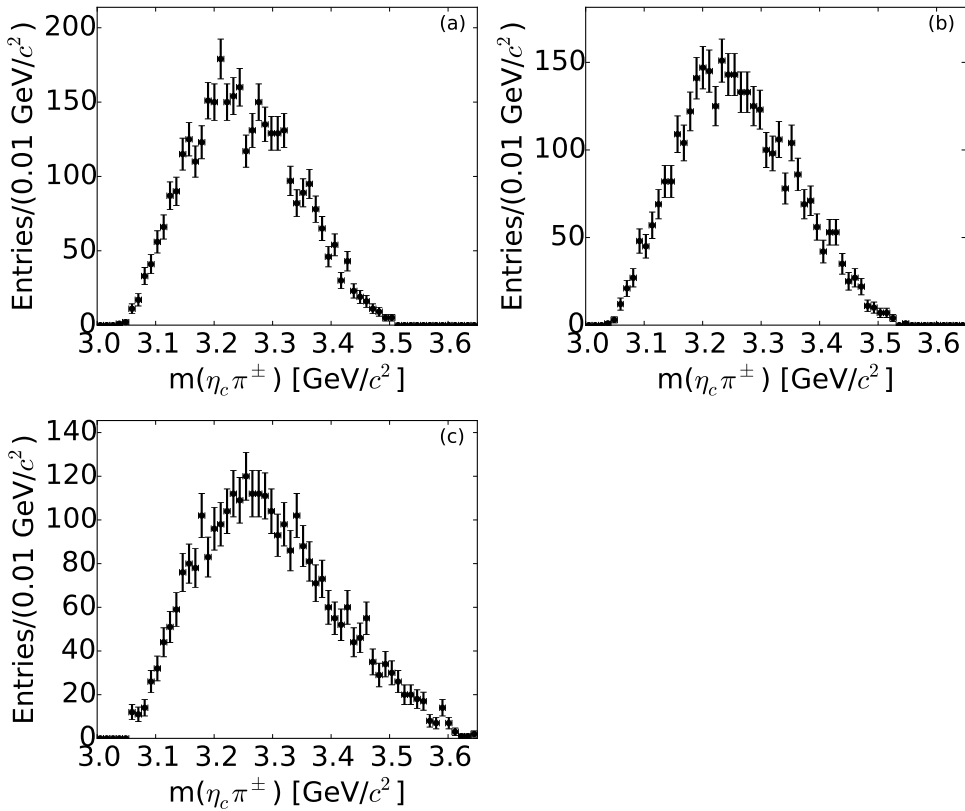

Figure 99: Reconstructed invariant mass distribution of the $\eta_c\pi^\pm$ system from data at $\sqrt{s} = 4.23$ GeV (a), $\sqrt{s} = 4.26$ GeV (b), and $\sqrt{s} = 4.36$ GeV (c).

8.2 Systematic Uncertainties

In this section the systematic uncertainties relevant for the cross section measurement and the upper limit estimation are studied. It should be noted that the $2(K^+K^-)$ final state of the η_c has been excluded from the simultaneous fit for this studies.

Fit Bias

The fit is tested for a possible bias by fitting the data distribution with the fit model used in the section above. The resulting background description is used to generate toy data. The number of generated events is chosen according to the number of events found in the data. In addition, artificial signals have been superimposed on the background toy data. The generated distributions are then fitted with the complete fit model and the value of the signal cross section is extracted. This procedure is repeated 500 times with different toy datasets. The means of the resulting distributions are reported in table 18, while figure 100 shows the distribution of the fitted cross section for an input cross section of 10 pb.

σ_{in} [pb]	$\sigma^{4.23\ GeV}$ [pb]	$\sigma^{4.26\ GeV}$ [pb]	$\sigma^{4.36\ GeV}$ [pb]
0	-0.13	-0.42	-0.64
10	9.34	9.15	10.02
20	19.94	19.00	19.56
30	29.88	28.95	29.88

Table 18: Mean of the cross section distributions after 500 toy fits for different values of the artificial cross sections at the three center of mass energies under study.

The largest bias is observed at a center of mass energy of 4.26 GeV. The bias, however, stays below 10% of the nominal cross section value and is small compared to the overall statistical uncertainty. Therefore, it can safely be ignored for the remaining studies.

Fit Range

The influence of the η_c mass range used during the fit is studied by narrowing and increasing the range of the fit by 5 MeV/c^2. The narrow range, therefore, is given by $2.655\ \text{GeV}/c^2 < m_{\eta_c} < 3.145\ \text{GeV}/c^2$ while the wider range is defined as $2.645\ \text{GeV}/c^2 < m_{\eta_c} < 3.155\ \text{GeV}/c^2$. The systematic uncertainty is calculated by taking the square root of the quadratic sum of the deviations from the nominal fit result. The result of this study are given in table 19.

$\sqrt{s}$ [GeV]	σ_{wide}[pb]	σ_{narrow} [pb]	σ_{sys} [pb]	σ_{sys} [%]
4.23	$-4.31^{+3.41}_{-3.01}$	$-4.13^{+3.38}_{-3.02}$	0.37	9.4
4.26	$-1.59^{+4.11}_{-3.52}$	$-0.62^{+4.31}_{-3.72}$	1.03	62.5
4.36	$7.97^{+7.36}_{-6.80}$	$10.62^{+7.19}_{-7.66}$	2.73	34.6

Table 19: Values of the cross section for narrow and wide fit ranges and resulting systematic uncertainty σ_{sys}.
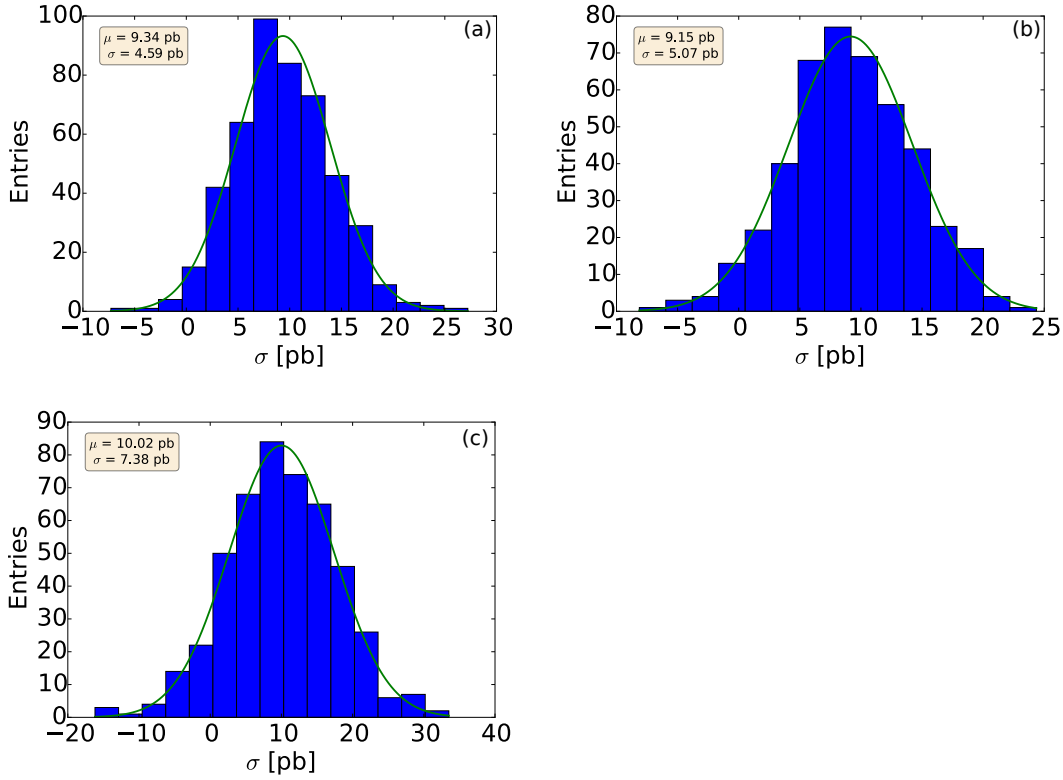
Figure 100: Distribution of the fitted cross section for 500 toy fits using an input cross section of 10 pb at $\sqrt{s} = 4.23$ GeV (a), $\sqrt{s} = 4.26$ GeV (b), and $\sqrt{s} = 4.36$ GeV (c).

Background Shape

The systematic uncertainty due to the description of the background shape by Chebychev polynomials is estimated by increasing the order of the polynomials by one for every η_c final state. The difference between the cross section obtained with this fit, and the nominal background shape is taken as systematic uncertainty. The uncertainty at the different center of mass energies is given in table 20.

$\sqrt{s}$ [GeV]	σ_{fit} [pb]	σ_{sys} [pb]	σ_{sys} [%]
4.23	$-3.06^{+3.74}_{-3.45}$	0.91	22.9
4.26	$-3.25^{+4.12}_{-3.62}$	1.60	96.9
4.36	$11.85^{+8.11}_{-7.46}$	3.96	50.2

Table 20: Value of the cross section σ_{fit} for fit with higher order background Chebychev polynomials and resulting systematic uncertainty σ_{sys}.

η_c Parameters

During the simultaneous fit the mean and width of the Breit-Wigner are fixed to the values given by the particle data group [1]. To account for the uncertainty of these values, 1000 fits are performed. For each toy dataset new values for the mean and width of the η_c are randomly generated from two independent Gaussian probability distributions before each fit. The mean of these Gaussian distributions is set to the values given by the particle data group for the η_c parameter in question. The width of the probability distributions is equal

to the respective measurement uncertainty by the measurement as indicated by the PDG. The standard deviations of the resulting cross section distributions are taken as systematic uncertainty. The uncertainty at the different center of mass energies is summarized in table 21.

$\sqrt{s}$ [GeV]	μ [pb]	σ_{sys} [pb]	σ_{sys} [%]
4.23	-3.97	0.17	4.3
4.26	-1.69	0.12	7.3
4.36	7.84	0.22	2.8

Table 21: Mean and standard deviation of the cross section distribution for varying values of the η_c position and width (for distribution see figure 119 in appendix E).

η_c Branching Ratio

The branching ratios used as input to the simultaneous fit are taken from a BESIII measurement [100], where the following relation was used for the calculation of the η_c branching ratios

$$\text{BR}(\eta_c \to X) = \frac{\text{BR}(\psi' \to \pi^0 h_c; h_c \to \gamma\eta_c; \eta_c \to X)}{\text{BR}(\psi' \to \pi^0 h_c; h_c \to \gamma\eta_c)}. \tag{8.3}$$

$\text{BR}(\psi' \to \pi^0 h_c; h_c \to \gamma\eta_c)$ is obtained by combining two measurements of BESIII [106] and CLEO [107]. Hence, the measured branching ratios of $\eta_c \to X$ are correlated. To take these correlations into account, random numbers are generated independently for the nominator and denominator. The random numbers are drawn from Gaussian distributions. The mean of each Gaussian distribution is set to the measured branching ratio while the width of the Gaussian distribution is set to the total uncertainty of the branching ratio measurement (see table 6 in [100]). For each toy fit first a random number for the denominator is drawn, and then random numbers for each η_c finals state in the nominator are calculated. From this the 12 input branching fractions for the fit are derived. In total 1000 fits are performed at each center of mass energy. The standard deviation of the resulting cross section distribution are taken as systematic uncertainty (see table 22). As the branching

$\sqrt{s}$ [GeV]	μ [pb]	σ_{sys} [pb]	σ_{sys} [%]
4.23	-3.92	0.79	19.9
4.26	-1.69	0.72	43.6
4.36	7.63	1.51	19.2

Table 22: Mean and standard deviation of the cross section distribution for different values of the η_c branching ratios (for distribution see figure 120 in appendix E).

ratios of the other unstable particles (η, π^0, and K_{s}) are measured much more precisely than the η_c branching ratios, no toy fits were performed to study their influence on the extracted cross section.

Reconstruction Efficiency

The systematic uncertainty on the global reconstruction efficiency has different sources like uncertainties in the description of the track reconstruction efficiency in the Monte

Carlo simulation or the photon reconstruction efficiency. The systematic uncertainty of the tracking efficiency for charged particles has been estimated to be 1% per track by the BESIII data quality group. The systematic uncertainty on the photon detection has been studied using the missing momentum and the π^0 decay angle method [108]. For the former the control sample $\psi' \to \pi^+\pi^- J/\psi$ with $J/\psi \to \rho^0\pi^0$ is used. The missing momentum of a photon is calculated and used to predict the direction and energy of the photon. The latter method uses a $J/\psi \to \rho^0\pi^0$ control sample. Since the π^0 decays via a two body decay, the expected energy distribution of the photons can be predicted. Both methods measure the difference between data and signal Monte Carlo to be smaller than 1%. The systematic uncertainty due to the π^0 and η reconstruction are estimated in [109] using the control samples $J/\psi \to \pi^+\pi^-\pi^0$ and $J/\psi \to \eta p\bar{p}$. The systematic uncertainty is found to be 1% per π^0/η. The systematic uncertainty on the K_s reconstruction has been estimated to be 1.2% using the control samples $J/\psi \to K^*(892)^{\pm}K^{\mp}$ with $K^*(892)^{\pm} \to K_s\pi^{\pm}$ and $J/\psi \to \phi K_s K^{\pm}\pi^{\mp}$ [110].

To study the influence of this systematic uncertainties, the reconstruction efficiency estimated using signal Monte Carlo datasets (see section 7.1) is multiplied with a factor α which is given by

$$\alpha = (\kappa_T)^{n_T} (\kappa_P)^{n_P} (\kappa_{\pi^0/\eta})^{n_{\pi^0/\eta}} (\kappa_{K_s})^{n_{K_s}} \tag{8.4}$$

where n is the number of tracks, photons etc. for the individual η_c final state. Each κ is drawn from a Gaussian probability distribution with mean equal to one and the width set to the value of the corresponding uncertainty, e.g. 1%, in order to simulate the deviation from the nominal value of the efficiency. Each κ is determined globally for one iteration of the toy study and used for all final states. This procedure is repeated 1000 times which means that 1000 different global efficiencies are calculated for each η_c final state. The standard deviation of the resulting cross section distribution is taken as a systematic error. The result is shown in table 23.

$\sqrt{s}$ [GeV]	μ [pb]	σ_{sys} [pb]	σ_{sys} [%]
4.23	-3.98	0.30	7.5
4.26	-1.68	0.14	8.4
4.36	7.86	0.52	6.6

Table 23: Mean and standard deviation of the cross section distribution for different values of the η_c reconstruction efficiency (for distribution see figure 121 in appendix E).

Luminosity Measurement

The integrated luminosity is determined by using Bhabha events. The systematic uncertainty of the luminosity measurement has been measured in [111] and a relative uncertainty of 1% is given.

Total Systematic Uncertainty

Under the assumption that the systematic uncertainties are uncorrelated, the total systematic uncertainty is calculated as the square root of the quadratic sum of the systematic uncertainties discussed above. The total systematic uncertainty for the center of mass energies investigated in this thesis are given in table 24 together with a complete listing of all systematic uncertainties taken into account. As can be seen, the total systematic un-

source	$\sigma_{sys}^{4.23\text{ GeV}}$	$\sigma_{sys}^{4.26\text{ GeV}}$	$\sigma_{sys}^{4.36\text{ GeV}}$
Fit Range	0.37 pb	1.03 pb	2.73 pb
Background Shape	0.91 pb	1.60 pb	3.96 pb
η_c parameters	4.3%	7.3%	2.8%
η_c branching ratio	19.9%	43.6%	19.2%
Reconstruction Efficiency	7.5%	8.4%	6.6%
Luminosity	1.0%	1.0%	1.0%
total	1.30 pb	2.04 pb	5.11 pb

Table 24: Total systematic uncertainty at the studied center of mass energies. The systematic uncertainty due to the fit range and background shape are given as absolute values while the remaining contributions are given in percent.

certainty is dominated by the shape of the background and the fit range. The final result for the cross section measurement including the systematic errors is, therefore, given by

$$\sigma_{4.23\text{ GeV}} = -3.97^{+3.42}_{-3.04} \pm 1.30 \,\text{pb}$$
$$\sigma_{4.26\text{ GeV}} = -1.65^{+4.19}_{-3.65} \pm 2.04 \,\text{pb}$$
$$\sigma_{4.36\text{ GeV}} = 7.86^{+7.38}_{-6.97} \pm 5.11 \,\text{pb}.$$

8.3 Upper Limit

As no significant value for the cross section of $e^+e^- \to \eta_c\eta\pi^+\pi^-$ was found, an upper limit on the cross section is calculated. Following an Bayesian approach, the upper limit θ^{up} on a parameter θ at the confidence level C is given by

$$C(\theta^{up}) = \frac{\int_{-\infty}^{\theta^{up}} L(\theta)\pi(\theta)d\theta}{\int_{-\infty}^{\infty} L(\theta)\pi(\theta)d\theta}, \tag{8.5}$$

where L is the likelihood function and $\pi(\theta)$ the prior distribution, i.e. some prior knowledge about the distribution of the parameter θ [112]. Making the assumption that the prior distribution for the cross section σ can not assume negative values and is constant for all values larger than zero, equation 8.5 modifies to

$$C(\sigma^{up}) = \frac{\int_{0}^{\sigma^{up}} L(\sigma)d\sigma}{\int_{0}^{\infty} L(\sigma)d\sigma}. \tag{8.6}$$

This definition is equivalent with choosing an upper limit θ^{up} in a way that the probability of finding a value $\theta > \theta^{up}$ is smaller than $1 - C$

$$P(\theta > \theta^{up}) < 1 - C.$$

To obtain the likelihood curve in dependence of the signal cross section, the calculated negative log-likelihood of the fit minimizer is evaluated for different values of the cross section using RooFit. From this the likelihood curve is calculated by shifting the minimum

of the obtained log-likelihood curve to zero and taking the exponential. With this method the following values for the upper limit at 90% confidence level are obtained

$$\sigma^{up}_{4.23\text{ GeV}} = 3.16\,\text{pb}$$
$$\sigma^{up}_{4.26\text{ GeV}} = 5.19\,\text{pb}$$
$$\sigma^{up}_{4.36\text{ GeV}} = 16.21\,\text{pb}.$$

The corresponding likelihood curves are depicted in figure 101. The curves reach their respective maximum at the fitted value of the cross section given in section 8.1.
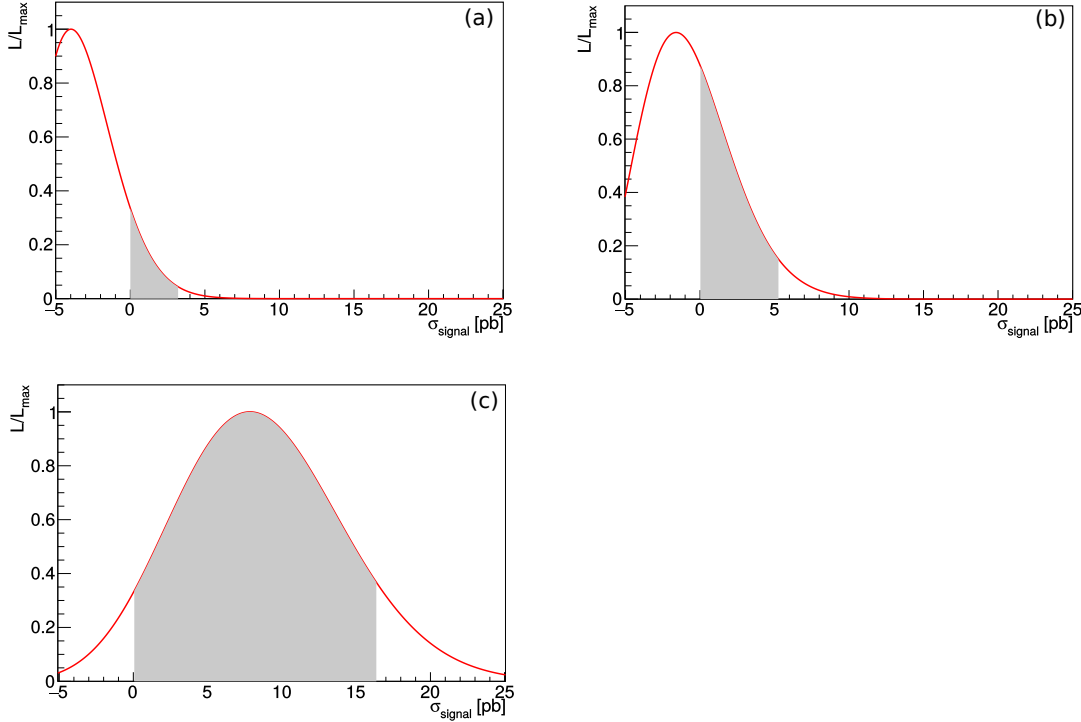

Figure 101: Likelihood curves for the cross section σ for $\sqrt{s} = 4.23$ GeV (a), $\sqrt{s} = 4.26$ GeV (b), and $\sqrt{s} = 4.36$ GeV (c). The interval equivalent with an upper limit at 90% confidence level is indicated as gray area.

As the likelihood curve only includes the statistical uncertainty on the cross section measurement, the systematic uncertainties have to be included by convolving the likelihood function with a Gaussian distribution whose width is set to the size of the total systematic uncertainty derived in section 8.2. Because of this, the likelihood in 8.6 is replaced by the term

$$L_{\text{sys}}(\sigma) = \int\limits_{-\infty}^{\infty} L(\sigma') \cdot G(\sigma'|\sigma, \sigma_{\text{sys}})d\sigma'. \tag{8.7}$$

The convoluted curves including the systematic uncertainties for the studied center of mass energies are shown in figure 102.

The calculated upper limits at 90% confidence level for the cross section of $e^+e^- \to \eta_c\eta\pi^+\pi^-$ are:

$$\sigma^{up}_{4.23\text{ GeV}} = 3.47\,\text{pb}$$
$$\sigma^{up}_{4.26\text{ GeV}} = 5.98\,\text{pb}$$
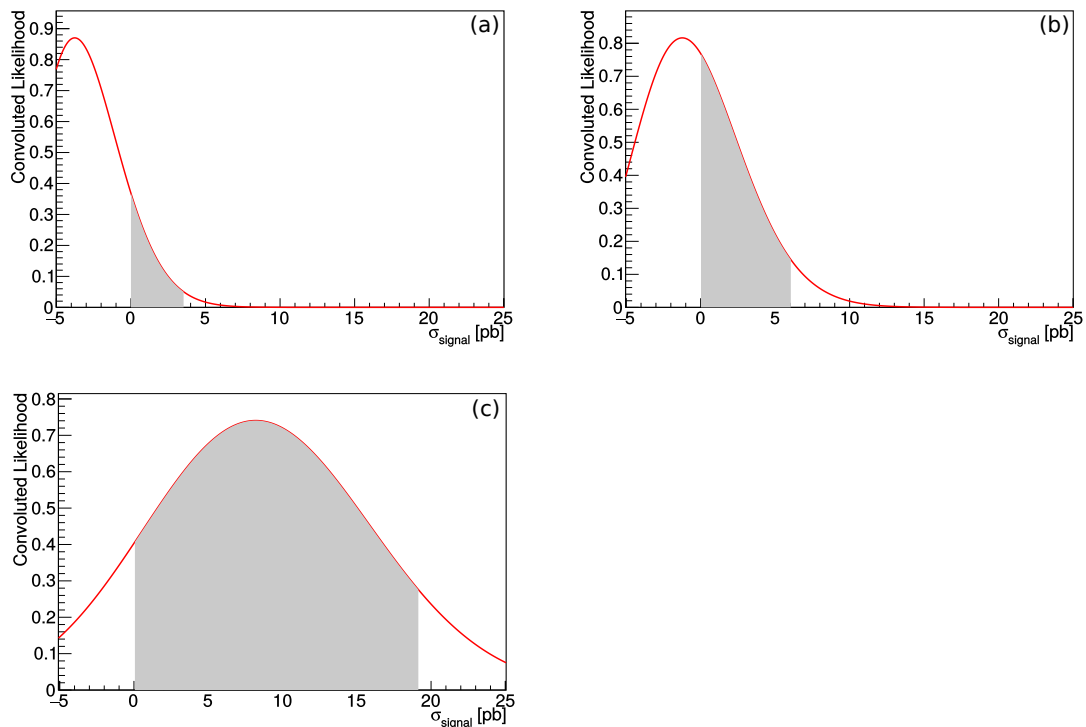$$\sigma^{up}_{4.36\text{ GeV}} = 19.02\,\text{pb}.$$

Figure 102: Likelihood curves convoluted with the Gaussian function representing the systematic uncertainties as a function of the cross section σ for $\sqrt{s} = 4.23$ GeV (a), $\sqrt{s} = 4.26$ GeV (b), and $\sqrt{s} = 4.36$ GeV (c). The interval equivalent with an upper limit at 90% confidence level is indicated as gray area.

8.4 Comparison with other Processes

In table 25 the measured cross sections for the processes $e^+e^- \to J/\psi\pi^+\pi^-$ and $e^+e^- \to h_c\pi^+\pi^-$ are summarized for the three studied center of mass energies. As can be seen the

Decay	$\sqrt{s} = 4.23$ GeV	$\sqrt{s} = 4.26$ GeV	$\sqrt{s} = 4.36$ GeV
$e^+e^- \to h_c\pi^+\pi^-$	50.2 ± 9.5 pb	41.0 ± 7.9 pb	52.3 ± 10.2 pb
$e^+e^- \to J/\psi\pi^+\pi^-$	85.3 ± 5.2 pb	60.1 ± 3.9 pb	23.3 ± 1.9 pb
$e^+e^- \to \eta_c\eta\pi^+\pi^-$	<3.47 pb	<5.98 pb	<19.02 pb

Table 25: Cross sections comparison with the processes $e^+e^- \to h_c\pi^+\pi^-$ and $e^+e^- \to J/\psi\pi^+\pi^-$ at the studied center of mass energies. The given errors combine the statistical and systematical uncertainties. Values are taken from [39] and [113] respectively.

upper limits for the cross section of $e^+e^- \to \eta_c\eta\pi^+\pi^-$ are in the same order of magnitude. There are two possible reasons why no signal has been seen in this analysis. Firstly, the reaction which is searched for does not exist. Secondly, the signature of the decay is too complex to be resolved easily in the detector. In the case of the other two processes, however, intermediate narrow resonances like the J/ψ or h_c are part of the analyzed decay chain which help to reduce the number of background events.

As the reaction $e^+e^- \to h_c\pi^+\pi^-, h_c \to \gamma\eta_c$ only differs by one additional photon from the decay analyzed in this work, the developed event reconstruction was adopted to select the reaction $e^+e^- \to h_c\pi^+\pi^-$. The invariant mass distributions of the selected η_c and h_c candidates are shown in figure 103.
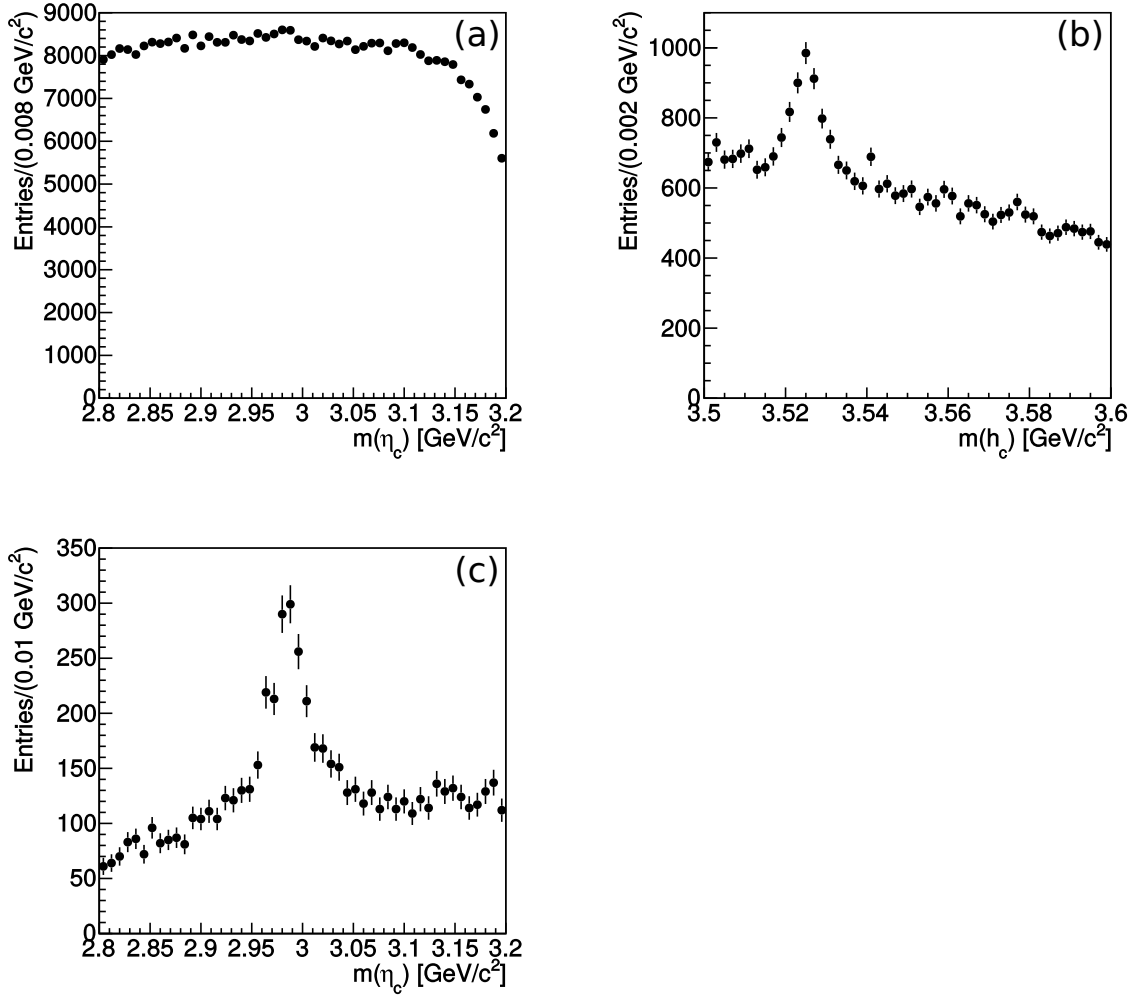
Figure 103: η_c mass from $e^+e^- \to h_c\pi^+\pi^-$ using the combined dataset at $\sqrt{s} = 4.23$ GeV and $\sqrt{s} = 4.26$ GeV. (a) η_c invariant mass distribution. (b) h_c invariant mass distribution. (c) η_c invariant mass distribution after cut on h_c mass.

As can be seen, no clear η_c signal is observed after the selection of the required track and photon multiplicities, and kinematic fitting. On the other hand the h_c is visible as a narrow resonance at a mass of $3.52 \text{ GeV}/c^2$. To improve the selection of the η_c, an additional cut on the h_c mass is employed. Figure 103c shows the η_c invariant mass where all h_c candidates fulfill the cut

$$3.518 \text{ GeV}/c^2 < m_{h_c} < 3.538 \text{ GeV}/c^2.$$

The η_c can now be seen as a peak around the nominal η_c mass. This shows that an additional handle is required to select possible η_c candidates in the reaction $e^+e^- \to \eta_c\eta\pi^+\pi^-$ from the concurring background events.

9
SUMMARY

In the last years new, charmonium-like states like the $X(3872)$ and the $Z_c(3900)$ have been discovered. Their properties suggest that these particles are not composed of a quark antiquark pair, but have a more complex internal structure. Measuring their properties and searching for additional new states is essential to clarify their structure and to solve many open question of QCD. The BESIII experiment in Beijing and the future PANDA experiment at Darmstadt play a leading role in this field of physics. BESIII offers the possibility to search for new states in the charmonium mass region with its high statistic datasets. PANDA will use a high quality antiproton beam to search for new resonances in the antiproton-proton annihilation process. Furthermore, PANDA measure the line shape and transitions of resonances with high precision to unravel their nature like for example in the case of the X(3872).

PANDA will determine the resonance line shapes by means of the energy scan method. During the extraction of a line shape from the scan data, the luminosity enters as a normalization factor and hence as a systematic uncertainty. For this reason, PANDA will use a dedicated luminosity detector to measure the luminosity with high precision. The luminosity detectors consists of four layers of novel high-voltage monolithic active pixel sensors (HV-MAPS). Prototypes of these sensors, which are called MuPix, have been characterized in Mainz. In order to do this, a test setup and a complete data acquisition system consisting of components which are suitable to be used in the final PANDA detector has been built. The performance of the sixth version of the MuPix prototype sensor has been measured with radioactive sources and lasers in the laboratory. In addition a tracking station has been built to quantify the efficiency of the MuPix sensor in two beam tests at the MAMI accelerator. The analogue performance and spatial resolution meet the requirements of the PANDA luminosity detector. The signal-to-noise ratio is in the order of 10 for 1 GeV electrons while the spatial resolution is in the order of 30 μm which is in good agreement with theory. The measured efficiency of 96.8% at a noise rate of 2.04 Hz per pixel do not fully coincide with the requirement of nearly 100% efficiency. The signal-to-noise ratio and efficiency, however, have been shown to improve with the seventh iteration of the MuPix chip which uses LVDS links that are less susceptible to cross talk and pickup noise than the currently used single ended signals. In addition, the usage of higher bias voltages in the order of 120 V are discussed which would further increase the signal-to-noise ratio and hence the efficiency.

As next steps the existing test setup has to be adopted to the LVDS-readout of the MuPix 7 prototype. This prototype houses the full analogue and digital part of the final MuPix sensor and has to be characterized during test beams and in the laboratory. In addition, its radiation hardness has to be investigated. Furthermore, the online GPU[1] trigger system of the luminosity detector, which is currently under development, needs to be integrated into the existing DAQ system.

---

1 Graphics Processing Unit

The $Z_c(3900)$ triplet was found by the BESIII collaboration in the reaction $e^+e^- \rightarrow J/\psi\pi\pi$ at a center of mass energy of 4.26 GeV. Its discovery suggest the existence of the yet unobserved triplet $\eta_c\pi^{\pm,0}$. If such a triplet is found, also the $\eta_c\eta$ singlet should exist. In this work the $\eta_c\eta$ singlet was searched for in the reaction $e^+e^- \rightarrow \eta_c\eta\pi^+\pi^-$. The reaction was exclusively reconstructed in twelve η_c decay modes at center of mass energies between 4.23 GeV and 4.36 GeV. The signal cross section has been estimated from the selected η_c mass distributions using a simultaneous maximum likelihood fit. The estimated cross sections are:

$$\sigma_{4.23 \text{ GeV}} = -3.97^{+3.42}_{-3.04} \pm 1.30 \, \text{pb}$$
$$\sigma_{4.26 \text{ GeV}} = -1.65^{+4.19}_{-3.65} \pm 2.04 \, \text{pb}$$
$$\sigma_{4.36 \text{ GeV}} = 7.86^{+7.38}_{-6.97} \pm 5.11 \, \text{pb}$$

where the first error gives the statistical uncertainty while the second error summarizes the systematic uncertainties. As no significant value of the signal cross section has been observed in the η_c mass region, an upper limit at 90% confidence level on the reaction cross section has been calculated to be 3.47 pb, 5.98 pb, and 19.02 pb at the center of mass energies 4.23, 4.26, and 4.36 respectively. The estimated upper limits have a comparable order of magnitude like the similar processes $e^+e^- \rightarrow h_c\pi^+\pi^-$ and $e^+e^- \rightarrow J/\psi\pi^+\pi^-$ which have been measured at BESIII, too.

In the future the search can be extended to the high statistic datasets at 4.42 GeV and 4.6 GeV of BESIII. Furthermore, within our group a second search for the isospin singlet state $J/\psi\eta$ is performed in the reaction channel $e^+e^- \rightarrow J/\psi\eta\eta$ and within BESIII a group searches for the isospin triplet which is decaying to $\eta_c\pi$ using the reactions $e^+e^- \rightarrow \eta_c\pi^+\pi^-$, $\eta_c\pi^+\pi^-\pi^0$ and $\eta_c\pi^0\gamma$. In addition the $Z(4051)$ and $Z(4248)$ are searched for in the reaction $e^+e^- \rightarrow \chi_{c1(c2)}\pi^+\pi^-$ using datasets collected by BESIII.

A

SEMICONDUCTORS

Energy Band Structure

Semiconductors are crystals made out of elements of the fourth main group of the periodic table like silicon or germanium. Mixed crystal systems build of elements from the third and fifth main group (e.g. gallium arsenide) are possible, too. In these crystals all valence electrons contribute to the covalent binding between the atoms. The periodic superposition of the wave functions of the close lying atoms gives rise to a discrete energy band structure. The lowest lying unoccupied energy band is called conduction band while the highest lying occupied band is referred to as valence band. Electrons in the valence band are bound and can not move, while electrons can freely propagate in the conduction band. Both bands can be separated by a forbidden energy gap where the probability density function of the electrons is zero.

The electronic properties of a material are defined by the width of this energy gap. The simplified band structures of metals, semiconductors and insulators are shown in figure 104. E_F denotes the Fermi level and the probability of an electron to occupy a state with energy E is given by the Fermi-Dirac statistics

$$P(E) = \frac{1}{e^{\frac{E-E_F}{k_b T}} + 1} \tag{A.1}$$

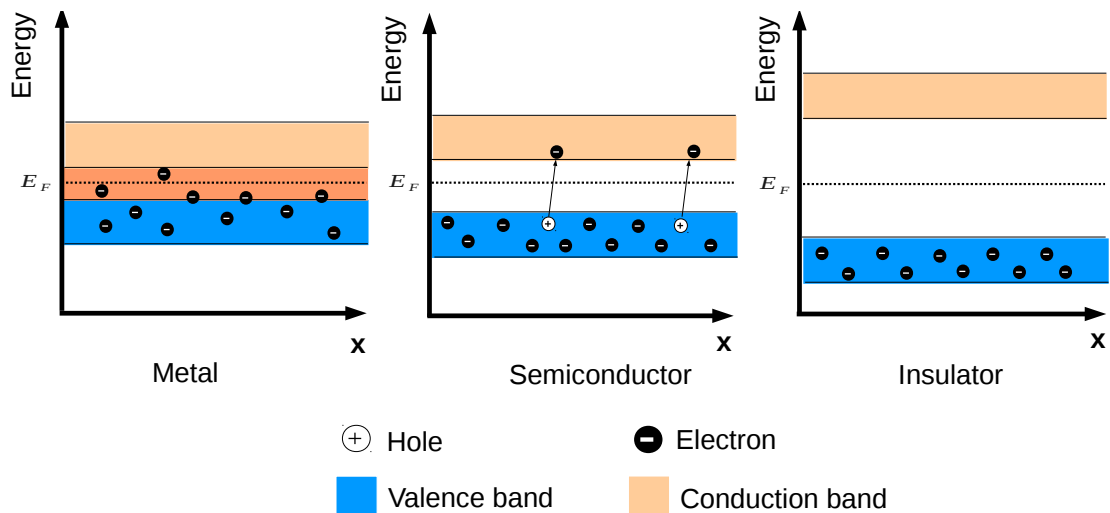with the Boltzmann constant k_b. In a metal the width of the forbidden gap is zero and

Figure 104: Electronic band structure of metals, semiconductors and insulator. E_F denotes the Fermi level at $T = 0$ K.

the Fermi level lies inside the conduction band. Due to this there are free electrons inside the conduction band at $T = 0$ K that can be accelerated in an electric field. In an insulator the width of the energy gap is too large for electrons to be excited from the valence into the conduction band and no current will flow if an external electrical field is applied to the insulator. The Fermi level of a semiconductor lies inside the forbidden

material	$T = 0$ K	$T = 300$ K
silicon	1.17	1.12
germanium	0.75	0.67

Table A1: Width of the energy gap for silicon and germanium for a temperature of 0 K and 300 K [73].

gap which has a typical, temperature dependent, width of around 1 eV (the width of the energy gap for silicon and germanium for different temperatures is shown in table A1). At $T = 0$ K the probability for an electron to be inside the conduction band is zero and the semiconductor is effectively an electric insulator. At room temperature, however, the probability distribution gets smeared out and electrons can be exited from the valence band into the conduction band, giving rise to an electric current if an external electrical field is applied. In a semiconductor this current is carried by two sources. Whenever an electron is excited into the conduction band it leaves a hole in the valence band. This hole can be easily filled by neighboring electrons which again leaves a hole. The moving hole acts as a positive charge carrier with a direction opposite to the movement of the electrons. The conductivity of a semiconductor is therefore given by

$$j = e(n_e \mu_e + n_p \mu_p)E \tag{A.2}$$

where n/μ is the number/mobility of electrons and holes and E the external electric field. The charge carrier concentration inside the semiconductor depends on temperature and the width of the energy gap and can be calculated using [71].

$$n_i = AT^{3/2} e^{-\frac{E_g}{2k_b T}}. \tag{A.3}$$

Doped Semiconductors

The charge carrier concentration in a pure or *intrinsic* semiconductor at room temperature is not sufficient to achieve the current densities needed for practical application in electronic circuits. For silicon the intrinsic charge carrier concentration at room temperature is in the order of $1.5 \cdot 10^{10}$ cm^{-3} [73]. To increase the charge carrier concentration impurity atoms can be introduced into the semiconductor material. This process is called *doping*. The impurities either have one additional electron compared to the semiconductor atoms (n-doping) or lack one electron (p-doping).

In the case of a trivalent dopant material (typically Boron or Gallium) there are not enough electrons to form four covalent bounds with the neighboring atoms, which leads to the creation of additional holes. In the energy band structure the doping leads to additional states in the forbidden gap close to the valence band (called acceptor level). Electrons can be easily excited from the valence band into the new states. In such a p-type semiconductor the electrical current is mainly carried by the holes which are then called majority carriers while the electrons are minority carriers. In a n-type semiconductor the dopant is a pentavalent atom (Arsenic, phosphor). The fifth electron is not needed to create the covalent bounds with the semiconductor atoms and an additional energy state is created close to the conduction band (called donor level). From this level the electron can be easily excited into the conduction band. In these kind of devices the current is mainly carried by the electrons. The charge carrier concentration of doped semiconductor detectors can

be several magnitudes higher compared to intrinsic semiconductors and typical dopant concentrations are between 10^{13} and 10^{18} dopant atoms per cubic centimeter [73].

In addition to intended doping of semiconductors unwanted impurities and crystal lattice defects play an important role for the properties of semiconductor detectors, too. They influence the process of recombination. Recombination is the process where an electron drops back into a hole in the valence band. Impurities lead to the formation of *recombination centers* by introducing additional states in the forbidden energy gap. These states may capture an electron and either release them after a certain holding time or capture a hole as well resulting in recombination. While the first effect lowers the mobility of free charges, the second effect leads to a loss of charge carriers. Furthermore impurities lead to trapping. Here the additional state can only capture one type of charge carrier and releases it after a given time. Structural defects in the semiconductor like missing atoms (point defect) or the displacement of an entire line of atoms (dislocation) may also lead to the formation of recombination centers.

B

DERIVATION OF CR-RC SHAPER RESPONSE FUNCTION

In this section the time and frequency response function of CR-RC shaper is derived by means of the Laplace and Fourier transformation.

The Laplace transformation $F(s)$ of a function $f(t)$ is defined by

$$F(s) = \mathbf{L}(f(t)) = \int\limits_{-\infty}^{+\infty} f(t)e^{-st}dt \tag{B.1}$$

Applying the Laplace transformation to the derivative of $f(t)$ with respect to t leads to the important result

$$\mathbf{L}\left(\frac{df(t)}{dt}\right) = s \cdot \mathbf{L}(f(t)) \tag{B.2}$$

In addition the application of the Laplace transformation to the convolution of to functions given by

$$h(\tau) = f_1(t) * f_2(t) = \int\limits_{-\infty}^{+\infty} f_1(t-\tau)f_2(t)dt$$

results in

$$\mathbf{L}(h(\tau)) = F_1(s) \cdot F_2(s)$$

In general the relation between the input and the output of a linear circuit is given by a differential equation of the form[114]

$$a_0 v_{out}(t) + a_1 \frac{dv_{out}(t)}{dt} + \cdots + a_n \frac{d^n v_{out}(t)}{dt^n} = b_0 v_{in}(t) + b_1 \frac{dv_{in}(t)}{dt} + \cdots + b_m \frac{d^m v_{in}(t)}{dt^m}$$

Applying equation B.2 leads to

$$V_{out}(s) = \frac{\sum\limits_{i=0}^{m} b_i s^i}{\sum\limits_{j=0}^{n} a_j s^j} V_{in} = H(s) \cdot V_{in}(s) \tag{B.3}$$

with the so called time domain transfer function $H(s)$. Alternatively the output response of a circuit to an arbitrary input signal can be described by the reaction of the circuit to a superposition of impulse (delta function) inputs[114]

$$v_{out}(t) = \int\limits_{-\infty}^{+\infty} h(t - \tau) \cdot v_{in}(\tau)d\tau = h(\tau) * v_{in}(\tau)$$

with the impulse response h of the circuit to delta function input. Applying the Laplace transformation leads to

$$V_{out}(s) = \mathbf{L}(h(\tau)) \cdot V_{in}(s)$$

Comparing this to B.3 one finds that $H(s) = \mathbf{L}(h(\tau))$ which finally leads to the result

$$v_{out}(t) = \int\limits_{-\infty}^{+\infty} \mathbf{L}^{-1}(H(\tau - t)) \cdot v_{in}(\tau)d\tau \tag{B.4}$$

with the inverse Laplace transformation $\mathbf{L}^{-1}$. During circuit design one is usually interested not only in the time domain response of a circuit, but furthermore in the frequency behavior or frequency domain transfer function (e.g. to optimize noise filtering characteristics). This can be obtained by replacing the Laplace transformation with the Fourier transformation

$$\mathbf{F}(f(t)) = \int\limits_{-\infty}^{+\infty} f(t)e^{-i\omega t}dt \tag{B.5}$$

and repeating the arguments above or by the substitution $s \to i\omega$ in the time domain transfer function $H(s)$.
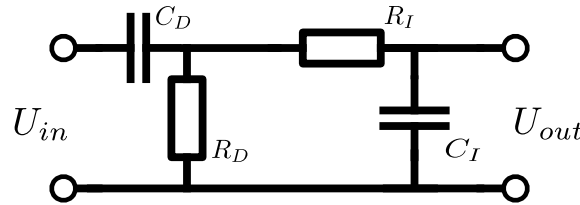

Figure 105: Schematic diagram of a CR-RC shaper.

Figure 105 shows the schematic of a CR-RC shaper. We start by deriving the response of the CR differentiator or high pass:

$$U_{in}(t) = \frac{Q(t)}{C} + U_{out}(t)$$

$$\Rightarrow \frac{dU_{in}(t)}{dt} = \frac{I(t)}{C_D} + \frac{dU_{out}(t)}{dt}; \quad I(t) = R_D \cdot U_{out}(t)$$

$$\Rightarrow \frac{dU_{in}(t)}{dt} = \frac{1}{R_D C_D}U_{out}(t) + \frac{dU_{out}(t)}{dt}$$

Replacing $\tau_D = R_D C_D$ and applying the Laplace transformation results in the transfer function

$$U_{out}(s) = \frac{\tau_D s}{1 + s\tau_D}V_{in}(s) \Rightarrow H(s) = \frac{\tau_D s}{1 + s\tau_D} \tag{B.6}$$

By approximating the input signal with a step function and applying the inverse Laplace transformation the final result reads

$$U_{in}(s) = \frac{U_0}{s}$$
$$\Rightarrow U_{out}(s) = \frac{\tau_D}{1 + s\tau_D} U_0$$
$$\Rightarrow U_{out}(t) = U_0 e^{-t/\tau_D} \tag{B.7}$$

The transfer function in the frequency domain is given by

$$G(i\omega) = \frac{i\omega\tau_H}{1 + i\omega\tau_H} \Rightarrow |G(i\omega)| = \frac{\omega\tau_H}{\sqrt{1 + \omega^2\tau_H^2}} \tag{B.8}$$

The transfer function of the RC integrator or low pass can be derived starting from the equation

$$U_{in}(t) = R_I I(t) + U_{out}(t); \quad I(t) = C_I \frac{dU_{out}(t)}{dt}$$
$$\Rightarrow U_{in}(t) = \tau_I \cdot \frac{dU_{out}(t)}{dt} + U_{out}(t)$$

with $\tau_I = R_I C_I$. Using the Laplace transformation yields the transfer function

$$U_{out}(s) = \frac{1}{1 + s\tau_I} V_{in}(s) \Rightarrow H(s) = \frac{1}{1 + s\tau_I} \tag{B.9}$$

Again approximating the input signal as a step function and using the inverse Laplace transformation one finds the time response

$$U_{out}(t) = U_0(1 - e^{-t/\tau_I}) \tag{B.10}$$

while the frequency response is then given by

$$G(i\omega) = \frac{1}{1 + i\omega\tau_I} \Rightarrow |G(i\omega)| = \frac{1}{\sqrt{1 + \omega^2\tau_I^2}} \tag{B.11}$$

The transfer function of the complete CR-RC shaper is given by the product of the CR and RC transfer functions

$$H(s) = \frac{1}{1 + \tau_I s} \frac{\tau_D}{1 + \tau_D s} \tag{B.12}$$

The response functions for the time and frequency domain are given by

$$U_{out}(t) = \frac{\tau_D U_0}{\tau_D - \tau_I} (e^{-t/\tau_D} - e^{-t/\tau_I}) \tag{B.13}$$
$$|G(i\omega)| = \frac{\tau_I \omega}{\sqrt{1 + \tau_D^2 \omega^2}\sqrt{1 + \tau_I^2 \omega^2}} \tag{B.14}$$

C
MUPIX 6 I/O-PADS AND DAC SETTINGS

I/O-Pads

Signal	I/0	Signal-Function	# Pads
LD_Pix			1
Pull down	I		1
Load_Col		readout	1
Read_Col			1
Priority Out	O		1
Time stamp_In	I		8
Time stamp_Out	O	hit information	8
Row Address	O		6
Column Address	O		6
1.5 V	I		1
1.8 V	I	supply voltage	several
Ground	I		several
Bias Voltage	I	bias	2
Injection	I	injection pulse	2
Baseline	I		1
Threshold	I	bias current	1
VPCasc	I		1
Hitbus	O	Comparator output	1

Table C1: I/O pads of the MuPix 6 prototype.

Signal Timing

Signal Timing	board w. inverter [clock cycles]	board w/o inverter [clock cycles]
Load Pixel to Pull Down	E	E
Pull Down to Load Column	E	E
Load Column to Read Column	E	1C
Read Column to Read Column	C	1C
Read Column to Pull Down	E	E
Read Column Width	A	18
Priority Signal Sampling	4	7
Data Sampling	5	7

Table C2: Timing between the readout signals controlling the MuPix readout state machine and sampling points given in hexidecimal format. The internal clock speed of the FPGA was set to 100 MHz, while the length of the readout cables was 2.5 m.

Chip DAC Settings

Chip DAC	normal	power saving
VPComp	3B	A
VNDel	9	9
VNLoad	9	2
VNFoll	E	A
VNFB	9	3
VN	3B	5
ThRes	3B	3B
BLRes	3E	3E
VN2	3B	5
VNLoad2	4	2
VNFB2	9	3
BLRes2	3E	5

Chip DAC	normal	power saving
VPComp	3C	A
VNDel	A	A
VNLoad	5	2
VNFoll	10	A
VNFB	A	3
VN	3C	5
ThRes	-	-
BLRes	-	-
VN2	3C	5
VNLoad2	5	2
VNFB2	A	3
BLRes2	A	A

Table C3: Normal and power saving chip DAC settings [115] used in this work (left table) and DAC settings used in [82] (right table). Given are the chip register entries in hexadecimal format. The ThRes and BlRes DACs only apply for the pixels with the MuPix 4 analogue part.

The chip DAC settings are listed in table C3. As can be seen the main difference compared to the DAC settings used in [82] is the value of the BlRes DAC. In case of the normal DAC settings it is set to a much lower value while in case of the power saving settings it is slightly higher. To illustrate the effects of this difference, figure 106 shows the shaper response function for the normal and power saving DAC settings. As can be seen for the
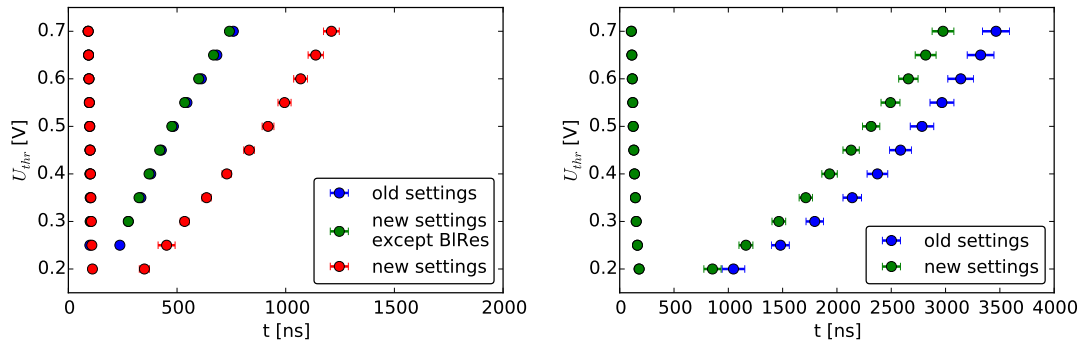

Figure 106: Comparison of the shaper response function using the normal and power saving DAC settings from both works.

normal DAC settings, the change of the BlRes DAC leads to a slower shaping time and a higher signal amplitude. Furthermore, it can be seen that the other DACs only have a minor impact on the shaper output. In case of the power saving DAC the difference between both curves is much smaller and the shaping time is slightly shorter. The power consumption of the sensor board and chip was measured with a volt meter. The power consumption for both normal DAC settings was found to be 715 mW while the power consumption for both versions of the power saving settings was measured to be 445 mW. It should be stressed again that this is the power consumption of the complete sensor board and chip and not the power consumption of the sensor alone.

D

ADDITIONAL MATERIAL FOR ANALYSIS OF $e^+e^- \to \eta_c \eta \pi^+ \pi^-$

Reconstruction Performance of η_c

In the following subsections the tables and figures referenced in chapter 7 are shown. These include the invariant mass distributions of the matched and mismatched η_c candidates for all 13 η_c final states as well as the reconstruction correctness. Furthermore, the results of the extended maximum likelihood fits for the efficiency determination are depicted. Lastly, the remaining background Monte Carlo samples and the distribution of the remaining background events after the event selection are depicted.
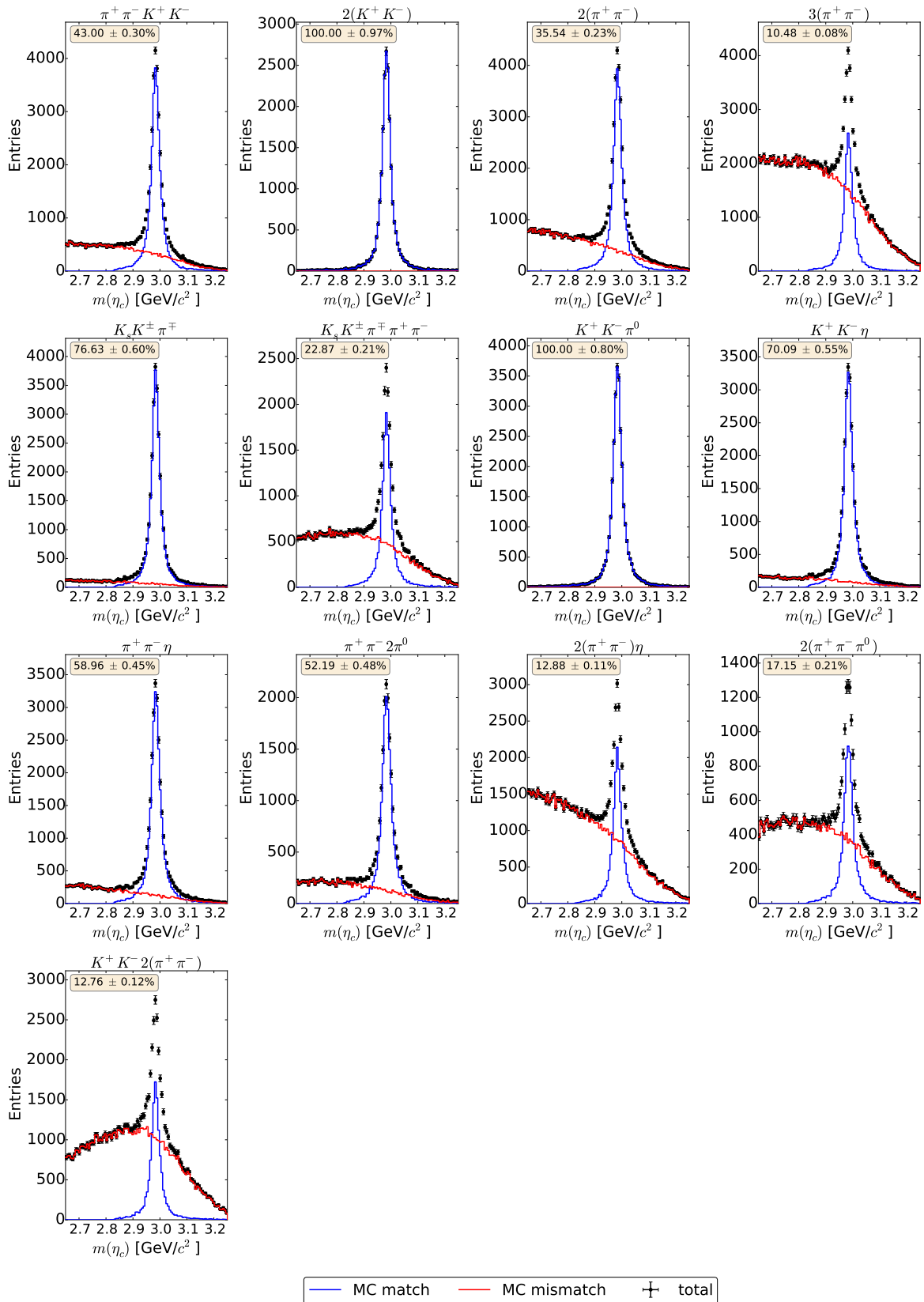
η_c Reconstruction Performance at $\sqrt{s} = 4.26$ GeV

Figure 107: Distribution of the η_c invariant mass separated into incorrectly and correctly reconstructed events at $\sqrt{s} = 4.26$ GeV.
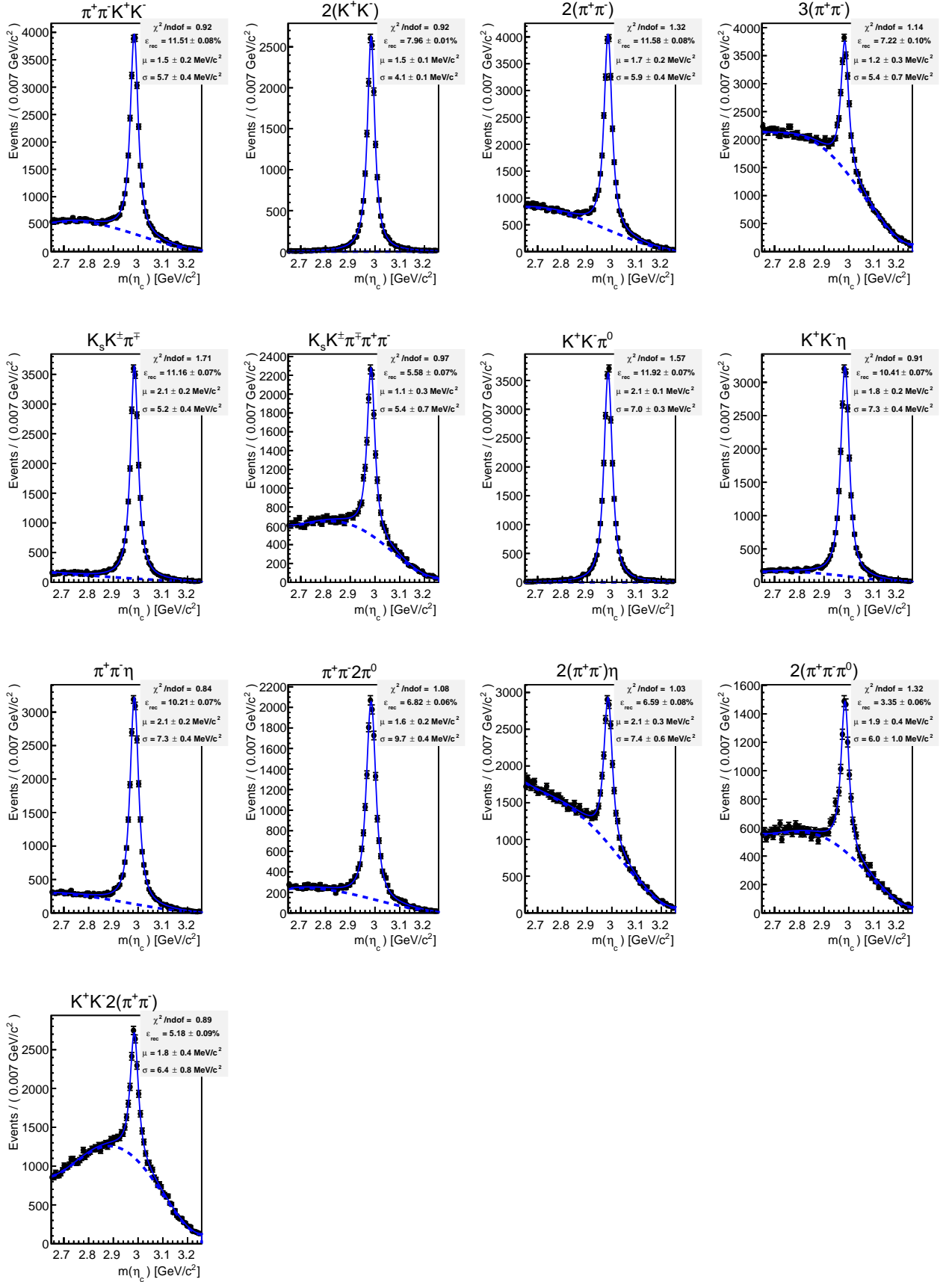
Figure 108: Fit to the reconstructed η_c mass distributions in oder to extract the reconstruction efficiency of $e^+e^- \to \eta_c\eta\pi^+\pi^-$ and resolution of the η_c mass for the analyzed η_c final states at $\sqrt{s} = 4.26$ GeV.
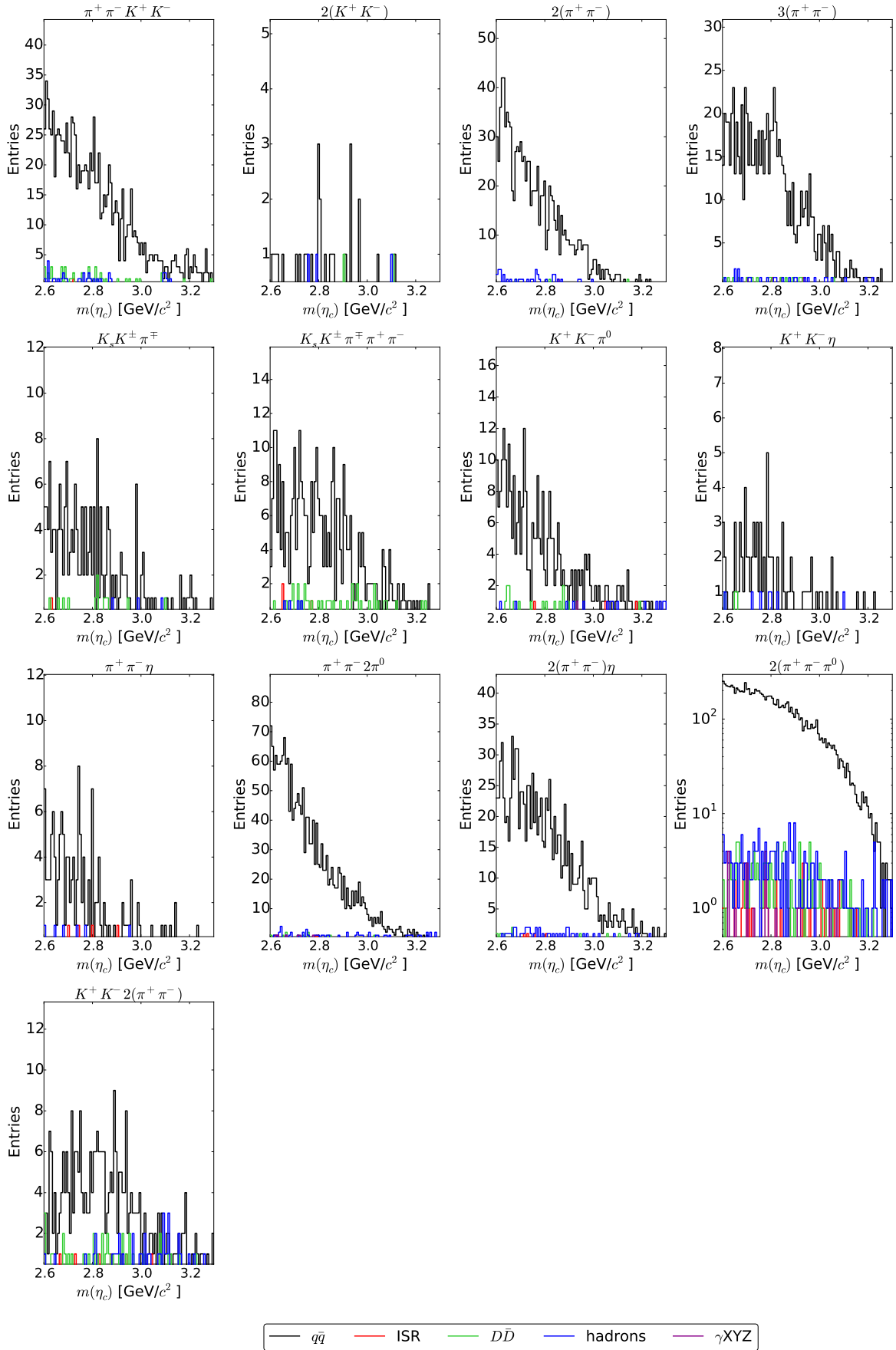
Figure 109: η_c candidate mass distribution from inclusive Monte Carlo for the different η_c final states at $\sqrt{s} = 4.26$ GeV.

η_c Reconstruction Performance at $\sqrt{s} = 4.23$ GeV

η_c final state	Correctness [%]
$\pi^+\pi^-K^+K^-$	74.35 ± 0.62
$2(K^+K^-)$	100 ± 1.05
$2(\pi^+\pi^-)$	70.50 ± 0.58
$3(\pi^+\pi^-)$	30.02 ± 0.27
$K_sK^{\pm}\pi^{\mp}$	93.59 ± 0.84
$K_sK^{\pm}\pi^{\mp}\pi^+\pi^-$	49.67 ± 0.55
$K^+K^-\pi^0$	100.00 ± 0.87
$K^+K^-\eta$	90.33 ± 0.83
$\pi^+\pi^-\eta$	86.76 ± 0.79
$\pi^+\pi^-\pi^0\pi^0$	80.29 ± 0.90
$2(\pi^+\pi^-)\eta$	37.84 ± 0.38
$2(\pi^+\pi^-\pi^0)$	40.60 ± 0.59
$K^+K^-2(\pi^+\pi^-)$	28.77 ± 0.31

Table D1: Correctness of the event reconstruction of $e^+e^- \to \eta_c\eta\pi^+\pi^-$ for the different η_c final states at a center of mass energy of 4.23 GeV.
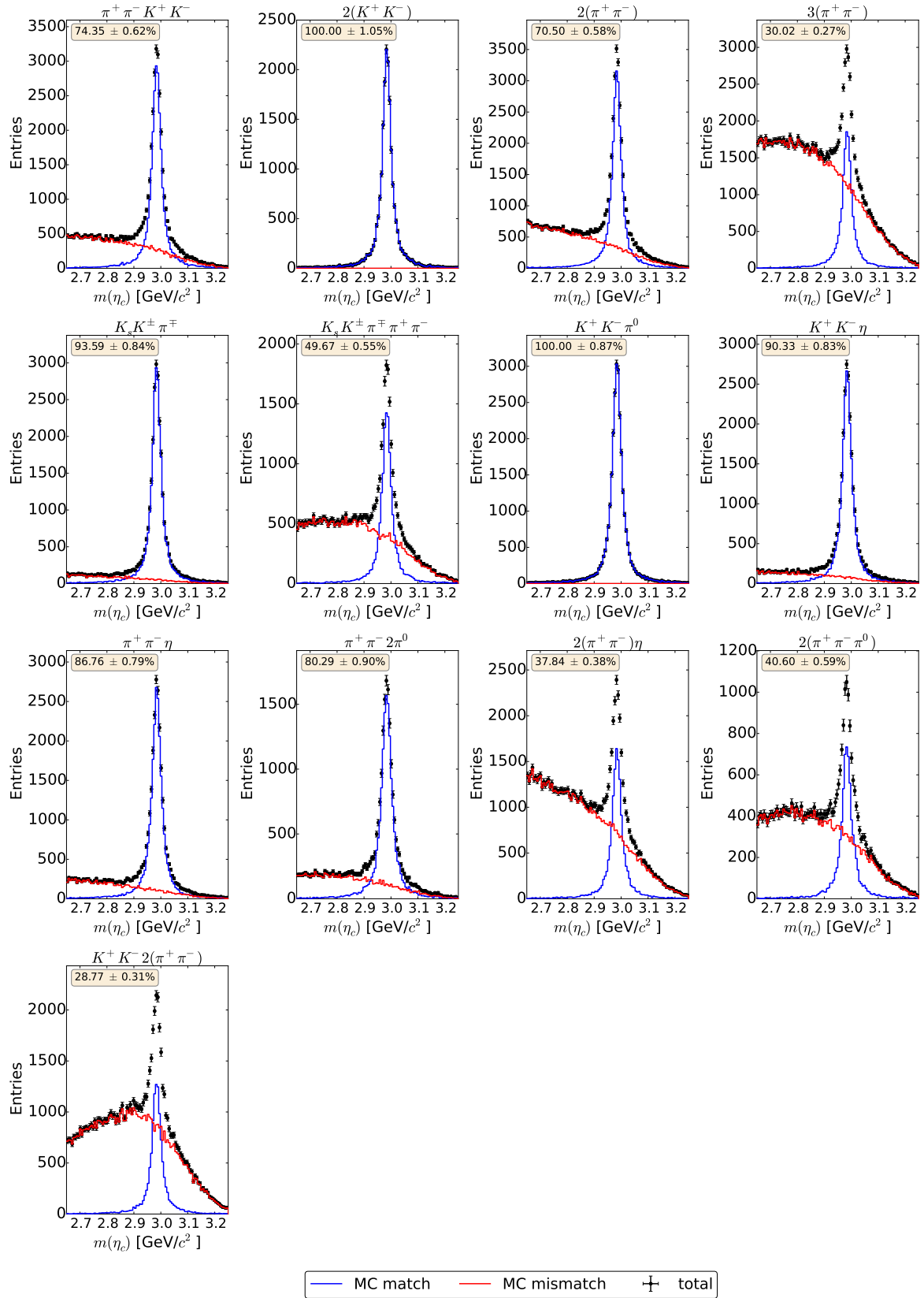
Figure 110: Distribution of the η_c invariant mass separated into incorrectly and correctly reconstructed events at $\sqrt{s} = 4.23$ GeV.
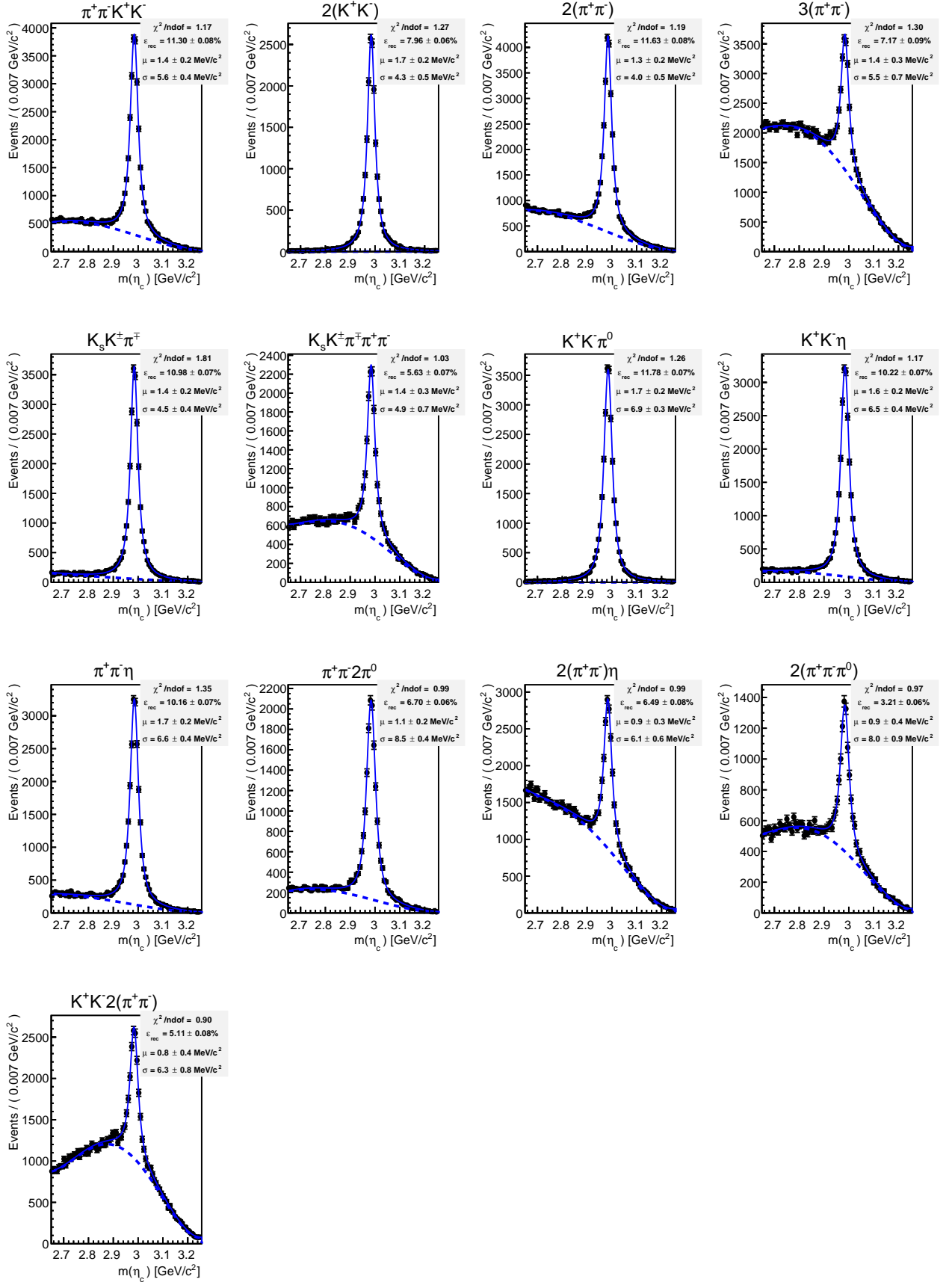
Figure 111: Fit to the reconstructed η_c mass distributions in oder to extract the reconstruction efficiency of $e^+e^- \to \eta_c\eta\pi^+\pi^-$ and resolution of the η_c mass for the analyzed η_c final states at $\sqrt{s} = 4.23$ GeV.

Background Source	Events	Scaling Factor
Hadrons	$5.0 \cdot 10^5$	1.0
$q\bar{q}$	$2 \cdot 10^7$	1.0
ISR	$1.6 \cdot 10^6$	1.0
$D\bar{D}$	$3.7 \cdot 10^6$	0.9
γXYZ	$6.5 \cdot 10^4$	1.5
Others	$4.8 \cdot 10^7$	0.8

Table D2: Number of generated events in inclusive Monte Carlo datasets and their respective scaling to the size of the $Y(4230)$ dataset. The channels to e^+e^- to e^+e^-, $\mu^+\mu^-$ and $\tau^+\tau^-$ have been summarized in the others category.

η_c final state	hadrons	$q\bar{q}$	ISR	DD	γXYZ	others
$\pi^+\pi^-K^+K^-$	41	1049	4	53	2	0
$2(K^+K^-)$	0	26	0	3	0	0
$2(\pi^+\pi^-)$	45	1516	30	7	0	0
$3(\pi^+\pi^-)$	39	612	34	26	0	0
$K_sK^\pm\pi^\mp$	8	135	0	13	0	0
$K_sK^\pm\pi^\mp\pi^+\pi^-$	10	330	8	53	0	0
$K^+K^-\pi^0$	15	314	2	21	2	0
$K^+K^-\eta$	2	73	0	6	0	0
$\pi^+\pi^-\eta$	16	243	8	1	1	0
$\pi^+\pi^-2\pi^0$	73	3454	24	11	8	0
$2(\pi^+\pi^-)\eta$	70	1491	0	0	0	0
$2(\pi^+\pi^-\pi^0)$	373	15743	96	120	61	0
$K^+K^-2(\pi^+\pi^-)$	3	184	15	24	0	0

Table D3: Background contributions to different η_c final states at center of mass energy of 4.23 GeV. The channels $e^+e^- \to e^+e^-$, $\mu^+\mu^-$ and $\tau^+\tau^-$ have been summarized in the others category.
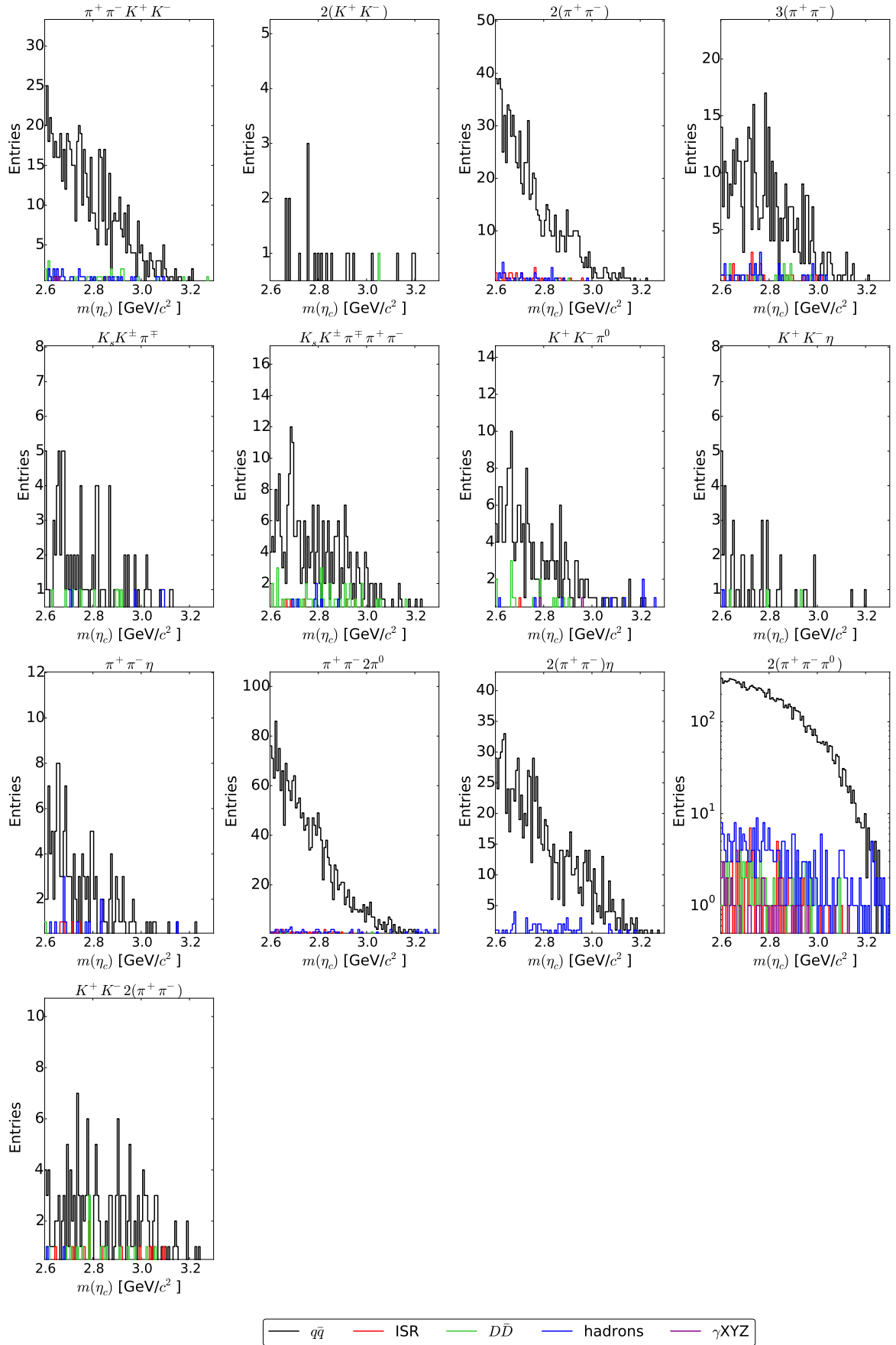
Figure 112: η_c candidate mass distribution from inclusive Monte Carlo for the different η_c final states at $\sqrt{s} = 4.23$ GeV.

η_c Reconstruction Performance at $\sqrt{s} = 4.36$ GeV

η_c final state	Correctness [%]
$\pi^+\pi^-K^+K^-$	73.50 ± 0.61
$2(K^+K^-)$	100 ± 1.05
$2(\pi^+\pi^-)$	69.44 ± 0.57
$3(\pi^+\pi^-)$	28.87 ± 0.26
$K_sK^\pm\pi^\mp$	93.22 ± 0.83
$K_sK^\pm\pi^\mp\pi^+\pi^-$	48.59 ± 0.54
$K^+K^-\pi^0$	100.00 ± 0.87
$K^+K^-\eta$	90.04 ± 0.82
$\pi^+\pi^-\eta$	86.17 ± 0.78
$\pi^+\pi^-\pi^0\pi^0$	79.57 ± 0.88
$2(\pi^+\pi^-)\eta$	36.37 ± 0.36
$2(\pi^+\pi^-\pi^0)$	39.43 ± 0.56
$K^+K^-2(\pi^+\pi^-)$	27.84 ± 0.30

Table D4: Correctness of the event reconstruction of $e^+e^- \to \eta_c\eta\pi^+\pi^-$ for the different η_c final states at a center of mass energy of 4.36 GeV.
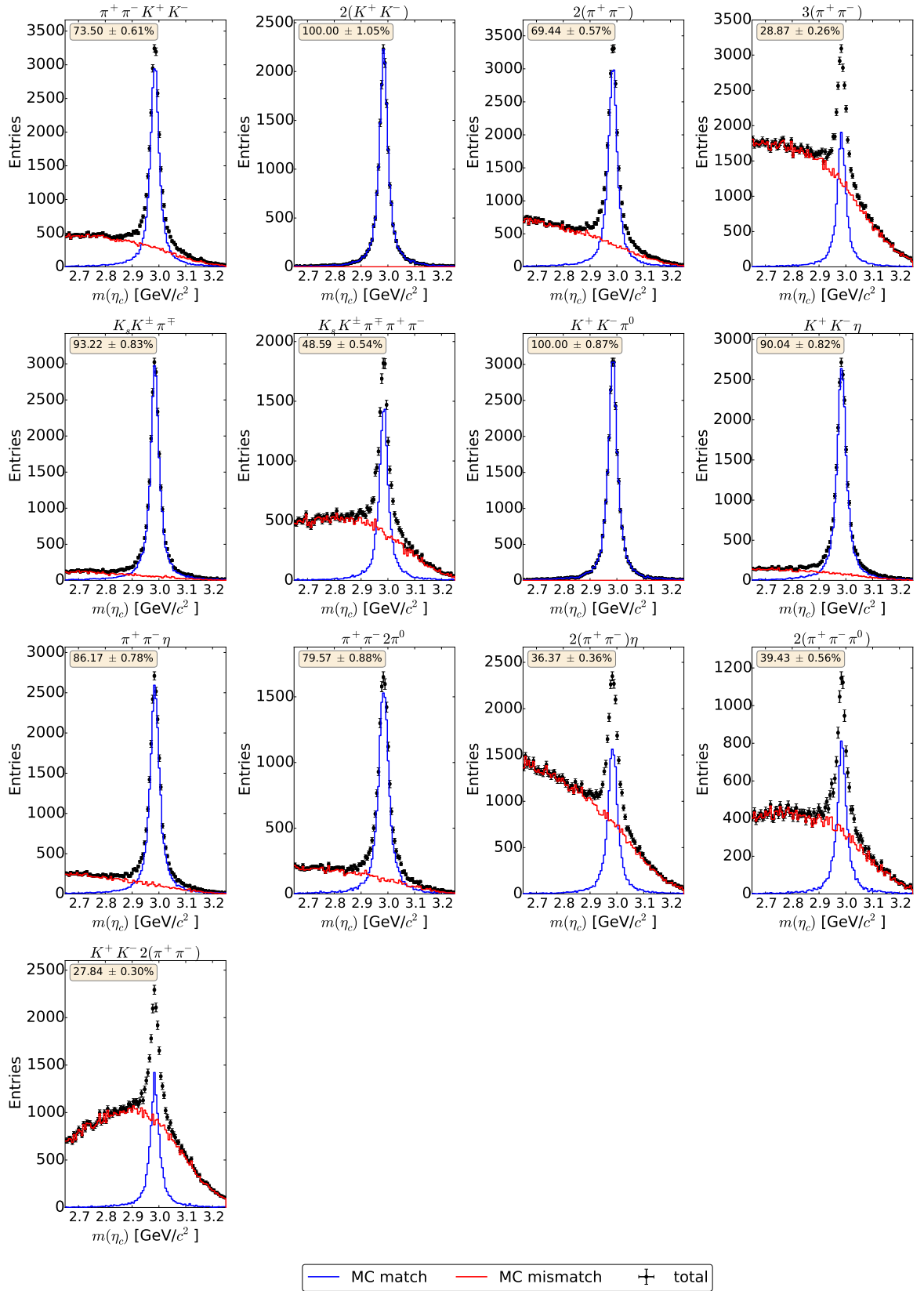
Figure 113: Distribution of the η_c invariant mass separated into incorrectly and correctly reconstructed events at $\sqrt{s} = 4.36$ GeV.
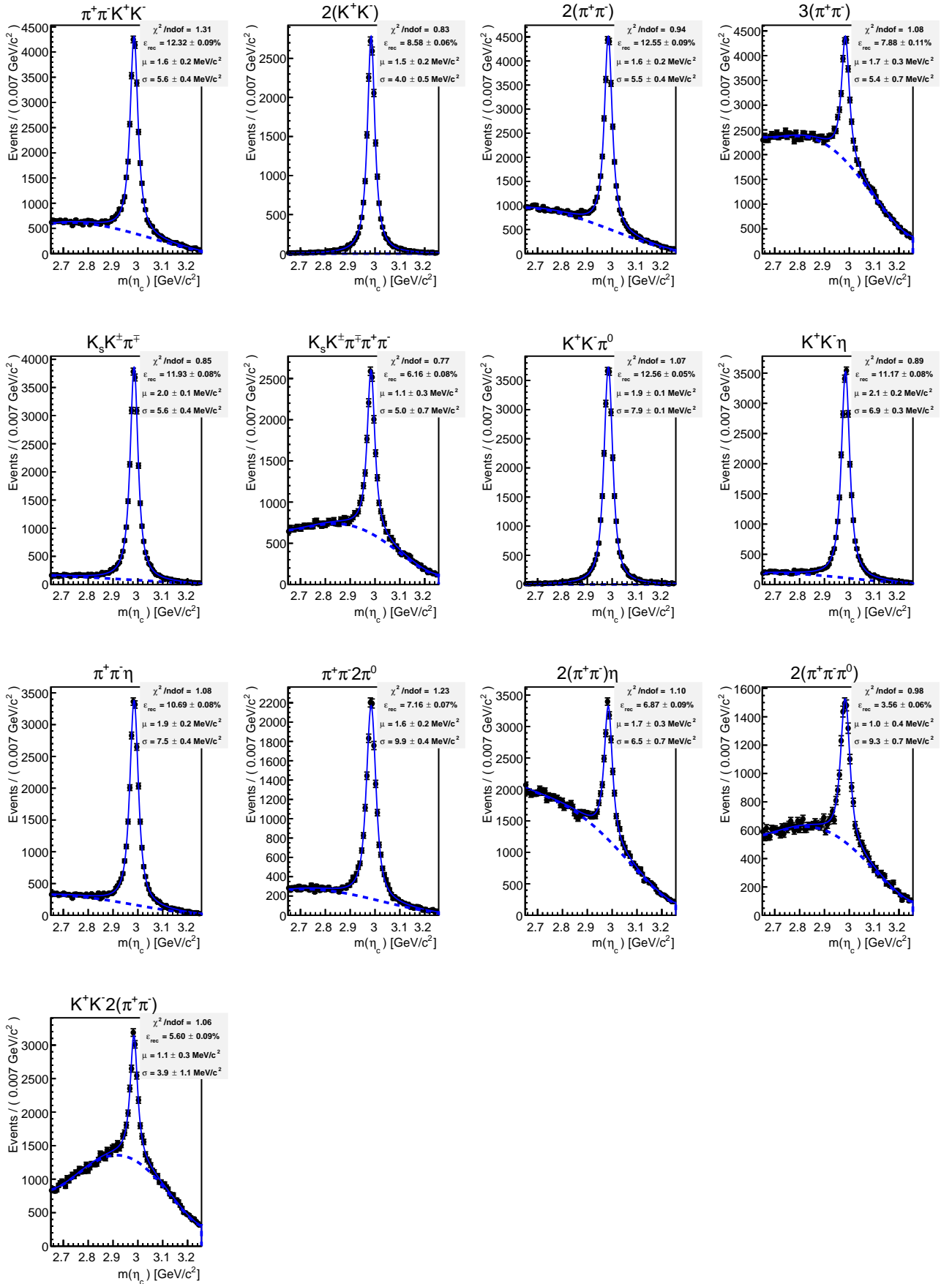
Figure 114: Fit to the reconstructed η_c mass distributions in oder to extract the reconstruction efficiency of $e^+e^- \to \eta_c\eta\pi^+\pi^-$ and the resolution of the η_c mass for the analyzed η_c final states at $\sqrt{s} = 4.36$ GeV.

Background Source	Events	Scaling Factor
Hadrons	$1.9 \cdot 10^5$	1.0
$q\bar{q}$	$9.4 \cdot 10^6$	1.0
ISR	$6.0 \cdot 10^5$	1.0
$D\bar{D}$	$5.0 \cdot 10^5$	0.9
γXYZ	$3.3 \cdot 10^4$	1.4
Others	$2.9 \cdot 10^7$	0.8

Table D5: Number of generated events in inclusive Monte Carlo datasets and their respective scaling to the size of the $Y(4360)$ dataset. The channels to e^+e^- to e^+e^-, $\mu^+\mu^-$ and $\tau^+\tau^-$ have been summarized in the others category.

η_c final state	hadrons	$q\bar{q}$	ISR	DD	γXYZ	others
$\pi^+\pi^-K^+K^-$	11	675	6	8	0	0
$2(K^+K^-)$	1	22	1	0	0	0
$2(\pi^+\pi^-)$	20	578	9	0	0	0
$3(\pi^+\pi^-)$	21	419	0	0	0	0
$K_sK^\pm\pi^\mp$	3	113	0	0	0	0
$K_sK^\pm\pi^\mp\pi^+\pi^-$	0	186	5	3	0	0
$K^+K^-\pi^0$	3	156	0	3	1	0
$K^+K^-\eta$	0	49	0	0	0	0
$\pi^+\pi^-\eta$	6	54	0	0	1	0
$\pi^+\pi^-2\pi^0$	33	644	14	1	2	0
$2(\pi^+\pi^-)\eta$	34	336	21	0	0	0
$2(\pi^+\pi^-\pi^0)$	124	2102	36	14	13	0
$K^+K^-2(\pi^+\pi^-)$	15	183	0	9	0	0

Table D6: Background contributions to different η_c final states at center of mass energy of 4.36 GeV. The channels $e^+e^- \to e^+e^-$, $\mu^+\mu^-$ and $\tau^+\tau^-$ have been summarized in the others category.
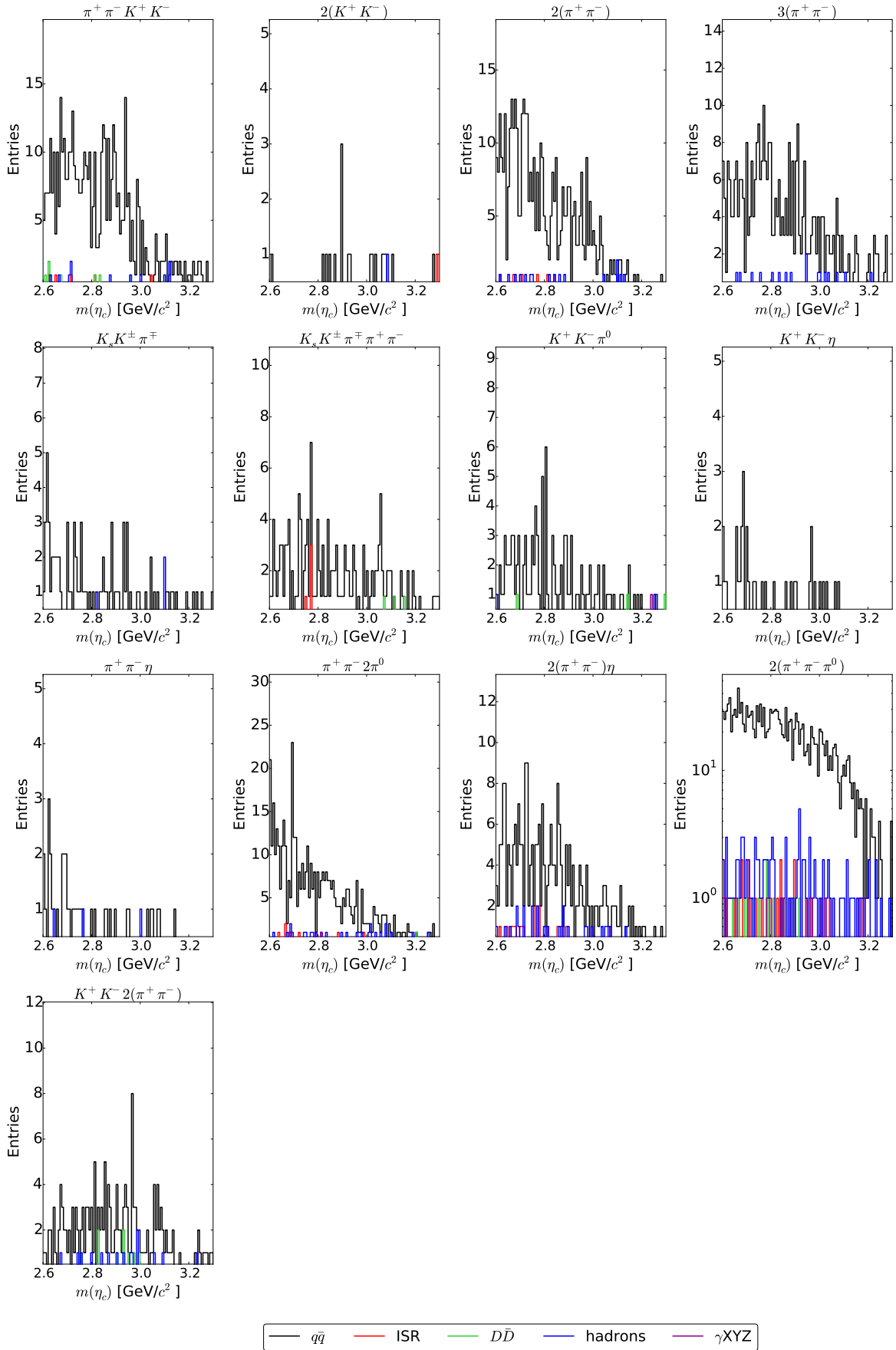
Figure 115: η_c candidate mass distribution from inclusive Monte Carlo for the different η_c final states at $\sqrt{s} = 4.36$ GeV.

E
SYSTEMATIC STUDIES OF UNCERTAINTIES

The following figures present the distributions of the extracted signal cross section of $e^+e^- \to \eta_c \eta \pi^+ \pi^-$ which were generated during the toy studies of the systematic uncertainties. For details refer to section 8.2.
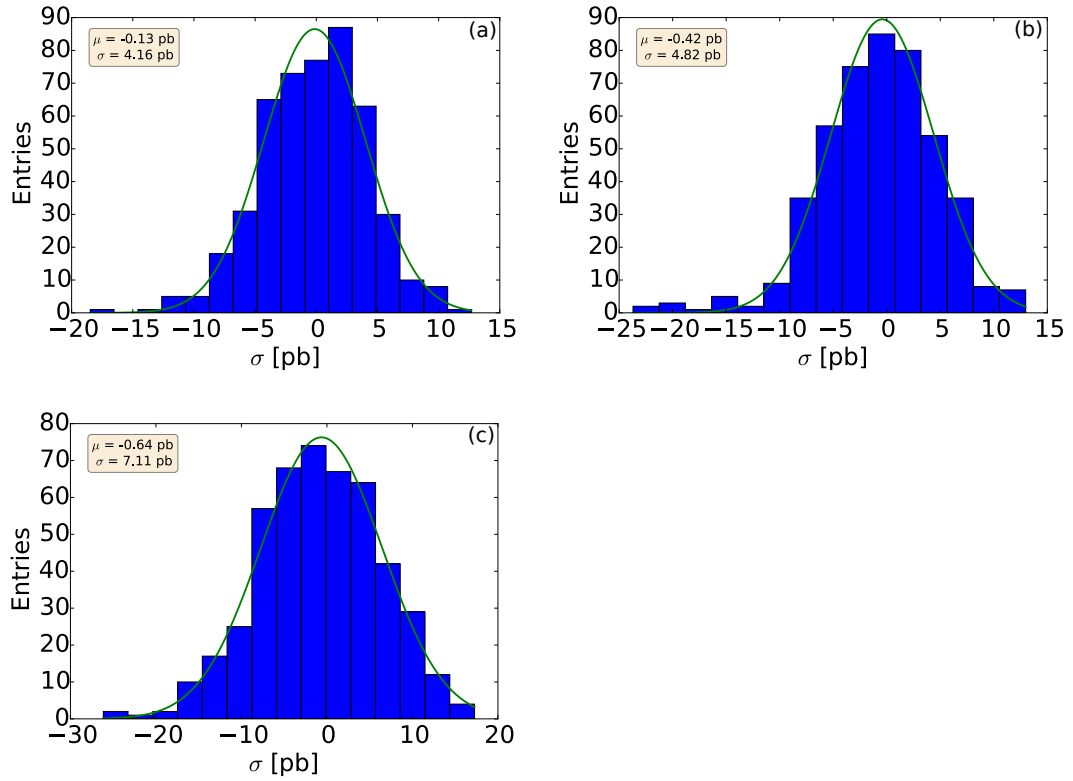

Figure 116: Distribution of the fitted cross section for 500 toy fits using an input cross section of 0 pb. (a) $\sqrt{s} = 4.23$ GeV, (b) $\sqrt{s} = 4.26$ GeV and (c) $\sqrt{s} = 4.36$ GeV

Figure 117: Distribution of the fitted cross section for 500 toy fits using an input cross section of 20 pb. (a) $\sqrt{s} = 4.23$ GeV, (b) $\sqrt{s} = 4.26$ GeV and (c) $\sqrt{s} = 4.36$ GeV
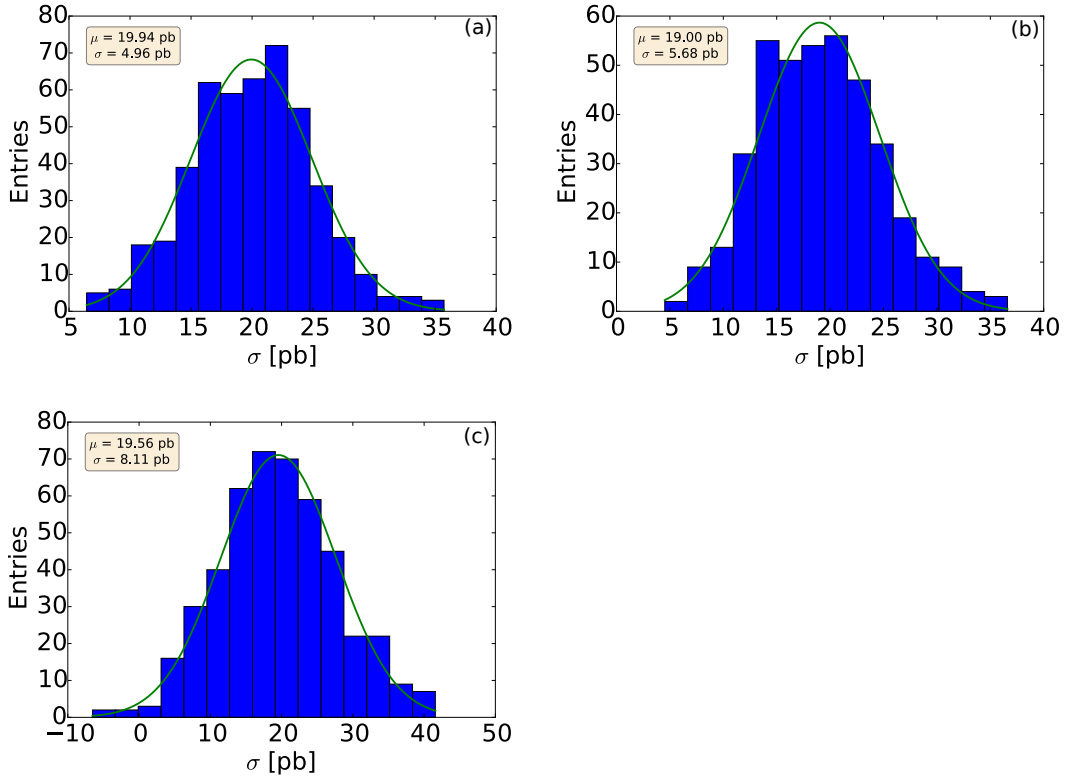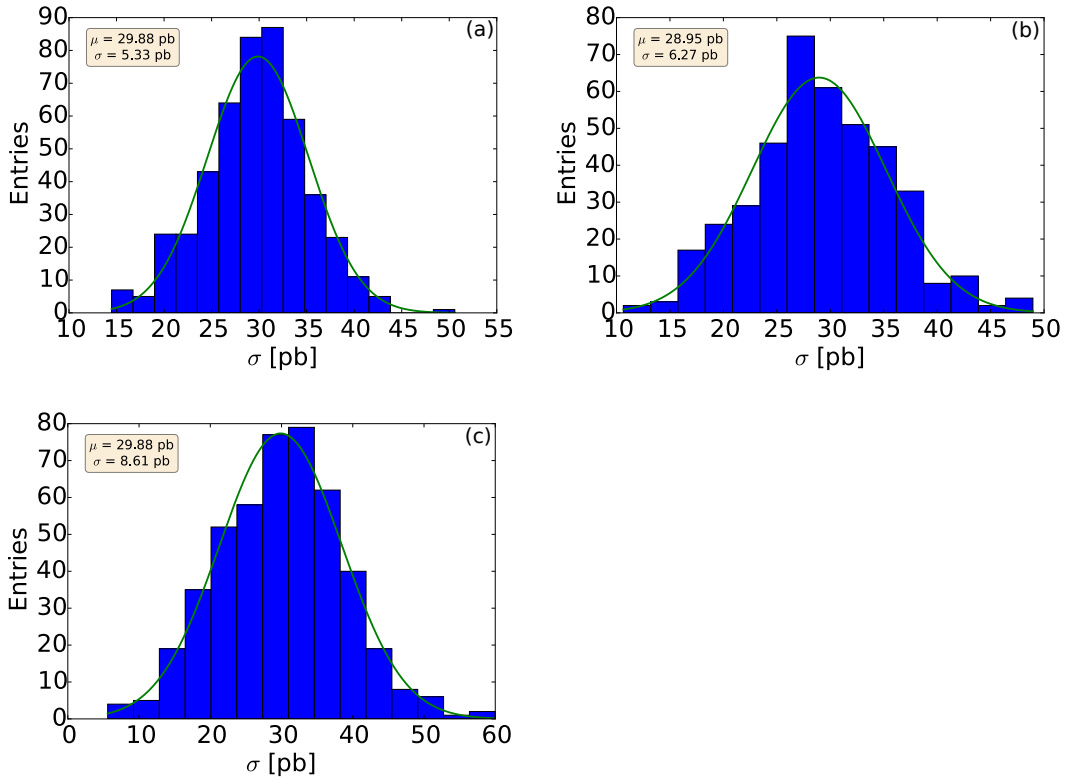

Figure 118: Distribution of the fitted cross section for 500 toy fits using an input cross section of 30 pb. (a) $\sqrt{s} = 4.23$ GeV, (b) $\sqrt{s} = 4.26$ GeV and (c) $\sqrt{s} = 4.36$ GeV
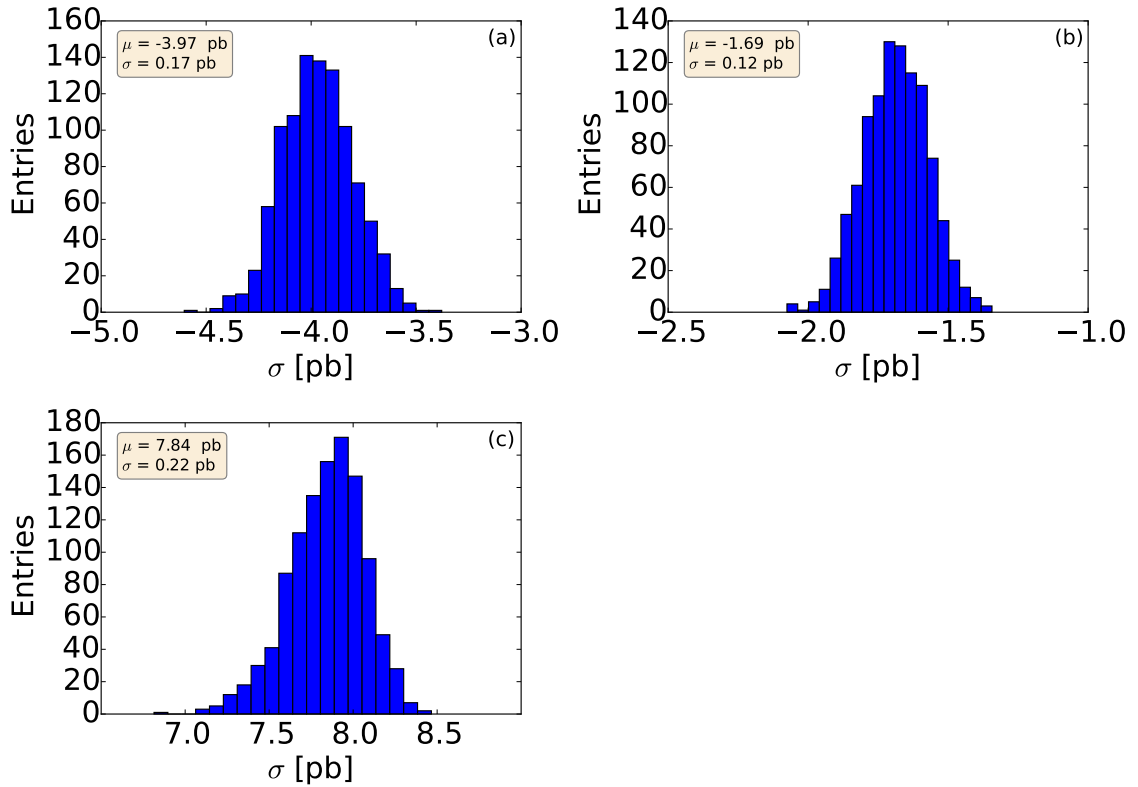
Figure 119: Distribution of the fitted cross section for the η_c parameter study. (a) $\sqrt{s} = 4.23$ GeV, (b) $\sqrt{s} = 4.26$ GeV, and (c) $\sqrt{s} = 4.36$ GeV.
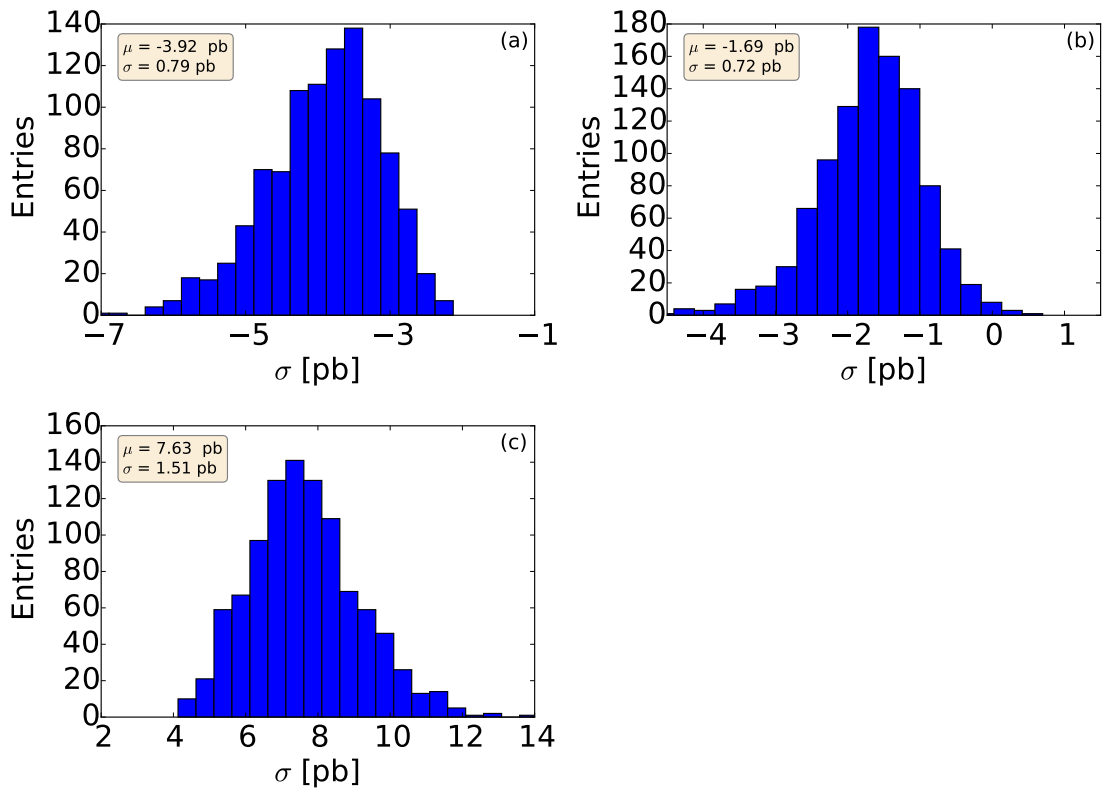

Figure 120: Distribution of the fitted cross section for the η_c branching ratio study. (a) $\sqrt{s} = 4.23$ GeV, (b) $\sqrt{s} = 4.26$ GeV, and (c) $\sqrt{s} = 4.36$ GeV.
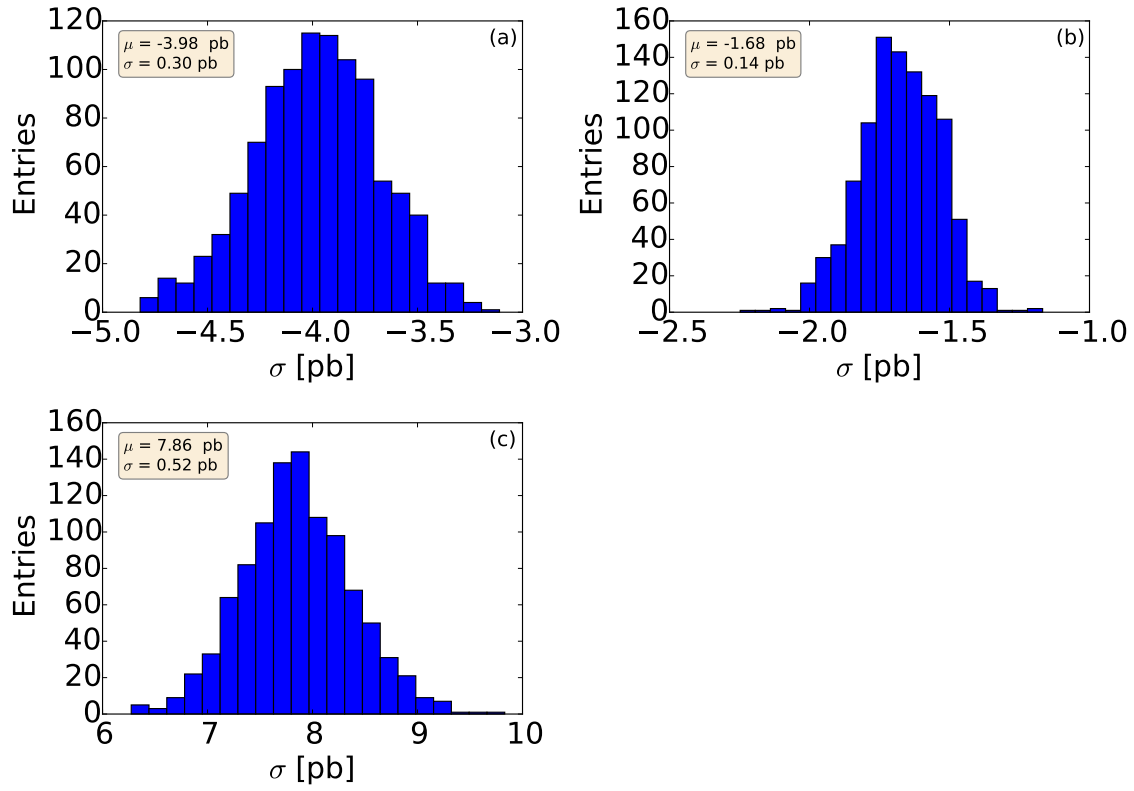
Figure 121: Distribution of the fitted cross section for the η_c reconstruction efficiency study. (a) $\sqrt{s} = 4.23$ GeV, (b) $\sqrt{s} = 4.26$ GeV, and (c) $\sqrt{s} = 4.36$ GeV.

ACRONYMS

BESIII Beijing Electron Synchroton III

CR Collector Ring

DAQ Data Acquisition

DAC Digital-to-Analogue Converter

DIRC Detector of Internally Reflected Cherenkov light

EMC Electromagnetic Calorimeter

FAIR Facility for Antiproton and Ion Research

FPGA Field Programmable Gate Array

GSI Helmholtzzentrum für Schwerionenforschung

MAPS Monolithic Active Pixel Sensor

HV-MAPS High Voltage - Monolithic Active Pixel Sensor

MDC Multilayer Drift chamber

MVD Micro Vertex Detector

HESR High Energy Storage Ring

HV-MAPS High Voltage Monolithic Active Pixel Sensor

PANDA Antiproton Annihilation at Darmstadt

PID Particle Identification

RESR Recycled Energy Storage Ring

STT Straw Tube Tracker

SODA Synchronization of Data Acquisition

QED Quantum Electrodynamics

QCD Quantum Chromodynamics

TOF Time-of-Flight

BIBLIOGRAPHY

[1] K.A. Olive et al. Review of Particle Physics. *Chin.Phys.*, C38:090001, 2014.

[2] G. Aad et al. Observation of a new particle in the search for the Standard Model Higgs boson with the ATLAS detector at the LHC. *Physics Letters B*, 716(1):1 – 29, 2012.

[3] S. Chatrchyan et al. Observation of a new boson at a mass of 125 GeV with the CMS experiment at the LHC. *Physics Letters B*, 716(1):30 – 61, 2012.

[4] Murray Gell-Mann. A Schematic Model of Baryons and Mesons. *Phys. Lett.*, 8:214–215, 1964.

[5] G. Zweig. An SU(3) model for strong interaction symmetry and its breaking. Version 1. 1964.

[6] O. W. Greenberg. Spin and Unitary Spin Independence in a Paraquark Model of Baryons and Mesons. *Phys. Rev. Lett.*, 13:598–602, 1964.

[7] M. Han and Y. Nambu. Three-Triplet Model with Double SU(3) Symmetry. *Phys. Rev. Lett.*, 139(4B), 1965.

[8] B. Povh, K. Rith, C. Scholz, and F. Zetsche. *Teilchen und Kerne.* Springer, 8. edition, 2009.

[9] D. Griffiths. *Introduction to Elementary Particles.* Wiley-VCH, 2. edition, 2008.

[10] K. G. Wilson. Confinement of quarks. *Phys. Rev. D*, 10:2445–2459, Oct 1974.

[11] E. Eichten et al. Spectrum of Charmed Quark-Antiquark Bound States. *Physical Review Letters*, 34(6), 1974.

[12] J. J. Aubert et al. Experimental Observation of a Heavy Particle J. *Phys. Rev. Lett.*, 33:1404–1406, Dec 1974.

[13] J. E. Augustin et al. Discovery of a Narrow Resonance in e^+e^- Annihilation. *Phys. Rev. Lett.*, 33:1406–1408, Dec 1974.

[14] S. L. Glashow, J. Iliopoulos, and L. Maiani. Weak Interactions with Lepton-Hadron Symmetry. *Phys. Rev. D*, 2:1285–1292, Oct 1970.

[15] E. G. Cazzoli et al. Evidence for $\Delta S = -\Delta Q$ Currents or Charmed-Baryon Production by Neutrinos. *Phys. Rev. Lett.*, 34:1125–1128, Apr 1975.

[16] R. Aaij et al. Observation of $J/\psi p$ Resonances Consistent with Pentaquark States in $\Lambda_b^0 \to J/\psi K^- p$ Decays. *Phys. Rev. Lett.*, 115:072001, Aug 2015.

[17] G. S. Bali. Lattice Calculations of hadron properties. *ArXiv e-prints*, 2003.

[18] S. Choi et al. Observation of a narrow charmonium-like state in exclusive $B^+ \to K^+\pi^+\pi^- J/\psi$. *Phys. Rev. Lett*, 91:262001, 2003.

[19] D. Acosta et al. Observation of a narrow state $X(3872) \to J/\psi\pi^+\pi^-$ in $p\bar{p}$ collisions at $\sqrt{s} = 1.96$ TeV. *Phys. Rev. Lett*, 93:072001, 2004.

[20] B. Aubert et al. Study of the $B^- \to J/\psi K^- \pi^+ \pi^-$ Decay and Measurement of the $B^- \to X(3872)K^-$ Branching Fraction. *Phys. Rev. Lett*, D71:071103, 2005.

[21] R. Aaij, , et al. Determination of the $X(3872)$ Meson Quantum Numbers. *Phys. Rev. Lett.*, 110:222001, May 2013.

[22] M. Ablikim et al. Observation of $e^+e^- \to \gamma X(3872)$ at BESIII. *Phys. Rev. Lett.*, 112:092001, Mar 2014.

[23] E. Braaten and M. Lu. Line shapes of the $X(3872)$. *Phys. Rev. D*, 76:094028, Nov 2007.

[24] C. Hanhart, Yu. S. Kalashnikova, A. E. Kudryavtsev, and A. V. Nefediev. Reconciling the $X(3872)$ with the near-threshold enhancement in the $D^0\overline{D}^{*0}$ final state. *Phys. Rev. D*, 76:034007, Aug 2007.

[25] R. Mizuk et al. Observation of two resonancelike structures in the $\pi^+\chi_{c1}$ mass distribution in exclusive $\overline{B}^0 \to K^-\pi^+\chi_{c1}$ decays. *Phys. Rev. D*, 78:072004, Oct 2008.

[26] J. P. Lees et al. Search for the $Z_1(4050)^+$ and $Z_2(4250)^+$ states in $\overline{B}^0 \to \chi_{c1}K^-\pi^+$ and $B^+ \to \chi_{c1}K_S^0\pi^+$. *Phys. Rev. D*, 85:052003, Mar 2012.

[27] B. Aubert et al. Observation of a Broad Structure in the $\pi^+\pi^-J/\psi$ Mass Spectrum around 4.26 GeV/c^2. *Phys. Rev. Lett.*, 95:142001, Sep 2005.

[28] B. Aubert et al. Evidence of a Broad Structure at an Invariant Mass of 4.32 GeV/c^2 in the Reaction $e^+e^- \to \pi^+\pi^-\psi(2S)$ Measured at *BABAR*. *Phys. Rev. Lett.*, 98:212001, May 2007.

[29] C. Yuan et al. Measurement of the $e^+e^- \to \pi^+\pi^-J/\psi$ Cross Section Via Initial-State Radiation at Belle. *Phys. Rev. Lett.*, 99:182004, Nov 2007.

[30] X. L. Wang et al. Observation of Two Resonant Structures in $e^+e^- \to \pi^+\pi^-\psi(2S)$ via Initial-State Radiation at Belle. *Phys. Rev. Lett.*, 99:142002, Oct 2007.

[31] T. Coan et al. Charmonium Decays of $Y(4260)$, $\psi(4160)$, and $\psi(4040)$. *Phys. Rev. Lett.*, 96:162003, Apr 2006.

[32] D. Cronin-Hennessy et al. Measurement of charm production cross sections in e^+e^- annihilation at energies between 3.97 and 4.26 GeV. *Phys. Rev. D*, 80:072001, Oct 2009.

[33] B. Aubert et al. Exclusive initial-state-radiation production of the $D\overline{D}$, $D^*\overline{D}$, and $D^*\overline{D}^*$ systems. *Phys. Rev. D*, 79:092001, May 2009.

[34] P.del Amo Sanchez et al. Exclusive production of $D_s^+D_s^-$, $D_s^{*+}D_s^-$, and $D_s^{*+}D_s^{*-}$ via e^+e^- annihilation with initial-state radiation. *Phys. Rev. D*, 82:052004, Sep 2010.

[35] Z. Q. Liu et al. Study of $e^+e^- \to \pi^+\pi^-J/\psi$ and Observation of a Charged Charmoniumlike State at Belle. *Phys. Rev. Lett.*, 110:252002, Jun 2013.

[36] T. Xiao et al. Observation of the charged hadron $Z_c^{\pm}(3900)$ and evidence for the neutral $Z_c^0(3900)$ in $e^+e^- \to J/\psi\pi^+\pi^-$ at $\sqrt{s} = 4170$ MeV. *Physics Letters B*, 727(4-5):366 – 370, 2013.

[37] M. Ablikim et al. Observation of $Z_c(3900)^0$ in $e^+e^- \to \pi^0\pi^0 J/\psi$. *Phys. Rev. Lett.*, 115(11):112003, 2015.

[38] M. Ablikim et al. Observation of a charged $(D\bar{D}^*)^{\pm}$ mass peak in $e^+e^- \to \pi D\bar{D}^*$ at $\sqrt{s} = 4.26$ GeV. *Phys. Rev. Lett.*, 112(2):022001, 2014.

[39] M. Ablikim et al. Observation of a Charged Charmoniumlike Structure $Z_c(4020)$ and Search for the $Z_c(3900)$ in $e^+e^- \to \pi^+\pi^- h_c$. *Phys. Rev. Lett.*, 111:242001, Dec 2013.

[40] M. Ablikim et al. Observation of $e^+e^- \to \pi^0\pi^0 h_c$ and a Neutral Charmoniumlike Structure $Z_c^0(4020)$. *Phys. Rev. Lett.*, 113:212002, Nov 2014.

[41] M. others Ablikim. Observation of a Charged Charmoniumlike Structure in $e^+e^- \to (D^*\overline{D}^*)^{\pm}\pi^{\mp}$ at $\sqrt{s} = 4.26$ GeV. *Phys. Rev. Lett.*, 112:132001, Apr 2014.

[42] M. Ablikim et al. Observation of a Neutral Charmoniumlike State $Z_c(4025)^0$ in $e^+e^- \to (D^*\overline{D}^*)^0\pi^0$. *Phys. Rev. Lett.*, 115:182002, Oct 2015.

[43] C. Zhang et al., editors. *Construction and Commisssioning of BEPCII*, 2009.

[44] D. Asner et al. Physics at BES-III. *arXiv:0809.1869*, 2008.

[45] M. Ablikim et al. Measurement of the Matrix Elements for the Decays $\eta \to \pi^+\pi^-\pi^0$ and $\eta/\eta' \to \pi^0\pi^0\pi^0$. *Phys. Rev. D*, 92(1):012014, 2015.

[46] M. Ablikim et al. Observation of the Dalitz Decay $\eta' \to \gamma e^+e^-$. *Phys. Rev. D*, 92(1):012001, 2015.

[47] J. Z. Bai et al. Observation of a Near-Threshold Enhancement in the $p\bar{p}$ Mass Spectrum from Radiative $J/\psi \to \gamma p\bar{p}$ Decays. *Phys. Rev. Lett.*, 91:022001, Jul 2003.

[48] M. Ablikim et al. Observation of a Resonance $X(1835)$ in $J/\psi \to \gamma\pi^+\pi^-\eta'$. *Phys. Rev. Lett.*, 95:262001, Dec 2005.

[49] M. Ablikim et al. Confirmation of the $X(1835)$ and Observation of the Resonances $X(2120)$ and $X(2370)$ in $J/\psi \to \gamma\pi^+\pi^-\eta'$. *Phys. Rev. Lett.*, 106:072002, Feb 2011.

[50] M. Ablikim et al. Design and construction of the BESIII detector. *Nuclear Instruments and Methods in Physics Research A*, 2010.

[51] H. H. Gutbrod et al. FAIR Baseline Technical Design Report, Executive Summary. *FAIR publications*, 2006.

[52] CBM collaboration. Letter of Intent for the Compressed Baryonic Matter Experiment at the Future Accelerator Facility in Darmstadt. 2004.

[53] R. Krücken and the NuSTAR collaboration. The NuSTAR facilty at FAIR. *Journal of Physics G: Nuclear and Particle Physics*, 31(10):S1807, 2005.

[54] Th. Stoehlker et al. APPA at FAIR: From fundamental to applied research. *Nuclear Instruments and Methods in Physics Research Section B: Beam Interactions with Materials and Atoms*, 365, Part B:680 – 685, 2015. Swift Heavy Ions in Matter, 18 - 21 May, 2015.

[55] G. Rosner. Future Facility: FAIR at GSI. *Nuclear Physics B - Proceedings Supplements*, 167:77 – 81, 2007. Proceedings of the 7th International Conference on Hyperons, Charm and Beauty Hadrons HYPERONS, CHARM AND BEAUTY HADRONS.

[56] L. Groening et al. The 70 MeV Proton LINAC for the Facility for Antiproton and Ion Research FAIR. In *Proceedings of LINAC 2006*, 2006.

[57] A. Dolinskii et al. Antiproton complex at the FAIR project. *NIM A*, 629, 2011.

[58] H. Xu et al. Day-1 Experiment at Panda for Parameters of $p\bar{p}$ elastic scattering determination. 2014.

[59] T. Stoehlker et al. New Strategy for Storage Ring Physics at FAIR. *Hyperfine Interact*, 227:45-53, 2014.

[60] H. Geissel et al. Deeply Bound $1s$ and $2p$ Pionic States in ^{205}Pb and Determination of the s-Wave Part of the Pion-Nucleus Interaction. *Phys. Rev. Lett.*, 88:122301, Mar 2002.

[61] M. Nekipelov, V. Koptev, and the ANKE Collaboration. Investigation of K + -meson Production in p A Collisions with ANKE. *Physica Scripta*, 2003(T104):40, 2003.

[62] P. Crochet et al. Sideward flow of K+ mesons in Ru + Ru and Ni + Ni reactions near threshold. *Phys. Lett.*, B486:6–12, 2000.

[63] PANDA Collaboration. Technical Design Report for the PANDA Luminosity Detector. to be published.

[64] W. Erni et al. Technical Design Report for the: PANDA Micro Vertex Detector. *arxiv:1207.6581*, 2012.

[65] W. Erni et al. Technical design report for the PANDA (AntiProton Annihilations at Darmstadt) Straw Tube Tracker. *Eur. Phys. J.*, A49:25, 2013.

[66] PANDA Collaboration. Physics Performance Report for PANDA: Strong Interaction Studies with Antiprotons. *arxiv:0903.3905*, 2009.

[67] H. Xu, Z.-A. Liu, Q. Wang, W. Kuehn, S. Lang, and M.Liu. Introduction to PANDA Data Acquisition System. *Physics Procedia*, 37:1855 – 1860, 2012. Proceedings of the 2nd International Conference on Technology and Instrumentation in Particle Physics (TIPP 2011).

[68] K. Korcyl et al. Modeling event building architecture for the triggerless data accquisiton system for PANA experiment at the HESR facility at FAIR/GSI. *Journal of Physics 396(012027)*, 2012.

[69] S. Trokenheim. Precision Measurements of Antiproton-Proton Elastic Scattering at Small Momentum Transfers. *Dissertation*, June 1995.

[70] H. Bethe. Zur Theorie des Durchgangs schneller Korpuskularstrahlen durch Materie. *Ann. Phys., 397: 325-400*, 1930.

[71] W.R. Leo. *Techniques for Nuclear and Particle Physics Experiments*. Springer, 2. edition, 1994.

[72] H. H. Leithoff. *A Cooling System for the PANDA Luminosity Detector*. Phd-thesis, Helmholtz Institute Mainz, too be published.

[73] H. Ibach and H. Lueth. *Festkörperphysik*. Springer, 7. edition, 2008.

[74] R. C. Alig, S. Bloom, and C. W. Struck. Scattering by ionization and phonon emission in semiconductors. *Phys. Rev. B*, 22:5565–5582, Dec 1980.

[75] H. Spieler. *Semiconductor Detector Systems*. Oxford Science Publications, 2009.

[76] R. Turchetta et al. A monolithic active pixel sensor for charged particle tracking and imaging using standard VLSI CMOS technology. *Nuclear Instruments and Methods A*, 458:677–689, 2001.

[77] A. Dorokov et al. High resistivity CMOS pixel sensors and their application to the STAR PXL detector. *Nuclear Instruments and Methods A*, 650:174–177, 2011.

[78] G. Deptuch et al. Design and Testing of Monolithic Active Pixel Sensors for Charged Particle Tracking. *IEEE Transactions on Nuclear Science*, 49, 2002.

[79] I. Perić. A novel monolithic pixelated particle detector implemented in high voltage CMOS technology. *Nucl. Instrum. Meth. A*, 582, 2007.

[80] I. Perić et al. The first beam test of a monolithic particle pixel detector in high-voltage CMOS technology. *Nucl. Instrum. Meth. A*, 628, 2011.

[81] N. Berger. The Mu3e Experiment. *Nuclear Physics B*, 248-250:35 – 40, 2014.

[82] H. Augustin. *Characterization of novel HV-MAPS Sensor with two Amplification Stages and first examination of thinned MuPix Sensors*. Master-thesis, University of Heidelberg, 2014.

[83] M. Traxler et al. A compact system for high precision time measurements (< 14 ps RMS) and integrated data acquisition for a large number of channels. *Journal of Instrumentation*, 6(12):C12004, 2011.

[84] The Qt-Company. Qt Framework. `https://www.qt.io/`, 2016.

[85] J. Phillip. *Effizienzanalyse von HV-MAPS anhand des MuPix Teleskops*. Bachelor-thesis, University of Heidelberg, 2015.

[86] J. Hammerich. *Studies of HV-MAPS analog performance*. Bachelor-thesis, University of Heidelberg, 2015.

[87] L. Huth. *Development of a Tracking Telescope for Low Momentum Particles and High Rates consisting of HV-MAPS*. Master-thesis, University of Heidelberg, 2014.

[88] S. Radovanovic et al. *High-Speed Photodiodes in Standard CMOS Technology*. Springer Science and Business Media, 2006.

[89] Yunan Fu. *Development of CMOS Pixel Sensors for a Vertex Detector Suited for the ILC*. Phd-thesis, University of Strasbourg, May 2012.

[90] I. Abt et al. CATS: A cellular automaton for tracking in silicon for the HERA-B vertex detector. *Nucl. Instrum. Meth.*, A489, 2002.

[91] A. Karavdina. *Preparation for the accurate luminosity measurement by antiproton-proton elastic scattering and feasibility study for observation of h_c hadronic decay modes at the PANDA experiment.* Phd-thesis, Johannes Gutenberg-Universität Mainz, 2015.

[92] G. Lutz et al. Optimum Track Fitting in the Presence of Multiple Scattering. *Nucl. Instrum. Meth.*, A273, 1988.

[93] V. Blobel and C. Kleinwort. A new method for the high precision alignment of track detectors. *arXiv:hep-ex:0208021*, 2002.

[94] I. Rubinskiy. An EUDET/AIDA pixel beam telescope for detector development. *Physics Procedia*, 37, 2012.

[95] M. Ablikim et al. Measurement of the center-of-mass energies at BESIII via the di-muon process. *arXiv, 1510.08654*, 2015.

[96] S. Agostinelli et al. GEANT4: A Simulation toolkit. *Nucl. Instrum. Meth.*, A506:250–303, 2003.

[97] S. Jadach, B. F. L. Ward, and Z. Wąs. Coherent exclusive exponentiation for precision Monte Carlo calculations. *Phys. Rev. D*, 63:113009, May 2001.

[98] Ping Rong-Gang. Event generators at BESIII. *Chinese Physics C*, 32(8):599, 2008.

[99] A. Ryd. EvtGen A Monte Carlo Generator for B-Physics. *Babar Analysis Document 522 V6 EvtGen V00-11-06*, 2004.

[100] M. Ablikim et al. Study of $\psi(3686) \to \pi^0 h_c$, $h_c \to \gamma \eta_c$ via η_c exclusive decays. *Phys. Rev. D*, 86:092009, Nov 2012.

[101] S. Mrenna T. Sjöstrand and P. Skands. A brief introduction to PYTHIA. *JHEP05 (2006) 026, Comput. Phys. Comm. 178 852*, 2008.

[102] W. Verkerke and D. P. Kirkby. The RooFit toolkit for data modeling. *eConf*, C0303241:MOLT007, 2003. [,186(2003)].

[103] G. C. Fox et al. Observables for the Analysis of Event Shapes in e^+e^- Annihilation and Other Processes. *Phys. Rev. Lett.*, 41(23), 1978.

[104] G. Hanson et al. Evidence for Jet Structure in Hadron Production by e^+e^- Annihilation. *Phys. Rev. Lett.*, 35(1609), 1975.

[105] W. Eadie et al. *Statistical Methods in Experimental Physics.* North-Holland Publ. Co., 1971.

[106] M. Ablikim et al. Measurements of $h_c(^1P_1)$ in ψ' Decays. *Phys. Rev. Lett.*, 104:132002, Mar. 2010.

[107] S. Dobbs et al. Precision Measurement of the Mass of the $h_c(^1P_1)$ State of Charmonium. *Phys. Rev. Lett.*, 101:182003, Oct. 2008.

[108] M. Ablikim et al. Study of χ_{cJ} radiative decays into a vector meson. *Phys. Rev. Lett.*, D:112005, 2011.

[109] M. Ablikim et al. Branching fraction measurement of χ_{c0} and χ_{c2} to $\pi^0\pi^0$ and $\eta\eta$. *Phys. Rev. Lett.*, D:052005, 2010.

[110] T. Ma. Study of D^+ to $K_s\pi$ and $K_L\pi$. BESIII Analysis Memo, 2015.

[111] The offline luminosity measurement of data for studying XYZ particles at BESIII, 2013.

[112] G. Zech and G. Bohm. *Einfuehrung in Statistik und Messwertanalyse fuer Physiker.* Deutsches Elektron Synchroton in der Helmholtz Gemeinschaft Zentralbibliothek, 2006.

[113] Z. Liu et al. Precise measurement of the $e^+e^- \to \pi^+\pi^- J/\psi$ cross section at BESIII. BESIII Analysis Memo, 2016.

[114] M. Meyer. *Signalverarbeitung.* Springer, 7. edition, 2014.

[115] H. Augustin. Personal Communication. March 2015.

Tobias Weber

136 Prospect Street
Honolulu, HI 96813
☎ *1 808 358 9148*
✉ *webert@hawaii.edu*

Personal Information

Name	Tobias Weber
Address	136 Prospect Street Honolulu, HI 96813
Date of Birth	20. Februar 1986, Neuwied Germany
Nationality	German

Professional Experience

July 2016 – present	Research Scholar at the Department of Physics and Astronomy, University of Hawaii
June 2015 – July 2016	Research Assistant at the Collaborative Research Center for The Low-Energy Frontier of the Standard Model, Institute for Nuclear Physics, Johannes Gutenberg-Universität Mainz, Germany
June 2013 – June 2015	Fellow at the DFG Graduate School Symmetry Breaking in Fundamental Interactions
April 2012 – June 2013	Research Assistant Helmholtz Institute Mainz, Germany

---

Education

April 2012 – June 2016	PhD studies in Physics, Johannes Gutenberg-Universität Mainz, Germany Titel of Dissertation: *High Voltage Monolithic Active Pixel Sensors for the Panda Luminosity Detector and Search for the Decay $Y(4260) \rightarrow \eta_c \eta \pi^+ \pi^-$ at BESIII*
November 2011	Diploma in physics (*grade: 1.1*), Titel of thesis: *Characterization of double sided silicon strip sensors and sumulation of a resonance scan of the X(3872)*
Aprile 2006 – November 2011	University studies of physics, Johannes Gutenberg-Universität Mainz, Germany
1998–2005	General qualification for university entrance, Martinus Gymnasium Linz, Germany *grade: 2.0*

Teaching Experience

Aprile 2008 – June 2011	Teaching assistant for lecture accompanying tutorial sessions
June 2012 – December 2013	Laboratory instructor *High Resolution Gamma Spectroscopy with Germanium Detectors* in advanced lab courses

---

Stays Abroad

August 2008 – Aprile 2009	Exchange Student, Lund University, Sweden

June 2013 – December 2014	Regulary researchs visits at the institute of high energy physics (IHEP) Beijing, China

Honolulu, October 26, 2016